Springer Tracts in Modern Physics 243

Alexander Petrovich Potylitsyn

Electromagnetic Radiation of Electrons in Periodic Structures

Springer

Springer Tracts in Modern Physics

Volume 243

For further volumes:
http://www.springer.com/series/426

Springer Tracts in Modern Physics

Springer Tracts in Modern Physics provides comprehensive and critical reviews of topics of current interest in physics. The following fields are emphasized: elementary particle physics, solid-state physics, complex systems, and fundamental astrophysics.

Suitable reviews of other fields can also be accepted. The editors encourage prospective authors to correspond with them in advance of submitting an article. For reviews of topics belonging to the above mentioned fields, they should address the responsible editor, otherwise the managing editor.

See also springer.com

Alexander Petrovich Potylitsyn

Electromagnetic Radiation of Electrons in Periodic Structures

Springer

Alexander Petrovich Potylitsyn
Tomsk Polytechnic University
Lenina Ave. 30
634050 Tomsk
Russia
e-mail: pap@interact.phtd.tpu.ru

ISSN 0081-3869 e-ISSN 1615-0430

ISBN 978-3-642-19247-0 e-ISBN 978-3-642-19248-7

DOI 10.1007/978-3-642-19248-7

Springer Heidelberg Dordrecht London New York

Cover design: eStudio Calamar, Berlin/Figueres

Printed on acid-free paper

Springer is part of Springer Science+Business Media (www.springer.com)

Foreword

The sources of quasimonochromatic radiation of electrons, which are based on their passing through various periodic structures (undulator, crystal, field of laser flash), as well as close to the optical gratings (Smith-Purcell radiation) are considered in this monograph. Alongside with such traditional radiation mechanisms, as the coherent bremsstrahlung and undulator radiation, which properties have been investigated in details in the last 50–60 years, relatively new radiation mechanisms (parametric X-ray radiation, Smith-Purcell radiation, radiation of electrons in the field of laser flash) have been significantly attended in this book.

The theory bases of the considered effects are stated, as well as the recent experimental results are described in this book.

Tomsk, 2010 Alexander Petrovich Potylitsyn

Preface

In the existing literature there are a number of monographs, with sufficient completeness describing such traditional radiation mechanisms, as undulator radiation, bremsstrahlung, coherent bremsstrahlung, transition radiation. However, the interest has appreciably increased in recent years to such effects, as parametric X-ray radiation, Smith-Purcell radiation, Compton-effect on the relativistic electrons (which can be treated as radiation in a "light" undulator).

These new mechanisms of radiation, as well as some others (for example, the resonant transition radiation) have the common characteristic i.e. the radiation is quasimonochromatic one because of the constructive interference of radiation fields from each element of periodic structure.

An attempt to assemble the results of the numerous theoretical and experimental works devoted to investigation of radiation, which is generated by relativistic electrons in different periodic structures with the period from $\sim 10^{-8}$ cm (the crystals) up to ~ 1 cm (undulators) is made in this book. Author tried to present the book contents in the form being available for researchers planning the usage of radiation beams for applied purposes, as well as for beginning scientists. So, the list of quoted literature does not claim to be exhaustive.

The author is very much obliged to colleagues B.N. Kalinin, V.N. Zabaev, I.E. Vnukov, Yu.N. Adischev, G.A. Naumenko, V.V. Kaplin, S.R. Uglov, A.S. Gogolev, V.A. Verzilov, D.V. Karlovets, L.G. Sukhikh (Tomsk Polytechnic University), prof. I. Endo (Hiroshima University, Japan), prof. K. Yoshida, prof. H. Okuno (the Institute of Nuclear Studies, Tokyo University, Japan), Dr. T. Suwada (the National Accelerating Center KEK, Japan), who are his co-authors in numerous experimental studies, in a varying level reflected in the book.

The author is also grateful to prof. B.M. Bolotovsky, prof. N.F. Shul'ga, prof. N.N. Nasonov, prof. E.G. Bessonov, prof. V.M. Katkov, prof. V.M. Strakhovenko, prof. V.G. Serbo, prof. M.N. Strikhanov, prof. M.I. Ryazanov, prof. K.A. Ispiryan, prof. H. Backe, Dr. G. Kube, Dr. A.V. Shchagin, Dr. A.A. Tishchenko for stimulating discussions, which certainly have influenced upon the content of the book.

Author expresses the special thanks to L.V. Puzyrevich, E.A. Babakhanyan for the invaluable help in preparing the manuscript for publication.

References

1. Ter-Mikaelyan, M.L.: High-Energy Electromagnetic Processes in Condensed Media, p. 7, 15. Wiley-Interscience, New York (1972)
2. Landau, L.D., Lifshitz, E.M.: The Classical Theory of Fields. Pergamon Press, Oxford (1987)
3. Jackson, J.D.: The Classical Electrodynamics, 3rd ed, Wiley, New York (1998)
4. Saenz, A.W., Uberall, H. (Eds.): Coherent Radiation Sources, (see Topics in Current Physics 38) Springer, Berlin (1985)
5. Ginzburg, V.L., Tsytovich, V.N.: Transition Radiation and Transition Scattering. Adam Hilger, Bristol (1990)
6. Baier, V.N., Katkov, V.M., Strakhovenko, V.M.: Electromagnetic Processes at High Energies in Oriented Single Crystals. World Scientific, Singapore (1998)

Contents

Chapter 1
Introduction

The periodic magnetic structures (undulators) are widely used in many accelerator centers for generation of the monochromatic radiation in the wavelength range from the far infrared up to the γ-range. The emission spectrum in such a periodic structure is quasimonochromatic due to a constructive interference of radiation fields generated by a charged particle on each element of the structure.

The trajectory of a particle in such a magnetic system is either a periodic plane curve (close to a sinusoidal one) in the plane undulator, or spiral one in the helical undulator. The period of a trajectory d in both cases is defined by the period of undulator and, as a rule, due to the technical reasons it cannot be chosen much less than 1 cm.

The resonance condition, connecting an emission frequency ω and the photon outgoing angle θ (along the unit vector $\mathbf{n}$), can be written in the form:

$$\omega = \frac{k\,\Omega}{1 - \mathbf{n}\frac{\langle \mathbf{V}_{\|} \rangle}{c}} = \frac{k\,\Omega}{1 - \frac{\langle \mathbf{V}_{\|} \rangle}{c}\cos\theta}; \quad k = 1, 2, 3, \ldots, \tag{1.1}$$

where Ω denotes the frequency of a trajectory disturbance, $\langle \mathbf{V}_{\|} \rangle$—an average longitudinal velocity of the electron. For ultrarelativistic particles with Lorentz-factor $\gamma \gg 1$ and emission angles of photons $\theta \sim \gamma^{-1} \ll 1$ this expression is written as [1]:

$$\omega = \frac{2k\Omega\gamma^2}{1 + \gamma^2\theta^2 + \gamma^2\langle \beta_{\perp}^2 \rangle}, \tag{1.2}$$

where $\langle \beta_{\perp}^2 \rangle$ is a mean square velocity of electron in transverse direction in units of the speed of light.

In the case of undulator radiation (UR)

$$\Omega \approx \frac{2\pi c}{d} \sim 10^{11}\ \mathrm{s}^{-1} \tag{1.3}$$

A. P. Potylitsyn, *Electromagnetic Radiation of Electrons in Periodic Structures*, Springer Tracts in Modern Physics, 243, DOI: 10.1007/978-3-642-19248-7_1,

It should be pointed out that relationship (1.2) does not depend on the determined mechanism of radiation. During the passing of relativistic electron through a crystal the straight trajectory of a particle has been disturbed with a period $d \sin \psi$ (d is a period of crystalline lattice, ψ is the angle between crystalline axis and particle momentum), which is just the reason of the quasimonochromatic radiation occurrence named the coherent bremsstrahlung (CBS).

In pioneering works devoted to the bremsstrahlung process in an oriented monocrystaline target [2, 3] authors used the term "interference effect of bremsstrahlung" and only a few years later in the work of Diambrini [4] the term "coherent bremsstrahlung" was introduced.

Nowadays one understands "coherent radiation" as a radiation from a charged particle ensemble (bunch) if the emission wavelength is greater than a bunch length. Authors of the works [5, 6] used the term "coherent bremsstrahlung" considering the process of radiation of a charged particles bunch caused by the collective electromagnetic field of the counterpropagating bunch.

In order to keep the traditional terminology the process of bremsstrahlung in a crystal will be described as the coherent bremsstrahlung. But a reader should have in mind that this process is the resonant bremsstrahlung only.

In the CBS case ($d \backsim 5$ Å, $\psi \sim 10^{-2}$ rad), and, therefore, $\Omega \approx 2\pi c\psi/d = 4 \times 10^{16}\,\mathrm{s}^{-1}$.

However despite such a big difference of natural frequencies (five orders of magnitude), the main characteristics of the radiation have been described by the similar formulae just because of the fact that spectral–angular distribution of both types of radiation is defined by the formula (1.2), so, as a rule, the typical energy of CBS photons is such that it is possible to neglect their absorption in crystal.

At present the UR and CBS generated by the beams of ultrarelativistic electrons in the modern accelerators are widely used both in the applied, and in the basic investigations (see, for example, the books [1, 7–9]) in many respects due to such characteristics, as monochromaticity, polarization, tunability, which are the result of radiation generation in the periodic structure.

In recent years the great interest has been attracted to such types of radiation generated by the electron beams, as the resonant transition radiation, Smith–Purcell radiation, Compton scattering of laser photons by a counterpropagated relativistic electron beam. In spite of the difference in mechanisms, the main characteristics of the radiation are defined by periodicity of the structure, through which (or close to which, as in the case of the Smith–Purcell radiation) the beam of electrons passes. From this point of view the process of Compton scattering of the laser photons on the beam of electrons can be considered as the radiation of electrons in the "light" undulator.

The theoretical approaches describing the different radiation mechanisms from the unified point of view are described in presented monograph, as well as the most interesting experimental results received last years are given here.

In conclusion it should be noted that all radiation mechanisms may be divided in two classes [1]:

- Radiation from the accelerated charge;
- Radiation from polarization currents induced in the condensed media through which (or close to) the relativistic charge passes.

The first class is more known (synchrotron and undulator radiation, bremsstrahlung, radiation from electrons interacting with intense laser field), and the second one called polarization bremsstrahlung includes such kinds of emission as Cherenkov radiation, transition radiation [10], Smith–Purcell radiation [11] and so on. Despite such a big distinction in origin of radiation mechanisms mostly important features of radiation from different periodic structures are common and may be calculated using the unified approach.

References

1. Rullhusen, P., Artru, X., Dhez, P.: Novel Radiation Sources using Relativistic Electrons. World Scientific, Singapore (1998)
2. Ter-Mikaelyan, M.L.: Interference radiation from superfast electrons. Zh. Eksp. Teor. Fiz. **25**, 296 (1953). (in Russian)
3. Uberall, H.: High-energy interference effect of Bremsstrahlung and pair production in crystals. Phys. Rev. **103**, 1055 (1956)
4. Diambrini Palazzi, G.: High-energy Bremsstrahlung and electron pair production in thin crystals. Rev. Mod. Phys. **40**, 611 (1968)
5. Ginsburg, I.F., Kotkin, G.L., Polityko, S.I., Serbo, V.G.: Coherent Bremsstrahlung at colliding beams. Phys. Lett. B **286**, 392 (1992)
6. Polityko, S.I., Serbo, V.G.: Coherent Bremsstrahlung at the B factories SLAC PEP II and KEK Tristan-B. Phys. Rev. E. **51**, 2493 (1995)
7. Ter-Mikaelyan, M.L.: High-Energy Electromagnetic Processes in Condensed Media. Wiley-Interscience, New York (1972)
8. Saenz, A.W., Uberall, H.: Coherent Radiation Sources. Topics in Current Physics, vol. 38. Springer, Heidelberg (1985)
9. Baier, V.N., Katkov, V.M., Strakhovenko, V.M.: Electromagnetic Processes at High Energies in Oriented Single Crystals. World Scientific, Singapore (1998)
10. Ginsburg, V.L., Tsytovich, V.N.: Transition Radiation and Transition Scattering. Adam Hilger, Bristol (1990)
11. Potylitsyn, A.P., Ryazanov, M.I., Strikhanov, M.N., Tishchenko, A.A.: Diffraction Radiation from Relativistic Particles. Springer, Berlin (2010)

Chapter 2
Basic Characteristics of Electromagnetic Radiation

2.1 Radiation Characteristics in the Classical and Quantum Electrodynamics

In case of charged particle motion in an external field, one of the most fruitful approaches allowing to calculate the characteristics of radiation, generated by a particle with charge e, is an approach, where a trajectory $\mathbf{r}(t)$ of the particle in the given field has been found at first, and then the electric and magnetic components of the electromagnetic field are defined according to the rules of classical electrodynamics [1]:

$$\mathbf{E}(t) = \frac{e\left(1-\beta^2\right)(\mathbf{n}-\boldsymbol{\beta})}{R^2(1-\mathbf{n}\boldsymbol{\beta})^3} + \frac{e\left[\mathbf{n}\left[(\mathbf{n}-\boldsymbol{\beta})\,\dot{\boldsymbol{\beta}}\right]\right]}{\mathrm{c}R(1-\mathbf{n}\boldsymbol{\beta})^3}, \tag{2.1.1a}$$

$$\boldsymbol{H}(t) = [\mathbf{n}(t')\mathbf{E}(t)]. \tag{2.1.1b}$$

In these expressions $c\beta = \dot{r}(t)$, $\mathbf{n}$ is a unit vector in direction connecting the observation point with a charge at the retarded moment of time t',

$$t - t' = \frac{|\mathbf{R} - \mathbf{r}(t')|}{c}. \tag{2.1.2}$$

Here $\mathbf{R}$ is a radius-vector of the observation point.

It is clear, the similar approach gives the reasonable results in a case when it is possible to neglect the particle energy losses due to photon emission (radiation losses), i.e. when the process of radiation has no influence upon a trajectory of the particle.

The first summand term in the formula (2.1.1a) being proportional to R^{-2} does not depend on acceleration of the charge $\dot{\boldsymbol{\beta}}$ and characterizes the quasi-stationary Coulomb field of the moving charge itself (so called "velocity field") while the

A. P. Potylitsyn, *Electromagnetic Radiation of Electrons in Periodic Structures*, Springer Tracts in Modern Physics, 243, DOI: 10.1007/978-3-642-19248-7_2,

second summand being inversely proportional to the distance R and depending on the charge acceleration, characterizes the radiation wave field ("acceleration field") [1]. The range of the distances R, where the contribution of the first summand is negligible in comparison with the contribution of the second one, refers to the wave (or far-field) zone. In the wave zone both components of the field (2.1.1a) and (2.1.1b) are perpendicular to the vector $\mathbf{n}$ that allows to introduce the Poynting's vector $\mathbf{S} = [\mathbf{EH}]$, directed along a wave vector and describing the density of the energy flow of the electromagnetic wave.

The angular distribution of an energy flow (intensity) in a solid angle $d\Omega$ (the value defined in the observation point) is determined through the Poynting's vector:

$$\frac{dI}{d\Omega} = \frac{cR^2}{4\pi}|\mathbf{S}| = \frac{cR^2}{4\pi}|\mathbf{E}|^2. \tag{2.1.3}$$

The angular distribution of the power of particle radiation losses (with a value determined in a particle position) is connected with intensity (2.1.3) as follows:

$$\frac{dP}{d\Omega} = (1 - \mathbf{n}\boldsymbol{\beta})\frac{dI}{d\Omega}. \tag{2.1.4}$$

Going over to Fourier-components of a field, it is possible to get the expressions

$$\begin{aligned} \mathbf{E}(\omega) &= \frac{e}{cR}e^{ikR}\int \frac{\left[\mathbf{n}\left[(\mathbf{E}-\boldsymbol{\beta})\dot{\boldsymbol{\beta}}\right]\right]}{(1-\boldsymbol{\beta}\mathbf{n})^2}e^{i(\omega t - kr)}dt, \\ H(\omega) &= [\mathbf{n}\,\mathbf{E}(\omega)]. \end{aligned} \tag{2.1.5}$$

Substituting the received expressions in (2.1.3), it is possible to receive the spectral–angular distributions:

$$\frac{dI}{d\omega\, d\Omega} = \frac{cR^2}{4\pi}|\mathbf{E}(\omega)|^2. \tag{2.1.6}$$

As a rule, the radiation is formed by a source with a finite area S, moreover, this source can emit the electromagnetic waves (the photons) anisotropically. In this case the radiation is characterized by *brightness*

$$L = \frac{dP}{d\Omega\, dS}\left[\frac{W}{\mathrm{sr}\times \mathrm{m}^2}\right] \tag{2.1.7}$$

and *spectral brightness*:

$$\frac{dL}{d\omega} = \frac{dP}{d\omega\, d\Omega\, dS}\left[\frac{W}{\mathrm{s}^{-1}\times \mathrm{sr}\times \mathrm{m}^2}\right]. \tag{2.1.8}$$

For the radiation with frequencies from optical and above ones the spectral brightness is often assigned through the number of photons. Using the Planck's

law $\varepsilon = \hbar\omega$ in semi-classical approach, the energy characteristics are expressed through the number of photons N:

$$dP = \varepsilon \frac{dN}{dt}. \tag{2.1.9}$$

Then instead the spectral brightness one may use the *brilliance*

$$\frac{dL}{d\varepsilon} = B = \frac{dN}{dt\ d\Omega\ dS\, d\varepsilon/\varepsilon}\left[\frac{\text{photon}}{\text{s} \times \text{sr} \times \text{m}^2 \times d\varepsilon/\varepsilon}\right]. \tag{2.1.10}$$

The spectral–angular density of radiation is got after the integration on the source area

$$I(\theta, \psi, \varepsilon) = \int\limits_S B\, dx\, dy \left[\frac{\text{photon}}{s \times sr \times \Delta\varepsilon/\varepsilon}\right]. \tag{2.1.11}$$

The spectral flux (spectral density) is calculated after the integration over a solid angle

$$\Phi_S(\varepsilon) = \int B\, dx\, dy\, d\Omega \left[\frac{\text{photon}}{\text{s} \times \Delta\varepsilon/\varepsilon}\right]. \tag{2.1.12}$$

And finally, the radiation flux is received via the integration over a spectrum:

$$\Phi = \int \Phi_S(\varepsilon)\, d\varepsilon/\varepsilon \left[\frac{\text{photon}}{\text{s}}\right]. \tag{2.1.13}$$

The field strength of the monochromatic electromagnetic wave (for example, the laser radiation) is characterized by the dimensionless parameter:

$$a_0 = \sqrt{\frac{2e^2\langle A^2\rangle}{(mc^2)^2}} = \frac{e\,E_0}{mc\,\omega}. \tag{2.1.14}$$

In the last formula by $\langle A^2\rangle$ a mean-square value of an electromagnetic vector potential is designated, E_0 is an amplitude of a wave.

In the majority of experiments the beams of the electromagnetic radiation, formed by means of different optical systems, including, for instance, mirrors, apertures, lenses, etc. are used. In this case, the radiation power can be distributed on the area of the target according to an arbitrary law. Then after the integration with respect to the beam cross-section, we can receive:

$$P = \int\limits_\sigma \frac{dP}{dS} d\sigma = I\sigma_{\text{eff}}, \tag{2.1.15}$$

where $I = \langle dP/dS \rangle$ is an averaged value of the power flux density, σ_{eff} is an effective area of the beam. In the laser physics, the parameter laser field strength [2] is often used

$$I = \frac{P}{\sigma_{\text{eff}}}, \qquad [I] = \text{W/cm}^2, \tag{2.1.16}$$

which can be expressed through the density of the energy of the laser flash ρ:

$$I = \frac{P \times c\tau}{\sigma_{\text{eff}} \times c\tau} = c\frac{W}{V} = c\rho. \tag{2.1.17}$$

In the last expression through τ is designated the flash duration, V is a volume, occupied with laser photons. Then instead of (2.1.14), it is possible to receive a more evident formula:

$$a_0^2 = \frac{2r_0 I\lambda^2}{\pi mc^3} = \frac{2r_0\lambda^2\,\rho}{\pi mc^2}, \tag{2.1.18}$$

where $r_0 = 2.82 \times 10^{-13}$ is the classical radius of an electron, as well as the "engineering" formula:

$$a_0 = 0.85 \times 10^{-9}\lambda\ [\mu]\ I^{1/2}\left[\text{W/cm}^2\right]. \tag{2.1.19}$$

In formulas (2.1.18) and (2.1.19), λ is a length of a monochromatic wave.

Going from the energy density to the concentration of photons per volume unit n: $n = \rho/\hbar\omega$, it is possible to receive the estimation of (2.1.18) through the number of photons in a volume $4\alpha\,\lambda_e^2\,\lambda$, i.e. in a parallelepiped with transverse cross section $\lambda\!\!\!^{-2}_e$ ($\lambda\!\!\!^{-}_e$ is the Compton wavelength of the electron) and length $4\alpha\lambda$:

$$a_0^2 = 4\alpha\,\lambda_e^2\,\lambda\,n, \tag{2.1.20}$$

$\alpha = 1/137$ is the fine structure constant.

For a field strength parameter $a_0 \geq 1$, it is spoken about the "strong" electromagnetic wave, whereas the "linear" model of the classical electrodynamics remains valid for $a_0 \ll 1$.

2.2 Polarization Characteristics of Radiation

Hereinafter, the usage of the term "the photon beam" supposes that it concerns the electromagnetic radiation propagating along the fixed direction with a negligibly small angular divergence, the characteristics of which (intensity, polarization, position of maximum in spectrum, temporal modulation, etc.) are possible to adjust in a rather large range.

A single photon, i.e. an elementary particle with a spin equal to 1, definitionally exists in a pure spin state (just as the flat monochromatic electromagnetic wave—a classical analogue of a photon—is always completely polarized). There is a whole ensemble of photons in a real beam, therefore, for the description of a beam polarization as a whole (after averaging on ensemble), the matrix of the density ρ_{ij} (Hermitian tensor of the second rank determined in a plane, which is perpendicular to a direction of photon beam propagation) is used:

$$\rho_{ij} = \frac{1}{2}\begin{pmatrix} 1+\xi_3 & \xi_1 - i\xi_2 \\ \xi_1 + i\xi_2 & 1-\xi_3 \end{pmatrix} = \frac{1}{2}\left(\delta_{ij} + \boldsymbol{\xi}\boldsymbol{\sigma}\right), \tag{2.2.1}$$

where $\boldsymbol{\sigma} = \{\sigma_1, \sigma_2, \sigma_3\}$ are the Pauli matrices.

Three real-valued parameters ξ_i ($i = 1, 2, 3$)—so-called Stokes parameters completely describe a polarization state of a photon beam. The Stokes parameters ξ_1, ξ_3 characterize the linear polarization of a beam, and ξ_2 the circular one. The values $\xi_1^2 + \xi_3^2$ and ξ_2 are the Lorentz-invariants. Parameters ξ_1, ξ_3 are scalars, and ξ_2 is pseudo-scalar.

In case when none of Stokes parameters is equal to zero, it is spoken about elliptic polarization, and when $\xi_2 = 0$—about linear polarization of the radiation.

In the last case, the following values are often used instead of the Stokes parameters:

$$P = \sqrt{\xi_1^2 + \xi_3^2} \tag{2.2.2}$$

is a degree of polarization;

$$\varphi_0 = (1/2)\,\mathrm{arctg}\,(\xi_1/\xi_3) \tag{2.2.3}$$

—the inclination angle of a plane of the maximal linear polarization concerning the chosen system of basis vectors (for instance, concerning a plane XZ, if Z-axis is directed along a photon beam direction).

The degree of linear polarization P can be determined as follows:

$$P = \left(N_{\parallel} - N_{\perp}\right)/\left(N_{\parallel} + N_{\perp}\right), \tag{2.2.4}$$

where $N_{\parallel(\perp)}$ is the number of the photons polarized parallel (perpendicularly) to a plane of the maximal linear polarization.

Reverse transition to the Stokes parameters follows from (2.2.2), (2.2.3):

$$\xi_1 = P\,\sin(2\varphi_0); \quad \xi_3 = P\,\cos(2\varphi_0). \tag{2.2.5}$$

An unpolarized beam can be always presented as superposition of two non-interacting completely polarized beams of photons with identical intensity and with mutually perpendicular planes of polarization. Similarly, it is possible to

present a partly polarized photon beam (for which $0<\xi_1^2+\xi_2^2+\xi_3^2<1$) as superposition of completely polarized and non-polarized beams with various intensities.

In the classical electrodynamics, the Stokes parameters are calculated as follows:

$$\xi_1=\frac{E_1^*E_2+E_1E_2^*}{|E_1|^2+|E_2|^2},\quad \xi_2=i\frac{E_1^*E_2-E_1E_2^*}{|E_1|^2+|E_2|^2},\quad \xi_3=\frac{|E_1|^2-|E_2|^2}{|E_1|^2+|E_2|^2}. \tag{2.2.6}$$

The components of the field are calculated in a system, where the third axis coincides with the direction of a wave vector. If the task has any chosen plane, the coordinate system is assigned via basis vectors. If in problem there is a chosen plane, then the coordinate system is

$$\mathbf{e}_1=c_1[\mathbf{n},\mathbf{b}];\quad \mathbf{e}_2=[\mathbf{e}_1,\mathbf{n}],\quad \mathbf{n}=\mathbf{k}/\omega, \tag{2.2.7}$$

where $\mathbf{b}$ is the vector, perpendicular to the chosen plane; $\mathbf{k}$ is a wave vector; ω is a frequency; c_1 is a normalization factor.

For the radiation of ultrarelativistic particles the cone of outgoing photons has an opening of order γ^{-1} (γ is the Lorentz-factor) relative to the average value of the electron momentum. Therefore, it is possible to speak about the mean polarization of a beam (with accuracy to γ^{-2}) if the radiation cone is formed by the aperture with opening $\Delta\Omega\sim\gamma^{-2}$. In this case, for calculation of average Stokes parameters in (2.2.6), it is necessary to use the bilinear combinations of fields $\langle E_i^*E_k\rangle$, averaged on the given angular interval:

$$\langle E_i^*\,E_k\rangle=\int\limits_{\Delta\Omega}d\Omega\,E_i^*\,E_k,\quad i,k=1,2. \tag{2.2.8}$$

Generally speaking, the averaging similar to (2.2.8) can be carried out not only by the angular variables but also by any other non-observable kinematic ones. Thus, during the calculation of polarization characteristics of coherent bremsstrahlung, the averaging similar to (2.2.8) is carried out by the momentum of a final electron [3].

2.3 The Formation Length of Radiation by a Charged Particle

Ter-Mikaelyan in his monograph [4] considering the spatial region, in which the bremsstrahlung is generated by ultrarelativistic electron moving in a medium, has shown that the longitudinal size of this region (along the direction of the initial electron) sharply increases with the growth of the electron Lorentz-factor and with decrease of the photon energy. This spatial scale, which was named "formation length" ℓ_f, can have macroscopic sizes greatly exceeding the wavelength of the

bremsstrahlung photon. After the passage of the length ℓ_f, the electron and emitted photon can be considered as independent particles.

The estimation of this spatial scale can be found from classical electrodynamics (see, for example, [5]). In this approach, the charge, which passes through a rather small area and where external fields are concentrated, is emitted an electromagnetic wave with the length λ without appreciable distortion of a charge trajectory and the change of its energy (see Fig. 2.1).

The determination of the formation length follows from the phase relationships: on the length ℓ_f, which a charge passes after the area of a field at velocity β, the front of a wave, emitted in angle θ, should "lag behind" a charge for a wave length:

$$\frac{\ell_{\mathrm{f}}}{\beta} - \ell_{\mathrm{f}} \cos\theta = \lambda, \tag{2.3.1}$$

and (2.3.1) directly results in the formula for the formation length:

$$\ell_{\mathrm{f}} = \frac{\lambda}{1/\beta - \cos\theta}. \tag{2.3.2}$$

In the ultrarelativistic approach $(1/\beta \approx 1 + \gamma^{-2}/2)$for the "straightforward" radiation we have

$$\ell_{\mathrm{f}} = 2\gamma^2\lambda. \tag{2.3.3}$$

If the following area of a field concentration is located along a trajectory on the distance $L < \ell_f$ (see Fig. 2.1), then in this case the electromagnetic waves, emitted by a charge in two areas of an external field, will interfere in a destructive manner, i.e. the intensity of resulting radiation will be less than the sum of intensities from two independent sources.

Let carry out the quantum consideration of the formation length problem on an example of bremsstrahlung, following to Ter-Mikaelyan [4].

We shall estimate the minimal value of a longitudinal recoil momentum q_l, which is transferred to a nucleus, during the process of bremsstrahlung of the ultrarelativistic electron with energy ε_1. Such situation is realized for collinear geometry, when the final electron with energy ε_2 and a photon with energy $\hbar\omega$ move along the direction of the initial electron:

$$q_{l\,\min} = p_1 - p_2 - k. \tag{2.3.4}$$

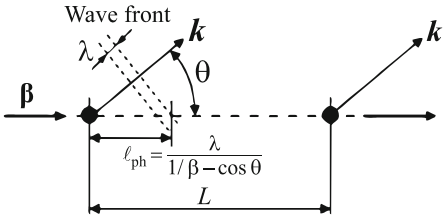

Fig. 2.1 The scheme illustrates the concept of the formation length

Here p_1, p_2, k are momenta of initial and final electrons and photons, accordingly. Neglecting the energy transferred to a nucleus (i.e. in case of fulfillment of a condition $\varepsilon_1 = \varepsilon_2 + \hbar\omega$), momentum p_i in the ultrarelativistic approach becomes

$$p_1 = \frac{\varepsilon_1}{c}\left(1 - \frac{1}{2\gamma_1^2}\right), \quad p_2 = \frac{\varepsilon_1 - \hbar\omega}{c}\left(1 - \frac{1}{2\gamma_2^2}\right),$$

and (2.3.4) results in

$$q_{l\,\min} = \frac{mc}{2\gamma_1}\frac{\hbar\omega}{\varepsilon_2}. \tag{2.3.5}$$

From the uncertainty principle it follows that the last expression defines the length:

$$\ell = \frac{h}{q_{l\,\min}} = 2\gamma_1 \lambda\!\!\!^{-}_e \frac{\varepsilon_2}{\hbar\omega}, \tag{2.3.6}$$

where $\lambda\!\!\!^{-}_e$ is the Compton wavelength of an electron. It is clear that for the case $\hbar\omega \ll \varepsilon_1, \varepsilon_2$ (i.e. $\varepsilon_2 \approx \varepsilon_1$) from the formula (2.3.6) follows the expression (2.3.3):

$$\ell = 2\gamma^2\lambda = \ell_\mathrm{f}$$

that illustrates the generality of the concept of the formation length both for quantum consideration, where recoil effects are important, and for classical one.

The concept of the formation length plays an important role in considering of various physical effects (see in detail the review [6]). With regard to the radiation in periodic structures, where a constructive interference is the reason of monochromaticity of the radiation spectrum (for the fixed radiation angle θ), the wavelength corresponding to the spectral line with minimal frequency (so-called "fundamental" harmonic), is defined from the relationship

$$\ell_\mathrm{f} = d, \tag{2.3.7}$$

where d is a period of the structure.

Expression (2.3.7) does not depend on the radiation mechanism and is applicable both in classical electrodynamics (for instance, for undulator radiation or Smith–Purcell radiation), and in quantum one (the typical example is the coherent bremsstrahlung). The mentioned mechanisms, as well as some others, are considered in the following chapters of this book.

2.4 Interference Factor and the Resonance Condition

Let us consider the electromagnetic radiation of the charge moving on a flat periodic trajectory (Fig. 2.2). Let us designate through $\mathbf{E}_1(\mathbf{k})$ the radiation field on the first period, where $\mathbf{k}$ is a wave vector; $\Delta t_e = d/\beta_\parallel c$ is time of the electron

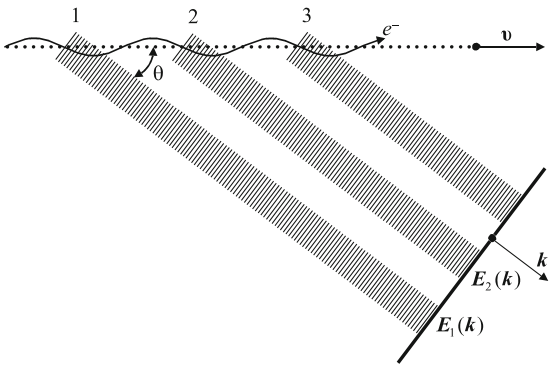

Fig. 2.2 Constructive interference of the electromagnetic radiation in the periodic structure

passing with velocity $\beta_{\|}c$ through the first period; $\Delta t_K = d\cos\theta/c$ is time of the wave front passing from the first period till identical position on the second period.

The phase difference of two wave packages generated by electron on the first and second periods are the follows:

$$\Phi = \omega(\Delta t_e - \Delta t_K) = \frac{2\pi}{\lambda}\beta_{||}c\left(\frac{d}{\beta_{||}c} - \frac{d\cos\theta}{c}\right) = 2\pi\frac{d}{\lambda}\Big(1 - \beta_{\|}\cos\theta\Big). \quad (2.4.1)$$

Thus, the field of radiation on the second period is defined by the expression

$$\mathbf{E}_2(\mathbf{k}) = \mathbf{E}_1(\mathbf{k})\ \exp(i\Phi). \quad (2.4.2)$$

Reasoning by analogy, it is possible to express the radiation field for the nth period as:

$$\mathbf{E}_n(\mathbf{k}) = \mathbf{E}_1(\mathbf{k})\ \exp(i(n-1)\Phi). \quad (2.4.3)$$

Then the total field from the periodic structure containing N elements is represented as the sum

$$\begin{aligned}\mathbf{E}_\Sigma(\mathbf{k}) &= \mathbf{E}_1(\mathbf{k}) + \mathbf{E}_2(\mathbf{k}) + \mathbf{E}_3(\mathbf{k}) + \cdots + \mathbf{E}_\mathrm{N}(\mathbf{k}) \\ &= \mathbf{E}_1(\mathbf{k})\{1 + \exp(i\Phi) + \exp(i\,2\,\Phi) + \cdots + \exp(i(N-1)\Phi)\}. \quad (2.4.4)\end{aligned}$$

Having designated ($\exp(i\Phi) = q$), we shall receive an expression for the total intensity of the field:

$$\begin{aligned}\mathbf{E}_\Sigma(\mathbf{k}) &= \mathbf{E}_1(\mathbf{k})\ \left\{1 + q + q^2 + \cdots + q^{N-1}\right\} \\ &= \mathbf{E}_1(\mathbf{k})\frac{1-q^N}{1-q} = \mathbf{E}_1(\mathbf{k})\ \frac{1-\exp(iN\Phi)}{1-\exp(i\Phi)}, \quad (2.4.5)\end{aligned}$$

using the well-known formula for a geometric progression.

The spectral–angular distribution of the radiation intensity can be calculated, knowing the field intensity:

$$\frac{d^2W_\Sigma}{d\omega\, d\Omega} = \text{const}\,|\mathbf{E}_\Sigma(\mathbf{k})|^2 = \underbrace{\text{const}\,|\mathbf{E}_1(\mathbf{k})|^2}_{\frac{d^2W}{d\omega\, d\Omega}} \frac{|1-\exp\,(iN\Phi)|^2}{|1-\exp\,(i\Phi)|^2} = \frac{d^2W}{d\omega\, d\Omega} F_N. \tag{2.4.6}$$

Here $\frac{d^2W}{d\omega\, d\Omega} = \text{const}\,|\mathbf{E}_1(\mathbf{k})|^2$ describes the radiation "collected" from one period of a trajectory, and a multiplier

$$F_N = \left|\frac{1-\exp(iN\Phi)}{1-\exp(i\Phi)}\right|^2 \tag{2.4.7}$$

refers to as an interference factor, since it describes the interference from N identical radiators.

Using known trigonometric rules, the last formula can be rewritten as

$$F_N = \frac{\sin^2(N\Phi/2)}{\sin^2(\Phi/2)}. \tag{2.4.8}$$

The function F_N has a set of sharp maxima for the values of an argument, which makes a denominator zeroth:

$$\frac{\Phi}{2} = \pi\frac{d}{\lambda_m}\Big(1-\beta_\parallel\cos\theta\Big) = m\,\pi, \quad m \text{ is an integer.}$$

The last formula is reduced to the following expression for the case $\beta \approx \beta_\parallel$

$$\lambda_m = \frac{d}{m}(1-\beta\cos\theta), \tag{2.4.9}$$

which was received regardless to any fixed radiation mechanism and can be applied to any type of radiation, which is characterized by the periodic disturbance of a trajectory. The received relationship is generalization of the resonance condition (2.3.7) for $m \neq 1$.

Frequently, the index $m = 1, 2, 3, \ldots$ refers to harmonic number. The harmonic $m = 1$ for ultrarelativistic particles with frequency

$$\omega_1 = \frac{4\pi\gamma^2 c}{d\big(1+\gamma^2\theta^2\big)} = \frac{2\gamma^2\omega_0}{1+\gamma^2\theta^2} \tag{2.4.10}$$

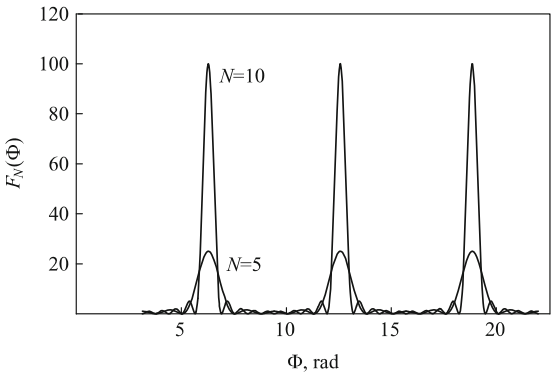

Fig. 2.3 An interference factor for periods $N = 5$, 10

is identified as fundamental. The resonance condition brings to the following conclusion: the frequencies of the higher harmonics in m time differ from fundamental ones:

$$\omega_m = m\,\omega_1. \tag{2.4.11}$$

The diagram of the function F_N is presented in Fig. 2.3 for $\theta = 0$ at $N = 5$ and 10.

As expected, the function F_N differs from zero in a small range of frequencies close by ω_m, and the width of this range is defined by a number of the periods:

$$\frac{\Delta\omega_m}{\omega_m} \sim \frac{1}{N}. \tag{2.4.12}$$

As it follows from the picture, the maximal value of the function is

$$F_{N\ \max} = N^2. \tag{2.4.13}$$

From (2.4.12) and (2.4.13) it follows that the area under the peak is

$$S \sim \Delta\omega_m \times F_{N\ \max} = N\omega_m \tag{2.4.14}$$

and linearly increases with a number of periods.

For big values $N \gg 10$ the function F_N (2.4.7) is approximated well by δ-function:

$$F_N \approx 2\pi N\delta(\Phi - 2m\,\pi) = \frac{N}{m}\,\delta\left(\frac{\omega}{m\,\omega_0}(1 - \beta\cos\theta) - 1\right). \tag{2.4.15}$$

References

1. Jackson, J.D.: Classical Electrodynamics. Wiley, New York (1998)
2. Nikishov, A.I., Ritus, V.I.: Quantum electrodynamics of effects in strong field. Trudy FIAN **111**, (1979) (in Russian)

3. Diambrini Palazzi, G.: High-energy Bremsstrahlung and electron pair production in thin crystals. Rev. Mod. Phys. **40**, 611 (1968)
4. Ter-Mikaelyan, M.L.: High-Energy Electromagnetic Processes in Condensed Media. Wiley-Interscience, New York (1972)
5. Akhiezer, A.I., Shulga, N.F.: High Energy Electrodynamics in Matter. Gordon and Breach, Amsterdam (1996)
6. Baier, V.N., Katkov, V.M.: Concept of formation length in radiation theory. Phys. Rep. **409**, 261 (2005)

Chapter 3
Undulator Radiation

3.1 Moving of Charged Particle in Periodic Magnetic Field

Let us consider a case, when the magnetic field is directed along x-axis and is periodic with the period λ_u along z-axis (so-called plane undulator, see Fig. 3.1a, and the law of magnetic field change is described by a sinusoid [1]:

$$\mathbf{H} = \{H_x, 0, 0\}, \quad H_x(z) = H \sin \frac{2\pi z}{\lambda_u}. \tag{3.1.1}$$

The equation of a charge e movement in an external electromagnetic field is given by expression:

$$\frac{d\mathbf{p}}{dt} = e\mathbf{E} + \frac{e}{c}[\boldsymbol{\upsilon} \times \mathbf{H}], \tag{3.1.2}$$

where $\mathbf{p} = \gamma mc\,\boldsymbol{\upsilon}/c$ is a particle momentum.

The relativistic electron ($\gamma \gg 1$) flies into the undulator along z-axis. It is clear that a trajectory of the electron is flat and lies in the yz-plane.

From (3.1.2) we can obtain a system of equations for two components of the electron velocity:

$$\begin{aligned} \frac{d\upsilon_z}{dt} &= \frac{e}{\gamma mc^2} H_x(z(t))\upsilon_y, \\ \frac{d\upsilon_y}{dt} &= \frac{e}{\gamma mc^2} H_x(z(t))\upsilon_z. \end{aligned} \tag{3.1.3}$$

Considering a magnetic field being weak enough (or, in other words, $|\upsilon_y| \ll \upsilon_z \approx c$), it is possible to obtain an approximate solution of system (3.1.3). The second equation in this approach ($z = ct$) gives the following dependence for $\upsilon_y(t)$:

A. P. Potylitsyn, *Electromagnetic Radiation of Electrons in Periodic Structures*, Springer Tracts in Modern Physics, 243, DOI: 10.1007/978-3-642-19248-7_3,

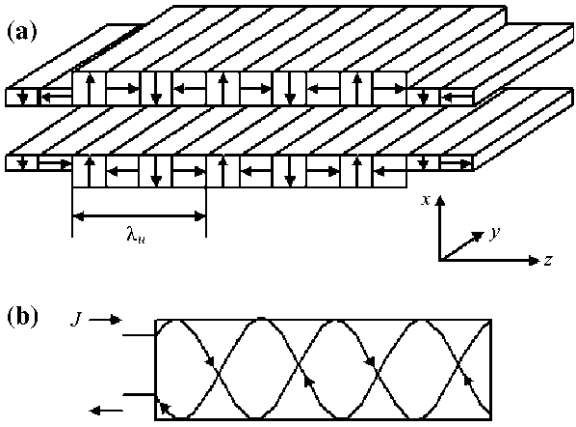

Fig. 3.1 **a** The scheme of plane magnetic undulator; **b** the scheme of helical magnetic undulator

$$c\beta_z = \upsilon_z(t) \approx \upsilon_{\parallel} = \text{const},$$
$$\beta_y = \frac{\upsilon_y(t)}{c} = -\frac{eH\lambda_u}{2\pi\gamma mc^2}\cos\frac{2\pi z}{\lambda_u}. \tag{3.1.4}$$

The velocity υ_z is easy to derive from a condition $\gamma = \frac{1}{\sqrt{1-\left(\upsilon_y^2+\upsilon_z^2\right)/c^2}} = \text{const}$ (the particle energy does not change in magnetic field).

Hence in the same approach, as before,

$$\upsilon_z(t) = c\sqrt{1-\gamma^{-2}-\beta_y^2} \approx c\left[1-\frac{1}{2}\left(\gamma^{-2}+\beta_y^2(t)\right)\right]. \tag{3.1.5}$$

From (3.1.4) it is possible to obtain the equation:

$$\left\langle\beta_y^2\right\rangle = \frac{1}{2}\left(\frac{eH\lambda_u}{2\pi\gamma mc^2}\right)^2. \tag{3.1.6}$$

Let us estimate this quantity for typical values: $H = 1\ T;\ \lambda_u = 5\,\text{cm};\ \gamma = 10^3$. Using the "engineering" formula: $eH = 3 \times 10^6$ (eV/cm) H [T], we obtain $\sqrt{\left\langle\beta_y^2\right\rangle} = 0.021 \ll 1$.

This value characterizes an average deflection of trajectory from a straight line. Often instead of (3.1.6) the so-called deflection parameter (undulator parameter) is used:

$$\langle\beta_y^2\rangle = \frac{K^2}{2\gamma^2};\quad K = \gamma\frac{eH\lambda_u}{2\pi\,\gamma\,mc^2}. \tag{3.1.7}$$

The physical meaning of parameter K is connected with the maximal angle ψ between the line tangent to a trajectory and average velocity of a the particle $\langle\boldsymbol{\beta}\rangle$:

$$K = \gamma\,\psi \approx \gamma(\lambda_u/R).$$

Having substituted to the expression for radius R of the trajectory of electron with energy E in a constant magnetic field H in the previous formula, we receive

$$K = \gamma(eH\lambda_u/\beta E) \approx \gamma(eH\lambda_u/E).$$

Then from (3.1.5) follows

$$\upsilon_{\|} = \langle \upsilon_z(t) \rangle = c\left[1 - \frac{1}{2\gamma^2}\left(1 + \frac{K^2}{2}\right)\right]. \tag{3.1.8}$$

Reasoning by analogy to the usual Lorentz-factor, the so-called longitudinal Lorentz-factor is often used:

$$\gamma_{\|}^2 = \frac{1}{1 - \upsilon_{\|}^2/c^2} = \frac{\gamma^2}{1 + K^2/2}. \tag{3.1.9}$$

In the next approximation the longitudinal velocity $v_z(t) = c\beta_z(t)$ will depend on time:

$$c\beta_z(t) = c\sqrt{\beta^2 - \frac{K^2}{\gamma^2}\cos^2\frac{2\pi\, V_{\|}\, t}{\lambda_u}} = c\sqrt{1 - \gamma^{-2} - \frac{K^2}{2\gamma^2}\left(1 + \cos\frac{4\pi\, V_{\|}\, t}{\lambda_u}\right)}.$$

From here we have

$$\begin{aligned}\beta_z(t) &= 1 - \frac{1}{2\gamma^2}\left(1 + \frac{K^2}{2}\right) - \frac{K^2}{4\gamma^2}\cos\frac{4\pi\,\upsilon_{\|}\, t}{\lambda_u} \\ &= \beta_{\|} - \frac{K^2}{4\gamma^2}\cos\frac{4\pi\,\upsilon_{\|}\, t}{\lambda_u}.\end{aligned} \tag{3.1.10}$$

That is to say the longitudinal velocity is modulated with the double frequency in comparison with transversal one. From (3.1.4) and (3.1.10) it is easy to derive the equations of the motion:

$$\begin{aligned} y &= -\frac{K\,\lambda_u}{\gamma\; 2\pi}\sin\omega_0 t, \\ z &= c\beta_{\|}\, t - \frac{K^2\lambda_u}{4\gamma^2\pi}\sin 2\omega_0 t, \\ \omega_0 &= 2\pi c\beta_{\|}/\lambda_u. \end{aligned} \tag{3.1.11}$$

The Eqs. (3.1.11) describe the electron trajectory in a yz-plane, being represented parametrically. In the system, where electron is at rest on the average, i.e. in the system moving with velocity $c\beta_{\|}$ in parallel with z-axis (further we shall designate it as R), after standard Lorentz-transformations we receive

$$\beta_{zR} = -\left(K^2/4\right)\cos 2\omega_R t_R; \quad \beta_{yR} = -K\cos\omega_R t_R,$$

where $\omega_R = \omega_0\,\gamma_\parallel = (2\pi c/\lambda_u)\gamma_\parallel$.

In this system the equation of trajectory is easily found after integration of the equations and exception of parameter t_R:

$$\left(\frac{y_R\omega_R}{c}\right)^2\left[K^2 - \left(\frac{y_R\omega_R}{c}\right)^2\right] = 16\left(\frac{z_R\omega_R}{c}\right)^2. \tag{3.1.12}$$

Evolution of a particle trajectory depending on parameter K is shown in Fig. 3.2. It is easy to see that for values of parameter $K \ll 0.1$ the trajectory comes nearer to a straight-line one (i.e. the particle makes along y-axis harmonious oscillations with small amplitude).

If the source moving with velocity $\beta_\parallel$ emits on frequency ω_R, then in the laboratory system a frequency $\omega(\theta)$ is registered under the angle θ

$$\omega(\theta) = \frac{\omega_R}{\gamma_\parallel\left(1 - \beta_\parallel\cos\theta\right)} = \frac{\omega_0}{1 - \beta_\parallel\cos\theta}. \tag{3.1.13}$$

The formula (3.1.13) can be rewritten as $\lambda_u = \lambda/1 - \beta_\parallel\cos\theta$, where in the right part there is the formation length that coincides with a condition (2.3.7). For the ultrarelativistic case

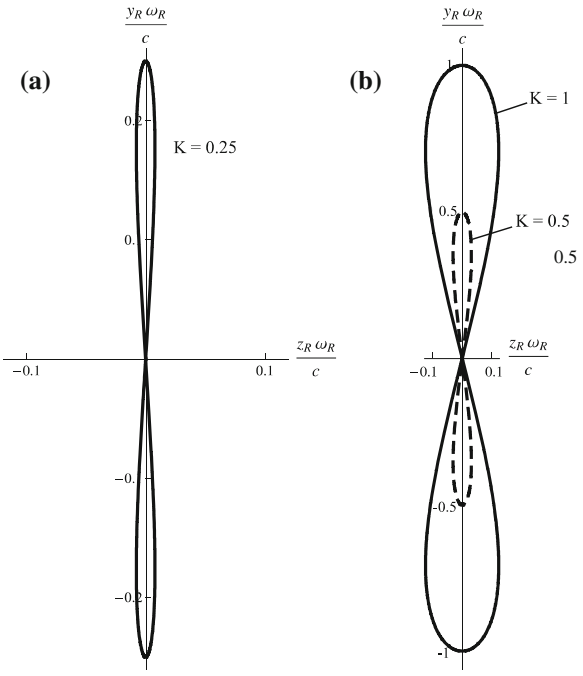

Fig. 3.2 An electron trajectory in R-system in yz-plane for various values of parameter K

$$\omega(\theta) = \frac{\omega_0}{1 - \left(1 - \frac{1+K^2/2}{2\gamma^2}\right)\left(1 - \frac{\theta^2}{2}\right)} = \frac{2\gamma^2\omega_0}{1 + K^2/2 + \gamma^2\theta^2}. \tag{3.1.14}$$

The typical wavelength of an undulator radiation (UR) in straightforward direction ($\theta = 0$) is defined by the Lorentz-factor and the undulator parameter:

$$\lambda_1 = \lambda_u\left(K^2 + 2\right)/4\gamma^2.$$

Relativistic electron ($\gamma \geq 100$), when moving on a sinusoid with macroscopic period λ_u, radiates on the wavelength more than by four order shorter, than the period of trajectory (at $K \ll 1$).

3.2 Radiation of Harmonically Oscillating Charge

Let consider the radiation of a charge in magnetic field of undulator at $K \ll 1$. In this case in R-system the radiation of a charge, which oscillates according to the harmonious law with non-relativistic velocity, is described by the known formulae of classical electrodynamics. In this paragraph we shall omit the index R for simplification of formulae. Further we shall use the unit vectors $\mathbf{e}_1, \mathbf{e}_2$, which are perpendicular to a wave vector $\mathbf{k}$:

$$\mathbf{e}_1 = C_n[\mathbf{n}, \mathbf{b}], \quad \mathbf{e}_2 = [\mathbf{e}_1\, \mathbf{n}]. \tag{3.2.1}$$

Here $\mathbf{n} = \mathbf{k}/|\mathbf{k}| = \{\sin\theta\sin\varphi,\ \sin\theta\cos\varphi,\ \cos\theta\}$, $\mathbf{b} = \{1, 0, 0\}$ is the unit vector, perpendicular to the charge oscillation plane, $C_n = 1\Big/\sqrt{\cos^2\theta + \sin^2\theta\cos^2\varphi}$ is a normalization factor.

Following [1, 2], we shall write the radiation field E in the observation point $\mathbf{R} = R\mathbf{n}$, bearing in mind, that the observation point is located in a wave zone ($R \gg \lambda$):

$$\mathbf{E} = \frac{e}{cR}\frac{\left[\mathbf{n}\left[(\mathbf{n} - \boldsymbol{\beta})\dot{\boldsymbol{\beta}}\right]\right]}{(1 - \mathbf{n}\boldsymbol{\beta})^3} \approx \frac{e}{c^2R}[\mathbf{n}[\mathbf{n}\,\dot{\mathbf{v}}\,]]. \tag{3.2.2}$$

The obtained expression (3.2.2) is valid for a case $\boldsymbol{\beta} \parallel \dot{\boldsymbol{\beta}}$ under condition of $|\boldsymbol{\beta}| \ll 1$. Using the known formulae of the vector analysis, we shall calculate the components E_1, E_2:

$$\begin{aligned} E_1 &= -\frac{e}{cR}(K\omega)\frac{\cos\theta}{\sqrt{\cos^2\theta + \sin^2\theta\,\cos^2\varphi}}\sin\omega t, \\ E_2 &= -\frac{e}{cR}(K\omega)\frac{\sin^2\theta\sin\varphi\cos\varphi}{\sqrt{\cos^2\theta + \sin^2\theta\cos^2\varphi}}\sin\,\omega t. \end{aligned} \tag{3.2.3}$$

The radiating power in a solid angle unit is found from the last formulae:

$$\frac{dP}{d\Omega} = \frac{c}{4\pi}R^2E^2 = \frac{c}{4\pi}R^2\left(E_1^2 + E_2^2\right)$$
$$= \frac{e^2}{4\pi\, c}K^2\omega^2\left(\cos^2\theta + \sin^2\theta\sin^2\varphi\right)\sin^2\omega\, t. \tag{3.2.4}$$

The physical meaning has a power averaged on the period of oscillations. If we are interested in radiation intensity, which is not dependent on azimuthal angle of a wave vector, the expression (3.2.4) is necessary to integrate over azimuthal angle φ:

$$\left\langle \frac{dP}{d\cos\theta} \right\rangle = \frac{e^2}{4c}K^2\omega^2\frac{1}{2}\left(1 + \cos^2\theta\right)$$
$$= \frac{e^2}{4c}K^2\gamma_\parallel^2\,\omega_0^2\frac{1}{2}\left(1 + \cos^2\theta\right). \tag{3.2.5}$$

Further the symbol of averaging will be omitted. As it was to be expected, the expression for radiation power in R-system in used approximation coincides with the formula describing radiation of an electric dipole. Therefore, the approximation $\upsilon_\parallel = \text{const}$, $K \ll 1$ is frequently called the dipole one.

3.3 Characteristics of Undulator Radiation in Dipole Approximation

Let us remind that all formulae in the previous paragraph are obtained in R-system. To get the expression for UR power in laboratory system, it is necessary to carry out the corresponding Lorentz-transformations. UR power in laboratory system is defined as $P = \Delta W/\Delta t$, where ΔW is energy, radiated by charge during time Δt. We are using following Lorentz transformations:

$$\begin{aligned}
\Delta W &= \frac{\Delta W_R}{\gamma_\parallel\left(1 - \beta_\parallel\cos\theta\right)},\\
\Delta t &= \gamma_\parallel\,\Delta t_R,\\
\cos\theta_R &= \frac{\cos\theta - \beta_\parallel}{1 - \beta_\parallel\cos\theta},\\
\frac{d\cos\theta_R}{d\cos\theta} &= \frac{1}{\gamma_\parallel^2\left(1 - \beta_\parallel\cos\theta\right)^2}.
\end{aligned} \tag{3.3.1}$$

Therefore, the resulting formula is written as

$$\frac{dP}{d\cos\theta} = \frac{dP_R}{d\cos\theta_R}\,\frac{\Delta W}{\Delta W_R}\,\frac{\Delta t_R}{\Delta t}\,\frac{d\cos\theta_R}{d\cos\theta}$$
$$= \frac{e^2}{4c}K^2\gamma_\parallel^2\omega_0^2\frac{1}{2}\left(1+\cos^2\theta_R\right)\frac{1}{\gamma_\parallel^4\left(1-\beta_\parallel\cos\theta\right)^3}. \tag{3.3.2}$$

In ultrarelativistic approximation $\theta \sim \gamma_\parallel^{-1}$, therefore the derived formula can be simplified, using relations:

$$\cos\theta_R = \frac{1-\gamma_\parallel^2\theta^2}{1+\gamma_\parallel^2\theta^2},$$
$$1-\beta_\parallel\cos\theta = \frac{1}{2\gamma_\parallel^2}\left(1+\gamma_\parallel^2\theta^2\right). \tag{3.3.3}$$

Further, to pass from the radiation power to the energy W, emitted by one electron during passage through undulator with the length $N_0\,\lambda_u$, we shall multiply (3.3.2) by the time $\Delta t \approx N_0\lambda_0/c = 2\pi N_0/\omega_0$:

$$\frac{dW}{d\left(\gamma_\parallel^2\theta^2\right)} = 2\pi\,\alpha\,N_0K^2\hbar\,\omega_0\,\gamma_\parallel^2\frac{1+\gamma_\parallel^2\theta^2}{\left(1+\gamma_\parallel^2\theta^2\right)^5}. \tag{3.3.4}$$

Here $\alpha = \frac{e^2}{\hbar c} = \frac{1}{137}$ is the fine structure constant.

As follows from the obtained equation, the energy lost due to undulator radiation in a weak sinusoidal field, is proportional to deflection parameter squared and to the longitudinal Lorentz-factor squared. In the considered approach the energy of a photon is determined by polar angle θ:

$$\hbar\omega(\theta) = \frac{\hbar\omega_0}{1-\beta_\parallel\cos\theta} \approx \frac{2\gamma^2\,\hbar\,\omega_0}{1+K^2/2+\gamma^2\theta^2}. \tag{3.3.5}$$

Hence a maximal energy of UR photon, occurs in a radiation spectrum proper to a radiation angle $\theta = 0$:

$$\hbar\omega_m = \frac{2\gamma^2\hbar\,\omega_0}{1+K^2/2}. \tag{3.3.6}$$

Introducing a relative variable:

$$\xi = \frac{\omega}{\omega_m} = \frac{1+K^2/2}{1+K^2/2+\gamma^2\theta^2}, \quad 0 \le \xi \le 1, \tag{3.3.7}$$

which characterizes the UR spectral distribution, instead of Eq. (3.3.4) it is possible to write the formula:

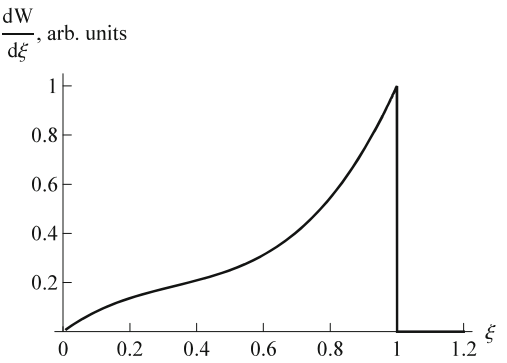

Fig. 3.3 Spectrum of UR intensity in plane undulator in dipole approximation

$$\frac{dW}{d\xi} = 2\pi\,\alpha N_0 K^2 \hbar\,\omega_0\,\gamma_\parallel^2\,\xi\left(1 - 2\xi + 2\xi^2\right), \tag{3.3.8}$$

which is presented in Fig. 3.3.

The spectrum is concentrated in area $\xi \le 1$ (in other words, $\hbar\omega \le \hbar\omega_m$), i.e. only a first (fundamental) harmonic exists in a spectrum, what is a consequence of the used approximation.

By integration of the last expression it is possible to obtain radiation losses in undulator:

$$W = \frac{2\pi}{3}\alpha N_0 K^2 \gamma_\parallel^2\,\hbar\,\omega_0 \approx \frac{2\pi}{3}\alpha N_0 K^2 \gamma^2\,\hbar\,\omega_0. \tag{3.3.9}$$

In quantum consideration with spectral distribution of emitted energy the so-called photon spectrum is frequently considered:

$$\frac{dN_{\mathrm{UR}}}{\hbar\,d\omega} = \frac{1}{\hbar\omega}\frac{dW}{\hbar\,d\omega}, \tag{3.3.10}$$

or, through a variable ξ

$$\frac{dN_{\mathrm{UR}}}{d\xi} = \frac{1}{\hbar\omega_m}\frac{1}{\xi}\frac{dW}{d\xi} = \pi\,\alpha N_0 K^2\left(1 - 2\xi + 2\xi^2\right). \tag{3.3.11}$$

From the last formula it is possible to obtain the total number of emitted photons

$$N_{\mathrm{UR}} = \int_0^1 d\xi \frac{dN_{\mathrm{UR}}}{d\xi} = \frac{2}{3}\pi\,\alpha N_0 K^2 \tag{3.3.12}$$

and average energy of photons in UR spectrum: $\langle\hbar\omega\rangle = \langle\xi\rangle\hbar\omega_m$, where

$$\begin{aligned} \langle\hbar\omega\rangle &= \frac{W}{N_{\mathrm{UR}}} = \gamma_\parallel^2\,\hbar\omega_0 = \frac{1}{2}\hbar\,\omega_m, \\ \langle\xi\rangle &= \frac{\int \xi \frac{dN_{UR}}{d\xi} d\xi}{N_{\mathrm{UR}}} = \frac{1}{2}. \end{aligned} \tag{3.3.13}$$

Once again we shall note that all obtained results refer to a case of ultrarelativistic electron radiation in the dipole approximation.

3.4 Undulator Radiation Spectrum in a Weak Sinusoidal Magnetic Field ($K \leq 1$)

Rigorous theory of UR in a plane undulator for arbitrary value of deflection parameter K is presented, for instance, in the monograph [3]. Omitting details of calculations, we will bring the result for a Fourier-transform of the field for one period of undulator:

$$\mathbf{E}(\omega) \approx \frac{e}{cR} e^{ikR} \frac{2\pi\omega}{\omega_0} \left[\frac{1}{T} \int_0^T [\mathbf{n}[\mathbf{n}\boldsymbol{\beta}]] e^{i(\omega t - \mathbf{kr})} dt \right], \tag{3.4.1}$$

where integration is carried out over the particle passage time through one undulator period.

It is necessary to note that the modulated longitudinal velocity (3.1.10) in a similar undulator results in rather cumbersome calculations. The term **kr** in expression (3.4.1) contains the trajectory of a particle (3.1.11) in the exponent, which depends on parameter K. The higher harmonics will give significant contribution in the integral (3.4.1) for values $K \geq 1$.

Using formulae (1.4.6) and (3.4.1) it is possible to get an expression for spectral–angular distribution of UR intensity:

$$\frac{dW}{d\Omega\, d\omega} = \frac{cR^2}{4\pi^2 c} |\mathbf{E}(\omega)|^2 F_N = \frac{e^2\omega^2}{4\pi^2 c} \left| \int_0^T [\mathbf{n}\boldsymbol{\beta}] e^{i(\omega t - \mathbf{kr})} dt \right|^2 F_N. \tag{3.4.2}$$

The spectral–angular distribution of the first three harmonics for $K \leq 1$ was investigated in works [4, 5]. Using the same basis vectors (3.2.1), written down in laboratory system, we will bring expressions for both polarization components of the first harmonic intensity:

$$\begin{aligned} \frac{dW_{1,1}}{d\Omega\, d\omega} &= 2\frac{e^2\gamma^2}{\pi^2 c} F_N \frac{(K^2/2)}{\left(1+\gamma^2\theta^2\right)^3} \left(1 - \gamma^2\theta^2 \cos 2\varphi\right)^2, \\ \frac{dW_{2,1}}{d\Omega\, d\omega} &= 2\frac{e^2\gamma^2}{\pi^2 c} F_N \frac{(K^2/2)}{\left(1+\gamma^2\theta^2\right)^3} \gamma^4\theta^4 \sin^2 2\varphi. \end{aligned} \tag{3.4.3}$$

Here the azimuthal angle φ is counted from the plane of oscillations. The first index in the left part of expression corresponds to the linear polarization along vectors $\mathbf{e}_1, \mathbf{e}_2$, whereas the second one—to the number of harmonic. According to

determination of basis vectors $\mathbf{e}_1, \mathbf{e}_2$, the radiation polarization is defined in a system connected with a wave vector. In the ultrarelativistic case practically almost all radiation is concentrated in an angle cone $\sim 1/\gamma \ll 1$, what allows to carry out averaging of expressions (3.4.3) over an azimuthal angle φ. In this case the system of basis vectors $\langle \mathbf{e}_1 \rangle$, $\langle \mathbf{e}_2 \rangle$ will be defined only by a plane, in which the particle trajectory is located. It is easy to show that for a flat trajectory of electron with the symmetry corresponding for a plane undulator, the radiation will have only a linear polarization. Using approximation of the "long" undulator ($N \to \infty$) we will carry out integration in (3.4.3) with respect to frequencies and azimuthal angle:

$$\begin{aligned}
\frac{dW_{1,1}}{\gamma^2 d\cos\theta} &= 2\pi\,\alpha\,N \frac{\gamma^2\hbar\omega_0}{\left(1+\gamma^2\theta^2+K^2/2\right)} \frac{K^2\left(1+\frac{1}{2}\,\gamma^4\theta^4\right)}{\left(1+\gamma^2\theta^2\right)^4}, \\
\frac{dW_{2,1}}{\gamma^2 d\cos\theta} &= 2\pi\,\alpha\,N \frac{\gamma^2\hbar\omega_0}{\left(1+\gamma^2\theta^2+K^2/2\right)} \frac{K^2\,\frac{1}{2}\gamma^4\theta^4}{\left(1+\gamma^2\theta^2\right)^4}.
\end{aligned} \tag{3.4.4}$$

Carrying out the similar integration of expressions for the second and the third harmonics, formulae for which are given in [5], it is possible to get the following expressions:

$$\begin{aligned}
\frac{dW_{1,2}}{\gamma^2 d\cos\theta} &= 2\pi\alpha N \frac{2\gamma^2\hbar\omega_0}{\left(1+\gamma^2\theta^2+K^2/2\right)} \frac{\frac{5}{8}K^4\,\gamma^2\theta^2\left(5-2\gamma^2\theta^2+\,\gamma^4\theta^4\right)}{\left(1+\gamma^2\theta^2\right)^6}, \\
\frac{dW_{2,2}}{\gamma^2 d\cos\theta} &= 2\pi\,\alpha\,N \frac{2\gamma^2\hbar\omega_0}{\left(1+\gamma^2\theta^2+K^2/2\right)} \frac{\frac{K^4}{4}\,\gamma^2\theta^2\left(1-\gamma^2\theta^2+5\gamma^4\theta^4\right)}{\left(1+\gamma^2\theta^2\right)^6}, \\
\frac{dW_{1,3}}{\gamma^2 d\cos\theta} &= 2\pi\,\alpha\,N \frac{3\gamma^2\hbar\omega_0}{\left(1+\gamma^2\theta^2+K^2/2\right)} \\
&\quad \times \frac{\frac{81}{64}K^6\,\left(1-14\gamma^2\theta^2+\frac{183}{2}\,\gamma^4\theta^4-41\gamma^6\theta^6+10\gamma^8\theta^8\right)}{\left(1+\gamma^2\theta^2\right)^8}, \\
\frac{dW_{2,3}}{\gamma^2 d\cos\theta} &= 2\pi\,\alpha\,N \frac{3\gamma^2\hbar\omega_0}{\left(1+\gamma^2\theta^2+K^2/2\right)} \frac{\frac{81}{64}K^6\,\gamma^4\theta^4\left(\frac{9}{2}-18\gamma^2\theta^2+18\gamma^4\theta^4\right)}{\left(1+\gamma^2\theta^2\right)^8}.
\end{aligned} \tag{3.4.5}$$

Going again from a polar angle to a relative spectral variable $\xi = \hbar\omega/2\gamma^2\hbar\omega_0$ for the first harmonic: $\xi \approx 1/(1+\gamma^2\theta^2+K^2/2)$ and summarizing with respect to polarizations, from (3.4.4) and (3.4.5) we will get the spectral distributions of intensity for the first three harmonics:

$$\frac{dW_1}{d\xi} = 2\pi\,\alpha N\gamma^2\hbar\omega_0 K^2\xi\left(1-2\xi+2\xi^2\right),\quad 0\le\xi\le 1/\left(1+K^2/2\right),$$

$$\frac{dW_2}{d\xi} = 2\pi\,\alpha N\gamma^2\hbar\omega_0 K^4\frac{1}{4}\left(\frac{\xi}{2}\right)^2\left(1-\frac{\xi}{2}\right)\left(15-22\xi+14\xi^2\right);$$

$$0\le\xi\le 2/\left(1+K^2/2\right);$$

$$\frac{dW_3}{d\xi} = 2\pi\,\alpha N\gamma^2\hbar\omega_0 K^6\frac{9}{64}\left(\frac{\xi}{3}\right)^3\left(252-513\xi+441\xi^2-165\xi^3+22\xi^4\right);$$

$$0\le\xi\le 3/\left(1+K^2/2\right). \tag{3.4.6}$$

As follows from the obtained expressions, the intensity of nth harmonic is defined by a factor K^{2n}, therefore in a weak field of the plane undulator the main part of energy is emitted on the first harmonic. From (3.4.4) and (3.4.5) it is possible to get the intensities of each polarization components $dW_1/d\xi$, $dW_2/d\xi$ after summation over the second index:

$$\frac{dW_1}{d\xi} = \sum_i \frac{dW_{1,i}}{d\xi},\quad \frac{dW_2}{d\xi} = \sum_i \frac{dW_{2,i}}{d\xi}. \tag{3.4.7}$$

The last formulae allow to calculate the linear polarization of UR in plane undulator.

The spectra of UR intensity for various values of parameter K are shown in Figs. 3.4 and 3.5.

It is necessary to note, that connection between frequency of emitted photon and the polar angle θ allows to achieve the so-called "monochromatization" of UR using hard angular collimation:

$$\theta < \theta_c \le 1/\gamma. \tag{3.4.8}$$

In this case in the spectrum corresponding to the first harmonic, there will be frequencies in the interval $1/1+\left(\gamma^2\theta_c^2\right)\le\xi\le 1$ and $2/1+\left(\gamma^2\theta_c^2\right)\le\xi\le 2$, $3/1+\left(\gamma^2\theta_c^2\right)\le\xi\le 3$ for the second and the third accordingly.

Monochromatized spectrum for a collimation angle in the case of $\theta_c = 0.5\,\gamma^{-1}$ is shown in Fig. 3.6. As follows from the figure, in this case the first harmonic monochromaticity will be defined by value $\gamma\,\theta_c : \Delta\omega/\omega_1 \sim \Delta\xi \approx \gamma^2\theta_c^2/\left(1+\gamma^2\theta_c^2\right) \approx 20\%$

As it was mentioned above, the UR polarization in a plane undulator will be linear. In an ultrarelativistic case the polarization characteristics of UR beam as a whole are defined after averaging over azimuthal angle:

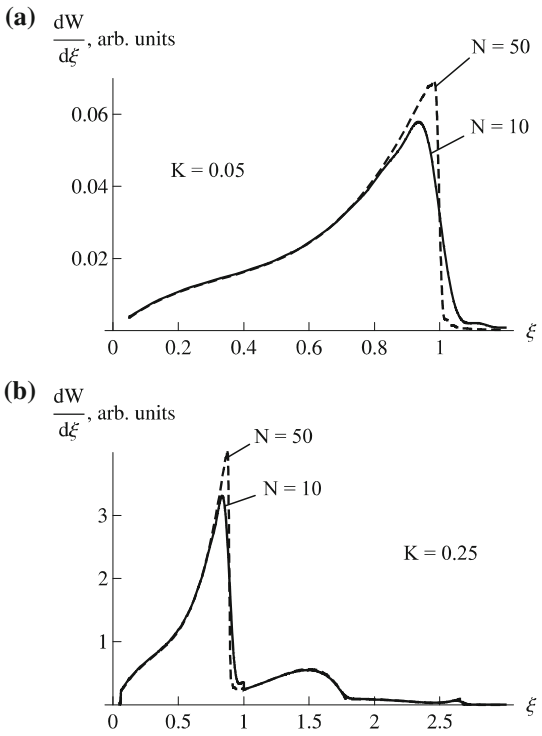

Fig. 3.4 A spectrum of UR intensity in undulator with a finite number of periods for $K = 0.05$ (**a**) and $K = 0.25$ (**b**)

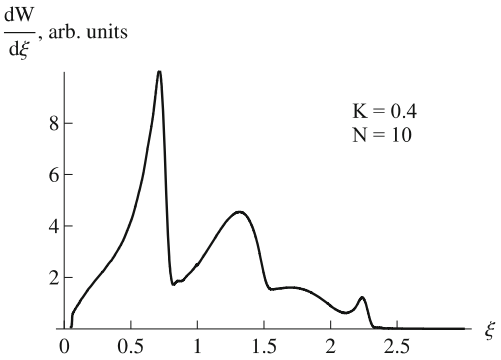

Fig. 3.5 A spectrum of UR intensity in plane undulator with $K = 0.4$ with taking into account the contribution of the first three harmonics

$$\langle \xi_1 \rangle = \int d\varphi \left(E_1 E_2^* + E_1^* E_2 \right) \Big/ \int d\varphi \left(|E_1|^2 + |E_2|^2 \right),$$
$$\langle \xi_3 \rangle = \int d\varphi \left(|E_1|^2 - |E_2|^2 \right) \Big/ \int d\varphi \left(|E_1|^2 + |E_2|^2 \right). \tag{3.4.9}$$

For a flat trajectory of electron in undulator the parameter $\langle \xi_1 \rangle$ becomes zero after this averaging, and for linear polarization in a plane of oscillations instead of (3.4.9) we have

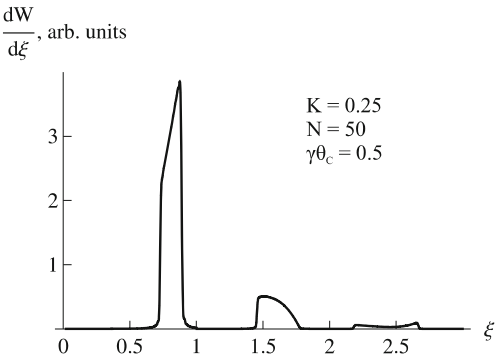

Fig. 3.6 A spectrum of UR intensity with the contribution of three harmonics in case of hard collimation ($\gamma\theta_c = 0.5$)

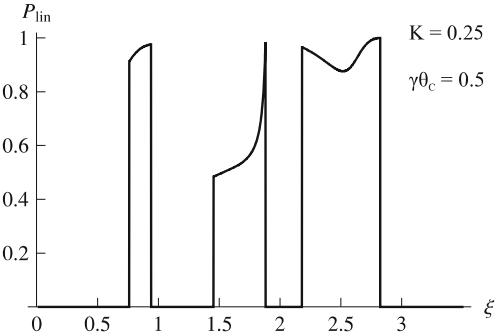

Fig. 3.7 The degree of linear polarization of UR in case of hard collimation ($\gamma\,\theta_c = 0.5$)

$$P_{lin} = \langle \xi_3 \rangle = \frac{\int d\varphi \left(\frac{dW_1}{d\Omega\, d\omega} - \frac{dW_2}{d\Omega\, d\omega} \right)}{\int d\varphi \left(\frac{dW_1}{d\Omega\, d\omega} + \frac{dW_2}{d\Omega\, d\omega} \right)}. \tag{3.4.10}$$

The Fig. 3.7 presents the calculation results of polarization of UR beam obtained for the case of hard collimation of radiation. It is possible to note that the radiation collimated on the first harmonic possesses practically 100%-polarization.

3.5 Radiation Along an Undulator Axis in a Strong Magnetic Field ($K \geq 1$)

For a plane undulator with arbitrary value of parameter K [6] one can obtain the analytical formula for intensity of radiation along an undulator axis:

$$\left.\frac{dW}{d\Omega\, d\omega}\right|_{\theta=0} = \frac{e^2\gamma^2}{c} \sum_{n=1}^{\infty} [1-(-1)^n] F_N\, nK^2 / \left(1+K^2/2\right) \times \left[J_{\frac{n-1}{2}}\left(\frac{nK^2}{4} \Big/ \left(1+K^2/2\right) \right) - J_{\frac{n+1}{2}}\left(\frac{nK^2}{4} \Big/ \left(1+K^2/2\right) \right) \right]^2. \tag{3.5.1}$$

As follows from this formula, the contribution of even harmonics at $\theta = 0$ becomes zeroth.

We again use the approximation of "long" undulator for integration with respect to frequency. Going to a variable $\gamma\theta$, after integration over azimuth, we will have

$$\left.\frac{dW_1}{d(\gamma^2\theta^2)}\right|_{\theta=0} = 2\pi\,\alpha N K^2 \frac{\gamma^2\,\hbar\,\omega_0}{(1+K^2/2)^3}\sum_{n=1}^{\infty} n^2 \times \left[J_{\frac{n-1}{2}}\left((nK^2)/(1+K^2/2)\right) - J_{\frac{n+1}{2}}\left((nK^2)/(1+K^2/2)\right)\right]^2. \quad (3.5.2)$$

For the case $K^2 \ll 1$ we will write an expression for intensity of the first harmonic, keeping summands, which are proportional to K^2:

$$\left.\frac{dW_{1,1}}{d(\gamma^2\theta^2)}\right|_{\theta=0} = 2\pi\,\alpha N K^2\,\gamma^2\,\hbar\,\omega_0. \quad (3.5.3)$$

Comparing the obtained formula with expression (3.3.4), one may see a good coincidence for $K^2 \ll 1$.

From (3.5.1), using approximation of a "long" undulator, it is possible to derive the spectral distribution of UR in the range of maxima in the radiation spectrum (radiation in a straightforward direction corresponds to these maxima, $\theta = 0$):

$$\left.\frac{dW_n}{\hbar d\omega}\right|_{\omega=\omega_n} = 2\pi\,\alpha N\,\frac{2\gamma^2\hbar\omega_0}{\omega_n}\sum_n \frac{n^2K^2/2}{(1+K^22)^2} \times \left[J_{n-1/2}\left(\frac{n\,K^2/4}{1+K^2/2}\right) - J_{n+1/2}\left(\frac{n\,K^2/4}{1+K^2/2}\right)\right]^2. \quad (3.5.4)$$

To compare the obtained expressions (valid for any K) with formulas (3.4.6), which are true for $K \ll 1$, we'll use in (3.5.4) a variable ξ (3.4.6): $d\omega_n \approx 2\gamma^2\,\omega_0\,n\,d\xi$.

Having written down through new variable the maximal value of UR intensity for $n = 1$, 3 and keeping the main term of expansion in square brackets:

$$\left.\frac{dW_1}{d\xi}\right|_{\xi=1} = 2\pi\,\alpha N\gamma^2\hbar\omega_0\frac{K^2}{(1+K^2/2)}, \qquad \left.\frac{dW_3}{d\xi}\right|_{\xi=3} = 2\pi\,\alpha N\gamma^2\hbar\omega_0\frac{81}{64}\,\frac{K^6}{(1+K^2/2)^3}, \quad (3.5.5)$$

one can see the coincidence of obtained quantities with (3.4.6) for $K^2 \ll 1$.

Calculations of maximal values of odd harmonics according to (3.5.4) are given in Fig. 3.8 for various values of deflection parameter K. As follows from Fig. 3.8c, for parameter $K > 1$ the maximum in a spectrum corresponds to higher harmonics ($n = 11$ for $K = 3$). Undulators with a field providing value $K \geq 1$ refer to wigglers.

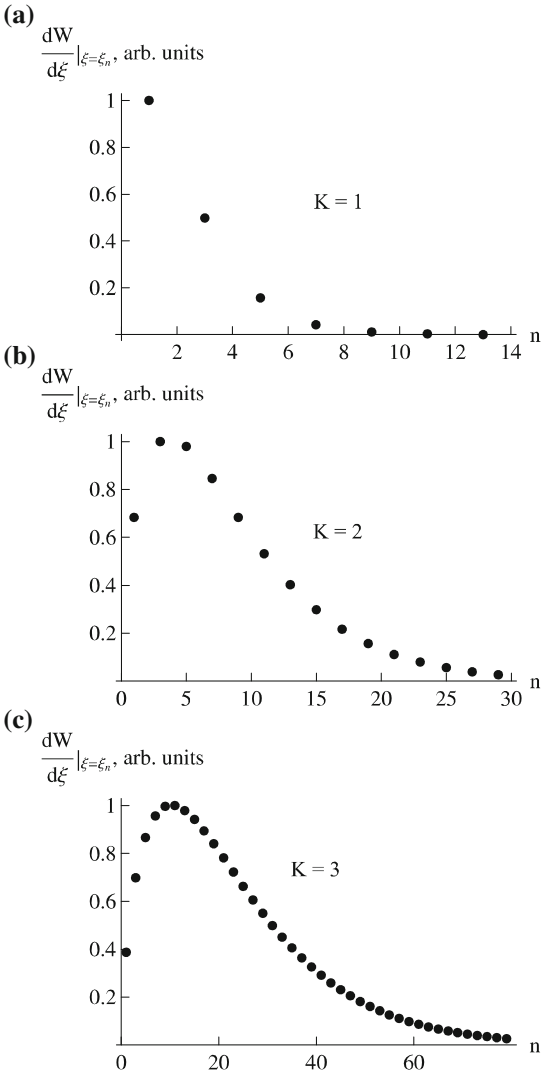

Fig. 3.8 UR intensity in plane undulator in a straightforward direction for various values of parameter K:$K = 1$**a**; $K = 2$ **b** and $K = 3$ **c** depending on number of harmonics

Spectral–angular distribution of radiation in a plane wiggler can be calculated with usage of extremely bulky formulas. However, for large enough values of K (see Fig. 3.8c) the spectral distribution for UR in a straightforward direction $(\theta = 0)$ is described by expression [6]

$$\left.\frac{dW}{d\xi}\right|_{\xi=\xi_n} = \text{const}\left[\frac{\xi_n}{K}\cdot K_{2/3}\left(\frac{2}{3}\,\frac{\xi_n}{K}\right)\right]^2, \tag{3.5.6}$$

where $\xi_n = \frac{\omega_n}{2\gamma^2\omega_0} = \frac{n}{1+K^2/2}$.

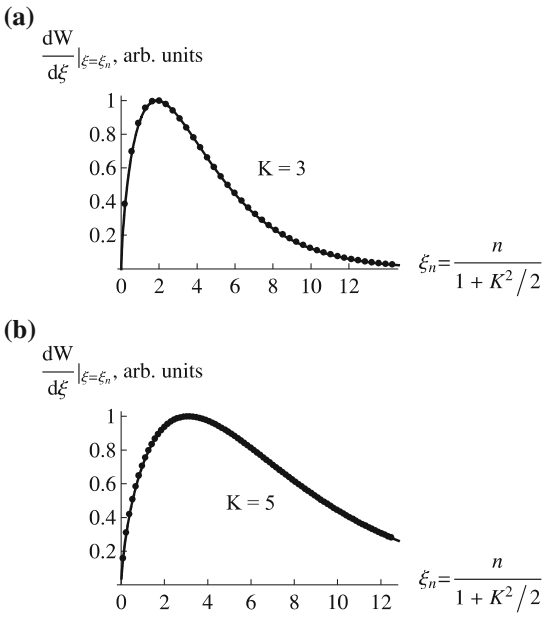

Fig. 3.9 Approximation of distributions, presented in the previous figure, for K=3 (**a**) and K=5 (**b**) by dependence (3.5.6)

Expression (3.5.6) achieves its maximum at $\xi_{\max} \approx 0.625\,K$.

The comparison of exact distribution and approximation (3.5.6) for various values of parameter K is shown in Fig. 3.9a, b. As follows from the figure, at $K \geq 3$ the wiggler radiation in straightforward direction is well described by expression (3.5.6).

3.6 Radiation in a Helical Undulator

In a helical undulator the magnetic field is created, for instance, by a solenoidal current, which describes by the formula

$$H = e_x H_m \sin\frac{2\pi}{\lambda_u} z + e_y H_m \cos\frac{2\pi}{\lambda_u} z. \tag{3.6.1}$$

Electron with velocity βc, entering in the undulator field in an initial point with coordinate $r_0 = \{R,\, 0,\, 0\}$, moves in a "right" helix:

$$r(t) = e_x R\cos\omega_0 t - e_y R\sin\omega_0 t + k\beta_{\|}\, c\, t, \tag{3.6.2}$$

where

$$R = \beta_{\perp} c/\omega_0,\ \beta_{\perp} = \frac{e H_m \lambda_0}{2\pi\gamma mc^2} = \frac{K}{\gamma},\ \beta_{\|} = \beta\left[1 - \left(\frac{\beta_{\perp}}{\beta}\right)^2\right]^{1/2} \approx 1 - \frac{1+K^2}{2\gamma^2},\ \omega_0 = \frac{2\pi}{\lambda_u}\beta_{\|}\, c.$$

By means of the Lorentz-transformation with parameters $\beta_{\|}$ and $\gamma_{\|} = \frac{\gamma}{\sqrt{1+K^2}}$ it is possible to go to a system, where electron rotates in a circular orbit (R-system).

In R-system the electron rotation velocity on the orbit of radius R achieves the value $\beta_R = K$.

The angular distribution of a power in this system is given by the Schott formula:

$$\frac{dP_R}{d\Omega_R} = \frac{e^2 c\,\beta_R^2}{2\pi R^2} \sum_n n^2 \left[\beta_R^2 J_n'^2(n\,\beta_R \sin\theta_R) + \mathrm{ctg}^2\theta_R\, J_n^2(n\,\beta_R \sin\theta_R)\right]. \tag{3.6.3}$$

For non-relativistic movement $\beta_R \ll 1$, what allows, keeping in the sum (3.6.3) the term with $n = 1$, to get the Larmor formula

$$\frac{dP_R}{d\Omega_R} = \frac{e^2 c\,\beta_R^4}{2\pi R^2} \cdot \frac{1}{4}\left(1 + \cos^2\theta_R\right) = \frac{e^2\,\beta_R^2\,\omega_R^2}{2\pi\, c} \cdot \frac{1}{4}\left(1 + \cos^2\theta_R\right). \tag{3.6.4}$$

Integrating with respect to azimuthal angle and expressing β_R and ω_R through parameters in laboratory system, we'll obtain

$$\frac{dP_R}{d\cos\theta_R} = \frac{e^2}{4c} K^2 \gamma_\parallel^2\, \omega_0^2 \left(1 + \cos^2\theta_R\right). \tag{3.6.5}$$

Comparing the obtained expression with similar one for a plane undulator (3.2.5), it is possible to note that they coincide in the case of

$$K_{\mathrm{hel}}^2 \to \frac{K_{\mathrm{pl}}^2}{2}. \tag{3.6.6}$$

That is all formulae describing UR in a plane undulator in dipole approximation in Sects. 3.2 and 3.3, remain true for the helical undulator in the case of substitution (3.6.6) as well. Using the exact expression for radiation power in R-system (3.6.3) and the procedure of transition to the laboratory system (see the formula (3.3.2)), we'll get the following expression for angular distribution of UR:

$$\frac{dW}{d\Omega} = \frac{8\,\alpha\,\hbar\,\omega_0 N\,\gamma^4}{\left(1 + K^2 + \gamma^2\,\theta^2\right)^3} K^2 \sum_{n=1}^{\infty} n^2 \left[J_{\mathrm{n}}'^2(nx) + \left(\frac{\gamma\,\theta}{K} - \frac{1}{x}\right)^2 J_n^2(nx)\right]. \tag{3.6.7}$$

The ultrarelativistic approximation is used here again $\left(\sin\theta \sim \theta, x = \frac{2K\gamma\,\theta}{1+K^2+\gamma^2\,\theta^2}\right)$.

Expression (3.6.7) allows to carry out the analytical summation over n, using known formulae [2]:

$$\sum_{n=1}^{\infty} n^2\, J_n'^2(nx) = \frac{4 + 3x^2}{16(1 - x^2)^{5/2}},$$

$$\sum_{n=1}^{\infty} n^2\, J_n^2(nx) = \frac{x^2(4 + x^2)}{16(1 - x^2)^{7/2}}.$$

In this case instead of the sum (3.6.7) we have

$$\frac{dW}{d\left(\gamma^2\,\theta^2\right)} = \frac{8\,\alpha\,\pi\,\gamma^2\hbar\,\omega_0 N}{\left(1+K^2+\gamma^2\,\theta^2\right)^3}\,K^2\,\frac{1}{16(1-x^2)^{5/2}} \times\left\{4+3x^2+\frac{4+x^2}{1-x^2}\,\frac{\left(1+K^2-\gamma^2\,\theta^2\right)^2}{\left(1+K^2+\gamma^2\,\theta^2\right)^2}\right\}. \tag{3.6.8}$$

The angular distributions of UR intensity (3.6.8) for various values of parameter K are shown in Fig. 3.10a, b.

As follows from Fig. 3.10a, the intensity of radiation for values $K \leq 0.5$ achieves a maximum in the straightforward direction, whereas for $K \geq 1$ the radiation maximum is generated at the angle $\theta_m \sim K/\gamma$ (see Fig. 3.10b). Radiation losses by an electron passing through one period of undulator are calculated by integration of expression (3.6.8):

$$W_0 = \frac{2}{3}\,\alpha\,\pi\,\gamma^2\,\hbar\,\omega_0\,K^2 \tag{3.6.9}$$

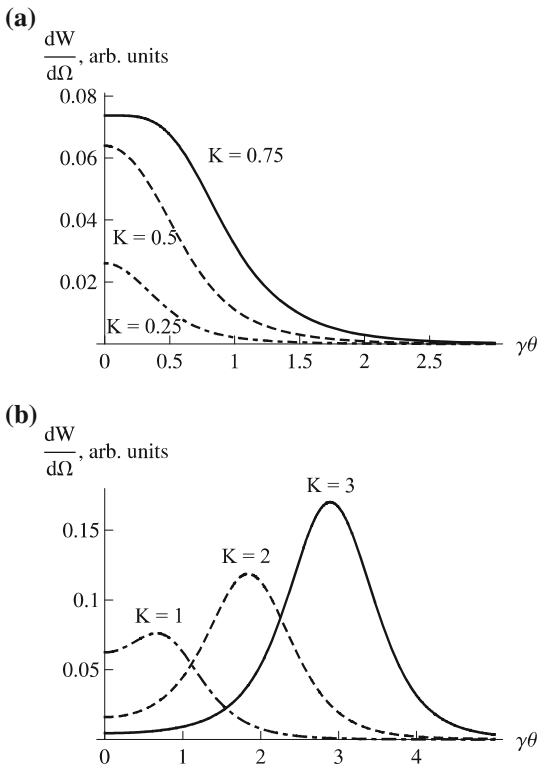

Fig. 3.10 Angular distribution of UR intensity in the helical undulator for various values of parameter K: $K \leq 0.75$ **a** and $K \geq 1$ **b**

and depend in the square-law on the parameter K. The exact UR theory in a helical undulator with arbitrary number of periods is developed, for example, in the work [6]. The spectral-angular distribution on nth harmonic in the ultrarelativistic approximation is written as

$$\frac{dW_n}{\hbar\, d\omega\, d\Omega} = \alpha K^2 \frac{4\gamma^2}{\left(1 + K^2 + \gamma^2\theta^2\right)^2} F_N\, n^2 G_n,$$
$$G_n = \left(\frac{\left(1 + K^2 - \gamma^2\theta^2\right)}{2K\gamma\theta}\right)^2 J_n^2(n\,x) + J_n'^2(n\,x). \tag{3.6.10}$$

The other designations in (3.6.10) are the same, as before.

An intensity spectrum of undulator radiation in a helical undulator for $K = 0.25$ and $N = 10$ is shown in Fig. 3.11 in case of summation with respect to three lowest harmonics:

$$\frac{dW}{\hbar\, d\omega} = \int d\Omega \sum_{n=1}^{3} \frac{dW}{\hbar\, d\omega}. \tag{3.6.11}$$

Integration in (3.6.11) will be carried out over angles $0 \le \varphi \le 2\pi;\ 0 \le \gamma\theta \le 4$.

Only the two first harmonics give the observable contribution to a radiation spectrum for the specified value of parameter K. For value $K < 1$, the intensity of the higher harmonics is proportional to K^{2n} (n is a number of harmonic), what is completely similar to a case of plane undulator. The following relative variable is used again: $\xi = \hbar\omega/2\gamma^2\hbar\omega_0$.

The maximal values of variable ξ for the first and second harmonics for a "long" undulator are:

$$\xi_1 = \frac{1}{1 + K^2} = 0.94; \quad \xi_2 = \frac{2}{1 + K^2} = 1.88. \tag{3.6.12}$$

For an undulator of finite length ($N = 10$, as in this case) a drop of intensity in UR spectrum near values (3.6.12) will be slightly "smearing".

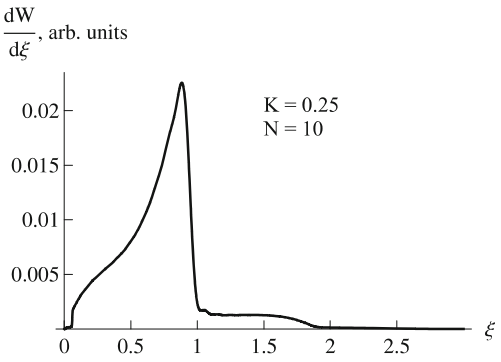

Fig. 3.11 A spectrum of UR intensity in a helical undulator for $K = 0.25$ with taking into account the contribution of the first three harmonics

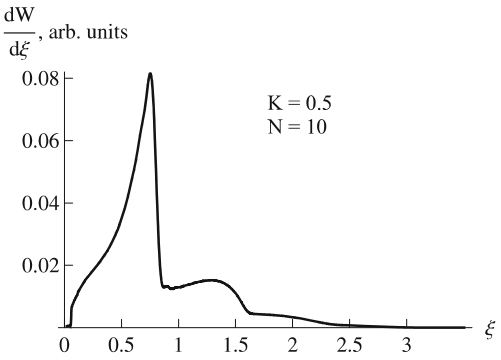

Fig. 3.12 The same, as in Fig. 3.11 for $K = 0.5$ with taking into account the contribution of the first ten harmonics

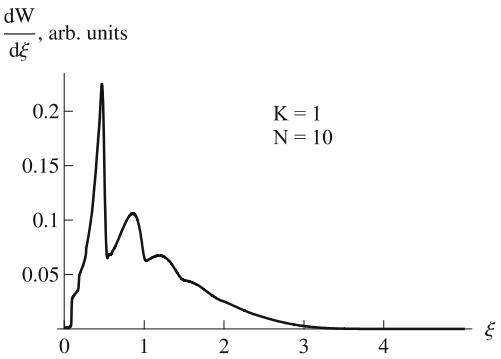

Fig. 3.13 The same, as in Fig. 3.11 for $K = 1$ with taking into account the contribution of the first ten harmonics

The spectra of UR intensity for $K = 0.5$ and $K = 1$ with taking into account contribution of ten harmonics are shown in Figs. 3.12 and 3.13. In the first case the main contribution to a spectrum are given by harmonics with $n = 1$, 2, 3 and $\xi_3 = \frac{3}{1+0.5^2} = 2.4$.

An appreciable shift of harmonics into a soft part of a spectrum occurs with increase of parameter K (up to $K = 1$, as in this case). So, for example, the maximum of the seventh harmonic corresponds to a value $\xi_7 = \frac{7}{1+1^2} = 3.5$.

For this case ten summands were kept in the sum (3.6.11) during calculation of spectrum, however, only the first seven harmonics give the main contribution (see Fig. 3.13).

As it was noted before, in the ultrarelativistic case it is possible to consider polarization of UR beam as a whole. For a helical undulator, where the electron trajectory represents the right or left helix, from the common reasons one may expect that UR polarization will be elliptic (with the large contribution of a circular one).

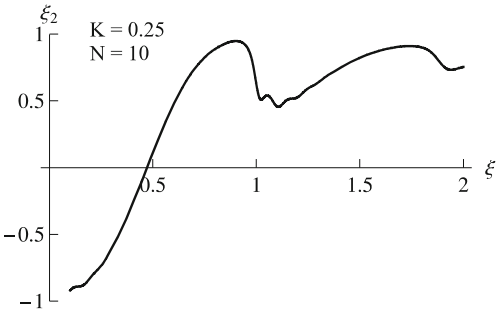

Fig. 3.14 A spectral dependence of a degree of circular polarization for helical undulator with $K = 0.25$ and $N = 10$

Spectral dependence of circular polarization can be found from the general formula (2.2.6), where basis vectors are chosen as:

$$e_1 = \frac{1}{\sqrt{2}}\left(e_x + ie_y\right), \quad e_2 = \frac{1}{\sqrt{2}}\left(e_x - ie_y\right). \tag{3.6.13}$$

Then, the required dependence $\bar{\xi}_2(\hbar\omega)$ may be found after integration of the following expression over a solid angle

$$\bar{\xi}_2(\hbar\omega) = \int d\Omega \sum_{n=1} 2\alpha K^2 \frac{4\gamma^2}{\left(1 + K^2 + \gamma^2\theta^2\right)^2} \times F_N\, n^2 \left[\frac{\left(1 + K^2 - \gamma^2\theta^2\right)}{2K\gamma} J_n(nx) J_n'(nx)\right] \Big/ \int d\Omega \sum_{n=1} \frac{dW_n}{\hbar\omega\, d\Omega}. \tag{3.6.14}$$

As follows from (3.6.14), for a radiation angle

$$\gamma\,\theta = \sqrt{1 + K^2} \tag{3.6.15}$$

circular polarization changes the sign regardless of harmonic number (in other words, for the angle (3.6.15) UR polarization becomes linear, and the polarization plane will be perpendicular to the radiation plane, which passes through the undulator axis and a wave vector k).

Dependence of circular polarization on a spectral variable ξ for $K = 0.25$ and $N = 10$ is shown in Fig. 3.14. The integration over a solid angle was carried out practically over a full cone: $0 \le \varphi \le 2\pi,\ 0 \le \gamma\,\theta \le 4$.

Expectedly, in the range $\xi \le \xi_0 = \frac{1}{2+0.25^2} = 0.485$ polarization becomes "left-circular" due to the contribution of radiation at angles $\gamma\,\theta > \sqrt{1 + K^2}$, whereas in more hard part of a spectrum the polarization is "right-circular" one.

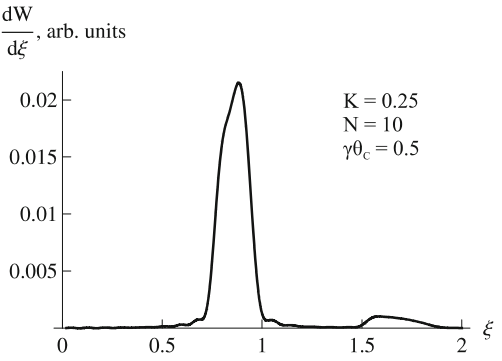

Fig. 3.15 UR spectrum for hard collimation ($\gamma\theta_c = 0.5$) with taking into account the contribution of the first three harmonics

In case of hard collimation of UR alongside with improvement of monochromatization it is possible to get a beam, for which the degree of circular polarization will be close to one.

Thus, the UR spectrum for $K = 0.25$ and $N = 10$ is shown in Fig. 3.15 in the case of collimation $\gamma\theta_c = 0.5$. In this case the calculated value of average circular polarization in the first maximum achieves $\left\langle \bar{\xi} \right\rangle \approx 0.96$.

References

1. Talman R.: Accelerator X-Ray sources, Wiley (2007)
2. Bordovitsyn, V.A.: (ed.) Synchrotron Radiation Theory and its Development. World Scientific, Singapore (1999)
3. Schmuser, P., Dolhus, M., Rossbach, J.: Ultraviolet and Soft X-ray Free Electron Lasers. Springer Tracts in Modern Physics, vol. 229 (2009)
4. Alferov, D.F., Bashmakov, Yu.A., Bessonov, E.G.: Undulator radiation. Trudy FIAN **80**, 100–124 (1975). (in Russian)
5. Didenko, A.N., Kozhevnikov, A.V., Medvedev, A.V., et al.: Radiation from electrons in magnetic undulator. JETP **76**, 1919–1932 (1979). (in Russian)
6. Kincaid, B.M.: A short-period helical wiggler as an improved source of synchrotron radiation. J. Appl. Phys. **48**, 2684 (1977)

Chapter 4
Coherent Bremsstrahlung

4.1 The Main Characteristics of Bremsstrahlung in the Screened Coulomb Field

The quantum theory of bremsstrahlung (BS) in the Coulomb field of nucleus was developed more than 60 years ago [1]. Later the development of bremsstrahlung theory has allowed to take into account such corrections as screening effect, BS on electron shells of target atoms [2, 3].

The formulae for calculation of characteristics of bremsstrahlung in the Born approximation are written most simply in the coordinate system connected with emitted photon (Fig. 4.1). The projections of momenta of initial and scattered electron on a plane, which is perpendicular to the photon momentum **k** are designated in this system of coordinates in dimensionless units through vectors **u** and ***v***. The system of units $m = c = 1$, (i.e. dimensionless variables), where energy is measured in units of mc^2, momentum—in terms of mc, length—in the Compton electron wave lengths, is used in this chapter everywhere, where it is not stipulated especially, for simplification of calculations and formulae. Let's put a designation

$$\mathbf{J} = \frac{4\pi e V(\mathbf{q})}{\hbar\omega}\mathbf{I}, \tag{4.1.1}$$

where

$$\mathbf{I} = \frac{\mathbf{u}}{1+u^2} - \frac{\boldsymbol{v}}{1+v^2} + \mathbf{n}\left(\frac{1}{1+u^2} - \frac{1}{1+v^2}\right),$$

$\mathbf{n} = \frac{\mathbf{k}}{\hbar\omega}$, $V(\mathbf{q})$ is a Fourier-transform of a field of nucleus $V(\mathbf{r})$, and cross-section of BS by non-polarized electron is written as follows:

$$d\sigma = \frac{e^2}{(2\pi)^4}\{F_0 + \xi_i F_i\}\hbar\omega d(\hbar\omega) d\Omega_1 \varepsilon_2^2 d\Omega_2,$$

A. P. Potylitsyn, *Electromagnetic Radiation of Electrons in Periodic Structures*, Springer Tracts in Modern Physics, 243, DOI: 10.1007/978-3-642-19248-7_4,

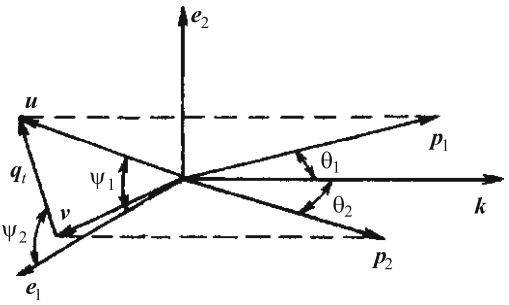

Fig. 4.1 The kinematic variables describing the bremsstrahlung process

where ξ_i are the Stokes parameters,

$$\begin{aligned} F_0 &= 2(\hbar\omega)^2|\mathbf{J}|^2 + 4\varepsilon_1\varepsilon_2|\mathbf{J}_t|^2 = 2\left(\varepsilon_1^2+\varepsilon_2^2\right)|\mathbf{J}|^2 - 4\varepsilon_1\varepsilon_2|\mathbf{J_3}|^2, \\ F_1 &= 8\varepsilon_1\varepsilon_2 J_1 J_2, \\ F_2 &= 0, \\ F_3 &= 4\varepsilon_1\varepsilon_2\left(|J_1|^2 - |J_2|^2\right). \end{aligned} \tag{4.1.2}$$

The following designations are made here: $J_1 = \mathbf{Je}_1, J_2 = \mathbf{Je}_2, J_3 = \mathbf{Jn}$, $\mathbf{J}_t = J_1\mathbf{e}_1 + J_2\mathbf{e}_2$, through $\varepsilon_1, \varepsilon_2, \hbar\omega$ are designated the energy of initial electron, scattered electron and photon.

As it is shown, for instance in [4], a linear polarization of BS does not depend on polarization of electron, i.e. it has a "classical" origin, whereas a circular polarization of BS appears only from polarized electrons.

We'll consider the linear polarization of photons relative to the plane defined by a geometry, i.e. a plane, which passes through momentum of initial electron $\mathbf{p}_1$ and emits photon $\mathbf{k}$. To designate a normal to this plane through $\mathbf{b}$, then as basis vectors it is possible to choose the followings: $\mathbf{e}_1 = [\mathbf{n}, \mathbf{b}]/|[\mathbf{n}, \mathbf{b}]|$, $\mathbf{e}_2 = [\mathbf{e}_1, \mathbf{n}]$, which together with a vector $\mathbf{n}$ form the right system of coordinates (see Fig. 4.1). We choose screening for a nucleus field according to the Thomas–Fermi model [4, 5]: $V(\mathbf{r}) = \frac{Ze}{r}\exp(-r/\rho_0), \rho_0 = \frac{0.81\lambda_e}{\alpha Z^{1/3}} \approx \frac{111}{Z^{1/3}}\lambda_e$, (where λ_e is Compton wavelength of an electron). Fourier-transform of potential will become $V(q) = Ze/\left(q^2 + \hbar^2/\rho_0^2\right)$ and integration in (4.1.2) with respect to an unobservable kinematic variables (i.e. over angles of scattered electrons) will be easily carried out analytically. However the other approach for a generality of description with the following material (with the theory of coherent bremsstrahlung) will be used here.

Let's introduce a variable $\mathbf{q}_t$ as a transverse nucleus recoil momentum, which is perpendicular to a photon momentum. There is the relationship from the law of momentum conservation of $\mathbf{q}_t = \mathbf{u} - \boldsymbol{v}$. It is easy to show that an element of a solid angle $d\Omega_2$ is connected with differential of the introduced variable as follows:

$$d\Omega_2 = \frac{1}{\varepsilon_2^2} d\mathbf{q}_t = \frac{1}{\varepsilon_2^2} q_t\, dq_t\, d\psi_2.$$

Here ψ_2 is an azimuthal angle of momentum $\mathbf{q}_t$ (see Fig. 4.1).

In new variables the vector $\mathbf{I}$ and its projections I_i are written in the form:

$$\begin{aligned}
\mathbf{I} &= \frac{\mathbf{q}_t}{1+u^2+q_t^2-2uq_t\cos\psi} - \frac{(\mathbf{u}-\mathbf{n})\left(2uq_t\cos\psi-q_t^2\right)}{(1+u^2)\left(1+u^2+q_t^2-2uq_t\cos\psi\right)};\\
I_1 &= \frac{q_t\cos\psi_2}{1+u^2+q_t^2-2uq_t\cos\psi} - \frac{u\cos\psi_1\left(2uq_t\cos\psi-q_t^2\right)}{(1+u^2)\left(1+u^2+q_t^2-2uq_t\cos\psi\right)};\\
I_2 &= \frac{q_t\sin\psi_2}{1+u^2+q_t^2-2uq_t\cos\psi} - \frac{u\sin\psi_1\left(2uq_t\cos\psi-q_t^2\right)}{(1+u^2)\left(1+u^2+q_t^2-2uq_t\cos\psi\right)};\\
I_3 &= \frac{2uq_t\cos\psi-q_t^2}{(1+u^2)\left(1+u^2+q_t^2-2uq_t\cos\psi\right)}.
\end{aligned} \tag{4.1.3}$$

An angle $\psi=\psi_1-\psi_2$ entered in expressions (4.1.3) is the angle between two vectors: $\mathbf{u}$ and $\mathbf{q}_t$.

Integration of expression (4.1.2) over unobservable kinematic variables reduces to integration with respect to the two-dimensional transverse recoil $\mathbf{q}_t$. Herewith in the integrand there are combinations of the type $J_1\cdot J_2, J_1^2$ etc. We'll illustrate the calculation of integrals on the following example:

$$\int J_1^2 d\Omega_2 = \frac{1}{2\varepsilon_2^2}\int J_1^2\, dq_t^2\, d\psi_2.$$

Everywhere in the integrand

$$\begin{aligned}
J_1^2 = \left(\frac{4\pi eV(q)}{\hbar\omega}\right)^2 \Bigg\{ &\frac{q_t^2\cos^2\psi_2}{\left(1+u^2+q_t^2-2uq_t\cos\psi\right)}\\
&+\frac{u^2\cos^2\psi_1\left(4u^2q_t^2\cos^2\psi-4uq_t^3\cos\psi+q_t^4\right)}{(1+u^2)^2\left(1+u^2+q_t^2-2uq_t\cos\psi\right)^2}\\
&+\frac{2uq_t\cos\psi_1\cos\psi_2\left(q_t^2-2uq_t\cos\psi\right)}{(1+u^2)\left(1+u^2+q_t^2-2uq_t\cos\psi\right)^2}\Bigg\}
\end{aligned} \tag{4.1.4}$$

it is expressed an angle ψ_2 through ψ_1 and ψ for simplification of azimuthal integrals:

$$\begin{aligned}
\cos\psi_2 &= \cos\psi_1\cos\psi+\sin\psi_1\sin\psi;\\
\cos^2\psi_2 &= \sin^2\psi_1+\cos^2\psi\cos(2\psi_1)+\sin\psi\cos\psi\sin(2\psi_1).
\end{aligned}$$

Since, $d\psi_2=d\psi$ it is necessary to calculate the azimuthal integrals of type

$$A=\int_0^{2\pi}\frac{d\psi}{a-b\cos\psi};\quad B_n=\int_0^{2\pi}\frac{\cos^n\psi d\psi}{(a-b\cos\psi)^2};\quad n=0,1,2;\quad C_0=\int_0^{2\pi}\frac{\sin\psi\cos\psi d\psi}{(a-b\cos\psi)^2},$$

since the potential $V(q)$ does not depend on an azimuthal angle. Evidently the last integral is equal to zero due to oddness of integrand. The others are easily calculated according to the residue theory:

$$A = \frac{2\pi}{Q^{1/2}}; \quad B_0 = \frac{2\pi a}{Q^{3/2}}; \quad B_1 = \frac{2\pi b}{Q^{3/2}}; \quad B_2 = \frac{2\pi}{b^2}\left(1 - \frac{a}{Q^{1/2}} + \frac{ab^2}{Q^{3/2}}\right).$$

Here $a = 1 + u^2 + q_t^2; b = 2uq_t; Q = a^2 - b^2 = (1+u^2)^2 + 2(1-u^2) \times q_t^2 + q_t^4$.

Thus, after reducing of expression (4.1.4) to a common denominator and azimuthal integration we have

$$\begin{aligned}\int_0^{2\pi} J_1^2 d\psi_2 &= \frac{(4\pi eV(q))^2}{\hbar^2\omega^2}\Big\{q_t^2\big(1+u^2\big)^2(B_0 - B_2) + q_t^2\cos^2\psi_1 \\ &\quad \times \Big[2\big(1+u^4\big)B_2 - \big(1+u^2\big)^2 B_0 + 2uq_t\big(1-u^2\big)B_1 + q_t^2u^2B_0\Big]\Big\} \\ &= \frac{(4\pi eV(q))^2}{\hbar^2\omega^2}\big(x + yu^2\cos^2\psi_1\big), \end{aligned} \tag{4.1.5}$$

where

$$\begin{aligned} x\big(q_t^2\big) &= \frac{2\pi}{4u^2}\left(\frac{1+u^2+q_t^2}{Q^{1/2}} - 1\right); \\ y\big(q_t^2\big) &= \frac{2\pi}{u^2(1+u^2)^2}\left\{\frac{1+u^4}{2u^2}\left(1 - \frac{1+u^2+q_t^2}{Q^{1/2}}\right)\right. \\ &\quad \left. + q_t^2\frac{(1-u^2)^2(1+u^2) + q_t^2(1+3u^2-2u^4) + u^2q_t^4}{Q^{3/2}}\right\}. \end{aligned}$$

During integration of expression (4.1.5) over the recoil momentum with taking into account a dependence of potential on q_t the following integrals appear:

$$\left.\begin{matrix} X \\ Y \end{matrix}\right\} = C\int \frac{\frac{1}{2}dq_t^2}{\big(q_t^2 + q_l^2 + \hbar^2/\rho_0\big)^2}\left\{\begin{matrix} x(q_t) \\ y(q_l) \end{matrix}\right\}, \tag{4.1.6}$$

where $C = (4\pi Ze^2/\varepsilon_2\omega)^2$. It is well-known that a longitudinal component of recoil momentum is satisfied the inequality: $q_l = \mathbf{qn} \sim \delta \ll \hbar/\rho_0$ (here $\delta = q_{l\min} = \hbar\omega/(2\gamma_1\varepsilon_2)$ is the minimal longitudinal recoil momentum), therefore the value q_l^2 in a denominator can be neglected in comparison with $\hbar^2/\rho_0^2$. Integrals over the transverse recoil momentum q_t^2 can be calculated in limits from 0 up to ∞, since integrand at big q_t decreases as q_t^{-3} or more prompt. Thus for simplification of calculations the region of integration will be divided into two parts: I: $0 \le q_t^2 < q_0^2$; and II: $q_0^2 \le q_t^2 < \infty$, where $\hbar^2/\rho_0^2 \ll q_0^2 \ll 1$, in each of which the integrals are reduced to the tabulated integrals after simplification of integrand. In region I $q_t^2 \ll 1$, therefore we shall expand the values x, y into a series in terms of q_t degrees leaving terms not above q_t^2:

$$\left.\begin{aligned} x_{\mathrm{I}} &= \frac{2\pi}{4u^2}\left[\frac{1+u^2+q_t^2}{1+u^2}\left(1-\frac{1-u^2}{(1+u^2)^2}q_t^2\right)-1\right]=\frac{\pi q_t^2}{(1+u^2)^2};\\ y_{\mathrm{I}} &= \frac{2\pi}{u^2(1+u^2)^2}\left[-q_t^2\frac{1+u^4}{(1+u^2)^2}+q_t^2\frac{(1-u^2)^2}{(1+u^2)^2}\right]=-\frac{4\pi q_t^2}{(1+u^2)^4}. \end{aligned}\right\} \tag{4.1.7}$$

The results of integration in region I:

$$X_{\mathrm{I}}=\frac{\pi C}{(1+u^2)^2}\left(\ln\frac{q_0}{\hbar/\rho_0}-\frac{1}{2}\right),\quad Y_{\mathrm{I}}=-\frac{4\pi C}{(1+u^2)^4}\left(\ln\frac{q_0}{\hbar/\rho_0}-\frac{1}{2}\right).$$

In region II of the integrand we neglect the value $\hbar^2/\rho_0^2$ in comparison with q^2 then integrals are easily calculated:

$$X_{\mathrm{II}}=-\frac{\pi C}{(1+u^2)^2}\left(\ln\frac{q_0}{1+u^2}+\frac{1}{2}\right);\quad Y_{\mathrm{II}}=\frac{4\pi C}{(1+u^2)^4}\left(\ln\frac{q_0}{1+u^2}+\frac{3}{2}\right).$$

Finally we have (in the system of units $\hbar=m=c=1$):

$$\begin{aligned} X &= X_{\mathrm{I}}+X_{\mathrm{II}}=\frac{\pi C}{(1+u^2)^2}\left(\ln\left(1+u^2\right)\rho_0^2-1\right),\\ Y &= Y_{\mathrm{I}}+Y_{\mathrm{II}}=-\frac{4\pi C}{(1+u^2)^2}\left(\ln\left(1+u^2\right)\rho_0^2-2\right),\\ &\int I_1^2 d\Omega_2 = X+Yu^2\cos^2\psi_1. \end{aligned} \tag{4.1.8}$$

As expected the result, does not depend on q_0.

Other integrals are similarly calculated as well:

$$\left.\begin{aligned} \int J_2^2 d\Omega_2 &= X+Yu^2\sin^2\psi_1;\\ \int J_3^2 d\Omega_2 &= X+Y\left(\frac{1-u^2}{2}\right)^2;\\ \int J_1 J_2 d\Omega_2 &= Yu^2\sin\psi_1\cos\psi_{1.} \end{aligned}\right\} \tag{4.1.9}$$

Further, from (4.1.9) it is possible to obtain

$$\begin{aligned} \int \mathbf{J}^2 d\Omega_2 &= \int\left(J_1^2+J_2^2+J_3^2\right)d\Omega_2 = 3X+Y\frac{(1+u^2)^2}{4}\\ &= \left(\frac{4\pi Ze^2}{\varepsilon_2\omega}\right)^2\frac{\pi}{(1+u^2)^2}(2\Gamma+3) \end{aligned} \tag{4.1.10}$$

where

$$\Gamma(u^2) = \ln\frac{(1+u^2)111}{Z^{1/3}} - 2. \tag{4.1.11}$$

From (4.1.2) and (4.1.9) we find the integrated cross-section over unobservable variables (i.e. angular distribution of the radiation):

$$\begin{aligned} d\sigma &= \frac{e^2}{(2\pi)^4}\hbar\omega d\,\hbar\omega d\,\Omega_1\varepsilon_2^2\int\{F_0+\xi_1F_1+\xi_3F_3\}d\Omega_2 \\ &= 4Z^2e^6\frac{d\hbar\omega}{\hbar\omega}\frac{udu}{(1+u^2)^4}\frac{d\psi_1}{2\pi}\left\{\frac{\varepsilon_1^2+\varepsilon_2^2}{\varepsilon_1^2}(1+u^2)^2(2\Gamma+3)\right. \\ &\quad -2\frac{\varepsilon_2}{\varepsilon_1}(1+u^2)^2-8\frac{\varepsilon_2}{\varepsilon_1}u^2\Gamma-\xi_1 8\frac{\varepsilon_2}{\varepsilon_1}u^2\Gamma\sin(2\psi_1) \\ &\quad \left.-\xi_3 8\frac{\varepsilon_2}{\varepsilon_1}u^2\Gamma\cos(2\psi_1)\right\}. \end{aligned} \tag{4.1.12}$$

In order to go on to the dimensional variables, it is necessary to replace in the last formula e^6 on αr_0^2, where r_0 is the classical radius of electron.

It should be noted that using a nucleus potential with more exact account of screening the cross-section (4.1.12) remains the same, only the values of X, Y and Γ (see (4.1.8), (4.1.11)) have been changed.

Stokes parameters for photons, emitted at angles $u = \varepsilon_1\theta_1$ and ψ_1 averaged over unobservable variables need to be defined:

$$\bar{\xi}_i = \int F_i\,d\Omega_2\Big/\int F_0\,d\Omega_2. \tag{4.1.13}$$

Then the linear polarization of BS is described by the following parameters:

$$\begin{aligned} \bar{\xi}_1 &= -\frac{8\varepsilon_1\varepsilon_2\left[u^2\Gamma/(1+u^2)^2\right]\sin(2\psi_1)}{(\varepsilon_1^2+\varepsilon_2^2)(2+3)-2\varepsilon_1\varepsilon_2\left[1+4u^2\Gamma/(1+u^2)^2\right]}; \\ \bar{\xi}_2 &= -\frac{8\varepsilon_1\varepsilon_2\left[u^2\Gamma/(1+u^2)^2\right]\cos(2\psi_1)}{(\varepsilon_1^2+\varepsilon_2^2)(2\Gamma+3)-2\varepsilon_1\varepsilon_2\left[1+4u^2\Gamma/(1+u^2)^2\right]}. \end{aligned} \tag{4.1.14}$$

As follows from (4.1.14), the plane of the maximal polarization is perpendicular to the plane of radiation (at $\psi_1 = 0, \bar{\xi}_1 = 0, \bar{\xi}_3 < 0$). From (4.1.14) it is easy to obtain the maximal linear polarization of a photon beam

$$\begin{aligned} P &= \sqrt{\bar{\xi}_1^2+\bar{\xi}_2^3} \\ &= \frac{8(1-x)u^2\Gamma(u^2)}{(1+u^2)^2(2\Gamma+3)\left[1+(1-x)^2\right]-2(1-x)\left[(1+u^2)^2+4u^2\Gamma\right]}. \end{aligned} \tag{4.1.15}$$

Here it is introduced variable $x = \hbar\omega/\varepsilon_1$, which is the photon relative energy.

It should be noted that expression (4.1.15) does not depend directly on the energy of initial electron ε_1. Evidently, the expression (4.1.15) is inapplicable for energy of electrons $\varepsilon_1 \geq 1$, since it is obtained in ultra-relativistic approximation. Cross-section (4.1.12) allows to get the spectral-angular distribution of bremsstrahlung intensity after an integration over an azimuth:

$$\frac{d^2I}{\hbar\, d\omega u\, du} = \int \frac{\hbar\omega\, d\sigma}{\hbar\, d\omega u\, du\, d\psi_1} d\psi_1 = 4Z^2\alpha r_0^2 \frac{1}{(1+u^2)^4} \times \left\{ \left[1+(1-x)^2\right](1+u^2)^2(2\Gamma+3) - 2(1-x)(1+u^2)2 - 8(1-x)u^2\Gamma \right\}. \tag{4.1.16}$$

The dimensionless variable $x = \hbar\omega/\varepsilon_1$ and condition $\hbar\omega + \varepsilon_2 = \varepsilon_1$ are used again in the formula (4.1.16).

The spectrum of BS intensity is presented in Fig. 4.2 after integration over a solid angle $0 < u \leq 1$ (the bottom curve) and $0 \leq u \leq 5$ (the top curve). As follows from the figure, the spectrum shape practically does not change. This fact is a consequence of one of important BS characteristics, i.e. a weak dependence of angular distribution of BS on energy of photons (a variable x) (see Fig. 4.3).

Neglecting the dependence on u in the logarithm in (4.1.16), it is possible to obtain spectral distribution of BS:

$$\frac{dI}{d\omega} = 4Z^2\alpha r_0^2 \int_0^\infty \frac{\frac{1}{2}du^2}{(1+u^2)^4} \times \left\{ \left[1+(1-x)^2\right](1+u^2)^2 \left(2\ln\frac{111}{Z^{1/3}} - 1\right) - 2(1-x)(1+u^2)^2 - 8(1-x)u^2\left(\ln\frac{111}{Z^{1/3}} - 2\right) \right\} = 4Z^2\alpha r_0^2 \left(\frac{4}{3} - \frac{4}{3}x + x^2\right)\left(\ln\frac{111}{Z^{1/3}} - \frac{1}{2}\right). \tag{4.1.17}$$

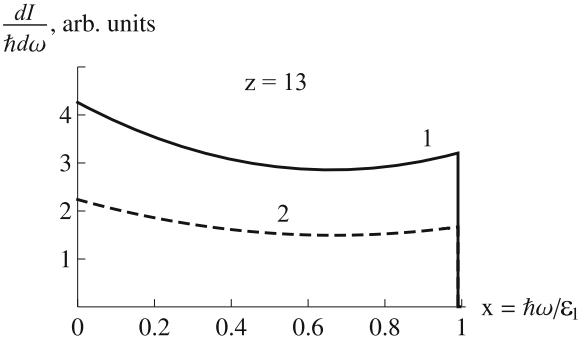

Fig. 4.2 Spectral dependence of BS intensity: *curve* 1 for angle of collimation $u_c = 5$; *curve* 2—for $u_c = 1$

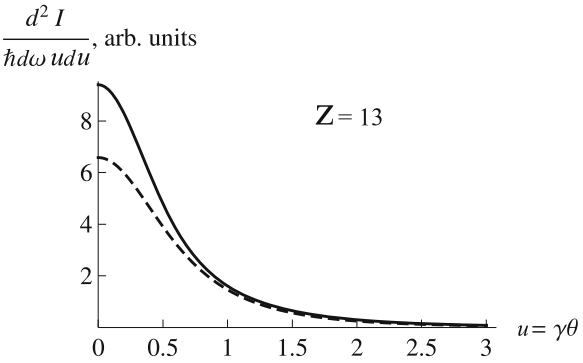

Fig. 4.3 Angular distribution of BS in a thin target, calculated by the formula (4.1.16) for $x = 0.2$ (the *top curve*) and for $x = 0.8$ (the *bottom curve*)

Integration over photon energy from (4.1.17) leads to the radiation losses connected with BS process of the relativistic electron in the screened nucleus field:

$$I = \int_0^{\varepsilon_1} \hbar d\omega \frac{dI}{\hbar d\omega} = 4Z^2 \alpha r_0^2 \varepsilon_1 \left(\ln \frac{111}{Z^{1/3}} - \frac{1}{2} \right). \tag{4.1.18}$$

From (4.1.18) it follows that radiation losses in the BS process are proportional to the initial electron energy ε_1. If n is nuclei concentration in a target, then it is possible to obtain the radiation losses of relativistic electron on unit of the path from (4.1.18):

$$\frac{dE_{\text{rad}}}{dx} \approx 4nZ^2 \alpha r_0^2 \varepsilon_1 \left(\ln \frac{111}{Z^{1/3}} - \frac{1}{2} \right), \tag{4.1.19}$$

where $n = N_A(\rho/A); N_A = 6.02 \cdot 10^{23}$ is the Avogadro number; ρ is density of a target matter; A is an atomic weight. Equation (4.1.19) in term of energy ε_1 is usually written as:

$$\frac{dE_{\text{rad}}}{dx} = -\frac{\varepsilon_1}{\mathrm{X}_0}, \quad \frac{1}{\mathrm{X}_0} = 4nZ^2 \alpha r_0^2 \left(\ln \frac{137}{Z^{1/3}} - \frac{1}{2} \right), \tag{4.1.20}$$

with the known solution for the electron energy in output from a thin target:

$$\varepsilon_1(x) = \varepsilon_1 \exp\left(-\frac{x}{\mathrm{X}_0} \right). \tag{4.1.21}$$

The parameter X_0 refers to as radiation length. More exact formula for X_0, taking into account the BS on the atomic electrons, is given by expression [6]:

$$\frac{1}{\mathrm{X}_0} = 4\alpha r_0^2 nZ(Z+1) \ln\left(\frac{183}{Z^{1/3}} \right) \left[1 + 0.12 \left(\frac{Z}{82} \right)^2 \right]. \tag{4.1.22}$$

Table 4.1 Values of radiation lengths for some substances

Substance	z	A	X_0, cm
Air	7.4	14.3	2.9×10^4
C	6	12	19.8
Al	13	27	9.1
Cu	29	63.6	1.52
Pb	82	207.2	0.58

Often the "engineering" formula is used:

$$X_0 = \frac{716A}{Z(Z+1)\ln\left(\frac{287}{\sqrt{Z}}\right)}\left[\mathrm{g/cm^2}\right]. \tag{4.1.23}$$

The values of radiation lengths for some materials are given in Table 4.1.

Definitely the spectra presented on Fig. 4.2 as well as formulae (4.1.20), (4.1.21), describe the radiation from thin targets, where the root-mean-square (rms) angle of multiple scattering of the initial electrons does not exceed γ^{-1}.

The multiple scattering angle of relativistic electrons with energy ε_1, passing a layer of thickness t, is calculated by the formula

$$\sqrt{\langle\theta_{\mathrm{ms}}^2\rangle} \approx \frac{21}{\varepsilon_1[\mathrm{MeV}]}\sqrt{\frac{t}{X_0}}. \tag{4.1.24}$$

Hence we have a criterion for a "thin" target:

$$\gamma^{-1} \geq \frac{21}{\gamma mc^2}\sqrt{\frac{t}{X_0}}, \quad \text{or} \quad t \leq 0.0006\, X_0 \tag{4.1.25}$$

Radiation losses in a thin target are found directly from (4.1.20), since BS absorption in a target is insignificant:

$$\Delta E_{\mathrm{rad}} = \frac{x}{X_0}\varepsilon_1. \tag{4.1.26}$$

As follows from (4.1.17), the photon spectrum of BS may be written as

$$\frac{dN}{\hbar\, d\omega} \sim \frac{d\sigma}{\hbar\, d\omega} = \frac{1}{\hbar\omega}\frac{dI}{\hbar\, d\omega}. \tag{4.1.27}$$

Evidently, it is diverged at $\hbar\omega \to 0$ (so-called infrared catastrophe).

As has been shown by Ter-Mikaelyan [7], in a soft part of BS spectrum for energy of photons $\hbar\omega < \gamma\hbar\omega_{\mathrm{p}}$ ($\hbar\omega_{\mathrm{p}}$ is energy of the target material plazmon) the process of BS is suppressed due to polarization of a medium. Energy of plazmon is defined by concentration of electrons in a target material nZ:

$$\hbar\omega_{\mathrm{p}} = \hbar\sqrt{4\pi nZr_0c^2}. \tag{4.1.28}$$

In a soft part of BS spectrum ($\hbar\omega \ll \varepsilon_1$) for a thin target the angular distribution is approximated by expression:

$$\frac{dI}{\hbar\, d\omega u\, du\, d\varphi} = \frac{2}{\pi}\frac{x}{X_0}\frac{1+u^4}{(1+u^2)^4}. \tag{4.1.29}$$

However the polarization of medium leads to the modification of the formula (4.1.29) (see [7]):

$$\frac{dI_{\mathrm{m}}}{\hbar\, d\omega u\, du\, d\varphi} = \frac{2}{\pi}\frac{x}{X_0}\frac{1+u^4}{(1+u^2)^2\left(1+u^2+\frac{\gamma^2\omega_{\mathrm{p}}^2}{\omega^2}\right)^2}. \tag{4.1.30}$$

Taking into account this effect (so-called effect of density in BS) results in a strong suppression of BS yield in the range $\hbar\omega \le \hbar\gamma\omega_{\mathrm{p}}$.

The intensity spectra of BS with taking into account a medium polarization and without this effect are given on Fig. 4.4:

$$\frac{dI_{\mathrm{m}}}{\hbar\, d\omega} = 2\frac{x}{\mathrm{X}_0}\int_0^{u_{\mathrm{c}}} \frac{du^2(1+u^4)}{(1+u^2)^2\left(1+u^2+\frac{\gamma^2\omega_{\mathrm{p}}^2}{\omega^2}\right)^2}. \tag{4.1.31}$$

The upper limit in (4.1.31) is defined by a collimation angle of radiation. The photon spectrum can be obtained from (4.1.31):

$$\frac{dN_{\mathrm{m}}}{\hbar\, d\omega} = \frac{1}{\hbar\omega}\frac{dI_{\mathrm{m}}}{\hbar\, d\omega}$$

and is shown on Fig. 4.5 (the bottom curve).

The "divergent" spectrum calculated according to the formula (4.1.17), i.e. neglecting the Ter-Mikaelyan's effect, is shown just here for comparison. It is necessary to note, that Ter-Mikaelyan's theory was developed about 50 years ago, whereas the experimental proof of this effect was obtained in 1995 in experiments at the Stanford electron accelerator [8].

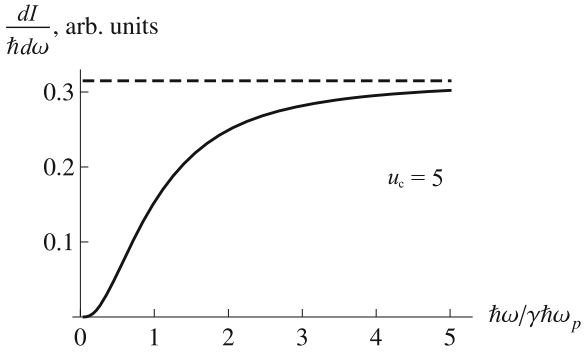

Fig. 4.4 A spectrum of BS intensity with taking into account the density effect (the *bottom curve*) and without this effect (the *upper* one) for the collimation angle $u_c = 1$

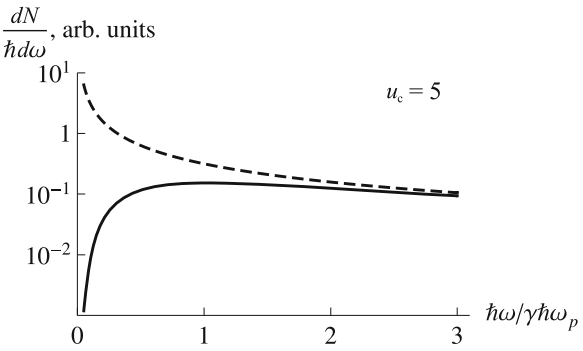

Fig. 4.5 The photon BS spectrum with taking into account the density effect (the *bottom curve*) and without one (the *top curve*)

The intensity spectrum of BS (4.1.17) is obtained for ultra-relativistic electrons in approximation of full screening, in other words, when the effective impact parameter of the initial electron trajectory exceeds the atom sizes well. For not so large electron energies $\gamma = \frac{\varepsilon_1}{mc^2} \leq \frac{111}{Z^{1/3}}$ (i.e. for moderately relativistic electrons) BS from trajectories with smaller impact parameters gives the significant contribution as well. In this case the logarithm in (4.1.17) will depend not only on a screening radius, but also from the minimal recoil momentum $q_{l\min} = \frac{mc}{2\gamma}\frac{x}{1-x}$:

$$\frac{dI}{\hbar\, d\omega} = 4Z^2\alpha r_0^2\left(\frac{4}{3} - \frac{4}{3}x + x^2\right) \times \left[\ln\frac{1}{\sqrt{\left(\frac{q_{l\min}}{mc}\right)^2 + \left(\frac{Z^{1/3}}{137}\right)^2}} - \frac{1}{2}\right]. \tag{4.1.32}$$

The spectra of BS intensity in lead (Z = 82) for electrons with $\varepsilon_1 = 20$ MeV, calculated according to (4.1.17) and (4.1.32), are shown on Fig. 4.6. As follows from the figure, for photons with energy $\hbar\omega < 0.5\varepsilon_1$ a difference does not exceed 10%, whereas with increase of $\hbar\omega$ it grows.

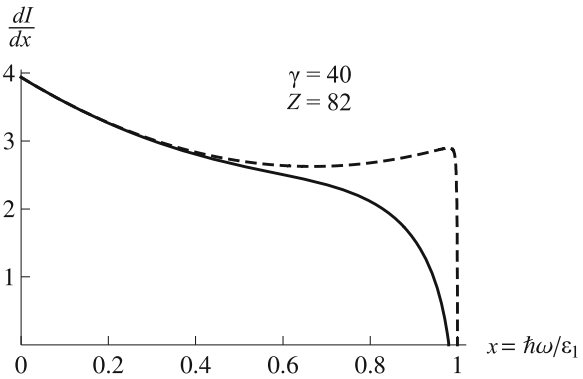

Fig. 4.6 Spectrum of BS intensity with taking into account of effect of recoil (the *bottom curve*) and without one (the *top*) for $\varepsilon_1 = 20$ MeV and $Z = 82$

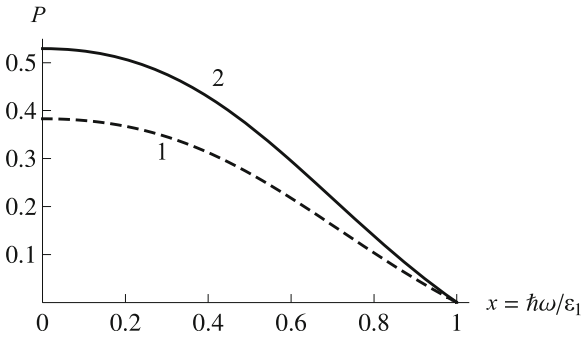

Fig. 4.7 The linear polarization of BS photons for electrons at the angle of radiation $u_0 = \gamma\theta = 1$. The *curve* 1 corresponds to calculation using the formula (4.1.33) for lead; the *curve* 2—for beryllium

From (4.1.15) it is possible to find the angle of photon emission, for which the polarization is maximal. Making a derivative equal to zero, $\partial P/\partial u^2 = 0$ we shall find the equation for required u_0^2.

Having done all calculations (neglecting a dependence from u^2 in argument of the logarithm, which is included in Γ), we shall conclude that for any photon energies $0 \leq x < 1$ the maximal value of polarization corresponds to the angle $u_0 = 1$:

$$P_{\max} = \frac{2(1-x)\Gamma(1)}{(2\Gamma(1)+3)\left[1+(1-x)^2\right] - 2(1-x)(1+\Gamma(1))}. \tag{4.1.33}$$

From the expression (4.1.33) it follows that at increase of photon energy a value $P_{\max}$ decreases and goes to zero for the maximal photon ($x \to 1$). In the opposite case for low-energy photons ($x \ll 1$) the most achievable value of polarization is

$$P_{\max}(x \to 0) = \Gamma(1)/(\Gamma(1)+2). \tag{4.1.34}$$

It is obvious that for producing of polarized γ-quanta by this method the usage of targets with small Z is more preferable, since a polarization degree in this case is higher. So, for beryllium $\Gamma(1) = 2.49$ i.e. $P_{\max} = 0.60$, whereas for lead $\Gamma(1) = 1.94$ and, hence consequently, $P_{\max} = 0.49$ (see Fig. 4.7).

4.2 The Bases of the Theory of Coherent Bremsstrahlung

The process of BS from ultrarelativistic electrons is drastically changed if instead an amorphous target there is used a crystalline one [7, 9]. This process is named as coherent bremsstrahlung (CBS) (see, for instance [10]).

The expressions for calculation of intensity and polarization obtained in the first Born approximation and being true for a thin crystal (for which it is possible to neglect the multiple scattering) are presented in a couple of the works (see for example, [10–12]).

In the same approximation these formulae can be obtained from expression (4.1.2), in which the vector **J** (see Eq. 4.1.1) is defined through Fourier-transform of the crystal lattice potential V_{cry} as follows:

$$\mathbf{J} = \frac{4\pi e}{\omega} V_{cry}(q)\mathbf{I}. \tag{4.2.1}$$

If we consider a homogeneous lattice, consisting of nuclei with screened Coulomb potential, then

$$V_{\text{cry}}(\mathbf{q}) = \sum_{v} \frac{Ze}{q^2 + (\hbar/\rho_0)^2} \exp(i\mathbf{q}_v \mathbf{L}_v). \tag{4.2.2}$$

In Eq. (4.2.2) $\mathbf{L}_v$ is the radius-vector of the lattice node; summation is carried out over all nuclei of a lattice. After substitution Eq. (4.2.1) into Eq. (4.1.2) we have (see, for instance, [13]):

$$\begin{aligned}
d\sigma_{\text{cry}} &= \frac{e^2}{(2\pi)^4}\frac{1}{\hbar\omega}\left\{F_{0\text{cry}} + \xi_i F_{i\,\text{cry}}\right\}(\hbar\omega)^2 d\hbar\omega\, d\Omega_1\, d\mathbf{q}_t;\\
F_{0\,\text{cry}} &= \frac{16\pi^2 e^2}{(\hbar\omega)^2}\left|V_{\text{cry}}(\mathbf{q})\right|^2\left\{2(\hbar\omega)^2\mathbf{I}^2 + 4\varepsilon_1\varepsilon_2\mathbf{I}_t^2\right\};\\
F_{1\,\text{cry}} &= \frac{16\pi^2 e^2}{(\hbar\omega)^2}\left|V_{\text{cry}}(\mathbf{q})\right|^2 8\varepsilon_1\varepsilon_2 I_1 I_2;\\
F_{2\,\text{cry}} &= 0;\\
F_{3\,\text{cry}} &= \frac{16\pi^2 e^2}{\omega^2}\left|V_{\text{cry}}(\mathbf{q})\right|^2\left\{4\varepsilon_1\varepsilon_2\left(I_1^2 - I_2^2\right)\right\},
\end{aligned} \tag{4.2.3}$$

where the vector **I** remains the same, as for ordinary bremsstrahlung on a single nucleus (see the formula (4.1.1). The obtained cross-section is proportional to a square of the lattice potential of Fourier-transform module. Carrying out a standard procedure of averaging over the lattice temperature (see, for example, [7]), we shall get:

$$\overline{\left|V_{\text{cry}}(\mathbf{q})\right|^2} = \left\{D(\mathbf{g}_\alpha)\exp\left(-\bar{r}^2 q^2\right)\delta(\mathbf{q} - \mathbf{g}_\alpha) + N\left[1 - \exp\left(-\bar{r}^2 q^2\right)\right]\right\}V^2(q). \tag{4.2.4}$$

Here $\mathbf{g}_\alpha$ is a radius-vector of a reciprocal crystal lattice; $D(\mathbf{g}_\alpha)$ is the diffraction factor, which takes into account the 3D periodicity of atoms in an elementary cell, type of a cell etc.; $\exp(-\bar{r}^2 q^2)$ is a Debye–Waller factor); $\bar{r}^2$ is the root-mean-square amplitude of temperature vibrations of lattice atoms; N is a number of atoms of monocrystal.

For complex lattice (in which the number of atoms in an elementary cell n is more than 1) we use the expression:

$$D(\mathbf{g}_\alpha) = \frac{N}{n}\frac{(2\pi)^3}{a^3}|S(\mathbf{g}_\alpha)|^2. \tag{4.2.5}$$

Here a^3 is a volume of an elementary cell; $S(\mathbf{g}_\alpha)$ is the structure factor. For simplicity of the description further everywhere it is meant, that a lattice is a cubic one.

For a diamond-type lattice

$$S(\mathbf{g}_\alpha) = \left[1 + \exp\left(i\frac{\pi}{2}(h_1 + h_2 + h_3)\right)\right] \times [1 + \exp(i\pi(h_1 + h_2)) + \exp(i\pi(h_2 + h_3)) + \exp(i\pi(h_3 + h_1))],$$

where $h_i (i = 1, 2, 3)$ are the Miller indices of the reciprocal lattice vector $(\mathbf{g}_a = \{h_1, h_2, \hbar_3\})$.. Hence it follows that

$$S(\mathbf{g}_\alpha) = \begin{cases} 64 - \text{for even } h_i, \text{ and } (h_1 + h_2 + h_3)/4 - \text{integer}; \\ 32 - \text{for odd } h_i; \\ 0 - \text{for remaining cases.} \end{cases}$$

It is possible to show that for the tungsten crystal

$$S(\mathbf{g}_\alpha) = \begin{cases} 16 - \text{for even } h_i; \\ 0 - \text{for remaining cases.} \end{cases}$$

Proceeding from (4.2.3), (4.2.4), let's write the CBS cross-sections in Born approximation on a lattice potential:

$$\begin{aligned} d\sigma_{\text{cry}} &= \{D(\mathbf{g}_\alpha)\exp(-\bar{r}^2q^2)\delta(\mathbf{q} - \mathbf{g}_\alpha) + N[1 - \exp(-r^2q^2)]\}d\sigma \\ &= d\sigma_{\text{coh}} + d\sigma_{\text{inc}}. \end{aligned} \tag{4.2.6}$$

Here $d\sigma_{\text{coh}}$ and $d\sigma_{\text{inc}}$ are the parts of cross-section, first of which (coherent) depends on orientation of a crystal, but the second (incoherent) does not depend on it.

Since the cross-section for the lattice potential (4.2.6) is proportional to N—the number of atoms of a lattice, further we shall use the cross-section $d\sigma_{\text{cry}} = d\sigma_{\text{coh}} + d\sigma_{\text{inc}}$, per single atom:

$$\begin{aligned} d\sigma_{\text{coh}} &= \frac{1}{n}\left(\frac{2\pi}{a}\right)^3 |S(\mathbf{g}_\alpha)|^2 \exp(-\bar{r}^2q^2)\delta(\mathbf{q} - \mathbf{g}_\alpha)d\sigma; \\ d\sigma_{\text{inc}} &= [1 - \exp(-\bar{r}^2q^2)]d\sigma. \end{aligned} \tag{4.2.7}$$

The cross-section on an isolated nucleus $d\sigma$ enters into both parts of cross-section (coherent and incoherent) (see the formula (4.1.2)). Polarization characteristics of CBS are defined as follows [13]:

$$\begin{aligned} \xi_{i\,\text{cry}} &= \frac{F_{i\,\text{cry}}}{F_{0\,\text{cry}}} = \frac{F_{i\,\text{coh}} + F_{i\,\text{inc}}}{F_{0\text{coh}} + F_{0\,\text{inc}}}; \\ F_{0,i\,\text{coh}} &= \frac{1}{n}\left(\frac{2\pi}{a}\right)^3 |S(\mathbf{g}_\alpha)|^2 \exp(-\bar{r}^2q^2)\delta(\mathbf{q} - \mathbf{g}_\alpha)F_{0,i}; \\ F_{0,i\,\text{inc}} &= [1 - \exp(-\bar{r}^2q^2)]F_{0,i}. \end{aligned} \tag{4.2.8}$$

Here for $F_{0,i}$ the expressions are the same, as for an ordinary BS (see 4.1.2).

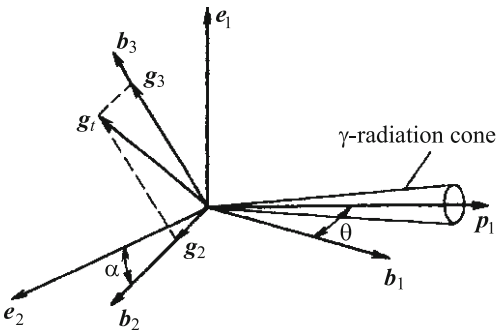

Fig. 4.8 The coordinate system for calculation of CBS characteristics

For convenience we shall carry out integration over the transverse recoil momentum of expressions (4.2.3) separately for coherent and incoherent parts of cross-section using the coordinate system shown in Fig. 4.8.

As it follows from (4.2.6), (4.2.8), the dominant contribution to a coherent part of cross-section gives the region of the recoil momenta $q^2 < \bar{r}^{-2}$. The root-mean-square amplitude of thermal vibrations is defined by parameters of a crystal (Debye temperature Θ and mass of atom M) and temperature of crystal T:

$$\bar{r}^2 = \frac{3}{4Mk\Theta}\left[1 + 4\left(\frac{T}{\Theta}\right)^2 \int_0^{\Theta/T} \frac{t}{e^t - 1} dt\right],$$

where k is Boltzmann's constant. At the temperature 20°C $\bar{r}^2$ has the following value for different crystals (in electron Compton lengths squared): diamond—101; silicon—290; tungsten—110. Hence, the coherent effect is significant in range $q_t \ll 1$, therefore for calculation of a coherent part of cross-section we'll keep terms not more than q_t^2. In this approximation

$$\mathbf{I} = \frac{q_t}{1+u^2} - \frac{2\mathbf{u}q_t(\mathbf{u}-\mathbf{n})}{(1+u^2)^2}; \quad \mathbf{I}^2 = \frac{q_t^2}{(1+u^2)^2}. \tag{4.2.9}$$

As basis vectors it is convenient to choose the followings:

$$\mathbf{e}_1 = \frac{[\mathbf{b}_1, \mathbf{k}]}{|[\mathbf{b}_1\mathbf{k}]|}; \quad \mathbf{e}_2 = \frac{[\mathbf{k}\mathbf{e}_1]}{\omega}. \tag{4.2.10}$$

Here b_1 is a crystallographic axis, at small angle to which there is propagated an electron (see Fig. 4.8). Then we have

$$\begin{aligned} I_1 &= \mathbf{I}\mathbf{e}_1 = -\frac{q_t \sin\psi_2}{1+u^2} + \frac{2uq_t u \sin\psi_1}{(1+u^2)^2}; \\ I_2 &= \mathbf{I}\mathbf{e}_2 = \frac{q_t \cos\psi_2}{1+u^2} - \frac{2uq_t u \cos\psi_1}{(1+u^2)^2}. \end{aligned} \tag{4.2.11}$$

In (4.2.11), as before, ψ_1 is an azimuthal angle of an outgoing photon; ψ_2 is an azimuthal angle of a recoil momentum. After substitution (4.2.11) in (4.2.3) we get

$$d\sigma_{\text{coh}} = \frac{1}{n}\left(\frac{2\pi}{a}\right)^3 \mathbf{g}|S(\mathbf{g}_\alpha)|^2 \exp\left(-\bar{r}^2 q^2\right)\delta(\mathbf{q}-\mathbf{g}_\alpha) \times \frac{2Z^2e^6}{\pi^2\left(q^2+1/\rho_0^2\right)^2}\{G_{0\,\text{coh}} + \xi_i G_{i\,\text{coh}}\}\frac{d\hbar\omega}{\hbar\omega}d\mathbf{\Omega}_1\, dq_t,$$

where

$$\begin{aligned}
G_{0\,\text{coh}} &= \left(\varepsilon_1^2+\varepsilon_2^2\right)\frac{q_t^2}{\left(1+u^2\right)^2} - 8\varepsilon_1\varepsilon_2\frac{u^2q_t^2\cos^2(\psi_1-\psi_2)}{\left(1+u^2\right)^4};\\
G_{1\,\text{coh}} &= 2\varepsilon_1\varepsilon_2\frac{q_t^2}{\left(1+u^2\right)^4}\left[-u^4\sin(2(2\psi_1-\psi_2)) + 2u^2\sin(2\psi_1) - \sin(2\psi_2)\right];\\
G_{2\,\text{coh}} &= 0;\\
G_{3\,\text{coh}} &= 2\varepsilon_1\varepsilon_2\frac{q_t^2}{\left(1+u^2\right)^4}\left[-u^4\cos(2(2\psi_1-\psi_2)) + 2u^2\sin(2\psi_1) - \cos(2\psi_2)\right].
\end{aligned} \tag{4.2.12}$$

One-dimensional δ-function $\delta(q_l - \mathrm{g}_{\alpha l})$ remains instead of three-dimensional one after integration over transverse recoil momentum. For its elimination we'll take the kinematic correlation between the photon angle u and the longitudinal recoil component q_l:

$$q_l = p_{1l} - p_{2l} - \omega = \frac{1}{2}\left(\frac{1+v^2}{\varepsilon_2} - \frac{1+u^2}{\varepsilon_1}\right).$$

This expression was deduced in ultra-relativistic approximation ($\varepsilon_i \gg 1, \theta_i \ll 1$) with taking into account the law of energy conservation. Having expressed v^2 through u, q_t, we'll deduce:

$$q_l = \frac{\omega(1+u^2)}{2\varepsilon_1\varepsilon_2} - \frac{2\mathbf{u}\mathbf{q}_t - q_t^2}{2\varepsilon_2} \approx \delta\left(1+u^2\right). \tag{4.2.13}$$

It is possible to neglect terms, which are proportional to q_t, (all the more q_t^2), since it was noted before $q_t \ll 1$.

Thus, $d\mathbf{\Omega}_1 = \frac{1}{2\varepsilon_1^2}du^2d\psi_1 = \frac{1}{2\delta\varepsilon_1\varepsilon_2}dq_l d\psi_1$.

The region of integration in momentum space is defined in a longitudinal direction by collimation angle of radiation $u_\text{c} = \varepsilon_1\theta_{1\text{c}}$ (see the formula (4.2.13)), and in transverse one—by Debye–Waller factor (range $q_t^2 > 4\hbar^2/\bar{r}^2$ in dimension units gives the contribution to the cross-section, not exceeding several percents):

$$\delta \le q_l \le \delta\left(1+u_\text{c}^2\right); \quad 0 \le q_t \le 2/\sqrt{\bar{r}^2}. \tag{4.2.14}$$

In momentum space the conditions (4.2.14) describe a disc, which radius is much larger, than its thickness, and which is located perpendicularly to a momentum of the initial electron (since photons are emitted in a cone with an opening angle $\theta_c \ll 1$, which axis coincides with an electron momentum)—so-called Uberall's "pancake" [9].

The cross-section (4.2.12) is obtained in coordinate system connected to the photon momentum. For calculations it is more convenient to pass in the system connected to initial electron momentum. Because of that these two systems are rotated relative to each other trough an angle $\theta_1 \sim \gamma^{-1} \ll 1$, the expression (4.2.12) in new system remains unchanged within accuracy up to terms γ^{-2}. Herewith the variables q_l, q_t will designate the longitudinal and transverse projections of recoil momentum relative to a direction of the initial electron.

Proceeding from (4.2.12) (taking into account the relationship 4.2.13), we obtain the following expression for the coherent contribution to intensity of radiation:

$$\begin{aligned}\frac{dI_{\mathrm{coh}}}{d\hbar\omega} &= \hbar\omega\frac{d\sigma_{\mathrm{coh}}}{d\hbar\omega} = \frac{2Z^2e^6}{\pi^2}\frac{1}{n}\left(\frac{2\pi}{a}\right)^3 \\ &\times \frac{1}{2\delta\varepsilon_1^2}\int d\psi_1\, d\mathbf{q}_t\, dq_l |S(\mathrm{g}_\alpha)|^2 \times \delta(\mathbf{q}-\mathrm{g}_\alpha)\frac{\exp(-\bar{r}^2q^2)}{\left(q^2+1/\rho_0^2\right)^2} \\ &\times \left[\left(\varepsilon_1^2+\varepsilon_2^2\right)\frac{q_t^2\delta^2}{q_l^2} - 8 - \varepsilon_1\varepsilon_2\frac{(q_l-\delta)\delta^3q_t^2\cos^2(\psi_1-\psi_2)}{q_l^4}\right] \\ &= \frac{2Z^2e^6}{\pi}\frac{1}{n}\left(\frac{2\pi}{a}\right)^3\sum_{g_\alpha}|S(g_\alpha)|^2\frac{\exp\left(-\bar{r}^2g_\alpha^2\right)}{\left(g_\alpha^2+1/\rho_0^2\right)^2}\frac{\delta g_{\alpha l}^2}{g_{\alpha l}^2} \\ &\times \left[1+(1-x)^2 - 4(1-x)\frac{\delta(\mathrm{g}_{\alpha l}-\delta)}{g_{\alpha l}^2}\right]. \end{aligned} \tag{4.2.15}$$

For obtaining of the formula (4.2.15), the integration over an azimuthal angle of outgoing photon ψ_1 is carried out. The integration over 3-dimensional recoil momentum is removed by δ-function and replaced with summation over the reciprocal lattice vectors getting into Uberall's pancake:

$$\delta \le \mathrm{g}_{\alpha l} \le \delta\left(1+u_c^2\right); \quad 0 \le \mathrm{g}_{\alpha t} \le 2/\sqrt{\bar{r}^2}. \tag{4.2.16}$$

The dependence of the coherent part of cross-section on orientation of a single-crystal target «is incorporated» just in the last two inequalities. Really, the Uberall pancake, as it was already mentioned above, is perpendicular to the electron momentum, and in case of crystal target rotation relative to electron beam the different reciprocal lattice vectors enter into pancake and leave one, resulting, finally, in the orientation dependence of the radiation yield. Direction of electron beam $\mathbf{p}_1$ relative to a crystallographic axis is possible to set by two angles, for example polar angle θ between the electron momentum and crystallographic

axis $\mathbf{b_1}$ and azimuthal angle α between a plane $(\mathbf{p}_1\mathbf{b}_1)$ and crystallographic plane $(\mathbf{b}_1\mathbf{b}_2)$ (see Fig. 4.8). In this case the longitudinal and transverse components of reciprocal lattice vector g_α (which is characterized by three projections $\mathrm{g}_{\alpha 1} = \frac{2\pi}{a}h, \mathrm{g}_{\alpha 2} = \frac{2\pi}{a}k, \mathrm{g}_{\alpha 3} = \frac{2\pi}{a}l$; h, k, l are the integers) are defined as follows:

$$\begin{aligned} \mathrm{g}_{\alpha l} &= \frac{2\pi}{a}(h\cos\theta + k\sin\theta\cos\alpha + l\sin\theta\sin\alpha), \\ \mathrm{g}_{\alpha t} &= \sqrt{\mathrm{g}_\alpha^2 - \mathrm{g}_{\alpha l}^2}. \end{aligned} \tag{4.2.17}$$

The incoherent contribution to intensity is calculated by integration of cross-section $d\sigma_{\mathrm{inc}}$ (4.2.7) over transverse recoil and over the photon outgoing angles. The first integration of the first summand ($d\sigma$) is carried out already (see the formula (4.1.12)). We'll carry out the similar integration for the second term:

$$\begin{aligned} \exp\left(-\bar{r}^2q^2\right)d\sigma = {} & \frac{2Z^2e^6}{\pi}\frac{d\omega}{\omega}\sin\theta\,d\theta\frac{d\psi_1}{2\pi}q_t\,dq_t\,d\psi_2 \\ & \times\frac{\exp(-\bar{r}^2q^2)}{\left(q^2+1/\rho_0^2\right)^2}\left[2\left(\varepsilon_1^2+\varepsilon_2^2\right)\mathbf{I}^2 - 4\varepsilon_1\varepsilon_2 I_3^2\right]. \end{aligned} \tag{4.2.18}$$

The integration over azimuth is carried out in the same way as earlier. As it was mentioned above, the exponential multiplier

$$\exp\left(-\bar{r}^2q^2\right) = \exp\left(-\bar{r}^2q_t^2\right)\left(\exp\left(-\bar{r}^2q_l^2\right)\right) \approx \exp\left(-\bar{r}^2q_t^2\right)$$

differs from zero in region $q_t^2 \le 4/\bar{r}^2 \ll 1$, in which the result of azimuthal integration can be written in the following form (see (4.1.5), (4.1.6), (4.1.9)):

$$\begin{aligned} \int I^2 d\psi_2 &= 3x(q_t) + y(q_t)\frac{(1+u^2)^2}{4} \approx 2\pi\frac{q_t^2}{(1+u^2)^2}; \\ \int I_3^2 d\psi_2 &= x(q_t) + y(q_t)\frac{(1-u^2)^2}{4} \approx 4\pi\frac{u^2q_t^2}{(1+u^2)^4}. \end{aligned}$$

Thus, after integration of the right part of expression (4.2.18) over transverse recoil momentum we have

$$4Z^2e^6\frac{d\omega}{\omega}\frac{u\,du}{(1+u^2)^2}\frac{d\psi_1}{2\pi}\left[2\frac{\varepsilon_1^2+\varepsilon_2^2}{\varepsilon_1^2} - 8\frac{\varepsilon_2}{\varepsilon_1}\frac{u^2}{(1+u^2)^2}\right]R\left(\bar{r}^2\right),$$

where $R(\bar{r}^2) = \int_0^{4/\bar{r}^2}\frac{(1/2)dq_t^2q_t^2\exp(-\bar{r}^2q_t^2)}{(q_t^2+1/\rho_0^2)^2}$.

Summarizing the received result with expression (4.1.12), it is possible to get the formula for the incoherent contribution to intensity

$$\frac{dI_{\text{inc}}}{\hbar d\omega} = \hbar\omega \frac{d\sigma_{\text{inc}}}{\hbar d\omega} = 4Z^2 e^6 \frac{u\,du}{(1+u^2)^2} \frac{d\psi_1}{2\pi} \times \left\{ \frac{\varepsilon_1^2 + \varepsilon_2^2}{\varepsilon_1^2}(2\Gamma_{\text{inc}} + 3) - 2\frac{\varepsilon_2}{\varepsilon_1} - 8\frac{\varepsilon_2}{\varepsilon_1} \frac{u^2}{(1+u^2)^2} \Gamma_{\text{inc}} \right\}. \tag{4.2.19}$$

The last expression coincides with expression for intensity of an ordinary bremsstrahlung, when replacing $\Gamma(u) \to \Gamma_{\text{inc}}(u)$, where

$$\Gamma_{\text{inc}}(u) = \Gamma(u) - R(\bar{r}^2) = \ln(1+u^2)\rho_0 - 2 - R(\bar{r}^2). \tag{4.2.20}$$

From the proceeding (4.2.19) and (4.2.20), it is possible to calculate the incoherent contribution for any choice of screening function $[1 - F(q^2)]^2 \Big/ q^4$, since the value $\Gamma(u)$ is calculated by formulae (4.1.6) and (4.1.10), and for the function $R(\bar{r}^2)$ we have the expression

$$R(\bar{r}^2) = \int_0^{4/\bar{r}^2} \frac{1}{2} d\,q_t^2 \exp(-\bar{r}^2 q_t^2) q_t^2 \frac{[1 - F(q^2)]^2}{q^4}.$$

Herewith it is necessary to mean, that $q^2 = q_t^2 + \delta^2(1+u^2)^2$ and, generally speaking, $R(\bar{r}^2) = R(\bar{r}^2, u)$. In some cases the function R can be calculated analytically. Let's divide the integration region into two parts as before: $0 \le q_t^2 \le q_0^2$ and $q_0^2 \le q_t^2 < \infty$, and $1/\rho_0^2 \ll q_0^2 \ll 1/\bar{r}^2$.

The last double inequality is not always fulfilled, however, for crystals representing interest, for example, diamond and silicon, it is true. The screening radius ρ_0 for these crystals considerably exceeds the amplitude of thermal vibrations $\bar{r}$. In the first region we use the expansion of the exponent

$$R_{\text{I}} = \int_0^{q_0^2} \frac{(1/2) q_t^2 (1 - \bar{r}^2 q_t^2) dq_t^2}{(q_t^2 + 1/\rho_0^2)^2} \approx \frac{1}{2} \left(\ln(q_0^2 \rho_0^2) - 1 - \bar{r}^2 q_0^2 \right).$$

The integration through the second region can be spread up to ∞, since the integrand decreases exponentially:

$$R_{\text{II}} = \int_{q_0^2}^{\infty} \frac{(1/2) \exp(-\bar{r}^2 q_t^2) dq_t^2}{q_t^2} = -\frac{1}{2} \text{Ei}(-\bar{r}^2 q_0^2).$$

Here $\text{Ei}(x)$ is an integral exponential function. For the values of argument $x \ll 1$ it is possible to use the expansion $\text{Ei}(-x) = \ln x - x + 0.577\ldots$. The boundary between two regions q_0^2 is chosen in this way that in our case this expression is applicable $(\bar{r}^2 q_0^2 \ll 1)$. Thus, we have the following expression for required integral: $R = R_{\text{I}} + R_{\text{II}} = -(1/2)[\ln(\bar{r}^2/\rho_0^2) + 1.577]$. Subsequently, the quantity

$\Gamma_{\text{inc}} = \ln(1+u^2)\rho_0 - 2 - R = \frac{1}{2}\ln[\bar{r}^2(1+u)^2] - 1.212$ does not depend on screening radius, i.e. the incoherent contribution is defined only by root-mean-square radius of thermal fluctuations for crystals with small Z and Debye temperature.

During calculation of the coherent contribution (see 4.2.14), the integration over photon outgoing angles $0 \le u \le u_c$ was made, which is necessary to carry out for the incoherent contribution also:

$$\frac{dI_{\text{inc}}}{dx} = 4Z^2e^6\left\{\left[1+(1-x)^2\right]\frac{\ln\bar{r}^2+0.577}{2}\left(1-\frac{1}{1+u_c^2}\right)\right.$$
$$\left.-(1-x)\left(1-\frac{1}{1+u_c^2}\right)-\frac{1}{3}(1-x)\left(\ln\bar{r}^2-2.523\right)\cdot\left(1-\frac{1+3u_c^2}{\left(1+u_c^2\right)}\right)\right\}. \tag{4.2.21}$$

During calculation (4.2.21), as before, it is neglected by the dependence on u^2 in the logarithm argument. Thus, the intensity of BS in a crystal is defined by the sum of two expressions (4.2.15) and (4.2.21):

$$dI_{\text{cry}} = dI_{\text{inc}} + dI_{\text{coh}}. \tag{4.2.22}$$

Let's calculate Stokes parameters ξ_1, ξ_3, which correspond to the linear polarization, in case of axial collimation of γ-radiation. For this purpose it is necessary to integrate numerator in (4.2.8) over unobservable variables, since the denominator is already calculated, see (4.2.15), (4.2.21), (4.2.22). We'll note at once that after averaging on the photon azimuthal angle $\bar{F}_{\text{inc}} = 0$ as well as in a case of an amorphous target. After the procedure of averaging which is similar to applied one for calculation (4.2.14) we have

$$\bar{F}_{1\,\text{coh}} = \frac{2Z^2e^6}{\pi}\frac{1}{n}\left(\frac{2\pi}{a}\right)^3\sum_{\mathrm{g}_\alpha}|S(\mathrm{g}_\alpha)|^2$$
$$\times\frac{\exp\left(-\bar{r}^2\mathrm{g}_\alpha^2\right)}{\left(\mathrm{g}_\alpha^2+1/\rho_0^2\right)}\frac{\delta\mathrm{g}_{\alpha t}^2}{\mathrm{g}_{\alpha l}^2}\left[-2(1-x)\frac{\delta^2}{\mathrm{g}_{\alpha l}^2}\sin(2\psi_{2\alpha})\right]. \tag{4.2.23}$$

The expression for $\bar{F}_{3\,\text{coh}}$ turns out from (4.2.23), when replacing $\sin(2\psi_2) \to \cos(2\psi_2)$.

The azimuthal angle $\psi_{2\alpha}$ in (4.2.23) is counted from the plane $\mathbf{p}_1\mathbf{b}_2$. As a rule, the angle θ between axis $\mathbf{b}_1$ and the electron momentum $\mathbf{p}_1$ (see Fig. 4.2) is small enough $\theta \ll 1$, therefore in a good approximation

$$\psi_{2\alpha} = \text{arctg}\left(\mathrm{g}_{3\alpha}/\mathrm{g}_{2\alpha}\right);$$
$$\sin(2\psi_{2\alpha}) = \frac{2\mathrm{g}_{2\alpha}\mathrm{g}_{3\alpha}}{\mathrm{g}_{2\alpha}^2+\mathrm{g}_{3\alpha}^2};\quad \cos(2\psi_{2\alpha}) = \frac{\mathrm{g}_{2\alpha}^2-\mathrm{g}_{3\alpha}^2}{\mathrm{g}_{2\alpha}^2+\mathrm{g}_{3\alpha}^2}.$$

The expression (4.2.15) with taking into account (4.2.14) can be classified as follows:

(a) the whole set of the reciprocal lattice vectors in the Uberall's pancake arranges a plane;
(b) the set of the reciprocal lattice vectors in the Uberall's pancake arranges a form of row;
(c) there is only one single reciprocal lattice vector in a pancake;
(d) the reciprocal lattice vectors are absent in a pancake.

In cases (a) and (b), which are named "*effect of a plane and row*", the coherent contribution to the radiation intensity is defined by the sum of contributions from all vectors getting in the pancake, and achieves values, several times as much exceeding the incoherent part, however the polarization degree is not too high (because of averaging over a set of reciprocal lattice vectors with various azimuthal angles $\psi_{2\alpha}$).

The case (c), so-called "*point effect*", corresponds to orientation, when in the sum (4.2.14) the single reciprocal lattice vector gives the contribution. In this case the coherent part of the radiation intensity not so much differs from the incoherent part, but polarization is much higher, than in the previous case (since does not occur averaging over an angle $\psi_{2\alpha}$.

In a case (d) the coherent effect is absent and all characteristics of radiation are defined by the incoherent part.

From (4.2.23) it follows that in a case of "point effect" the plane of the maximal polarization is perpendicular to the plane, in which the recoil momentum and electron momentum p_1 are placed.

The orientations of a single crystal, which correspond to described effects, are illustrated in Fig. 4.9. Note that the case of a plane effect corresponds to orientation, when the beam of electrons goes along any crystallographic axes, and the

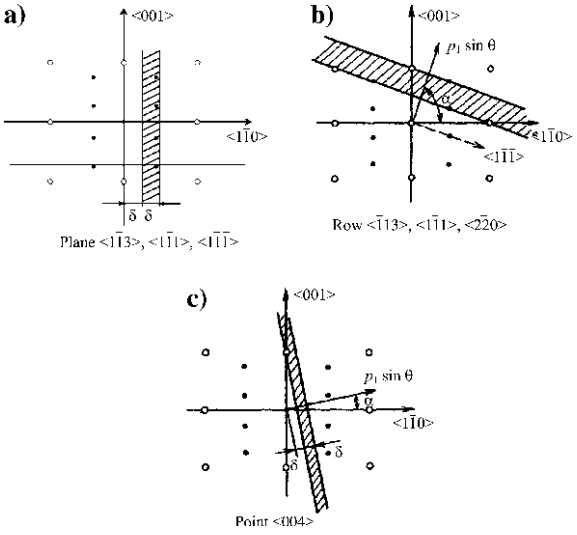

Fig. 4.9 The orientation of the Uberall's pancake relative to the reciprocal lattice in case of a plane effect (**a**), a row effect (**b**) and a point effect (**c**)

row effect corresponds to orientation, when the beam of electrons goes along the crystallographic plane. Really, the family of crystallographic reciprocal lattices $\langle 1\bar{1}\bar{1}\rangle$ getting in the pancake (Fig. 4.9b), corresponds to family of crystallographic planes, which are perpendicular to the reciprocal lattice vector $(1\bar{1}\bar{1})$. The same vector is perpendicular to the electron momentum. It means this orientation corresponds to the channeling in a plane $(1\bar{1}\bar{1})$.

The orientation corresponding to the point effects is achieved in case of increase of disorientation angle θ with regard to the crystallographic axes and in case the electron momentum lies outside the crystallographic plane.

The plane effect, otherwise named coherent radiation of B-type [14] will be considered in the next paragraph.

The CBS process can be described also in the coordinate space (see, for example, the book [15]). To show the connection between the described approach and the approach developed in [15], let's consider the elementary case of a point effect, when the coherent effect is caused by the lattice vector $\langle 010\rangle$ for angles of orientation $\theta \ll 1, \alpha \approx 0$. In this case from (4.2.17) we have

$$g_l \approx \frac{2\pi}{a}\sin\theta\cos\alpha \approx \frac{2\pi}{a}\theta.$$

For CBS in the straightforward direction ($u_c = 0$) from (4.2.14) it is possible to derive the expression for relative energy of CBS photons:

$$\frac{2\pi}{a}\theta = \frac{1}{2\gamma}\frac{x}{1-x},$$

from which directly follows

$$x = \frac{\hbar\omega}{\varepsilon_1} = \frac{4\pi\frac{\gamma\hat{\lambda}_e}{a}\theta}{1 + 4\pi\frac{\gamma\hat{\lambda}_e}{a}\theta}. \tag{4.2.24}$$

In the last expression the lattice parameter a is substituted in dimensional units. The second summand in a denominator (4.2.24) is caused by the recoil effect. With the increase of the electron Lorentz-factor the value x grows and, generally speaking, if the following condition is satisfied

$$\frac{\gamma\hat{\lambda}_e}{a}\theta \gg \frac{1}{4\pi} \tag{4.2.25}$$

it can achieve the values close to unity (i.e. $\hbar\omega \to \varepsilon_1$). For relatively small values of γ and θ, when the condition opposite to (4.2.25) $4\pi\frac{\gamma\hat{\lambda}_e}{a}\theta \ll 1$ is satisfied, then the relative energy of photon is calculated from the simple elementary formula

$$\hbar\omega = 4\pi\gamma^2 mc^2\frac{\hat{\lambda}_e}{a}\theta. \tag{4.2.26}$$

It is easy to deduce the expression for the photon wavelength from the last formula:

$$\lambda = \frac{1}{2\gamma^2}\frac{a}{\theta} \tag{4.2.27}$$

which can be rewritten as $\ell_f = d_{CBS}$.

Here $d_{CBS} = a/\theta$ designates the "perturbation" period of the electron trajectory by the crystalline lattice, and the value $2\gamma^2\lambda$ is none other than CBS formation length in straightforward direction.

Let's estimate the maximum available linear polarization P_{max} of CBS beam. We'll consider, first of all, the point effect (since in this case the polarization is higher) and, secondly, the case of "hard" collimation of radiation. As it is shown in [16], the hard collimation ($u_c < 1$) results in the effective suppression of the incoherent part of cross-section and, as a consequence, to increase of photon beam polarization. The influence of collimation on the coherent part comes to the monochromatization of maxima without their reduction. In case of collimation $u_c^2 \leq 1$ the incoherent part is much less than coherent one, therefore calculating P_{max}, the former one can be neglected. Since in the sums (4.2.15), (4.2.23) only one summand remains, it is easy to see that Stokes parameters are defined as follows: $\bar{\xi}_i = \bar{G}_{i\,coh}/\bar{G}_{0\,coh}$.

A line designates here the result of integration of expressions (4.2.12) over the azimuthal angle of photon:

$$\bar{G}_{0\,coh} = \frac{2\pi\delta^2 q_t^2}{q_l^2}\left[1 + (1-x)^2 - 4(1-x)\frac{\delta(q_l-\delta)}{q_l^2}\right];$$

$$\bar{G}_{1\,coh} = \frac{2\pi\delta^2 q_t^2}{q_l^2} 2(1-x)\frac{\delta^2}{q_l^2}\sin(2\psi_2);$$

$$\bar{G}_{3\,coh} = -\frac{2\pi\delta^2 q_t^2}{q_l^2} 2(1-x)\frac{\delta^2}{q_l^2}\cos(2\psi_2).$$

Hence we have

$$P = \sqrt{\bar{\xi}_1^2 + \bar{\xi}_3^2} = \frac{2(1-x)\delta^2/q_l^2}{1 + (1-x) - 4(1-x)\delta(q_l-\delta)/q_l^2}.$$

It is clear that the polarization achieves the maximal value at $q_l = \delta$:

$$P_{max} = \frac{2(1-x)}{1+(1-x)^2}. \tag{4.2.28}$$

The expression (4.2.28) gives the limiting value of polarization (for example, for $x = 0.3$ the linear polarization is equal to $P_{max} = 0.94$), whereas the effect of real conditions of experiment (the contribution of incoherent part, divergence of electron beam, influence of target thickness etc.) results in the essential reduction of a linear polarization degree.

4.3 Coherent Bremsstrahlung of B-type

For electrons moving along the crystallographic axis (i.e. for $\theta = 0$), the pancake in the space of reciprocal lattice is oriented perpendicularly to the crystallographic axes and, consequently, into one will get the whole set of reciprocal vectors, which satisfy to following condition

$$\frac{1}{2\gamma\hat{\lambda}_e}\frac{x}{1-x} = \frac{2\pi}{a}n, \quad n = 1, 2, 3\ldots \tag{4.3.1}$$

In other words, the whole plane of reciprocal vectors, i.e. a set of ones with any h, k (the plane effect) gets into the Uberall's pancake. The expression for energy of coherent maxima follows from (4.3.1)

$$x_n = \frac{\hbar\omega_n}{\varepsilon_1} = \frac{\frac{4\pi\gamma\hat{\lambda}_e}{a}n}{1+\frac{4\pi\gamma\hat{\lambda}_e}{a}n}. \tag{4.3.2}$$

For energy $\varepsilon_1 \sim$ 1000 MeV, as follows from (4.3.2), the first maximum for a diamond single crystal corresponds to the relative energy of photons $x \approx 0.97$ and it is positioned in an energy range near to the end of a spectrum, where the coherent effects are expressed very weakly.

However for electrons with energy $\varepsilon_1 \sim 100$ MeV the situation is sharply changed. The dependence of the first coherent maximum position in a spectrum is shown in Fig. 4.10 depending on electron energy for a single diamond crystal and silicon one [17].

The monochromaticity of a peak is defined by a collimation angle θ_c determining the lower bound of coherent maximum:

$$\frac{1}{2\gamma\hat{\lambda}_e}\frac{x_{\min}}{(1-x_{\min})}\left(1+\gamma^2\theta_c^2\right) = \frac{2\pi}{a}n, \tag{4.3.3}$$

For the energy of photons with $x < x_{\min}$ the pancake shifts towards the origin of coordinates in reciprocal lattice in such manner that a whole plane of reciprocal

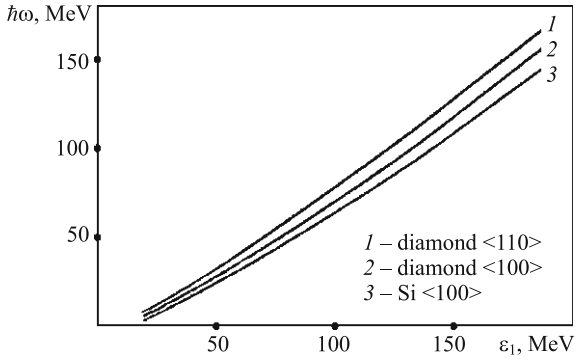

Fig. 4.10 Energy dependence of the first coherent peak in radiation spectrum on the electron energy for different crystals and different orientations

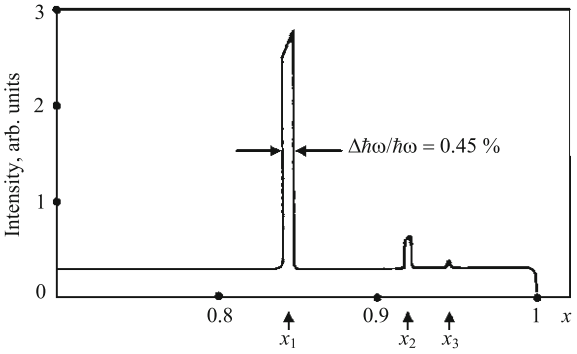

Fig. 4.11 The spectrum of CBS intensity of B-type for collimation $\theta_c = 0.6$ mrad. Arrows mark the positions of coherent peaks for $n = 1, 2, 3$

vectors escapes the pancake and the radiation spectrum will be determined by the incoherent part only.

The CBS spectrum of B-type is shown in Fig. 4.11, which is calculated for electrons with energy $\varepsilon_1 = 150$ MeV, moving in a thin diamond crystal along an axis $\langle 110 \rangle$, for the collimation angle $\theta_c = 0.6$ mrad ($\gamma\theta_c = 0.18$). From (4.4.1) and (4.4.2) it is possible to obtain an estimation of the spectrum monochromaticity of CBS beam (neglecting the multiple scattering):

$$\frac{\hbar\Delta\omega}{\hbar\omega_n} = \frac{\Delta x}{x_n} = (1 - x_n)\gamma^2\theta_c^2. \tag{4.3.4}$$

As follows from (4.3.4), the monochromaticity for collimation angles $\theta_c \ll \gamma^{-1}$ can achieve $\sim 1\%$.

The estimation using the formula (4.3.4) for $\gamma\theta_c = 0.18$ gives the value $\Delta\omega/\omega \approx 0.5\%$, what well agrees with the result of calculation by the exact formulae (see Fig. 4.11).

4.4 Coherent Bremsstrahlung Beams and its Applications

Due to such characteristics of CBS as polarization, quasimonochromaticity, tunability, etc., coherent bremsstrahlung beams are widely used at various facilities to produce photon beams for investigations in nuclear physics and high energy physics [18–20]. It is evidently the advantages of such beams are defined by the relation between $d\sigma_{coh}$ and $d\sigma_{inc}$. Very roughly this relation is determined by the ratio $\exp(-\bar{r}^2 g^2)/(1 - \exp(-\bar{r}^2 g^2))$ calculated for the minimal reciprocal vector **g** coming to the Uberall pancake (see Eq. (4.2.7)). Also the coherent effect is the highest for the shortest crystal lattice constant. From these criteria the diamond is the best crystalline radiator. The diamond possesses other important feature—a high thermal conductivity, much higher than ones for such crystals, as Si, Ge, W [21]. A high energy intense electron beam passing through a crystalline target results in significant energy deposition in a volume around the beam axis, which leads to the local temperature rise. This local heating can change crystalline

properties of a target or even destroy it. The main part of experiments with the coherent bremsstrahlung beams have been carried out using diamond targets. The main part of experiments with the coherent bremsstrahlung beams have been carried out using diamond targets.

Using crystals as targets is inevitably connected with the procedure of orientation of a crystal, which essence consists in the repeated carrying out the following operations:

(a) investigation of an orientation of crystallographic planes relative to the electron beam and their identification, i.e. reconstruction of a "map" of planes;
(b) maximum exact matching chosen crystallographic axis or plane with the direction of electron beam (for example, with accuracy not worse than 0.1 mrad for $\varepsilon_1 = 1$ GeV);
(c) crystal rotation in order to achieve the chosen orientation.

Since the orientation of crystal relative to the electron beam is defined by two angles (for example, θ and α), for an achievement of any given orientation it is enough to have the goniometric device with two axes of rotation. As a rule, there is used a goniometer with two perpendicular axes of rotation, one of which is perpendicular to an electron beam (see Fig. 4.12).

The relationship between angles of rotation around of horizontal and vertical axes (ψ_H and ψ_V) with angles of orientation is given by the following formulae:

$$\theta = \sqrt{\psi_\mathrm{H}^2 + \psi_\mathrm{V}^2}, \quad \alpha = \mathrm{arctg}(\psi_\mathrm{H}/\psi_\mathrm{V}) - \beta. \tag{4.4.1}$$

In (4.4.1) β is the angle between the vertical axis of rotation and crystallographic axis $\mathbf{b}_3$ (in case of coincidence of the electron momentum $\mathbf{p}_1$ with an axis $\mathbf{b}_1$). The obtained expression is valid for goniometric angles $\psi_\mathrm{H}, \psi_\mathrm{V}$, which is counted off from angles $\psi_\mathrm{H}^0, \psi_\mathrm{V}^0$ corresponding to the zero orientation of a crystal, when the crystallographic axis coincides with direction of electron beam.

It is possible to show that the longitudinal projection of the reciprocal vector is expressed through goniometric angles and Miller indices as follows (in case of orientation of the electron momentum close to the axis $\langle 100 \rangle$):

$$g_l = (2\pi/a)[h + k\psi_V \cos\beta + l\psi_H \sin\beta], \tag{4.4.2}$$

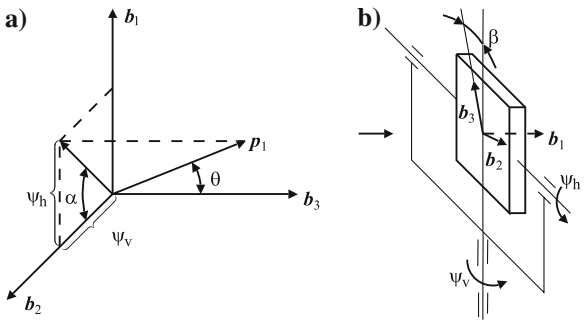

Fig. 4.12 The orientation of single crystal: Angles θ, α being determined in respect to crystallographic axes (**a**); angles $\psi_\mathrm{H}, \psi_\mathrm{V}$, being determined in respect to goniometric axes (**b**)

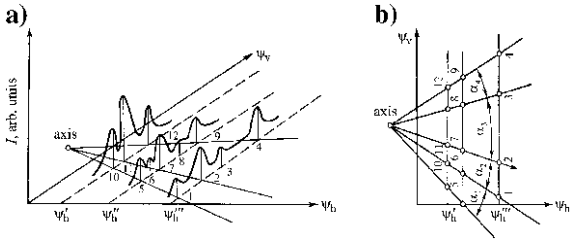

Fig. 4.13 Graphical interpretation of the procedure of identification of crystallographic axis: the dependence of the radiation intensity from a single crystals in respect to the rotation angles around the vertical (ψ_V) and horizontal (ψ_H) axes accordingly (**a**); definition of the crystallographic axis position by the positions of maxima of orientation dependences on a plane of angles ψ_V and ψ_H ("map") (**b**)

where h, k, l are the Miller's indices in the cubic basis. The expression (4.4.2) is convenient for using during calculations of different orientation dependences which are measured during rotation of a crystal in the goniometer.

If the crystal is oriented in such a manner that the electron momentum is directed, for example, close to the axes $\langle 111 \rangle$, the similar formula can be easily obtained, using the known trigonometric transformations in case of initial basis turn on the given angle.

The simplest technique of preliminary orientation was proposed in the work [22], were the orientation dependence (OD) of the current from a thin-walled ionization chamber was measured, which is sensitive to a low-energy part of radiation spectrum. The measured OD and the map of the crystalographic planes are given on Fig. 4.13, on which "the turn routes" of crystal relative to the electron beam direction are shown. Maxima in OD correspond to an orientation, when electrons move along crystallographic plane. In case of route closing to the axis, the intense maxima occur and finally merge in one global maximum corresponding to the zeroth orientation. These maxima (plane and axial) are caused by the low-energy radiation appearing in moving electrons in conditions of the plane or axial channeling. After finding of the zeroth orientation of crystal the obtaining of the chosen orientation does not represent particular difficulties.

The single-crystal target orientation is chosen depending on the requirements needed for operation with a photon beam (position of maximum, intensity, polarization degree, monochromaticity, ratio I_{coh}/I_{inc} etc.) during experiment.

All formulae given in the present chapter are obtained for the monodirected electron beam and thin single-crystal. The crystals used in experiment, as a rule, have thickness far higher than condition (4.1.25). Consequently, in calculations of CBS characteristics it is necessary to take into account the angular distribution of electron beam in process of its passage through a single crystal.

In the experiment [23] the linearly polarized CBS beam was used for measurements of an asymmetry of the deuteron photodisintegration. In order to perform similar measurements there was a necessity to change polarization plane

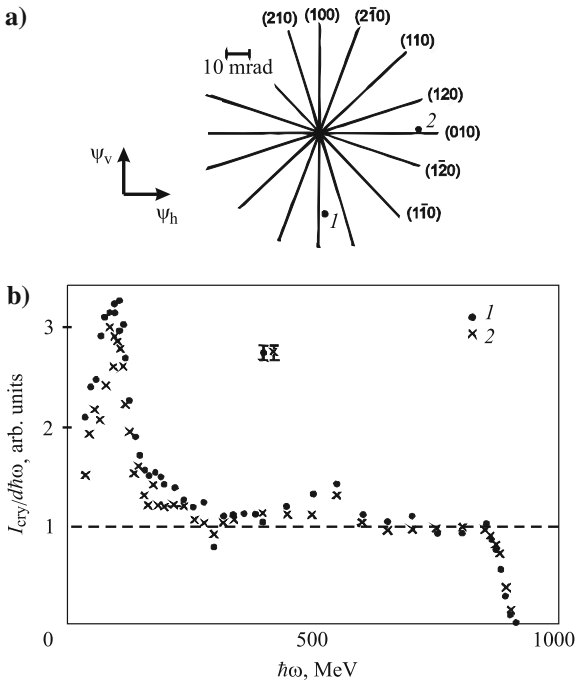

Fig. 4.14 Crystallographic planes chosen orientations (No. 1 and No. 2) (**a**); CBS spectra measured for two crystal orientations (No. 1—*dots*, No. 2—*crosses*) (**b**)

periodically during the experiment. In Fig. 4.14 it is shown the crystallographic "map" of the used diamond crystal [24], where No. 1 and No. 2 denote the crystal orientations, each of them provided the CBS beams obtaining with identical spectral characteristics but the inclination angle of the polarization plane was rotated for 90 ° without the polarization degree changing. In other words, passing from the orientation No. 1 to No. 2 the sign of Stokes parameter ξ_3 is changed to opposite $(\xi_3^{(1)} = -\xi_3^{(2)})$.

The orientation No. 1 was chosen in order to provide the "point effect" from the contribution of (0,4,0), reciprocal vector but for orientation No. 2—from the vector (4,0,0). The diamond target with thickness 0.5 mm and transverse sizes 6 × 10 mm has been cut in such a manner when axes $\langle 100\rangle$, $\langle 010\rangle$, $\langle 001\rangle$ were perpendicular to sample surfaces. The electron beam with energy $\varepsilon_1 = 900$ MeV passed through a target close to the axis $\langle 001\rangle$.

To obtain the polarized photons with energy $\hbar\omega = 100$ MeV for the asymmetry γd measurements [23] the orientations were following:

$$\text{No. 1: } \psi_V = 40\,\text{mrad}, \quad \psi_H = 1.5\,\text{mrad}$$
$$\text{No. 2: } \psi_V = 1.5\,\text{mrad}, \quad \psi_H = 40\,\text{mrad}$$

In Fig. 4.14b two CBS spectra for orientations No. 1 and No. 2 measured by a pair magnet spectrometer are shown. Within accuracy of the experiment both spectra were equal. The result of simulation with taking into account the effect of CBS beam collimation ($\theta_c = 0.6$ mrad) and multiple electron scattering is shown

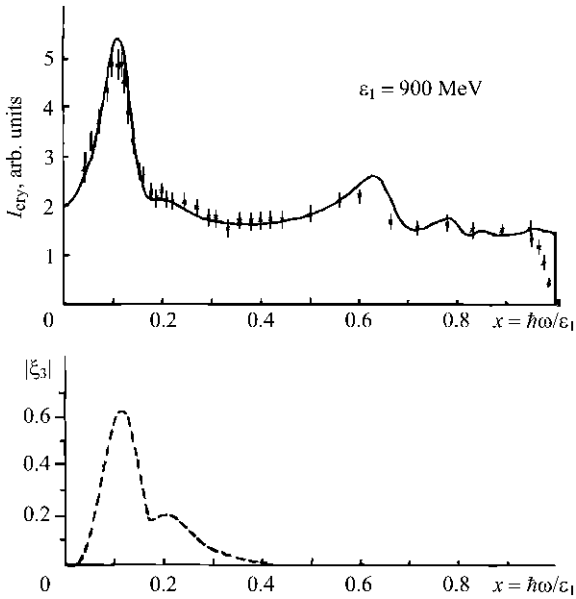

Fig. 4.15 Comparison of the measured spectrum (*dots*) and simulation results for $\psi_V = 40$ mrad; $\psi_H = 1.5$ mrad (*top*) and CBS simulations for the Stokes parameter ξ_3 (*bottom*)

in Fig. 4.15 (top) [25]. The bottom curve describes the dependence of Stokes parameter ξ_3 on a photon energy. The measured values of Stokes parameter ξ_3 confirmed the simulation results ($\xi_3^{(1)} = +0.70$; $\xi_3^{(2)} = -0.73$, see [24]).

As a rule, there are "thick" crystals used, for which the r.m.s. angle of multiple scattering is much more than characteristic angle γ^{-1}. But due to the hard collimation of the CBS beam a contribution from incoherent part can be diminished significantly and, as a result, the CBS beam gets a high polarization degree and acceptable monochromaticity (see, for instance, [26–28]).

To study the dependence of a cross-section of some photoprocess on a photon energy it is possible to utilize such the characteristic of a collimated CBS beam as a quasimonochromaticity. In case of hard collimation of CBS beam, besides the suppression of incoherent part, the monochromatization of CBS spectral maxima (on the full analogy of the undulator radiation) occurs. Changing an energy of the collimated CBS peak (rotating a crystalline target or changing an incident electron energy) and measuring the yield of a process it is possible to reconstruct a cross-section. In the experiment [29] this technique was used to investigate the process $\gamma p \to \pi^{\pm} X$.

Electrons with energy 20 GeV passed through the diamond target with thickness 80 μ in order to produce a quasimonochromatic photon peak in the energy range 8–14 GeV by a collimation $\theta_c = 0.011$ mrad. Note that during the experiment approximately $2 \cdot 10^{19}$ electrons passed through the diamond crystal without a significant radiation damage.

The same technique may be used in the nuclear physics for a photon energy $\hbar\omega \leq 100$ MeV. In this case it is possible to use a beam produced by the CBS-B mechanism.

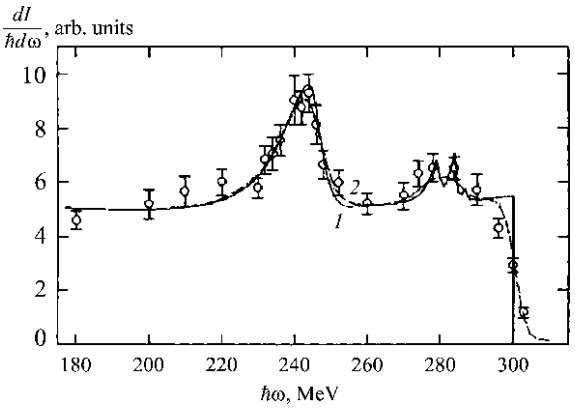

Fig. 4.16 Experimental CBS spectrum of B-type for $\varepsilon_1 = 300$ MeV

The results of measurement of CBS spectrum of B-type for the energy of electrons $\varepsilon_1 = 300$ MeV at passage through the diamond crystal with the thickness of 0.35 mm along $\langle 110 \rangle$ axis [30] are shown in Fig. 4.16.

The calculations of CBS spectrum of B-type with taking into account the electron multiple scattering in a diamond target are given here as well. It is possible to specify the good coincidence of experimental data with results of calculations, having in mind that the ratio "peak/background" in this experiment is appreciably lower, than theoretical ones for the ideal case (see Fig. 4.11). Such reduction of the coherent contribution in comparison with incoherent one is caused by the effect of multiple scattering in target, which thickness wittingly does not satisfy to the criterion of a "thin" target (see expression (4.1.25)). During multiple scattering the electrons of initial beam change the entering angle in respect to the initial direction (along the crystallographic axis) and leave CBS mode of B-type passing to the mode of ordinary CBS (i.e. the plane effect is replaced with the point effect). In this case the radiation spectrum will be defined only by the angle θ between electron momentum and crystallographic axis (one may expect the electron scattering has azimuthal symmetry, what results in averaging in respect to an angle α).

The evolution of CBS spectra in case of orientation angle θ changing in the interval $0 \leq \theta \leq 1.8$ mrad for diamond crystallographic axis $\langle 100 \rangle$ and energy of electrons 4.5 GeV [31] is shown in Fig. 4.17. As distinct from CBS spectra of B-type, the essential enrichment of spectrum in the soft part is observed in this case.

When an electron beam moves through a crystalline target nearly a crystallographic axis (the disorientation is less than the so-called channeling critical angle or Lindhard's angle ψ_L [32]), electrons can be captured in the mode of axial channeling and generate the intense radiation at channeling in the range of relative energies of photons $x \leq 0.1$. The estimation of the Lindhard's angle for $\langle 111 \rangle$ axis of tungsten and electron energy $\varepsilon_1 = 1$ GeV gives a value $\psi_L \sim 1$ mrad [3].

However, because of multiple scattering in the crystalline target only the small part of initial electrons moves in the channeling mode, whereas the main part of

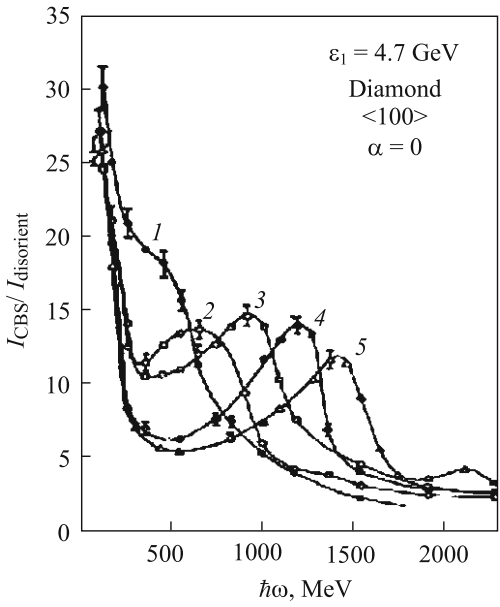

Fig. 4.17 The radiation spectra of electrons at various entering angles of electrons with $\varepsilon_1 = 4.7$ GeV in the diamond crystal. Orientation angles $\theta = 0.4$ mrad (1), $\theta = 0.6$ mrad (2), $\theta = 0.8$ mrad (3), $\theta = 1.2$ mrad (4), $\theta = 1.4$ mrad (5)

the electron beam moves at the angles $\theta \geq \psi_L$, that results in CBS generation in the soft part of spectrum.

This effect is used in a case of creation of the positron sources on the basis of oriented crystalline converters. The beam of high-energy electrons passing through the "thick" crystal gets the angular divergence, which determined, on the average, by the angle of multiple scattering (4.1.24). The divergent electron beam generates, mainly, the coherent bremsstrahlung (the except for a small part of the beam, which moves at the angle $\theta \leq \psi_L$ in respect to axis, remaining in a mode of axial channeling). CBS beam enriched with photons in the "soft" part of spectrum, generates the electron–positron pairs, positron component of which is separated and accelerated in the subsequent sections of the accelerator. As distinct from traditional positron sources, where the amorphous converters are used, in which the electron–positron pairs are formed by photons with ordinary bremsstrahlung spectrum, the crystalline converters can provide the increase of pairs yield. It is clear, both the total number of photons in CBS spectrum, and the number of photons in the "soft" part of CBS spectrum exceeds the similar characteristics in the Bethe–Heitler spectrum, therefore the positron yield from the oriented crystalline converter will exceed one from an amorphous converter of the same thickness. Increasing of the yield of "soft" CBS photons has been shown in the experiment [33] in case of interaction of electrons with the energy $\varepsilon_1 = 0.9$ GeV with the single crystal tungsten target with thickness 0.64 mm being oriented by axis $\langle 111 \rangle$ along the momentum of electrons (see Figs. 4.18, 4.19). These figures present the results of measurements of a photon yield with a fixed energy when an electron beam passes close to the plane $(00\bar{1})$ (Fig. 4.18) and the axis $\langle 111 \rangle$ (Fig. 4.19).

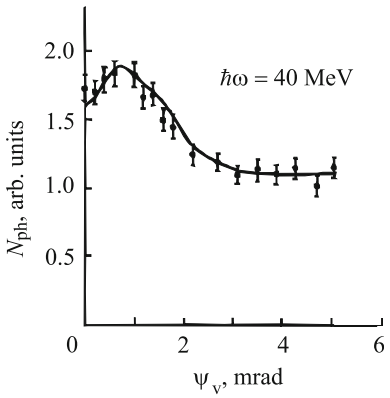

Fig. 4.18 Orientation dependence of the photon yield with energy $\hbar\omega = 40$ MeV for the electron beam with energy $\varepsilon_1 = 900$ MeV crossing the (110) plane (for $\psi_V = 0$) of the tungsten target with thickness 0.64 mm. Experiment—*dots*; CBS simulation—*solid curve*

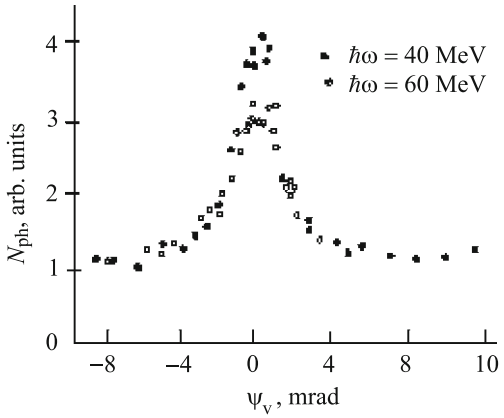

Fig. 4.19 Orientation dependence of the photon yield with energy $\hbar\omega = 40$ MeV and 60 MeV for the electron beam with energy $\varepsilon_1 = 900$ MeV crossing the (111) axis (for $\psi_V = 0$) for the same conditions

One of the first experiments, devoted to investigations of positron production via CBS mechanism was carried out using electron beam with energy $\varepsilon_1 = 1$ GeV [34]. The results of measurements of an efficiency of positron production with the momentum 20 MeV/c generated in tungsten crystals with orientation $\langle 111 \rangle$ and different thicknesses ($t_1 = 0.4$ mm and $t_2 = 1.2$ mm) are presented in Fig. 4.20.

As one may see the results of simulations where a contribution from CBS mechanism only was taken into account agree with experiment good. Parameters FWHM of the measured curves are defined, mainly, by the multiple scattering processes. In the approximation where this process is the same as for an amorphous target $\bar{\theta}^1_{ms} = 4.9$ mrad and $\bar{\theta}^2_{ms} = 8.8$ which are closed to quantities FWHM/2.

It is necessary to specify that for not too "thick" crystals ($t \leq L_0$) the agreement between the experiment and calculations is rather good. With the increase of crystal thickness for improvement of fit it is necessary to take into account the contribution of the cascade processes, in which the radiation spectrum is defined by a varied angle of movement of electrons in respect to the crystallographic axis.

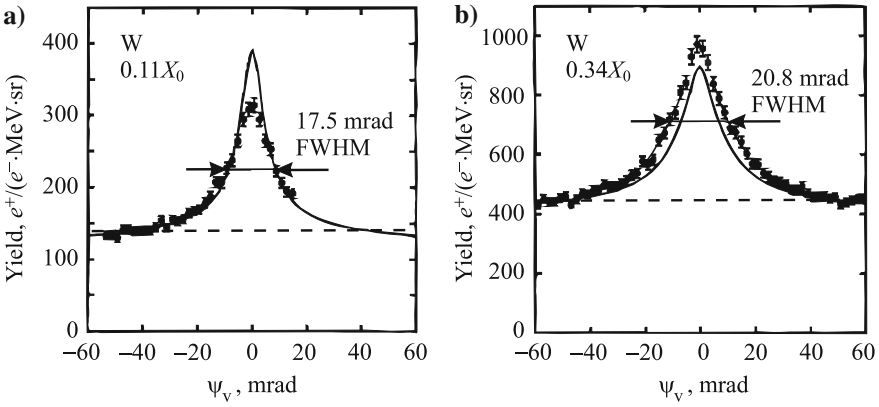

Fig. 4.20 Orientation dependence of the positron yield per initial electron per MeV per steradian generated at the outgoing positron angle $\theta = 0$. Experiment—*dots*; CBS simulation—*solid curves*

It can be pointed that the positron source realized according to described principle, was used at the linear accelerator-injector of the electron–positron collider KEKB [35], which has provided the increase of stored up positron current on 25 % in comparison with the traditional positron source.

References

1. Heitler, W.: Quantum Theory of Radiation. Oxford University Press, Oxford (1954)
2. Olsen, H., Maximon, L.C., Wergeland, H.: Theory of high-energy bremsstrahlung and pair production in s screened field. Phys. Rev. **106**, Z7 (1957)
3. Baier, V.N., Katkov, V.M., Strakhovenko, V.M.: Electromagnetic Processes at High Energies in Oriened Single Crystals. World Scientific, Singapore (1998)
4. Olsen, H., Maximon, L.C.: Photon and electron polarization in high-energy bremsstrahlung and pair production with screening. Phys. Rev. **114**, 887 (1959)
5. Landau, L.D., Lifshitz, E.M.: Quantum Mechanics. Nonrelativistic Theory. Pergamon Press, Oxford (1965)
6. Tsai, Y.S.: Pair production and bremsstrahlung of charged leptons. Rev. Mod. Phys. **46**, 815 (1974)
7. Ter-Mikaelyan, M.L.: High-Energy Electromagnetic Processes in Condensed Media. Wiley-Interscience, New York, NY (1972)
8. Anthony, P.L., Becker-Srendy, R., Bosted, P.E., et al.: Measurement of dielectric suppression of bremsstrahlung. Phys. Rev. Lett. **76**, 3350 (1996)
9. Uberall, H.: High-energy interference effect of bremsstrahlung and pair production in crystals. Phys. Rev. **103**, 1055 (1956)
10. Diambrini Palazzi, G.: High-energy bremsstrahlung and electron pair production in thin crystals. Rev. Mod. Phys. **40**, 611 (1968)
11. Coherent Radiation Sources: In: Saenz, A.W., Uberall, H. (eds.) Topics in Current Physics, vol. 38. Springer, NY (1985)
12. Rullhusen, P., Artru, X., Dhez, P.: Novel Radiation Sources using Relativistic Electrons. World Scientific, Singapore (1998)

13. Potylitsyn, A.P.: Polarized High-Energy Photon Beams. Energoatomizdat, Moscow (1987). (in Russian)
14. Uberall, H., Saenz, A.W.: Channeling radiation and coherent bremsstrahlung. Phys. Lett. A. **901**, 370 (1982)
15. Akhiezer, A.I., Shulga, N.F.: High Energy Electrodynamics in Matter. Gordon and Breach, Amsterdam (1996)
16. Tsuru, T., Kurokawa, S., Nishikawa, T., et al.: Production of monochromatic gamma rays by collimation of coherent bremsstrahlung. Phys. Rev. Lett. **27**, 609–612 (1971)
17. Potylitsyn, A.P.: Coherent type-B bremsstrahlung as a possible source of monochromatic gamma-rays. JETP Lett. **53**, 12–15 (1991)
18. Barbiellini, G., Bologna, G., Diambrini, G., Murtas, G.P.: Measurement of the polarization of the Frascati 1-GeV electron synchrotron γ-ray beam from a diamond crystal radiator. Phys. Rev. Lett. **9**, 396 (1962)
19. Zabaev, V.N., Kuznetsov, V.M., Potylitsyn, A.P., et al.: Production of pi + mesons by polarized photons in energy region 220–280 MeV. Sov. J. Nucl. Phys. USSR **21**, 286–288 (1975)
20. Bilokon, H.B., Bologua, G., Gelani, F., et al.: Coherent bremsstrahlung in crystals as a tool for producing high energy photon beams to be used in photoproduction experiments at CERN SPS. Nucl. Instrum. Methods **204**, 299–310 (1983)
21. Davis, J.W.: *ITER Material Properties Handbook*, AM01-211 (1997)
22. Kalinin, B.N., Konovalova, E.I., Pleshkov, G.A., et al.: Automatic orientation system for single-crystal targets in an electron accelerator. Instrum. Exp. Tech. **28**, 533–535 (1985)
23. Vnukov, I.E., Glavanakov, I.V., Kalinin, B.N., et al.: Asymmetry of the photodisintegration of the deuteron by linearly-polarized gamma-rays below the pion-production threshold for the angle 60 degrees. JETP Lett. **60**, 576–579 (1994)
24. Ananin, P.S., Vnukov, I.E., Zabaev, V.N., et al.: Measurement of polarization of coherent bremsstrahlung of 900 MeV electrons in diamond for photon-to-electron energy ration of less-than-or-equal-to 0.15. Instrum. Exp. Tech. **28**, 538–543 (1985)
25. Vnukov, I.E., Glavanakov, I.V., Krechetov, Y.F., et al.: Photodisintegration of the deuteron by linearly polarized photons below the pion-production threshold. Sov. J. Nucl. Phys. **47**, 581–585 (1988)
26. Timm, U.: Coherent bremsstrahlung of electrons in crystals. Fortschr. der Phys. **17**, 765–768 (1969)
27. Lohman, D., Peise, J., Arhens, J., et al.: Linearly polarized photons at MAMI (Mainz). Nucl. Instrum. Methods A **343**, 494–507 (1994)
28. Natter, F.A., Grabmayer, P., Helh, T., et al.: Monte-Carlo simulation and analytical calculation of coherent bremsstrahlung and its polarization. Nucl. Instrum. Methods B **211**, 465 (2003)
29. Kaune, W., Miller, G., Oliver, W., Williams, R.W., Yong, K.K.: Inclusive cross-sections for pion and photon production by photons using collimated coherent bremsstrahlung. Phys. Rev. D **11**(3), 478–494 (1975)
30. Balayan, A.S., Kalinin, B.N., Naumenko, G.A., et al.: Experimental research of channeling radiation and type-B coherent bremsstrahlung for 300 electrons. Phys. Lett. A **159**, 433–436 (1991)
31. Taroyan, S.P.: Investigation of Radiation from High Energy Electrons for Small Orientation Angles in a Diamond Monocrystal. Thesis, Yerevan Physical Institute (in Armenia) (1982)
32. Lindhard, J.: Mat.- Fys. Medd. Dan. Vid. Selsk. **34**(14) (1965)
33. Potylitsyn, A.P., Kalinin, B.N., Kurkov, A.A., et al.: Measurement of characteristics of the gamma-radiation of ultrarelativistic electrons in tungsten and silicon crystals cooled to temperature T = 90°K. Sov. J. Nucl. Phys. USSR **45**, 571–574 (1987)
34. Anami, S., Andreyashkin, M.Yu., Enomoto, A., et al.: Experimental study of positron production from crystal targets by 0.6–1.0 GeV electrons. Nucl. Instrum. Methods B **183**, 459–475 (2001)
35. Suwada, T., Satoh, M., Furukawa, K., et al.: First application of a tungsten single-crystal positron source at the KEK-B factory. Phys. Rev. ST-AB. **10**, 073501 (2007)

Chapter 5
Resonant Transition Radiation

5.1 The Basic Characteristics of Transition Radiation

Transition radiation (TR) arises in case, when a moving charge is crossing a boundary of two media. Ginzburg and Frank predicted this effect in the work [1], considering a problem within the framework of classical electrodynamics. Later, the theory of transition radiation was generalized and was investigated in details in many experimental works.

The detailed description of TR characteristics can be found in books and papers [2–6]. Following the approach of [3], let's consider the geometry shown in Fig. 5.1, when the charged particle with velocity $\mathbf{v} = \boldsymbol{\beta} c$ comes out from a medium with the permittivity ε in vacuum ($\varepsilon = 1$) through tilted boundary.

In coordinate system, in which the axis z is directed along a perpendicular to a boundary, and the axis y is located in a plane passing through this perpendicular and particle velocity, the components of radiation field $\mathbf{E} = \{E_x, E_y, E_z\}$ are written in the form [3]

$$\begin{aligned} E_x &= -\Pi_z n_x n_z - \Pi_y n_x n_y; \\ E_y &= -\Pi_z n_y n_z + \Pi_y \left(1 - n_y^2\right); \\ E_z &= \Pi_z \left(1 - n_z^2\right) - \Pi_y n_y n_z. \end{aligned} \tag{5.1.1}$$

There are the projections of a unit wavevector introduced in (5.1.1)

$$\mathbf{n} = \frac{\mathbf{k}}{\omega} = \left\{n_x, n_y, n_z\right\} = \left\{\cos\theta_x, \cos\theta_y, \cos\theta_z\right\} = \{\sin\theta\cos\varphi, \sin\theta\sin\varphi, \cos\theta\}$$

and vector $\boldsymbol{\beta} = \{0, \beta_y, \beta_z\} = \beta\{0, \sin\psi, \cos\psi\}$. Components of the Hertz vector Π_y, Π_z, which are used in (5.1.1), were found in the work [3]

A. P. Potylitsyn, *Electromagnetic Radiation of Electrons in Periodic Structures*, Springer Tracts in Modern Physics, 243, DOI: 10.1007/978-3-642-19248-7_5,

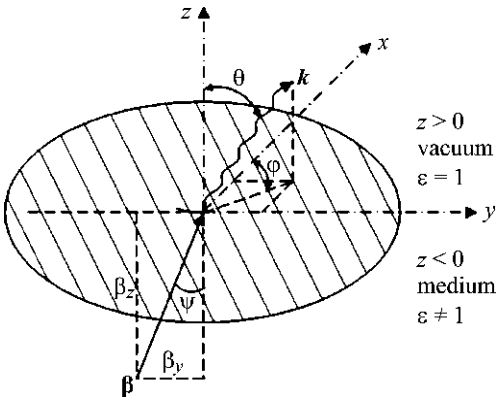

Fig. 5.1 The kinematic variables describing the "forward transition radiation"

$$\Pi_y = -\frac{e}{\pi c}\frac{\beta_z(1-\varepsilon)n_z}{\left(\varepsilon n_z + \sqrt{\varepsilon-\left(1-n_z^2\right)}\right)} \times \frac{\beta_y\beta_z\left[1-n_z^2+n_z\sqrt{\varepsilon-\left(1-n_z^2\right)}\right]}{\left[\left(1-\beta_y n_y\right)^2-\beta_z^2 n_z^2\right]\left(1-\beta_y n_y-\beta_z\sqrt{\varepsilon-\left(1-n_z^2\right)}\right)},$$
$$\Pi_z = \frac{e}{\pi c}\frac{\beta_z(1-\varepsilon)n_z}{\left(\varepsilon n_z + \sqrt{\varepsilon-\left(1-n_z^2\right)}\right)} \times \frac{\left(1-\beta_y n_y\right)\left(1-n_z\sqrt{\varepsilon-\left(1-n_z^2\right)}\right)-\beta_z^2-\beta_y\beta_z n_y n_z}{\left[\left(1-\beta_y n_y\right)^2-\beta_z^2 n_z^2\right]\left(1-\beta_y n_y-\beta_z\sqrt{\varepsilon-\left(1-n_z^2\right)}\right)}. \quad (5.1.2)$$

The factors $\exp(i\omega R/c)/R$ describing a spherical wave with frequency ω at the distance R from a source are omitted in expressions (5.1.2). Dependence of the TR characteristics on frequency is defined by behaviour of dielectric permittivity $\varepsilon(\omega)$.

Let's start with consideration of TR characteristics for the simplest case, when the charged particle passes from an ideal conductor into a vacuum (i.e. in case $|\varepsilon| \to \infty$). It should be noted that this approximation works well for metals in the range of frequencies from optical and lower ones.

In this case instead of (5.1.1) and (5.1.2) we have

$$E_x = C_1 n_x n_z; \quad E_y = C_1\left(n_y n_z - \beta_y n_z\right);$$
$$E_z = C_1\left(-1+n_z^2+\beta_y n_y\right);$$
$$C_1 = \frac{e}{\pi c}\frac{\beta_z}{\left(1-\beta_y n_y\right)^2-\beta_z^2 n_z^2} = \frac{e}{\pi c}\frac{\beta\cos\psi}{\left[1-\beta\left(n_y\sin\psi+n_z\cos\psi\right)\right]\left[1-\beta\left(n_y\sin\psi-n_z\cos\psi\right)\right]}. \quad (5.1.3)$$

From (5.1.3) it is easy to get the spectral-angular distribution of TR using the known relationships:

$$\frac{dW}{d\omega\, d\Omega} = cR^2\left(|E_x|^2+|E_y|^2+|E_z|^2\right) = \frac{e^2}{\pi^2 c}\frac{\beta_z^2\left[1-n_z^2-2\beta_y n_y+\beta_y^2\left(1-n_x^2\right)\right]}{\left[\left(1-\beta_y n_y\right)^2-\beta_z^2 n_z^2\right]^2}. \tag{5.1.4}$$

As it follows from (5.1.3) and (5.1.4), the TR intensity in this approximation ($|\varepsilon| \to \infty$) does not depend on frequency (the spectral density remains constant for any frequency).

Let's consider the radiation in a cone of angles near particle velocity direction. In a plane specified by equation $n_x = 0$, the direction cosines n_y, n_z are expressed through a polar angle θ: $n_y = \sin\theta$; $n_z = \cos\theta$. In this case the denominator in (5.1.4) can be rewritten in the following form:

$$[1-\beta(\sin\psi\sin\theta-\cos\psi\cos\theta)]^2\times[1-\beta(\sin\psi\sin\theta+\cos\psi\cos\theta)]^2 = [1+\beta\cos(\psi+\theta)]^2[1-\beta\cos(\psi-\theta)]^2. \tag{5.1.5}$$

It is clear, that in the range of angles $\theta \sim \psi$ the second factor in (5.1.5) achieves the minimal values, i.e. the spectral-angular distribution of TR (5.1.4) reaches the maximal values just for this range of TR photon outgoing angles (see Fig. 5.2):

As it follows from the figure, the minimal value of the TR yield coincides with a direction of charge velocity. The angular distributions of TR for various values of the Lorentz-factor (and accordingly β) in dependence of the direction cosines, which can change from -1 up to $+1$ are shown in the presented figure. An appreciable asymmetry in angular distribution (for example, for $\gamma = 10$, see Fig. 5.2a) is observed for relatively small values of the Lorentz-factor, what practically disappears for $\gamma \geq 100$ (see Fig. 5.2b). Further, as it is shown above, the range of angles near velocity vector direction, where the main part of TR intensity

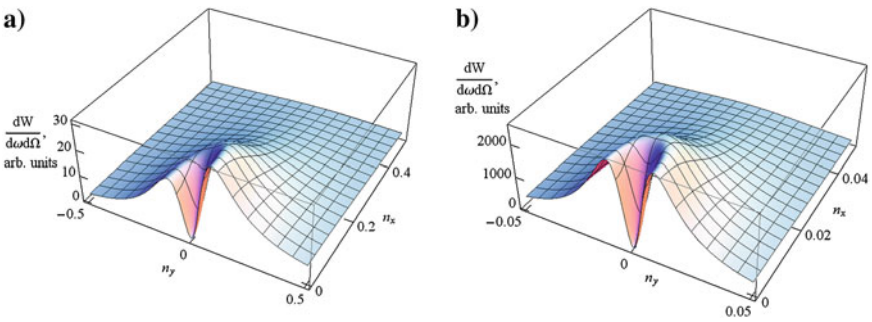

Fig. 5.2 Two-dimensional angular distributions of TR for various values of the Lorentz-factor: $\gamma = 10$ (**a**) and $\gamma = 100$ (**b**)

is concentrated, is characterized by a scale $\sim\gamma^{-1}$. Therefore, the description of TR characteristics of ultrarelativistic particles is convenient to carry out in the coordinate system x', y', z', where the axis z' is directed along the initial particle velocity and which is obtained from the initial one via rotation around x-axis at an angle ψ.

In the new (primed) system the unit wavevector $\Delta = (\Delta_x, \Delta_y, \Delta_z)$ will be expressed through initial direction cosines by the known rules:

$$\begin{aligned} \Delta_x &= n_x, \\ \Delta_y &= n_y \cos\psi - n_z \sin\psi, \\ \Delta_z &= n_y \sin\psi + n_z \cos\psi. \end{aligned} \tag{5.1.6}$$

It is clear, that in the rotated system the values Δ_x, Δ_y take values of order γ^{-1}, and $\Delta_z \sim 1$. The inverse transformation is following:

$$\begin{aligned} n_x &= \Delta_x, \\ n_y &= \Delta_y \cos\psi + \Delta_z \sin\psi, \\ n_z &= -\Delta_y \sin\psi + \Delta_z \cos\psi. \end{aligned} \tag{5.1.7}$$

Substituting (5.1.7) in (5.1.4), taking into account a relationship $\Delta_z = 1 - \frac{\Delta_y^2 + \Delta_x^2}{2}$ and using ultrarelativistic approximation

$$\beta = 1 - \frac{\gamma^{-2}}{2}. \tag{5.1.8}$$

neglecting the terms $\sim\gamma^{-4}$ both in numerator and denominator we get

$$\frac{dW}{d\omega\, d\Omega} = \frac{e^2}{\pi^2 c} \frac{\Delta_x^2 + \Delta_y^2 + \Delta_y \tan\psi\left(\gamma^{-2} + \Delta_x^2 + \Delta_y^2\right)}{\left(\gamma^{-2} + \Delta_x^2 + \Delta_y^2\right)^2}. \tag{5.1.9}$$

For perpendicular flight of a particle through a target ($\beta_y = 0$, $\beta_z = \beta$, $n_z = \cos\theta$) instead of (5.1.4) we have the Ginzburg-Frank formula [1]:

$$\frac{dW}{d\omega\, d\Omega} = \frac{e^2}{\pi^2 c} \frac{\beta^2 \sin^2\theta}{\left(1 - \beta^2 \cos^2\theta\right)^2}, \tag{5.1.10}$$

or, in ultrarelativistic approximation:

$$\frac{dW}{d\omega\, d\Omega} = \frac{e^2}{\pi^2 c} \frac{\Delta_x^2 + \Delta_y^2}{\left(\gamma^{-2} + \Delta_x^2 + \Delta_y^2\right)^2}. \tag{5.1.11}$$

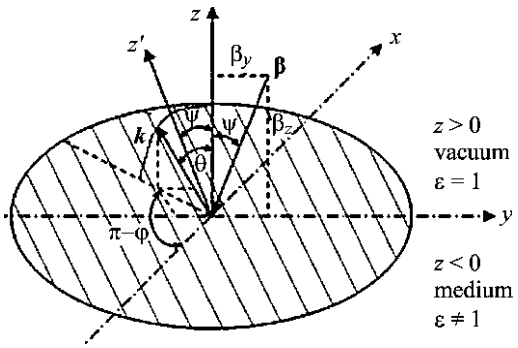

Fig. 5.3 The variables describing a process of backward transition radiation, i.e. when the charge is moving from vacuum into a medium

Having replaced the signs of a particle velocity components ($\beta_{y,z} \to -\beta_{y,z}$) in the formula (5.1.4) we obtain the formula describing TR from a charge, incident from vacuum onto an ideal conductor. As it is easy to see from the formula (5.1.4), in this case the minimum of a denominator corresponds to a direction $n_y = -\sin\psi$; $n_z = \cos\psi$, i.e. TR is concentrated near direction of the specular reflection.

It is easy to show that angular distribution of TR for this geometry, referring to "backward transition radiation" (see Fig. 5.3), is described by the same formula (5.1.9) with replacement of an angle ($\Delta_y \to -\Delta_y$), where angles Δ_x, Δ_y are counted off from a direction of the specular reflection.

Two-dimensional angular distributions of backward TR calculated by formula (5.1.9) with substitution (5.1.7) $\Delta_x \to -\Delta_y$ are shown in Fig. 5.4.

One may see that for small values of the Lorentz-factor the maximum in asymmetric angular distribution of "forward TR" in a plane $\Delta_x = 0$ is located between the distribution axis and a target surface. The same law is kept for "backward TR" as well (see Fig. 5.5).

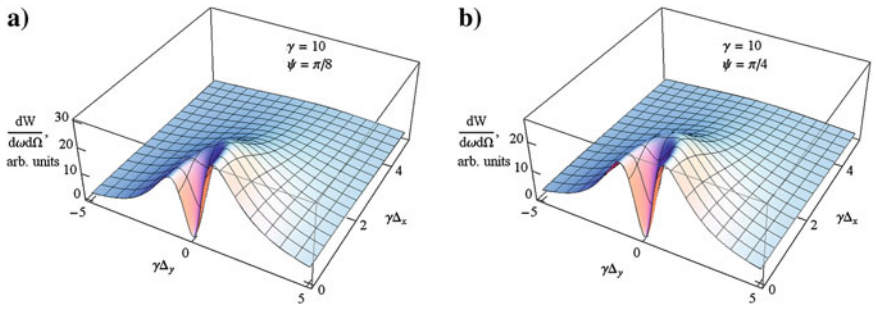

Fig. 5.4 Angular distributions of "backward TR" for different angles of a target inclination

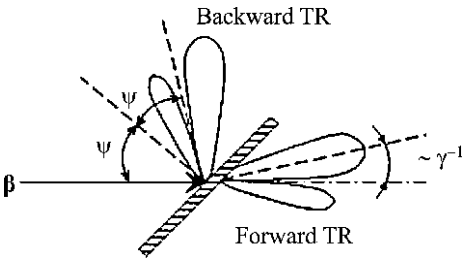

Fig. 5.5 Diagrams of directivity for forward TR and backward TR

5.2 Transition Radiation in the X-ray Range

The medium dielectric permittivity being far from the frequencies corresponding to the absorption edges, in the X-ray range is described by simple expression [7]

$$\varepsilon(\omega) = 1 - \omega_p^2 \Big/ \omega^2 = 1 - \chi, \tag{5.2.1}$$

where ω_p is a plasmon frequency of a target material, which is defined by concentration of electrons n_e in the target material:

$$\omega_p = \sqrt{4\pi n_e r_0 c^2} = \sqrt{4\pi \frac{Z}{A} N_0 \rho r_0 c^2}. \tag{5.2.2}$$

In the last formula r_0 is the classical radius of electron, Z is a charge and A is atomic mass of the target atoms, N_0 is the Avogadro number, ρ is density. Instead of (5.2.2) the "engineering" formula is often used.

$$h\omega_\mathrm{p} \approx 21\sqrt{\frac{2Z}{A}}\rho[\mathrm{eV}] \tag{5.2.3}$$

where density is substituted in units g/cm^3.

For such typical target materials as aluminum and silicon, the plasmon energy of target is close to 30 eV. It is clear that in the X-ray range ($\hbar\omega \geq$ 1 keV) the dielectric permittivity (5.2.1) a little bit differs from 1: $\chi = |1 - \varepsilon| \ll 1$, that allows having expanded the value ε in power of $(\omega_\mathrm{p}/\omega)^2$, to keep in the final result only the main term.

For calculation of polarization characteristics of TR we will use the system of unit vectors, determined through a normal to an interface $\mathbf{b} = \{0, 0, 1\}$:

$$\mathbf{e}_1 = \frac{[\mathbf{n}, \mathbf{b}]}{|[\mathbf{n}, \mathbf{b}]|}; \quad \mathbf{e}_2 = [\mathbf{n}, \mathbf{e}_1]. \tag{5.2.4}$$

The unit vectors (5.2.4) are written through direction cosines of a wavevector as follows:

$$\begin{aligned}\mathbf{e}_1 &= \frac{1}{\sqrt{1-n_z^2}}\{n_y, -n_x, 0\},\\ \mathbf{e}_2 &= \frac{1}{\sqrt{1-n_z^2}}\{n_x n_z, n_y n_z, -(1-n_z^2)\}.\end{aligned} \tag{5.2.5}$$

The Hertz vector in the considered approximation has the following components:

$$\begin{aligned}\Pi_y &= \frac{e}{\pi c} C_2\left[-\beta_y\beta_z\left(1-n_z^2+n_z\sqrt{n_z^2-\chi}\right)\right];\\ \Pi_z &= \frac{e}{\pi c} C_2\left[1-\beta_y n_y-\beta_z n_z-\beta_z^2\right],\end{aligned} \tag{5.2.6}$$

where

$$\begin{aligned}C_2 = \chi &\frac{\beta_z n_z}{\left[n_z(1-\chi)+\sqrt{n_z^2-\chi}\,\right]}\\ &\times\frac{1}{\left[\left(1-\beta_y n_y\right)^2-\beta_z^2 n_z^2\right]\left[1-\beta_y n_y-\beta_z\sqrt{n_z^2-\chi}\right]}.\end{aligned} \tag{5.2.7}$$

After substitution of expression (5.2.6) in (5.1.1) it is possible to find all three components of TR field in the coordinate system connected with a wavevector, which characterize the TR polarization.

$$\begin{aligned}E_1 &= (\mathbf{e_1}\mathbf{E}) = \frac{e}{\pi c} C_2 \frac{\beta_y\beta_z n_x}{\sqrt{1-n_z^2}}\left(1-n_z^2+n_z\sqrt{n_z^2-\chi}\right),\\ E_2 &= (\mathbf{e_2}\mathbf{E}) = \frac{e}{\pi c} C_2 \frac{1}{\sqrt{1-n_z^2}}\\ &\quad\times\left[\beta_y\beta_z n_y n_z-\left(1-n_z^2\right)\times\left(1+\beta_y n_y+\beta_z n_z-\beta_z^2\right)\right],\\ E_3 &= (\mathbf{n}\mathbf{E}) = 0.\end{aligned} \tag{5.2.8}$$

As before, let's pass on the system connected with an electron momentum via transformation (5.1.7) taking into account the ultrarelativistic approximation $(\Delta_x, \Delta_y \sim \gamma^{-1})$. Keeping the main terms, we get

$$\begin{aligned}C_2 &\approx \frac{\chi}{\cos\psi\left(\gamma^{-2}+\Delta_x^2+\Delta_y^2\right)\left(\gamma^{-2}+\Delta_x^2+\Delta_y^2+\chi\right)},\\ \sqrt{1-n_z^2} &\approx \sin\psi.\end{aligned} \tag{5.2.9}$$

Then, instead of (5.2.8) we have

$$\begin{aligned} E_1 &\approx \frac{e}{\pi c}\frac{C_2}{\sin\psi}\beta^2 \sin\psi\cos\psi\Delta_x \\ &= \frac{e}{\pi c}\frac{\chi\Delta_x}{\left(\gamma^{-2}+\Delta_x^2+\Delta_y^2\right)\left(\gamma^{-2}+\Delta_x^2+\Delta_y^2+\chi\right)}, \\ E_2 &\approx \frac{e}{\pi c}\frac{C_2}{\sin\psi}\beta^2 \sin\psi\cos\psi\Delta_y \\ &= \frac{e}{\pi c}\frac{\chi\Delta_y}{\left(\gamma^{-2}+\Delta_x^2+\Delta_y^2\right)\left(\gamma^{-2}+\Delta_x^2+\Delta_y^2+\chi\right)}. \end{aligned} \tag{5.2.10}$$

In the last expressions it is omitted, as before, a factor describing a spherical wave.

Thus, the spectral-angular distribution of the "forward TR" intensity in the X-ray range is calculated on the basis of formulae (5.2.10):

$$\begin{aligned} \frac{dW}{d\omega\, d\Omega} &= cR^2\left(|E_1|^2+|E_2|^2\right) \\ &= \frac{e^2}{\pi^2 c}\frac{\chi^2\left(\Delta_x^2+\Delta_y^2\right)}{\left(\gamma^{-2}+\Delta_x^2+\Delta_y^2\right)^2\left(\gamma^{-2}+\Delta_x^2+\Delta_y^2+\chi\right)^2} \end{aligned} \tag{5.2.11}$$

and, as follows from the derived expression, it does not depend on the target tilt angle ψ (it is necessary to emphasize that this conclusion concerns the relativistic energies of the charged particle).

The angular distributions of the "forward TR" intensity in X-ray range for beryllium target are given in Fig. 5.6a–c for various values of the Lorentz-factor, from which follows that asymmetry in the angular distribution is observed for $\gamma < 100$.

It is necessary to specify that in the ultrarelativistic limit the values

$$\begin{aligned} \frac{dW_{\perp,\parallel}}{d\omega\, d\Omega} &= cR^2\left|E_{1,2}\right|^2 = \frac{e^2}{\pi^2 c}\left(\frac{\omega_p}{\omega}\right)^4 \\ &\times \frac{\Delta_{x,y}^2}{\left(\gamma^{-2}+\Delta_x^2+\Delta_y^2\right)^2\left(\gamma^{-2}+\Delta_x^2+\Delta_y^2+\omega_p^2/\omega^2\right)^2} \end{aligned} \tag{5.2.12}$$

with accuracy to the terms $\sim\gamma^{-1}$ characterize the TR intensity components in a plane, which is perpendicular (parallel) to the "reflection" plane, i.e. containing both the vector of particle velocity and the normal vector to the target surface. As follows from the above-mentioned formula, a parallel component is proportional to a projection angle Δ_x and perpendicular component is proportional to Δ_y. In other words, in ultrarelativistic approximation the position of linear polarization plane is defined only by an azimuthal angle of an outgoing TR photon

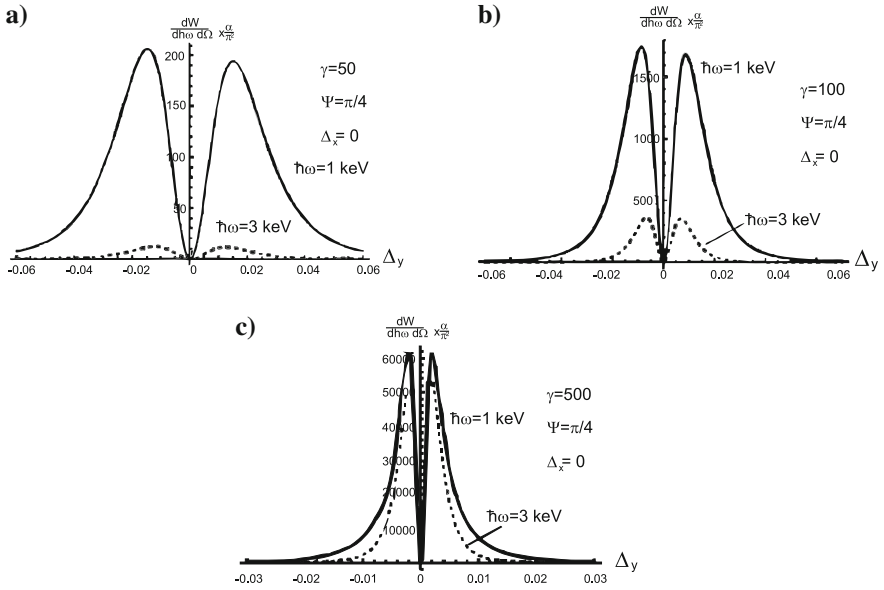

Fig. 5.6 The angular distributions of the "forward TR" for electrons with different energies in a beryllium target

$\left(\arctan\varphi = \Delta_x/\Delta_y = |E_1|/|E_2|\right)$, i.e. the linear polarization is radial one and practically does not depend on frequency.

The deviation from the radial polarization can be found, having calculated a degree of polarization in a plane, which passes through a wavevector and a momentum of initial electron. In other words, it is necessary to calculate the Stokes parameter ξ_3 in the basis

$$\mathbf{e}_{1\beta} = \frac{[\mathbf{n}, \boldsymbol{\beta}]}{|[\mathbf{n}, \boldsymbol{\beta}]|}, \quad \mathbf{e}_{2\beta} = [\mathbf{n}, \mathbf{e}_1]. \tag{5.2.13}$$

In this basis it is possible to get the expressions similar to (5.2.8), which are written through the angular variables Δ_x, Δ_y:

$$\begin{aligned} E_{1\beta} &= \left(\mathbf{e}_{1\beta}\mathbf{E}\right) = \frac{e}{\pi c} C_2 \frac{\Delta_x \sin\psi}{\sqrt{\Delta_x^2 + \Delta_y^2}} \left(\frac{\gamma^{-2} + \Delta_x^2 + \Delta_y^2 - \chi\cos^2\psi}{2}\right), \\ E_{2\beta} &= \left(\mathbf{e}_{2\beta}\mathbf{E}\right) = \frac{e}{\pi c} C_2 \frac{\left(\Delta_x^2 + \Delta_y^2\right)\cos\psi}{\sqrt{\Delta_x^2 + \Delta_y^2}}. \end{aligned} \tag{5.2.14}$$

Only the main summands have been kept in the last formulae. As it follows from the obtained expressions, the ratio of polarization components

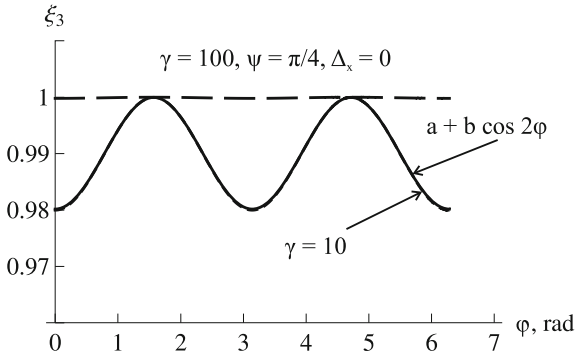

Fig. 5.7 Dependence of the Stokes parameter ξ_3 on an azimuthal angle of TR photon with $\hbar\omega = 3$ keV relative to a plane $(\mathbf{n}, \boldsymbol{\beta})$. The *upper curve* corresponds $\gamma = 100$, the *lower* $\gamma = 10$

$$\frac{|E_{1\beta}|}{|E_{2\beta}|} \sim \{\gamma^{-1}, \chi\} \ll 1 \tag{5.2.15}$$

shows that a polarization TR component intensity $|E_{2\beta}|^2$ (along a plane $(\mathbf{n}\boldsymbol{\beta})$ essentially exceeds the intensity of component $\sim |E_{1\beta}|^2$ in a perpendicular plane and within accuracy $\sim\gamma^{-2}$ coincides with total intensity of X-ray transition radiation (see formula (5.2.11)).

The calculation results of the Stokes parameter depending on an azimuthal angle of photon output $\varphi_\beta(\varphi_\beta = \arctan\Delta_x/\Delta_y)$ are given in Fig. 5.7. Calculations were carried out for a polar angle of a photon in the primed system $\Delta = \sqrt{\Delta_x^2 + \Delta_y^2} = \gamma^{-1}$ for an aluminum target. The upper curve (nearly the constant) describes the parameter ξ_3 for $\gamma = 100$, whereas the lower one—for $\gamma = 10$. In the last case it is possible to say that in case of oblique incidence of a charge on a target $(\psi \approx \pi/4)$ the linear polarization remains radial one with accuracy of a few percent. The approximation $\xi_3 = a + b\cos 2\varphi$ is shown here also.

5.3 Spectrum of the Transition Radiation

The "forward TR" spectrum is calculated by means of integration of expression (5.1.4) over angular variables for chosen dielectric permittivity $\varepsilon(\omega)$, generally speaking, for the complex one. Approximation $|\varepsilon| \to \infty$, which is used for the description of TR characteristics from a metal target in an optical and infrared range, gives the spectral distribution as constant.

In X-ray range the spectral-angular distribution is given by the sum of expressions (5.2.8), which we write down as

$$\frac{dW}{h\, d\omega\, d\Omega} = \frac{\alpha}{\pi^2}\gamma^2\left(\frac{\gamma\hbar\omega_p}{\hbar\omega}\right)^4 \frac{\gamma^2\theta^2}{\left(1+\gamma^2\theta^2\right)^2\left(1+\gamma^2\theta^2+\gamma^2\omega_p^2/\omega^2\right)^2}. \tag{5.3.1}$$

After integration of the received expression over a solid angle ($d\Omega = d\Delta_x d\Delta_y = \frac{1}{2} d\varphi\, d\theta^2$) it is possible to obtain the TR spectrum

$$\frac{dW}{\hbar\, d\omega} = \frac{\alpha}{\pi}\left\{\left[1 + 2\left(\frac{\hbar\omega}{\gamma\hbar\omega_{\mathrm{p}}}\right)^2\right]\ln\left[1 + \left(\frac{\gamma\hbar\omega_{\mathrm{p}}}{\hbar\omega}\right)^2\right] - 2\right\}. \tag{5.3.2}$$

The spectrum (5.3.2) (the upper curve) is given in Fig. 5.8. The spectrum of TR intensity for the fixed collimation angle of photons $\gamma\theta_c = 1$ is shown here for comparison, as well. As follows from figure, the spectrum of TR intensity is rapidly going down function with an increase of energy of TR photons. With increasing of energy $\hbar\omega$ from the value $\gamma\hbar\omega_p$ to 10 $\gamma\hbar\omega_p$ the yield of radiation decreases approximately by three orders of magnitude.

As a whole, the used approximation for spectral-angular distribution of TR is valid for small outgoing angles of a photon ($\theta \sim \gamma^{-1}$) and in the range of frequencies of photons $\omega \geq 2\omega_p$.

Integrating a spectrum (5.3.2) over energy of emitted photons from certain minimal value $\hbar\omega_0 \ll \gamma\hbar\omega_p$ to the upper boundary of the spectrum, which may tend to infinity, energy losses on the transition radiation may be estimated:

$$W = \int_{\hbar\,\omega_0}^{\infty} \frac{dW}{\hbar\, d\omega}\hbar\, d\omega \approx \frac{1}{3}\alpha\left[\gamma\hbar\omega_{\mathrm{p}} - \frac{6\hbar\omega_{\mathrm{p}}}{\pi}\ln\frac{\gamma\hbar\omega_{\mathrm{p}}}{\hbar\omega_0}\right] \approx \frac{1}{3}\alpha\gamma\hbar\omega_{\mathrm{p}}. \tag{5.3.3}$$

From the calculated result follows that total losses depend linearly on energy of the charged particle. Just this characteristic of TR is widely used in detectors of elementary particles, where the measurements of particle total radiation losses allow to define its Lorentz-factor.

Let's note that the last result is valid for one boundary only. In the real experiment, when the charged particle crosses a target, where TR is generated on the entrance and exit surfaces of target, then for a rather thick target the result (5.3.3) must be double.

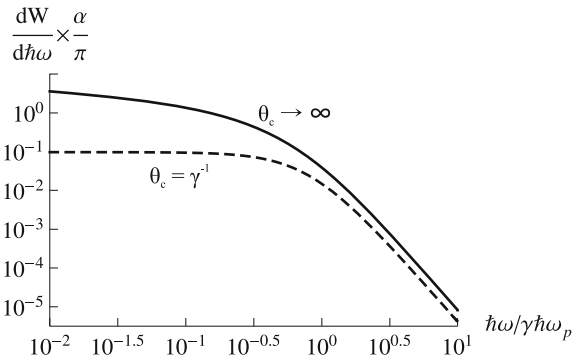

Fig. 5.8 Spectrum of TR intensity in a total cone (the *upper curve*) and in a cone $\theta_c = 1/\gamma$ (the *lower curve*)

5.4 X-ray Transition Radiation of Ultrarelativistic Particles in Layered Targets

As it is shown above, forward TR has a continuous spectrum in the range of frequencies from $\omega_{\min} \sim 10^{11}$ s^{-1} (a millimeter wave region) to the X-ray range (for $\gamma \geq 50$). However, the spectrum of resonant transition radiation (RTR) arising in case of flight of a charged particle through a layered target (for example, through a periodic set of the foils, see Fig. 5.9), becomes quasimonochromatic.

The nonrelativistic particle with velocity $\mathbf{v} = \boldsymbol{\beta} c$ moving through the similar periodic structure will mainly emit at a frequency being proportional to frequency of the passing of periodic structure:

$$\omega_k = k\Omega = k\frac{2\pi v}{d}, \quad k = 1, 2, \ldots, \quad d = \ell_1 + \ell_2. \tag{5.4.1}$$

For the ultrarelativistic particle, in full analogy with the undulator radiation, position of a monochromatic line in a spectrum of radiation is shifted in a hard part proportionally to value $2\gamma^2$, what allows to use RTR for generation of monochromatic X-ray radiation [8].

The resonance condition for RTR, which is generated in the periodic stack, consisting of layers of a various material, was obtained by Ter-Mikaelyan [2]:

$$\cos\theta = \frac{d - \frac{2\pi k}{\omega}}{\frac{v}{c}\left(\sqrt{\varepsilon_1}\ell_1 + \sqrt{\varepsilon_2}\ell_2\right)}, \quad k = 1, 2, \ldots. \tag{5.4.2}$$

The dielectric permittivity of layers with an index 1, 2 and thickness ℓ_1 and ℓ_2 (see Fig. 5.9) is designated in (5.4.2) through ε_1, ε_2, accordingly. Further we'll consider RTR in a X-ray range, where

$$\varepsilon_n(\omega) = 1 - \frac{\omega_{p_n}^2}{\omega^2}, \tag{5.4.3}$$

where ω_{p_n} is plasmon frequency of medium with number $n = 1, 2$.

As in the case considered in Sect. 5.2, X-ray transition radiation of ultrarelativistic particle from the infinite boundary between two media, is mainly

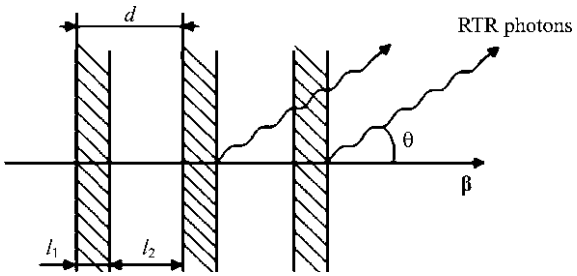

Fig. 5.9 The producing of RTR when an electron crosses a layered target

concentrated in a cone with opening angle equal to $\theta \sim \gamma^{-1} \ll 1$ along a particle momentum direction. The radiation intensity can be calculated in the following manner (see, for instance, [6]):

$$\frac{d^2 W_{\mathrm{TR}}}{d\Omega\, d\omega} = \frac{e^2}{4\pi^2 c^3}\omega^2 \sin^2\theta (Z_1 - Z_2)^2. \tag{5.4.4}$$

In (5.4.4) $Z_{(1,2)}$ is a value, which differs from the radiation formation length with frequency ω in medium 1 (2) on the value π:

$$Z_{1(2)} = \frac{4c}{\omega\left[\gamma^{-2} + \theta^2 + \frac{\omega_{\mathrm{p}1(2)}^2}{\omega^2}\right]}. \tag{5.4.5}$$

The formula (5.4.4) can be expressed through the field $\mathbf{E}_{\mathrm{TR}}$

$$\frac{d^2 W_{\mathrm{TR}}}{d\Omega\, d\omega} = \frac{4\pi^2}{c}|\mathbf{E}_{\mathrm{TR}}|^2,$$

which for the infinite boundary between two media is given by the formula:

$$\mathbf{E}_{\mathrm{TR}} = \frac{ie}{2\pi^2}\left(\frac{\theta}{\gamma^{-2} + \theta^2 + \frac{\omega_{\mathrm{p}1}^2}{\omega^2}} - \frac{\theta}{\gamma^{-2} + \theta^2 + \frac{\omega_{\mathrm{p}2}^2}{\omega^2}}\right). \tag{5.4.6}$$

It is easy to show that TR field at the exit surface of a layer will have an opposite sign in comparison with field, which is generated on the entrance surface: $\mathbf{E}_2 = -\mathbf{E}_1$.

Then, taking into account a phase difference for radiation at an angle θ between points of particle entrance and exit in the first layer, it is possible to write down:

$$E_{\mathrm{layer}} = \mathbf{E}_1 + \mathbf{E}_2 = \mathbf{E}_1[1 - \exp(-i\varphi_1)], \tag{5.4.7}$$

where

$$\begin{aligned}\varphi_1 &= \frac{\omega\ell_1}{v} - \frac{k_1\ell_1\cos\theta}{c} = \frac{\omega\ell_1}{\beta c}(1 - \beta\sqrt{\varepsilon_1}\cos\theta)\\ &\approx \frac{\omega\ell_1}{2c}\left(\gamma^{-2} + \theta^2 + \frac{\omega_{p_1}^2}{\omega^2}\right) = \frac{\ell_1}{Z_1}.\end{aligned} \tag{5.4.8}$$

Finally, let's introduce absorption of emitted photons in material of a layer:

$$\mathbf{E}_{\mathrm{layer}} = \mathbf{E}_1\left[1 - \exp\left(+i\varphi_1 - \frac{1}{2}\sigma_1\right)\right], \tag{5.4.9}$$

where $\sigma_1 = \mu_1\ell_1$, μ_1 is a linear factor of absorption of photons with frequency ω. In full analogy one may deduce a TR field, which is generated by a particle while it

is passing the first period of a layered target (i.e. the first and second layers, see Fig. 5.9):

$$\mathbf{E}_{\text{per}} = \mathbf{E}_1\left[1 - \exp\left(i\varphi_1 + i\varphi_2 - \frac{1}{2}\sigma_1 - \frac{1}{2}\sigma_2\right)\right]. \tag{5.4.10}$$

From (5.4.10) it is easy to obtain the spectral-angular distribution of TR from a target consisting of N periods:

$$\left(\frac{d^2W}{d\omega\, d\Omega}\right)_N = \left(\frac{d^2W}{d\omega\, d\Omega}\right)_{\text{TR}} F_2F_3, \tag{5.4.11}$$

where the factor

$$F_2 = 1 + \exp(-\sigma_2) - 2\exp\left(\frac{\sigma_1}{2}\right)\cos\varphi_1 \tag{5.4.12}$$

takes into account the interference and absorption of radiation in the first period, whereas the factor

$$F_3 = \frac{1 + \exp(-N\sigma) - 2\exp\left(-\frac{1}{2}N\sigma\right)\cos[N(\varphi_1 + \varphi_2)]}{1 + \exp(-\sigma) - 2\exp\left(-\frac{\sigma}{2}\right)\cos(\varphi_1 + \varphi_2)}, \tag{5.4.13}$$

is essentially the interference coefficient, which, in case of a constructive interference, defines the range of angles and frequencies, where the resonant transition radiation is generated effectively. In (5.4.13) $\sigma = \sigma_1 + \sigma_2$. It is easy to show that neglecting absorption, the factor F_3 reaches its maximal values under the conditions:

$$\varphi_{12} = \varphi_1 + \varphi_2 = 2k\pi, \quad k = 1, 2, \ldots \tag{5.4.14}$$

Having substituted the used approximations in (5.4.14), we get

$$\frac{\ell_1\omega}{v}\left[\gamma^{-2} + \theta^2 + \frac{\omega_{p_1}^2}{\omega^2}\right] + \frac{\ell_2\omega}{v}\left[\gamma^{-2} + \theta^2 + \frac{\omega_{p2}^2}{\omega^2}\right] = 2k\pi. \tag{5.4.15}$$

The last relationship is often written in the following form:

$$\frac{\varphi_{12}}{2} = \frac{\varphi_1 + \varphi_2}{2} = \frac{\ell_1}{Z_1} + \frac{\ell_2}{Z_2} = k\pi. \tag{5.4.16}$$

By analogy with (5.4.8), a phase φ_2 is expressed as follows:

$$\varphi_2 = \frac{\ell_2}{Z_2}. \tag{5.4.17}$$

One may see that the resonance condition (5.4.14) (or (5.4.16)) coincides with the condition of a resonance (5.4.2) obtained by Ter-Mikaelyan.

Neglecting absorption ($\sigma \to 0$) the coefficient F_3 transforms to a form

$$F_3 = \frac{\sin^2\left(N\frac{\varphi_{12}}{2}\right)}{\sin^2\left(\frac{\varphi_{12}}{2}\right)}. \tag{5.4.18}$$

Then under fulfillment of the resonance conditions (5.4.14) we obtain $F_3 = N^2$, and, consequently, from (5.4.11) we get

$$\left(\frac{d^2W}{d\omega\, d\Omega}\right)_N = 4N^2 \sin^2\left(\frac{\varphi_1}{2}\right)\left(\frac{d^2W}{d\omega\, d\Omega}\right)_{\mathrm{TR}}. \tag{5.4.19}$$

As follows from (5.4.19), the maximal yield of radiation has been reached under fulfillment of the following condition:

$$\sin^2\left(\frac{\varphi_1}{2}\right) \to 1, \quad \text{i.e. } \varphi_1 = (2m-1)\frac{\pi}{2}, \quad m = 1, 2, \ldots \tag{5.4.20}$$

It should be noted that abovementioned formulae were deduced in classical approximation, however the quantum approach gives the identical results, that allows to use the received formulas for calculation of an yield of photons with energy $\hbar\omega$:

$$\frac{d^2N_{\mathrm{TR}}}{\hbar\, d\omega\, d\Omega} = \frac{1}{\hbar\omega}\cdot\frac{d^2W_{\mathrm{TR}}}{\hbar\, d\omega\, d\Omega}, \tag{5.4.21}$$

where $\frac{d^2W_{\mathrm{TR}}}{\hbar\, d\omega\, d\Omega} = \frac{\alpha}{16\pi^2c^2}\omega^2|Z_1 - Z_2|^2 \sin^2\theta$, $\alpha = 1/137$ is the fine structure constant.

Further, the formula (5.4.19) gives the quadratic dependence on the number of the periods for the fixed frequency of radiation (energy of photons) and an angle of outgoing TR photon. However, in the real case with usage of collimator with the finite aperture, the photon yield will be proportional to N only (a linear dependence occurs).

The spectra of RTR intensity for the fixed angle of radiation $\theta = 5$ mrad and energy of electron beam $E = 100$ MeV in the stacks of the beryllium foils separated by vacuum gaps, with thickness $\ell_1 = 10$ μm and the period $d = 60$ μm for $N = 10$ (the curve 1) and $N = 5$ (the curve 2) without taking into account the absorption are given in Fig. 5.10. Calculation was carried out by formulas (5.4.11)–(5.4.13).

The maximum position in a spectrum is defined by the relationship (5.4.16). For the fixed angle θ the dependence of a phase φ_{12} on the photon energy is nonlinear (see formula (5.4.15)).

The dependence of the value $\varphi_{12}/2\pi$ on the energy of photons is shown in Fig. 5.11. As follows from the diagram, in the energy interval 0.5 keV $\leq \omega \leq$ 5 keV, the peaks corresponding to $k = 4, 5, 6$ appear in the spectrum. Two peaks correspond to each order of diffraction due to the nonlinear dependence of $\varphi_{12}(\omega)$.

It follows from the nonlinear equation of a resonance (5.4.16), which can be rewritten as the quadratic equation for resonance frequency ω_k ($k = 1, 2, 3, \ldots$ is the diffraction order)

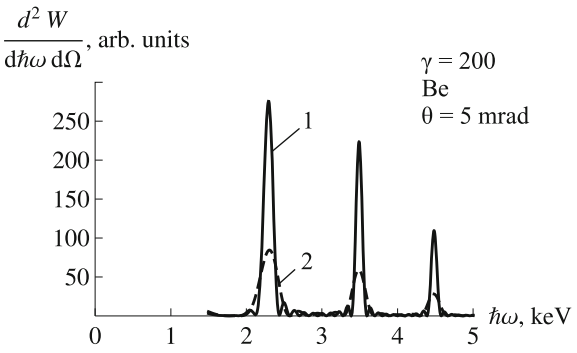

Fig. 5.10 Spectrum of RTR generated by an electron beam with energy $E = 100$ MeV in a stack from $N = 10$ beryllium foils (the *curve 1*), separated by vacuum gaps ($\ell_1 = 10\,\mu$, $\ell_2 = 50\,\mu$), and in the stack with $N = 5$ foils (the *curve 2*). The angle of observation $\theta = 5$ mrad

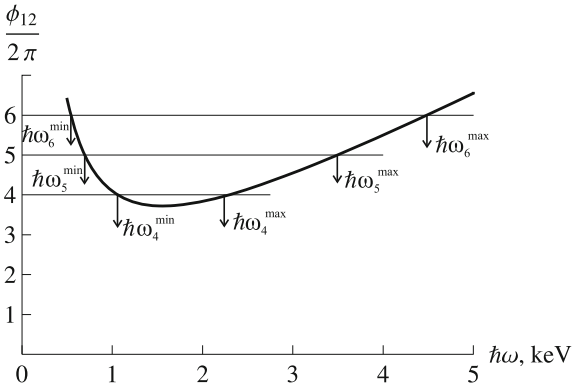

Fig. 5.11 Dependence of a phase $\varphi_{12}(\theta, \omega)$ on energy of photons for the same target

$$\frac{\omega_k^2}{\omega_0}\left(1 + \gamma^2\theta^2\right) - k\omega_k + \omega_T = 0. \tag{5.4.22}$$

In the Eq. (5.4.22) designations [9] are used:

$$\omega_0 = \gamma^2\frac{4\pi\beta c}{d}, \quad \omega_T = \omega_p^2\frac{\ell_1}{4\pi c}. \tag{5.4.23}$$

Frequency ω_0 corresponds to the "vacuum" frequency of radiation in "straightforward direction" for the charged particle with the Lorentz-factor γ and trajectory of such a particle perturbs with the period d. The frequency ω_T characterizes a target with thickness ℓ_1, made of a material with the plasma frequency ω_p.

It is obviously that the Eq. (5.4.22) has solutions for diffraction orders

$$k^2 > 4\frac{\omega_T}{\omega_0}\left(1 + \gamma^2\theta^2\right), \tag{5.4.24}$$

which are written in the form

$$\omega_{k\,\min} = \frac{\omega_0}{2\left(1+\gamma^2\theta^2\right)}\left[k - \sqrt{k^2 - 4\frac{\omega_T}{\omega_0}\left(1+\gamma^2\theta^2\right)}\right],$$
$$\omega_{k\,\max} = \frac{\omega_0}{2\left(1+\gamma^2\theta^2\right)}\left[k + \sqrt{k^2 - 4\frac{\omega_T}{\omega_0}\left(1+\gamma^2\theta^2\right)}\right]. \tag{5.4.25}$$

So, for $k = 4$ the positions of peaks $\hbar\omega_4^{\min} \approx 1.2$ keV; $\hbar\omega_4^{\max} \approx 2.3$ keV. Further for $k = 5$ we have $\hbar\omega_5^{\min} \approx 0.7$ keV; $\hbar\omega_5^{\max} \approx 3.6$ keV; for $k = 6$ – $\hbar\omega_6^{\min} \approx 0.5$ keV; $\hbar\omega_6^{\max} \approx 4.5$ keV (see Fig. 5.11).

Comparing the widths of RTR lines in the hard part of a spectrum (at $\hbar\omega_k > 2$ keV, see Fig. 5.10) we can note that the relative spectral width is determined by the number of periods $\frac{\Delta\omega}{\omega_k} \approx \frac{1}{N}$.

For the further calculations the linear coefficient of absorption of photons in beryllium (in inverse micrometers) was approximated by expression

$$\mu(\omega)\left[\mu^{-1}\right] = 1.85\left(\frac{0.0542}{\omega^3} + \frac{0.0013}{\omega^2} - \frac{0.0006}{\omega}\right), \tag{5.4.26}$$

where the energy of photons ω is substituted in keV. The plasmon energy in the beryllium target calculated by the formula (5.4.4), reaches the value $\hbar\omega_{p_1} = 26$ eV. For the lithium targets $\hbar\omega_{p_1} = 13.8$ eV.

The phase diagram for layered targets from Be (the upper curve) and Li (lower one) is shown in Fig. 5.12. Calculations were carried out for the Lorentz-factor $\gamma = 100$ for a target consisting of 10 layers with $\ell_1 = 10$ μm, $\ell_2 = 50$ μm and the observation angle $\theta = 1$ mrad.

The RTR spectra for considered targets, which are given in the same units for comparison, are given in Fig. 5.13a, b. As follows from the figure, the RTR yield from a beryllium target is much higher than from a lithium one, for other identical parameters. First of all, such increasing of the yield is determined by the dependence $\chi^2 = (\omega_p/\omega)^4$ (see formula (5.2.11)), which provides an increase of RTR

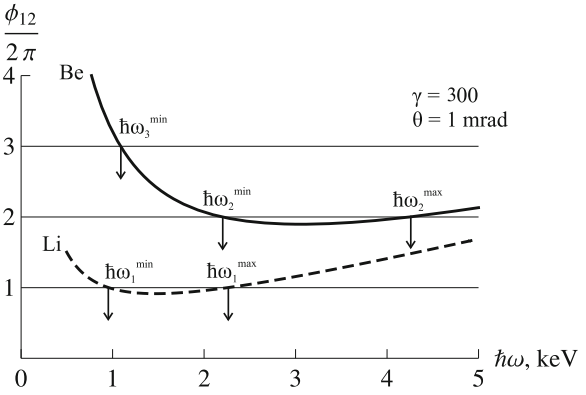

Fig. 5.12 The phase diagram for targets from Be (the *upper curve*) and Li (*lower one*). Calculation parameters: $\gamma = 300$; $\ell_1 = 10$ μm; $\ell_2 = 50$ μm; $N = 10$; $\theta = 0.001$

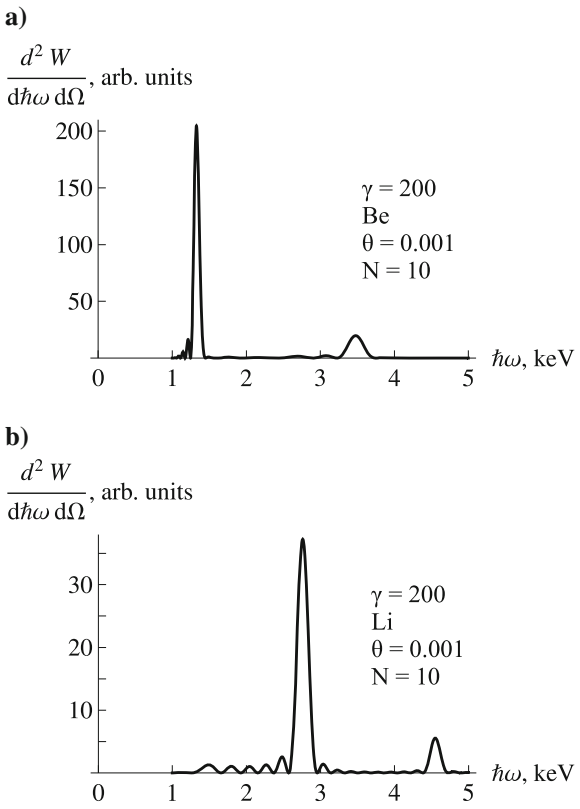

Fig. 5.13 The RTR spectra for layered targets from different materials

yield of photons with increasing of charge Z of the target atoms. Certainly, the absorption of RTR photons will grow up just in a target material with increase of Z. This effect will be considered later.

Let's consider a collimation effect of RTR in more detail.

Two dependences $\varphi_{12}(\hbar\omega)$ for various outgoing angles θ of the photon are given in Fig. 5.14. Calculation was carried out for energy of electrons $E = 50$ MeV, a periodic beryllium target from foils with thickness $\ell_1 = 10$ μm and the period 20 μm ($\ell_2 = 10$ μm). The upper curve is received for $\theta_1 = 5$ mrad, the lower one—for $\theta_2 = 0$ mrad. As follows from the diagram, in case of radiation collimation for outgoing angles of photons $\theta_2 \le \theta \le \theta_1$, a relatively broad line 3 keV $\le \hbar\omega_{4\,\max} \le$ 4 keV will appear in the energy range $\hbar\omega > 3$ keV. The left and right boundaries of maxima corresponding to $k = 4$ are calculated from intersection of lines $\varphi_{12}/\pi = k = 4$ with two dependences $(1/2\pi) \cdot \varphi_{12}$ ($\theta = 0$ mrad, ω) and $(1/2\pi) \cdot \varphi_{12}$ ($\theta = 5$ mrad, ω). Results of integration of the formula (5.4.11) over a solid angle $\Delta\Omega = \theta\Delta\theta\Delta\varphi$ are given in Fig. 5.15.

As mentioned above, the width of a spectral line is inversely proportional to the number of periods, if resonance conditions are fulfilled, therefore the total number of photons under a RTR peak will be defined by number of periods:

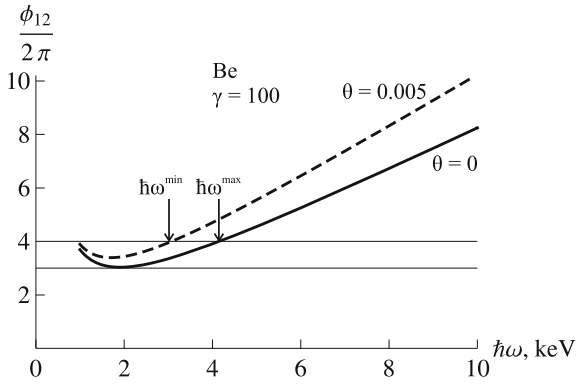

Fig. 5.14 The phase diagram for the outgoing angles of RTR photons $\theta = 0$ (the lower curve) and $\theta = 5$ mrad for $E = 50$ MeV; Be—$\ell_1 = 10$ μm, $\ell_2 = 10$ μm

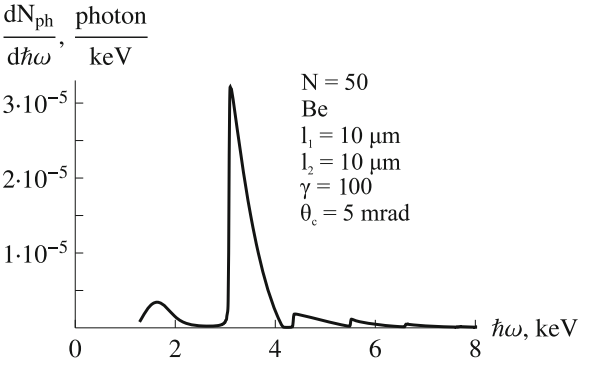

Fig. 5.15 The RTR photon spectrum in a layered Be target

$$\Delta N_{ph} \sim \frac{dW}{\hbar\, d\omega\, d\Omega}\frac{\Delta\hbar\omega}{\hbar\omega} \sim N^2 \cdot \frac{1}{N} \approx N.$$

V.N. Baier and V.M. Katkov in their work [9] have estimated the number of RTR photons, which are emitted in the given cone θ_c from a target containing N layers (neglecting the absorption of photons in the target):

$$\Delta N_{k\,\min} \approx 2\alpha N\pi \frac{1}{k^3}\left(\frac{\ell_2}{d}\right)^3 \left(\gamma^2\theta_c^2\frac{\omega_M}{\omega_0}\right)^2.$$

This estimation is obtained for the peak with the energy close to $\omega_{k\,\min}$. The number of photons, with taking into account of absorption, can be found via integrating the expression (5.4.21) (after multiplying by functions F_2 and F_3 (see formulas (5.4.12), (5.4.13)) over the given solid angle and energy interval as well. The dependence of RTR photon yield on a number of layers N for the spectrum presented in the Fig. 5.15 is shown in the Fig. 5.16. The number of photons was calculated for the energy range $3 \leq \hbar\omega \leq 4$ keV. As follows from the figure, for a relatively small number of layers ($N < 50$) the linear increase of yield of RTR photons concerns with N is observed, whereas for $N \geq 100$ the "saturation" is observed and the further growth of number of layers N does not result in increase of RTR yield.

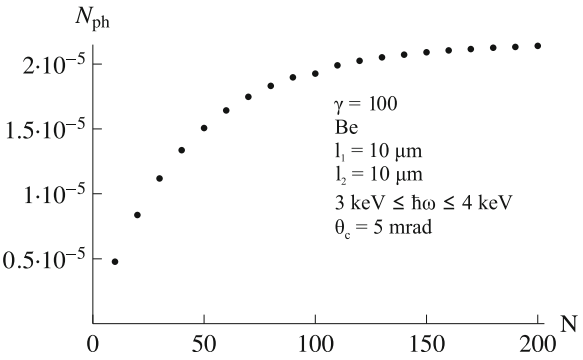

Fig. 5.16 Dependence of the RTR photon yield on the number of the target layers with account of the absorption

It should be noted that efficiency of RTR generation by the electron beam with energy $E \sim 50$ MeV in a cone of angles $\theta \leq \theta_c = 5$ mrad is not too high ($N_{ph} \sim 10^{-5}$ photons/electrons). However, with the increase of the initial electron energy the yield of photons in the same solid angle grows quadratically. Besides, with increase of the Lorentz-factor the boundary of "cutting" of TR spectrum ($\hbar\omega_{\max} \sim \gamma\hbar\omega_p$) is "shifted" in the hard part. The authors of work [9] have estimated a yield of RTR photons for a lithium target with 50 layers ($\ell_1 = 26$ μm, $\ell_2 = 52$ μm) and have shown that for electrons with energy $E \sim 1$ GeV the number of photons in a cone $\theta \leq 5$ mrad reaches the value $N_{ph} \sim 0.05$ photons/electrons.

5.5 Resonant Transition Radiation in the Layered Targets (Experiment)

As it follows from expression (5.4.5), the yield of TR photons depends on dielectric permittivity of materials of layers, in the following form:

$$N_{ph} \sim (Z_1 - Z_2)^2 \sim \left(\omega_{p_1}^2 - \omega_{p_2}^2\right)^2. \tag{5.5.1}$$

It is clear that if one of layers represents a vacuum gap ($\omega_{p_2} = 0$) the difference in brackets (5.5.1) will reach the maximal value. For this reason targets for generation of RTR as a periodic stack of foils separated by vacuum gaps have been widely used.

The target consisting of 10 mylar foils with thickness $\ell_1 = 1\,2$ μm having vacuum gaps $\ell_2 = 24$ μm, in which RTR in X-ray range $\omega \gg \omega_{p_1}$ was generated by a beam of electrons with energy $E = 900$ MeV (see Fig. 5.17), was used in one of the first experiments [10]. In the ultrarelativistic case for the considered target the condition of a resonance (5.4.22) is written as

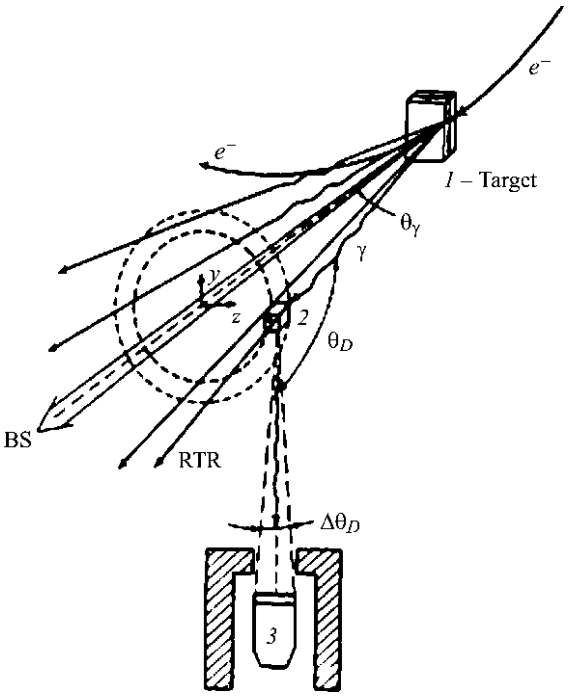

Fig. 5.17 The scheme of the experiment [10]

$$\theta_k^2 = k\frac{2\lambda}{d} - \gamma^{-2} - \frac{\ell_1}{d}\left(\frac{\omega_{p_1}^2}{\omega^2}\right), \quad k = 1, 2\ldots. \tag{5.5.2}$$

For the mylar $\hbar\omega_{\mathrm{p}_1} = 24$ eV, therefore the first order resonance ($k = 1$) for energy of RTR photons $\hbar\omega \approx 20$ keV corresponds to a radiation angle $\theta_1 \approx 1.7$ mrad, which is approximately three times as much as the typical value of an angle of ordinary transition radiation $\theta_{\mathrm{TR}} \approx \gamma^{-1} \approx 0.6$ mrad.

The angular distribution of RTR for the energy interval $\hbar\omega = 10$–30 keV was measured in the experiment [10] using a NaI-detector during moving the Compton scatterer in respect to a beam axis (see Fig. 5.17).

The experimental results (the upper curve) are given in Fig. 5.18. The maximum position in the measured distribution coincides with the estimation $\theta_{\mathrm{exp}} = 1.7$ mrad.

The angular distribution of hard photons ($\hbar\omega > 60$ keV), which are generated due to the bremsstrahlung mechanism is shown in the same figure by the curve 2. In the energy range of photons $\hbar\omega \geq \gamma\hbar\omega_p$ the RTR yield is suppressed as $(\gamma\omega_{\mathrm{p}}/\omega)^4$. As expected, the BS maximum for $\theta = 0$ with angular width $\sim\gamma^{-1}$ is observed in this case.

The similar experiment was carried out at the MAMIB microtron electron beam with energy $E = 855$ MeV [11]. The scheme of the experimental setup is shown in Fig. 5.19. Unlike the previous experiment, the radiation was directly detected

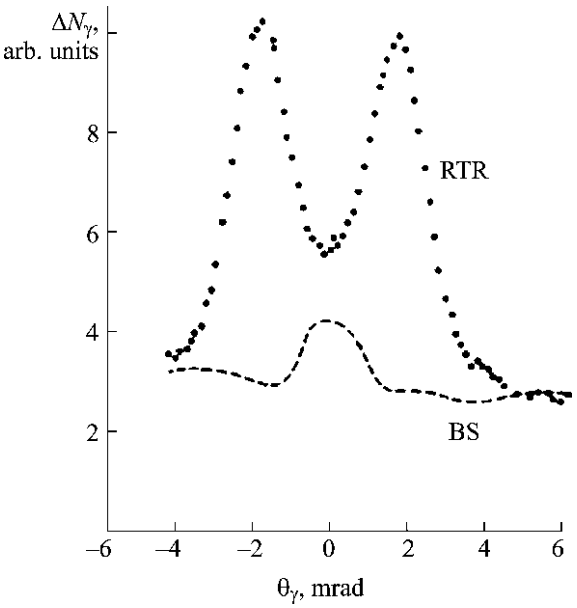

Fig. 5.18 Angular distribution of RTR with energy of photons 10 keV $\leq \hbar\omega \leq$ 30 keV in a target consisting of 10 mylar foils with thickness 12 μm and period 36 μm

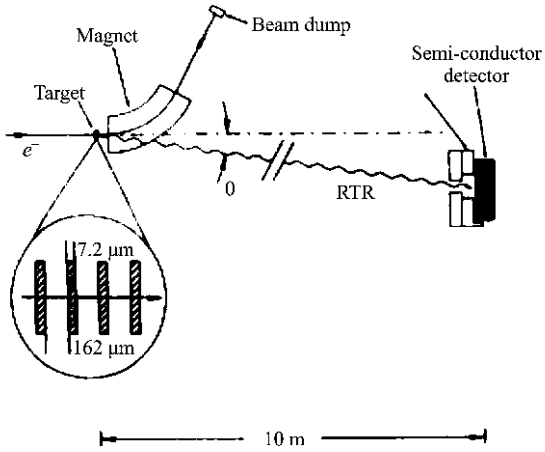

Fig. 5.19 The scheme of experiment for measurement of RTR spectrum [11] for the fixed angle of outgoing photons

under the fixed angle θ. As a target a set of four polyamide foils with thickness 7.2 μm with a vacuum gap 162 μm was used.

The results of measurements of the spectral-angular distribution of RTR intensity in comparison with the results of calculation are given in Fig. 5.20.

It should be noted that the experiment corresponds with theory. The resonances with $k = 1, 2, 3$ were observed in experiment. As follows from the theory, with the increase of a resonance order, the RTR photons are emitted at the large angles with

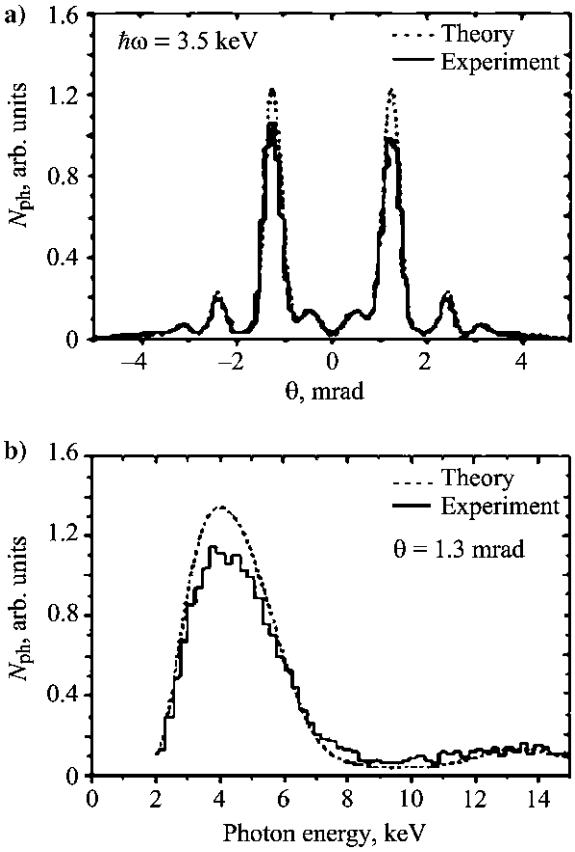

Fig. 5.20 The angular distribution of RTR measured for $\hbar\omega = 3.5$ keV (on the *left*) and spectrum of RTR for radiation angles $\theta_x = 1.3$ mrad; $\theta_y = 0$ (from the experiment [11])

an essential reduction of the intensity. The beam of monochromatic X-ray radiation is usually formed by a collimator with finite aperture θ_c, located coaxially with a direction of the initial electron beam. In order to calculate the RTR spectrum, it is necessary to integrate the expression (5.4.11) over the polar angle in the interval $0 \leq \theta \leq \theta_c$ (the azimuthal integration reduces to the multiplier 2π). The important characteristic of the X-ray radiation beams is the number of photons in the given solid angle, which is calculated basing on RTR spectrum (so-called photon spectrum):

$$\left(\frac{dN}{\hbar\, d\omega}\right)_N = \frac{2\pi}{\hbar\omega}\int_0^{\theta_c} \sin\theta\, d\theta \left(\frac{d^2W}{\hbar\, d\omega\, d\Omega}\right)_{\mathrm{TR}} F_2 F_3. \tag{5.5.3}$$

The photon spectrum of RTR in a case of the axial collimation of radiation is shown on the Fig. 5.21 for an illustration. The calculation results for a target from 16 beryllium foils with thickness 32 μm and the period 100 μm for electrons with

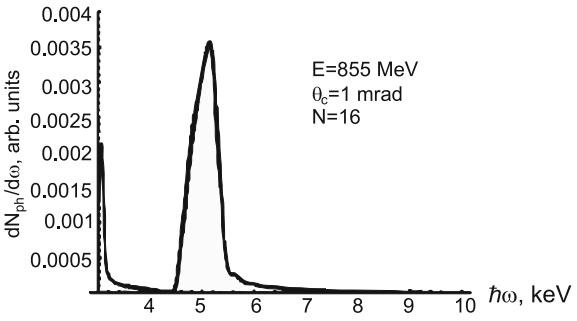

Fig. 5.21 The photon spectrum of RTR for $E = 855$ MeV, 16-layered beryllium target ($\ell_1 = 32$ μm, $\ell_2 = 61$ μm) in case of the axial collimation of radiation ($\theta_c = 1$ mrad)

energy 855 MeV and collimation $\theta_c = 1$ mrad are given here. It may be noted that the quasimonochromatic peak in the photon spectrum is observed for the appropriate choice of target characteristics. As follows from the figure, the peak width in a spectrum is equal to $\Delta\hbar\omega \approx 1$ keV (in other words, the monochromaticity of radiation $\Delta\hbar\omega/\hbar\omega \approx 20\%$). The yield of RTR photons for the given case reaches 0.003 photon/e^-.

The RTR spectrum generated by the electron beam with energy 1 GeV in the layered targets from 1, 4 and 8 layers of mylar with thickness of 50 μm with the vacuum gaps of 200 μm was measured in experiment [12]. The experimental setup is shown in Fig. 5.22.

The RTR beam was collimated by a slit (parallel or perpendicular to the reflection plane) with the adjustable sizes. The radiation spectrum was measured by a crystal-diffractometer. The results of measurements in comparison with measured and calculated dependences are given in Fig. 5.23. It can be noted the satisfactory agreement between the experiment and calculation.

It should be noted that the improvement of RTR monochromaticity can be achieved using the well-known technique of the X-ray radiation monochromatization applied for synchrotron radiation beams.

The scheme of RTR beam monochromatization with a help of monochromator from pyrolytic graphite is shown in Fig. 5.24.

The experimental spectrum measured by a semiconductor spectrometer [13] is shown in Fig. 5.25. In view of the finite resolution of the used spectrometer (~0.3 keV) the real width of an X-ray radiation line is much less than 1 keV.

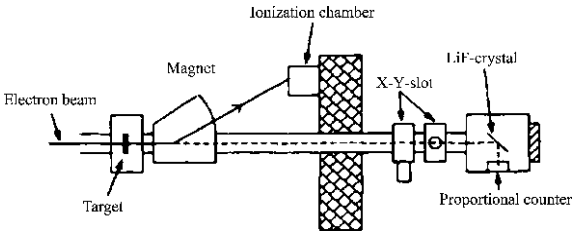

Fig. 5.22 Experimental setup [12]

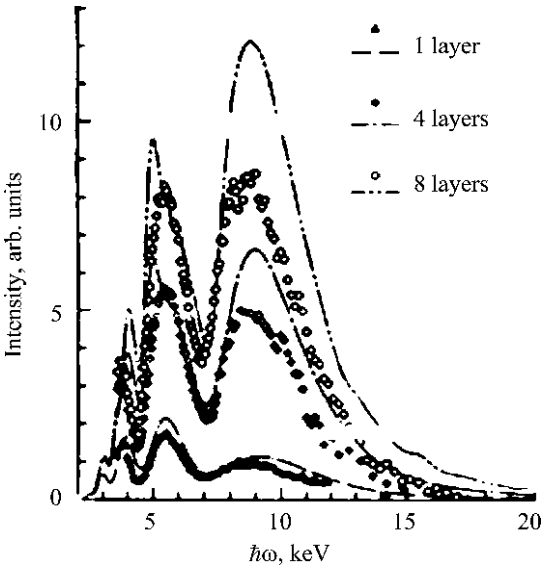

Fig. 5.23 Comparison of measured and calculated RTR spectra of electrons with energy 1 GeV in a target from mylar of 1, 4, 8 layers, with thickness $\ell_1 = 50$ μm and period $d = \ell_1 + \ell_2 = 250$ μm

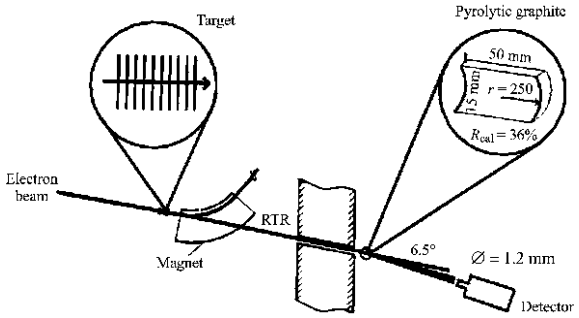

Fig. 5.24 The scheme of experiment for RTR beam monochromatization with a help of a pyrolytic graphite crystal

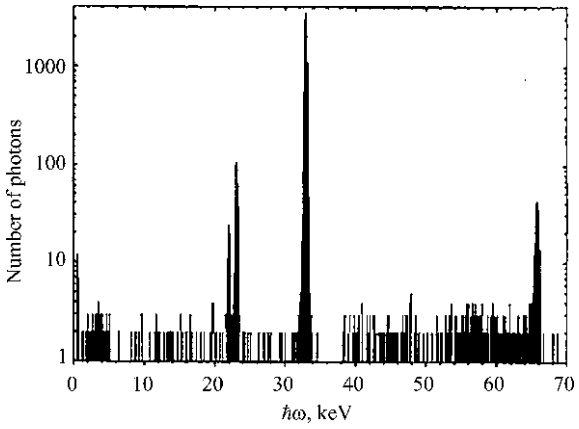

Fig. 5.25 The monochromatized RTR spectrum, which is measured using Ge (Li)-spectrometer with the resolution $\Delta\hbar\omega = 265$ eV. A spectral line $\hbar\omega = 32.9$ keV corresponds with an angle of diffraction 6.5°. Weak lines for $\hbar\omega = 22.0$ and 23.3 keV correspond to the K_α and K_β germanium lines

As it follows from the formulae (5.4.7) and (5.4.14), the position of peaks in RTR spectrum is defined by two conditions, for which factors F_2 and F_3 reach the maximum (neglecting absorption of photons in a target):

$$\varphi_1 = (2m-1)\pi/2, \quad m \text{ is integer}; \quad \varphi_1 + \varphi_2 = 2k\pi, \quad k \text{ is integer}. \tag{5.5.4}$$

To obtain a single peak in the radiation spectrum, under the conditions (5.5.4) it is necessary to choose $m = k = 1$. In other words, the phases in both layers should be equal to $\pi/2$:

$$\varphi_1 = \frac{\ell_1}{Z_1} = \frac{\pi}{2}; \quad \varphi_1 = \frac{\ell_2}{Z_2} = \frac{\pi}{2}. \tag{5.5.5}$$

It is clear that if the second medium is a vacuum, the second ratio can be satisfied for very small gaps ℓ_2, which is hardly feasible.

The periodic heterogeneous target consisting of nickel layers separated by layers of carbon is suggested in the work [14] to use for RTR generation. The thickness of nickel layer was 176 nm, the one of carbon layer was 221 nm, with total number of the periods equal 10. The target was produced by layer deposition level-by-level sputtering. The technology guaranteed a constancy of layer thickness of nickel and carbon with 3% accuracy.

The RTR spectra calculated and measured for the given target, for electron energy $E = 15$ MeV and for various angles of observation are shown in Fig. 5.26. The position of single peak in a radiation spectrum is determined by the observation angle:

$$\theta_k^2 = 2k\frac{\lambda}{d} - \gamma^{-2} - \frac{\ell_1\omega_{p_1}^2 + \ell_2\omega_{p_2}^2}{d\omega^2}. \tag{5.5.6}$$

The results of measurement of RTR spectrum at an angle $\theta = 25.5$ mrad using the 15 MeV electron beam with the divergence less than 6 mrad are given in Fig. 5.27. The background spectrum measured for a target consisting of the nickel foils with thickness 2 μm and a carbon foil of the same thickness is shown in Fig. 5.27. Intensity of the background spectrum in this energy range is caused mainly by bremsstrahlung, the intensity of which is significantly lower than RTR.

The possibility of peak position tuning in a radiation spectrum in case of target rotation for an angle ψ around an axis perpendicular to the electron beam (see the scheme in Fig. 5.28) was investigated in the same experiment. In this case the thickness of layers ℓ_1 and ℓ_2 grows according to the law $\ell_{1(2)}/\cos\psi$, which will result in a shift of the line toward a spectrum soft part at a fixed angle of observation. The calculations results are presented in Fig. 5.29. The experimental results confirm the conclusions of the theory.

So, the process of resonant transition radiation can be used for generation of quasimonochromatic radiation toward the energy range $\omega \sim 10$ keV even using electron beams with energy $E < 20$ MeV.

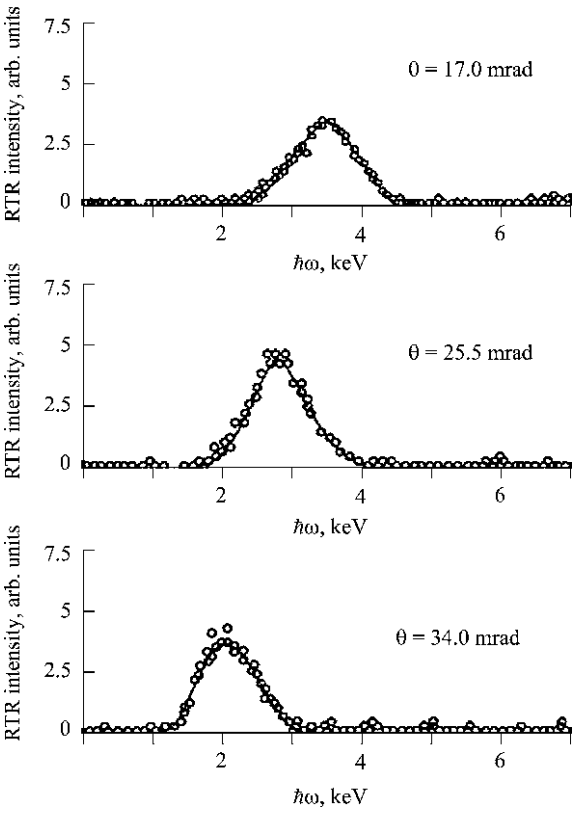

Fig. 5.26 The measured RTR spectra in experiment [14] in comparison with calculated ones

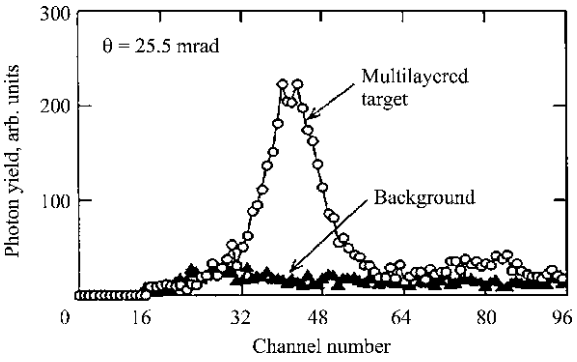

Fig. 5.27 Comparison of experimentally measured RTR spectrum and bremsstrahlung spectrum from a target of the identical thickness

Using the device shown in Fig. 5.22, it is possible to investigate the polarization characteristics of RTR, since the coefficient of reflection of X-ray radiation polarized in a plane perpendicular to the reflection plane, is equal to one ($P_{\perp} = 1$), whereas for the opposite component $P_{||} = \cos^2 2\theta_B$, where θ_B is the Bragg angle of

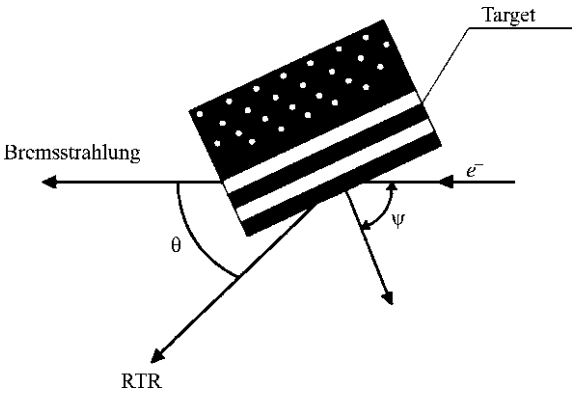

Fig. 5.28 The scheme of RTR generation in a multilayered target rotated at an angle ψ

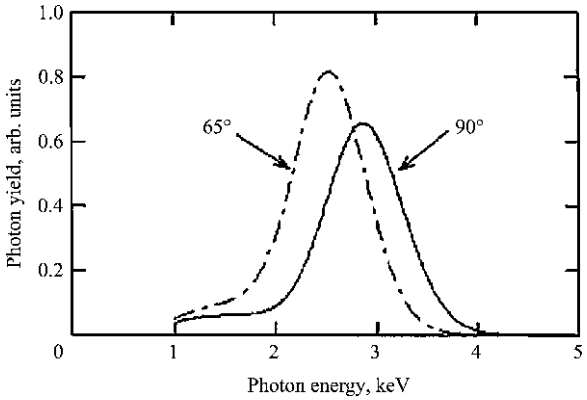

Fig. 5.29 Calculation of RTR-spectra in case of normal flight through a layered target and for rotation of a target at an angle $\frac{\pi}{2} - \psi = 65^\circ$

crystal orientation. Thus, for $\theta_B = 45^\circ$ we have the zeroth former one $P_{\|} = 0$. Consequently, the intensity of reflected component of RTR $W_{\|}$ will be close to zero.

The authors of the experiment [15] investigated RTR polarization characteristics using a LiF-crystal as a polarimeter. The LiF orientation was $\theta_B = 45^\circ$ in respect to the RTR beam axis that corresponds to the energy of the reflected photons 4.3 keV.

The calculated angular distribution of the RTR photon yield for a layered target (8 beryllium targets) with thickness $\ell_1 = 7.5$ μm and vacuum gaps $\ell_2 = 400$ μm for the energy of RTR photons $\hbar\omega = 4.3$ keV is shown in Fig. 5.30.

The lines of level of angular distributions of RTR components polarized in a reflection plane and in a perpendicular plane are presented in Fig. 5.31. Calculations were carried out by the formula (5.4.11):

$$\left(\frac{dW_{||,\perp}}{\hbar\, d\omega\, d\Omega}\right)_N = \frac{dW_{||,\perp}}{\hbar\, d\omega\, d\Omega} F_2 F_3, \tag{5.5.7}$$

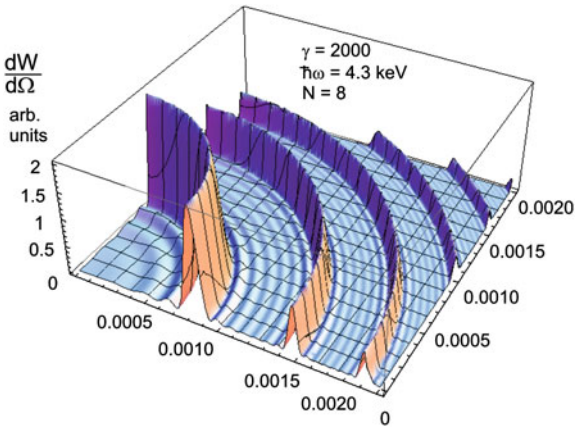

Fig. 5.30 Angular distribution of a RTR yield in a layered target from eight beryllium foils with thickness 7.5 μm and a vacuum gap 400 μm

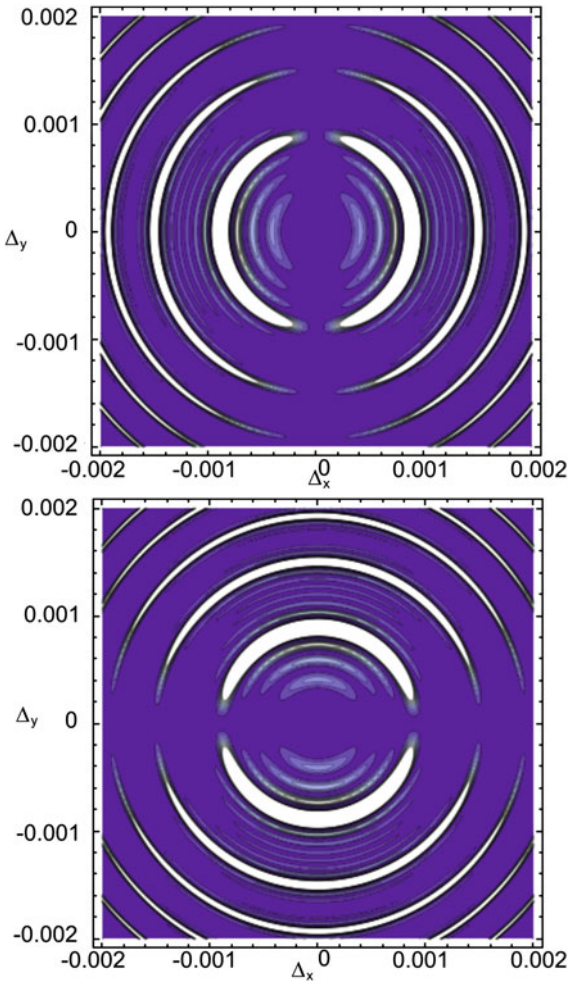

Fig. 5.31 The lines of level of polarized RTR components for angular distribution presented in Fig. 5.30

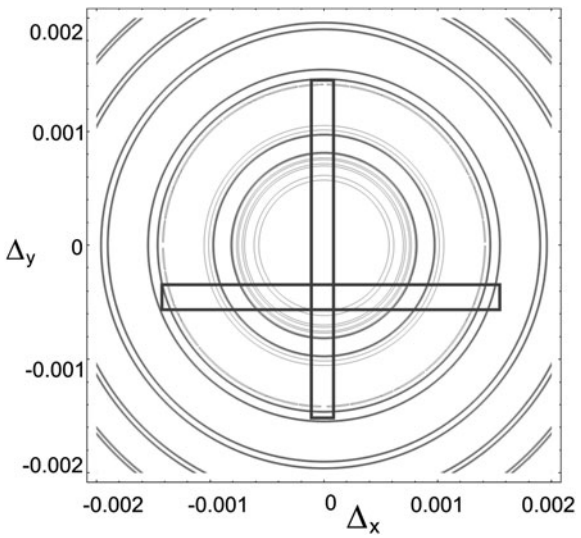

Fig. 5.32 A positioning of the slit collimators relative to RTR cone in the experiment [15]

where

$$\frac{dW_{||,\perp}}{\hbar\, d\omega\, d\Omega} = \frac{\alpha}{\pi^2}\gamma^2\left(\frac{\gamma\hbar\omega_p}{\hbar\omega}\right)^4 \times \frac{\gamma^2\Delta_{x,y}^2}{\left(1+\gamma^2\Delta_x^2+\gamma^2\Delta_y^2\right)^2\left(1+\gamma^2\Delta_x^2+\gamma^2\Delta_y^2+\gamma^2\omega_p^2/\omega^2\right)}.$$

The positioning of the polarimeter slit with angular sizes 3×0.2 mrad is shown in Fig. 5.32. For RTR averaged on a vertical slit the calculated value of the Stokes parameter ξ_3 measured with the help a crystal-diffractometer:

$$\bar{\xi}_3 = \frac{\int d\Delta_x d\Delta_y \left(\frac{dW_{||}}{d\hbar\omega\, d\Omega} - \frac{dW_{\perp}}{d\hbar\omega\, d\Omega}\right)}{\int d\Delta_x d\Delta_y \left(\frac{dW_{||}}{d\hbar\omega\, d\Omega} + \frac{dW_{\perp}}{d\hbar\omega\, d\Omega}\right)} = 0.993. \tag{5.5.8}$$

The experimental value $\bar{\xi}_{3\,\mathrm{exp}} = 0.88$, what corresponds to 94%-contribution of component $\frac{dW_{||}}{d\hbar\omega\, d\Omega}$ into the total intensity. For the horizontal position of the slit the measured value of $dW_{||}$ contribution in the total intensity was equal to 40 % (in other words, $\bar{\xi}_3 = -0.20$), what was explained by the authors of the experiment as displacement of the slit center from the axis of RTR beam (see Fig. 5.32). It can be shown that shift of the slit center on the value of $\Delta_y^0 = 0.45$ mrad leads to the values measured in experiment.

Summarizing the results of the experiment [15], it can be noted that by means of slit collimator, one of sizes of which (for example, Δ_y) corresponds to the

angular capture $\Delta_y \ll \gamma^{-1}$, it is possible to produce the linearly-polarized quasi-monochromatic beam of X-ray radiation with a polarization degree close to 100%.

References

1. Ginzburg, V.L., Frank, I.M.: Sov. Phys. JETP **16**(15), 220 (1946)
2. Ter-Mikaelyan, M.L.: High-Energy Electromagnetic Processes in Condensed Media. Wiley, New York (1972)
3. Pafomov, V.E.: Trudy FIAN. **44**, 28–167 (1969). (In Russian)
4. Ginsburg, V.L., Tsytovich, V.N.: Transition Radiation and Transition Scattering. Adam Hilger, Bristol (1990)
5. Rullhusen, P., Artru, X., Dhez, P.: Novel Radiation Sources using Relativistic Electrons. World Scientific, Singapore (1998)
6. Jodh, G.B.: Transition radiation. In: Saenz, A.W., Uberall, H. (eds.) Coherent Radiation Sources, p. 195. Springer, Berlin (1985)
7. Landau, L.D., Lifshitz, E.M.: Electrodynamics of Continuous Media. Nauka, Moscow (1982). (In Russian)
8. Cherry, M.L., Hartmann, G., Muller, D.: Transition radiation from relativistic electrons in periodic radiators. Phys. Rev. D **10**, 594 (1974)
9. Baier, V.N., Katkov, V.M.: Transition radiation as a source of quasi-monochromatic X-rays. Nucl. Instrum. Methods B **439**, 189 (2000)
10. Vorobiev, S.A., Zabaev, V.N., Kaplin, V.V., et al.: Observation of resonant transition X-radiation excited by 900-MeV electrons in a layered target. JETP Lett. **53**, 332–336 (1991)
11. Backe, H., Gampert, S., Grendel, A., et al.: Resonant transition radiation in the X-ray region from a low emmittance 855 MeV electron beam. Zeitschrift fur Physik A **349**, 87 (1994)
12. Awata, T., Yajima, K., Tanaka, T., et al.: Resonance effects of transition radiation emitted from thin foil stacks using electron beam. Radiat. Phys. chem. **50**, 207 (1997)
13. Backe, H., Brenzinger, K.-H., Buskirk, F., et al.: Transition radiation in the X-ray region from a low emittance 855 MeV electron beam. Am. Inst. Phys.: Conf. Proc. **390**, 57 (1997)
14. Yamada, K., Hosokawa, T., Takenaka, H., et al.: Observation of soft x-rays of single-mode resonant transition radiation from a multilayer target with a submicrometer period. Phys. Rev. A **59**, 3673 (1999)
15. Yajima, K., Awata, T., Ikeda, M., et al.: Generation of linearly polarized transition radiation X-ray beam. Nucl. Instrum. Methods A **460**, 227 (2001)

Chapter 6
Parametric X-ray Radiation

6.1 The Parametric X-ray Radiation Process as a Diffraction of Virtual Photons

As it was noted in the previous chapter, at the incidence of a charged particle from a vacuum on an oblique conducting target the backward TR is generated with frequencies in an optical range and lower close to the direction of a specular reflection. Such a radiation mechanism can be interpreted as a process of the relativistic charge electric field scattering by a surface of the conducting target in a full analogy with a process of electromagnetic wave scattering by a perfect mirror.

Figure 6.1 schematically shows the deformation of the Coulomb field of a rest particle in case of its uniform motion with velocity $\mathbf{v}$ along the axis z. It is clear that for relativistic particles in case of $v \to c$ the electric field will be more and more "flattened" and transverse components of the field are γ times as much than the longitudinal component [1]:

$$\frac{E_z}{E_{x,y}} \sim \gamma^{-1}. \tag{6.1.1}$$

The approximation, which neglect the longitudinal component of the field, corresponds to the transition to an exactly transverse field, i.e. to the electromagnetic wave. In this approximation, the interaction of a moving charge field with electrons of the matter comes to reflection and refraction of the electromagnetic wave packet describing the field of the initial particle.

The parametric X-ray radiation (PXR) in such interpretation is nothing else than the diffraction of X-ray part of the spectrum, describing the field of an ultrarelativistic charge in the crystalline target. In other words, the interaction of a real electron with the crystal is replaced by the interaction of the field of virtual photons with the target.

A. P. Potylitsyn, *Electromagnetic Radiation of Electrons in Periodic Structures*, Springer Tracts in Modern Physics, 243, DOI: 10.1007/978-3-642-19248-7_6,

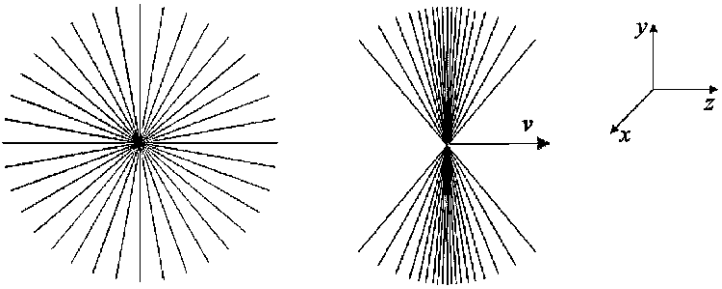

Fig. 6.1 The force lines of the electric field from a charge at rest (on the *left*) and moving with velocity $v = 0.94$ c (on the *right*)

Let's write down the expression for the field of an electron moving with velocity $\mathbf{v} = \boldsymbol{\beta} c$ in a medium with permittivity ε:

$$\mathbf{E}(\mathbf{k}', \omega) = \frac{ie}{2\pi^2}\left(\omega\boldsymbol{\beta} - \frac{\mathbf{k}'}{\varepsilon}\right)\frac{\delta(\omega - c\mathbf{k}'\boldsymbol{\beta})}{k'^2 - \omega^2\varepsilon}, \tag{6.1.2}$$

where $\omega, \mathbf{k}'$ are the energy and momentum of a virtual photon. The argument of δ-function gives the relationship between the momentum and energy of the virtual photon:

$$\omega = c\mathbf{k}'\boldsymbol{\beta}, \tag{6.1.3a}$$

whereas a similar relationship for real photons in a vacuum is given by the known expression:

$$\omega = c|\mathbf{k}|. \tag{6.1.3b}$$

The intensity of real photons reflected from the medium is determined in a usual way [2]:

$$\frac{dW}{d\omega\, d\Omega} = \frac{4\pi^2}{c}\omega^2\left\{|E_\perp R_\perp|^2 + \left|E_\parallel R_\parallel\right|^2\right\}. \tag{6.1.4}$$

In (6.1.4) by means of $R_\perp, R_\parallel$, the Fresnel reflection coefficients are designated, $E_\parallel, E_\perp$ are determined from (6.1.2) for a diffraction plane and for a perpendicular plane. The diffraction plane is perpendicular to the crystallographic plane and passes through the vector $\boldsymbol{\beta}$ (Fig. 6.2).

In the X-ray range the permittivity is usually approximated by the expression (see 5.2.1)

$$\varepsilon = 1 - \chi = 1 - \frac{\omega_p^2}{\omega^2}, \quad |\chi| = \frac{\omega_p^2}{\omega^2} \ll 1. \tag{6.1.5}$$

The diffraction on a set of crystallographic planes with the interplanar distance a is most simply described by terms of reciprocal lattice vectors, each of which is perpendicular to the crystallographic plane:

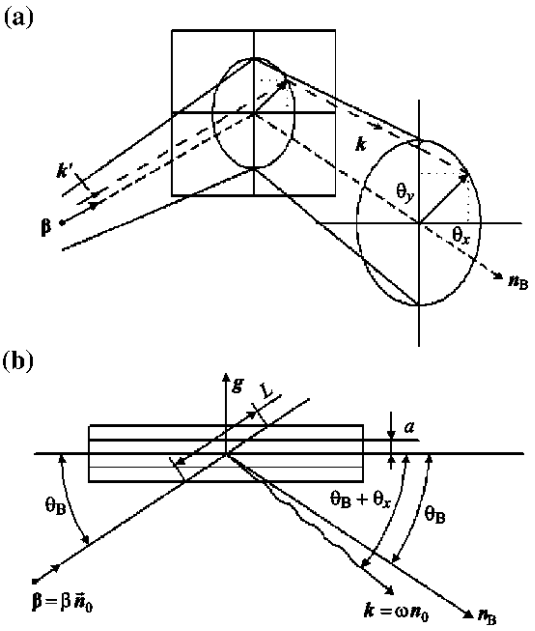

Fig. 6.2 The scheme of virtual photons scattering (**a**); the scheme of PXR process for the Bragg geometry (**b**)

$$|\mathbf{g}_n| = \frac{2\pi\hbar}{a}n, \quad n = 1, 2, 3, \ldots \tag{6.1.6}$$

In (6.1.6) n denotes the order of diffraction. In case of the diffraction in a crystal, as well as in any periodic structure, the function χ in (6.1.5) can be expanded into a Fourier series in reciprocal lattice vectors. The intensity of a diffracted wave on the plane, which is characterized by the vector $\mathbf{g}$, will be determined by this expansion factor of χ_g:

$$\left|\chi_g\right|^2 = |S(\mathbf{g})|^2 \exp(-2W)\left(-\frac{\omega_p^2}{\omega^2}\frac{F(\mathbf{g})}{Z}\right)^2, \tag{6.1.7}$$

where $|S(\mathbf{g})|^2$ is a structure factor; $\exp(-2W)$ is the Debye-Waller factor (see Chap. 4); $F(\mathbf{g})$ is the Fourier-transform of the electron density distribution of the atom with the charge Z. The same characteristic for a screened Coulomb field of nucleus and atomic shells is considered in Chap. 4.

The periodicity of a crystallographic target leads to the occurrence of a resonance factor in the expression (6.1.4)

$$F_N = 2\pi N\delta(\mathbf{k}' - \mathbf{k} - \mathbf{g}), \tag{6.1.8}$$

where $N = L_a/(a/\sin\theta_B)$ is a number of crystallographic planes intersected by a particle on the absorption length L_a (see Fig. 6.2b), θ_B denotes the angle between the electron momentum and the crystallographic plane (so-called the Bragg angle). In (6.1.8) by $\mathbf{k}$ a momentum of the real PXR photon is designated.

The reflection coefficients in (6.1.4) are defined by the scattering geometry and a crystal type [3]:

$$R_{\perp} = \frac{\chi_g}{2}\frac{1}{2\sin^2\theta_{\mathrm{B}}}, \quad R_{\parallel} = \frac{\chi_g}{2}\frac{\cos 2\theta_{\mathrm{B}}}{2\sin^2\theta_{\mathrm{B}}}. \tag{6.1.9}$$

After the substitution of (6.1.7) in (6.1.4) and taking the delta function (6.1.8) into account, the considered model makes it easy to obtain the angular distribution of PXR [4]:

$$\begin{aligned}\frac{dW}{d\Omega} &= \frac{\alpha\hbar}{2\pi^2 c}\frac{\omega_{\mathrm{B}}^2\left|\chi_g\right|^2}{\sin^2\theta_B}\frac{\theta_x^2\cos^2 2\theta_B + \theta_y^2}{\left(\gamma^{-2} + \theta_x^2 + \theta_y^2 + \omega_p^2/\omega^2\right)^2}L_a \\ &= \frac{\alpha\hbar}{2\pi^2 c}\frac{\omega_{\mathrm{B}}^2\left|\chi_g\right|^2}{\sin^2\theta_B}L_a\Lambda\left(\theta_x,\theta_y\right).\end{aligned} \tag{6.1.10}$$

In the last expression ω_{B} is the frequency of PXR photons in the direction of the Bragg reflection $\mathbf{n}_{\mathrm{B}}$ (see Fig. 6.2):

$$\omega_{\mathrm{B}} = \frac{\mathbf{g}\boldsymbol{\beta}c}{1 - \sqrt{\varepsilon}\mathbf{n}_{\mathrm{B}}\mathbf{g}}.$$

The angles θ_x and θ_y in (6.1.10) are defined relative to the Bragg direction in the plane of diffraction and in the perpendicular plane, respectively.

Thus, it is possible to say that in the PXR process the virtual photons with a continuous spectrum, being scattered by the crystallographic lattice, transform into a beam of real quasimonochromatic photons, which are detected by physical devices.

It should be noted that formula (6.1.10) is obtained by the usage of the simplest model. However, as it will be shown in the following paragraphs, the received expression (6.1.10) satisfactorily agrees with the so-called kinematic theory of PXR [5], which is much more exact. The detailed theory of PXR, including so-called the "dynamical effects" can be found in the book [6].

6.2 The Kinematics of the PXR Process

To begin with, let's consider the process of real photons scattering by the crystalline lattice. The relationship between the energy of the scattered photon (which coincides with the energy of the initial photon) and the angle of orientation (the Bragg angle) is found from the conservation laws:

$$\mathbf{k}_0 - \mathbf{k} - \mathbf{g} = 0; \quad |\mathbf{k}_0| = |\mathbf{k}| = \omega. \tag{6.2.1}$$

Hence we receive $\mathbf{k}^2 = \mathbf{k}_0^2 - 2\mathbf{k}_0\mathbf{g} + \mathbf{g}^2$ and, consequently, $\omega = \frac{\mathbf{g}^2}{2\mathbf{n}_0\mathbf{g}}$. Substituting instead of $\mathbf{g}$ its expressions from (6.1.6), we receive the energy of the scattered photon at an angle θ_{B}:

$$\hbar\omega_{\mathrm{B}}^{0} = \hbar c\frac{\pi n}{a\sin\theta_{\mathrm{B}}}. \tag{6.2.2}$$

The kinematics of the PXR process is determined by the argument of δ-function in (6.1.8):

$$\mathbf{k}' - \mathbf{k} - \mathbf{g} = 0. \tag{6.2.3}$$

Hence after multiplying by $\boldsymbol{\beta}$ we find:

$$\boldsymbol{\beta}\mathbf{k}' = \boldsymbol{\beta}\mathbf{k} + \boldsymbol{\beta}\mathbf{g}. \tag{6.2.4}$$

Using (6.1.3a) and (6.1.3b), we have:

$$\hbar\omega = \sqrt{\varepsilon}\,\omega\mathbf{n}\boldsymbol{\beta} + \boldsymbol{\beta}\mathbf{g}. \tag{6.2.5}$$

Here the momentum of a real photon propagating in a medium differs from the momentum of a photon in a vacuum by the factor $\sqrt{\varepsilon}$. From (6.2.5) it follows the so-called dispersion relation for PXR:

$$\hbar\omega = \frac{\mathbf{g}\boldsymbol{\beta}}{1 - \sqrt{\varepsilon}\,\mathbf{n}\boldsymbol{\beta}} = \frac{2\pi}{a}\hbar cn\frac{\beta\sin\theta_{\mathrm{B}}}{1 - \sqrt{\varepsilon}\beta\cos(2\theta_{\mathrm{B}} + \theta_x)}. \tag{6.2.6}$$

In the last expression θ_x corresponds the angle of an outgoing photon (see Fig. 6.2b) with respect to the Bragg direction. In contrast to the diffraction of real photons, in the PXR process the photons can be emitted at angles that differ from the Bragg angle θ_{B}. We calculate the energy shift of the PXR photons emitted at the angle θ_{B} relative to the energy of the scattered real photons (6.2.2). In the ultrarelativistic approximation and taking (6.1.5) into account, from (6.2.6) we obtain

$$R = \frac{\omega(\theta = \theta_{\mathrm{B}})}{\omega_{\mathrm{B}}^{0}} = \left[1 - \frac{\gamma^{-2}}{4}\frac{1}{\sin^2\theta_{\mathrm{B}}} - \frac{\omega_{\mathrm{p}}^{2}}{4\omega_{\mathrm{B}}^{2}}\frac{\cos 2\theta_{\mathrm{B}}}{\sin^2\theta_{\mathrm{B}}}\right]. \tag{6.2.7}$$

Here ω_{B}^{0} is the Bragg frequency in the scattering of real photons.

As it follows from (6.2.7), for particles with the Lorentz-factor $\gamma > 10^2$ for $\theta = \theta_{\mathrm{B}}$ the dispersion relation (6.2.6) coincides with (6.2.2), which is valid for real photons, with an accuracy better than $\sim 10^{-2}$. It is easy to estimate the shift of a PXR line in case of changing the orientation angle θ. In case of a slight difference of θ from the Bragg angle, which is measured relative to the crystallographic plane (see Fig. 6.2b) $\theta = \theta_{\mathrm{B}} - \Delta\theta$, $\Delta\theta \ll \theta_{\mathrm{B}}$, and neglecting the terms of order γ^{-2}, we receive from (6.2.6)

$$\omega = \omega_{\mathrm{B}}(1 - \Delta\theta\cot\theta_{\mathrm{B}}). \tag{6.2.8}$$

From (6.2.8) it follows that the PXR line is shifted in a more hard range in case of decreasing the photon outgoing angle θ. And quite on the contrary, in case of

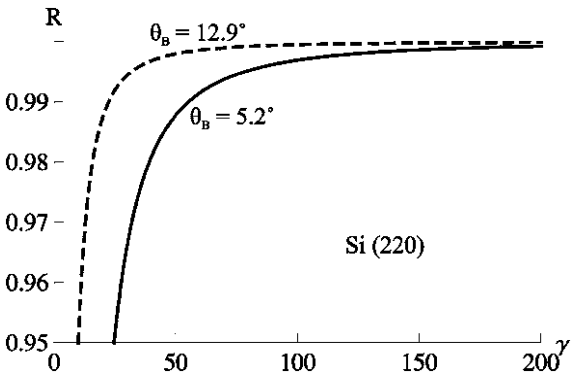

Fig. 6.3 The ratio of the energy of PXR lines in respect to the energy of the Bragg scattered real photons

increasing the angle θ, the energy of the PXR line becomes smaller than the Bragg one (6.2.2).

If we fix the observation angle of PXR, for example, $\theta = \theta_B$ (see Fig. 6.2b), and change a little the orientation of the crystal $\Delta\theta_B \ll \theta_B$, then we can obtain again the formula (6.2.8): $\omega = \omega_B(1 - \Delta\theta_B \cot\theta_B)$.

Figure 6.3 shows the ratio $R = \omega_{PXR}(\theta = \theta_B)/\omega_B^0$ depending on the Lorentz-factor of an electron for two different angles θ_B of the plane (220) of Si. From this figure, one can see the difference between the quantities ω_B^0 and $\omega_{PXR}(\theta = \theta_B)$ which is negligible for ultrarelativistic particles.

6.3 The Angular Distribution of PXR and the Orientation Dependence of the PXR Yield

In the work [5], H. Nitta has developed a model of PXR in the kinematic approximation. The built model is applicable to relatively thin crystals, and allows to calculate not only the spectral-angular distribution of PXR but also its polarization characteristics. Following this work, we write down the angular distribution of PXR photons (without taking into account an absorption in the target material)

$$\frac{dN}{dz\,d\Omega} = \frac{\alpha(\omega/c)\left|\chi_g\right|^2}{2\pi\varepsilon^{3/2}\beta(1-\sqrt{\varepsilon}\boldsymbol{\beta}\mathbf{n})} \times \sum_{\alpha}\left[\frac{(\omega/c\boldsymbol{\beta}-\mathbf{g})\mathbf{e}_\alpha}{(\mathbf{k}_\perp+\mathbf{g}_\perp)^2+\frac{\omega^2}{c^2\beta^2}\left[\gamma^{-2}+\beta^2(1-\varepsilon)\right]}\right]^2. \tag{6.3.1}$$

Here the index $\perp$ denotes the projection of a vector onto the plane, which is perpendicular to the velocity of the initial particle $\mathbf{v} = c\beta\mathbf{n}_0$.

Let's introduce the polarization unit vectors associated with the diffraction plane:

$$\mathbf{e}_1 = \frac{[\mathbf{n}, \mathbf{n}_0]}{|[\mathbf{n}, \mathbf{n}_0]|}, \quad \mathbf{e}_2 = [\mathbf{e}_1, \mathbf{n}]. \tag{6.3.2}$$

Then, keeping the second order terms, we obtain instead of (6.3.1):

$$\begin{aligned}
\frac{dN}{dz\,d\Omega} &= \frac{\alpha\omega_B|\chi_g|^2}{4\pi c\sin^2\theta_B}\frac{\left(\tilde{E}_1^2+\tilde{E}_2^2\right)}{\left(\theta_x^2+\theta_y^2+\gamma^{-2}+\omega_p^2/\omega^2\right)^2},\\
\tilde{E}_1 &= \frac{\theta_y\cos\theta_B}{\sin 2\theta_B\sqrt{1+2\theta_x ctg2\theta_B}}\frac{cg}{\omega},\\
\tilde{E}_2 &= \frac{1}{\sin 2\theta_B\sqrt{1+2\theta_x ctg2\theta_B}}\times\left[\left(1-\frac{1}{2\gamma^2}\right)\sin^2 2\theta_B(1+2\theta_x ctg2\theta_B)\right.\\
&\quad\left.-\frac{cg}{\omega}(\sin 2\theta_B\cos\theta_B+\theta_x\cos 3\theta_B)\right],\\
\frac{cg}{\omega} &= \frac{1-\cos 2\theta_\mathrm{B}+\theta_x\sin 2\theta_\mathrm{B}+\frac{1}{2}\left(\theta_x^2+\theta_y^2\right)\cos 2\theta_\mathrm{B}+\frac{\gamma^{-2}}{2}+\frac{\omega_\mathrm{p}^2}{2\omega^2}\cos 2\theta_\mathrm{B}}{\sin\theta_B}.
\end{aligned} \tag{6.3.3}$$

If keeping in (6.3.3) only the first order terms, one may obtain

$$\tilde{E}_1 \approx \theta_y, \quad \tilde{E}_2 \approx -\theta_x\cos 2\theta_\mathrm{B}. \tag{6.3.4}$$

In this case, for a thin crystal ($L \ll L_a$) in the ultrarelativistic approximation the expression (6.3.3) is reduced to the relatively simple expression:

$$\begin{aligned}
\frac{dN}{d\Omega} &= \frac{\alpha}{4\pi c}\frac{L\omega_\mathrm{B}|\chi_g|^2}{\sin^2\theta_\mathrm{B}}\frac{\theta_x^2\cos^2 2\theta_\mathrm{B}+\theta_y^2}{\left(\theta_x^2+\theta_y^2+\gamma^{-2}+\frac{\omega_\mathrm{p}^2}{\omega^2}\right)^2}\\
&= \frac{\alpha}{4\pi c}\frac{L\omega_\mathrm{B}|\chi_g|^2}{\sin^2\theta_\mathrm{B}}\Lambda(\theta_x,\theta_y).
\end{aligned} \tag{6.3.5}$$

As a rule, the geometry of PXR generation is such one that the path which the emitted photon passes in the target material does not coincide with its thickness L. In order to take such geometry into account, in the form (6.3.5) the following value is often substituted instead of thickness L [7]

$$L_\mathrm{geo} = L_a\frac{|\boldsymbol{\sigma}\boldsymbol{v}|}{|\boldsymbol{\sigma}\boldsymbol{v}_0|}\left[1-\exp\left(-\frac{L}{L_a}|\boldsymbol{\sigma}\boldsymbol{v}|\right)\right]. \tag{6.3.6}$$

Here $\boldsymbol{\sigma}$ denotes a unit vector which is perpendicular to the crystal surface. As it follows from expression (6.3.5), the angular distribution of PXR photons is described by the universal angular distribution $\Lambda(\theta_x, \theta_y)$ [6], which is often written in terms of angular variables $t_x = \gamma\theta_x$, $t_y = \gamma\theta_y$

$$\Lambda(t_x, t_y) = \frac{t_x^2 \cos^2 2\theta_B + t_y^2}{\left[1 + t_x^2 + t_y^2 + \left(\frac{\gamma\omega_p}{\omega_B}\right)^2\right]^2}. \tag{6.3.7}$$

As it follows from (6.3.7), the angular distribution of PXR is defined by a parameter $t_{ph} = \gamma\theta_{ph} = \gamma\sqrt{\gamma^{-2} + \omega_p^2/\omega_B^2}$, which depends on the particle energy, crystal type and orientation angle.

Figure 6.4 shows the typical angular distribution of PXR. It is clear that in case of $t_{ph} \ll 1$ ($\gamma\omega_p \ll \omega_B$, i.e. for moderately relativistic particles) the angular distribution of PXR is determined by the Lorentz-factor ($\Delta t_{x,y} \sim 1, \Delta\theta \sim \gamma^{-1}$), whereas in the ultrarelativistic case ($\gamma\omega_p \gg \omega_B$) the angular distribution will be considerably wider than the angle γ^{-1}($\Delta t \sim t_{ph}, \Delta\theta \sim \frac{\omega_p}{\omega_B} \gg \gamma^{-1}$). Besides, as it follows from the figure, the angular distribution of PXR strongly depends on the angle θ_B.

In the first experiments held at the Tomsk synchrotron (see works [8, 9]), measurements of the PXR angular distributions were carried out by a technique of scanning of PXR reflections by means of collimated X-ray spectrometer, which is moved in two mutually perpendicular directions, and which measured the PXR yield behind the slit collimator.

Figure 6.5 shows the geometry of experiment for the case of incidence of the electron beam at an angle $\theta_B = 45°$ to the diamond crystal plane (100). The registration of photons in this case was carried out at the angle $\theta_D = 2\theta_B = 90°$ to the beam of electrons. The slit collimator installed in front of the detector, which is the proportional counter, had sizes 2.5 × 16 mm, which corresponds to the angular aperture $\Delta\theta_x = \pm 2.5$ mrad and $\Delta\theta_y = \pm 16$ mrad. Moving the counter with a collimator was made along two mutually perpendicular directions *X* and *Y*.

Figure 6.6 shows the angular distributions for reflections (400), (220), (440) of X-rays generated by electrons with an energy $E = 900$ MeV in the diamond single crystal with thickness of 350 μm. The photon energies for these peaks are, respectively, $\hbar\omega_{400} = 9.8$ keV, $\hbar\omega_{220} = 6.9$ keV, $\hbar\omega_{440} = 13.8$ keV. The solid curves show the results of calculations based on the kinematic PXR theory.

Influence of the sizes of the rectangular detector entrance window and its position relative to the center of the PXR cone on the shape of the measured angular distribution of PXR was taken into account by integrating of the expression (6.3.6) over the detector aperture.

As can be seen from Fig. 6.6, there is a good coincidence of the measured angular distributions with the calculations. The full width at half maximum of the angular distribution of the reflection (400) in case of detector scanning along the direction *X* is equal to $\Delta\theta_x = 9 \pm 0.5$ mrad, and for the reflection (220) the similar value is equal to $\Delta\theta_x = 12 \pm 0.5$ mrad, and for the reflection (440) $\Delta\theta_x = 7 \pm 0.5$ mrad. Thus, the increase of PXR photon energy leads to a significant decrease in the width of the PXR angular distribution in correct accordance with the theory. The vertical distribution of such a distribution consists of two

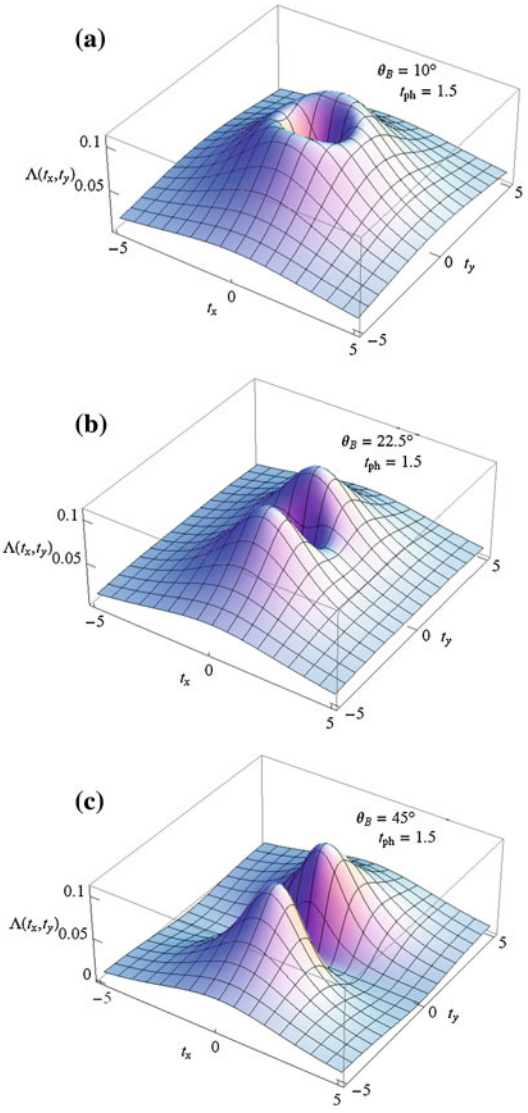

Fig. 6.4 Angular distribution of PXR, which depends on the universal variables t_x, t_y

maxima separated in space (see Fig. 6.4), the angular spread between which also decreases with increasing the photon energy. The calculated curve is slightly narrower than the experimental one, and the depth of the central dip obtained in the experiment is less than the calculated one. Small discrepancies are connected with the influence of the angular divergence of the electron beam due to multiple scattering.

It should be noted that the obtained results are well described by formulae (6.3.6) and (6.3.7) due to the fact that the measurements were performed for

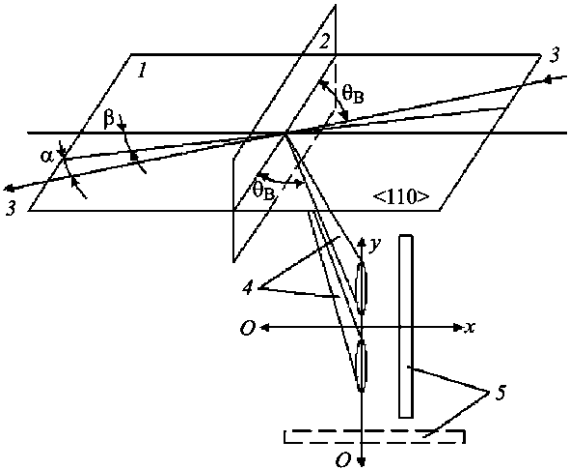

Fig. 6.5 The geometry of the experiment [9]: 1—(001) plane; 2—(110) plane of a diamond; 3—electron beam; 4—PXR reflection; 5—detector with a slit collimator

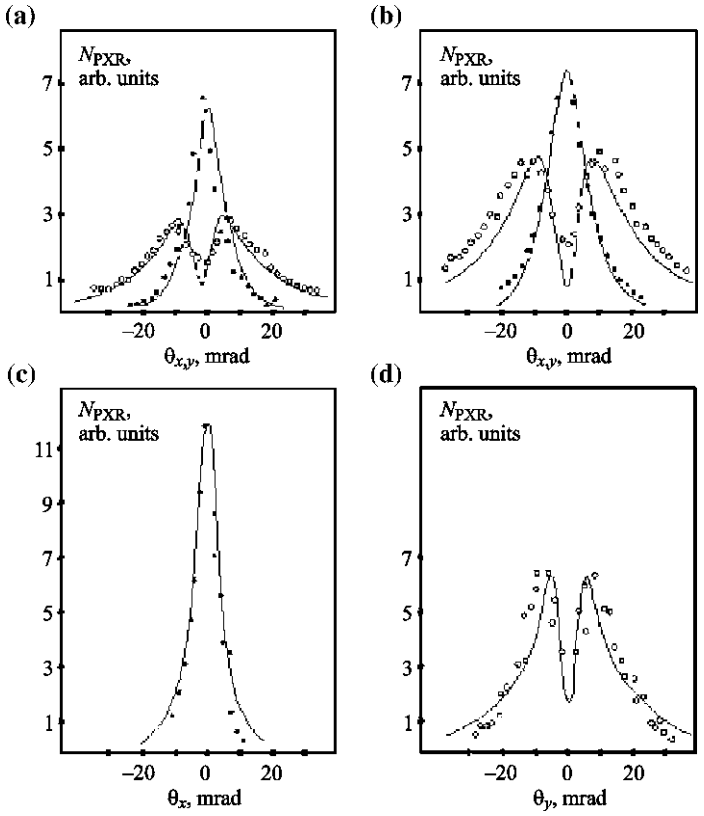

Fig. 6.6 The angular distribution of PXR for a diamond crystal in the horizontal direction (*black dots*) and vertical (*light dots*) for reflections (400) (**a**); (220) (**b**) and (440) (**c**, **d**). The full curves are the results of calculations with taking into account the slit aperture of the detector

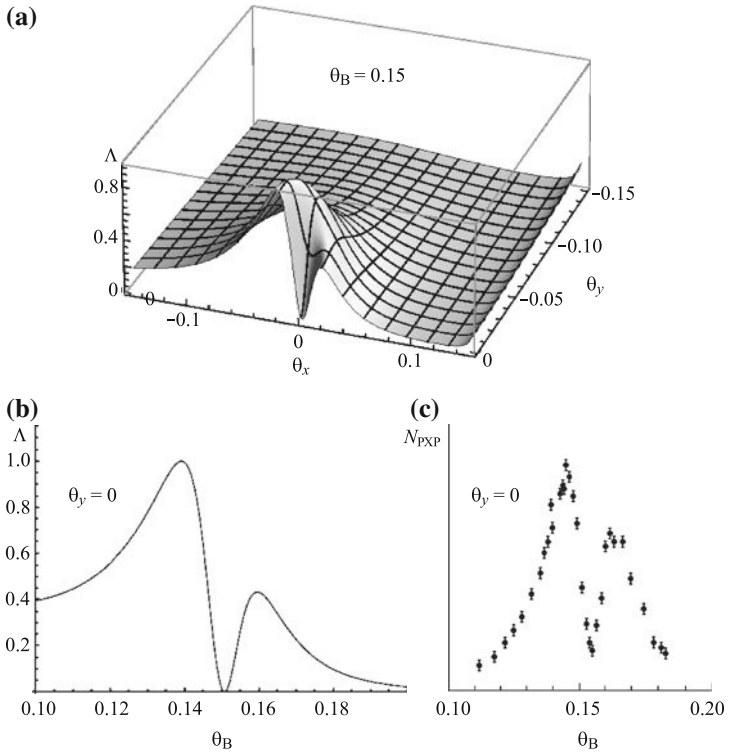

Fig. 6.7 The angular distribution of PXR intensity for $\gamma = 50$ and for the angle of orientation of the plane (220) Si $\theta_B = 150$ mrad (**a**) and orientation dependences of the PXR yield in case of changing the angle θ_B, calculation (**b**); experiment (**c**)

ultrarelativistic Lorentz-factor ($\gamma \sim 1800$). For low energies of the initial electrons from the expression (6.3.3) follows the asymmetric distribution of the angular distribution of PXR in the plane of diffraction (see Fig. 6.7a).

The dependence of yield of the PXR photons generated by an electron beam with energy of 25 MeV in the silicon crystal, in case of changing the orientation angle θ_B at a fixed observation angle (orientation dependence) is measured in the experiment [10]. The orientation dependence on a small angle Δ near θ_B can also be calculated in a first approximation by the formulas (6.3.3) by substituting

$$\theta_B \to \theta_B + \Delta_x, \theta_x \to -2\Delta_x. \tag{6.3.8}$$

In the last expression the angle doubling comes because of the "effect of the light spot", when the angle of the reflected ray is twice the angle of the mirror rotation.

Figure 6.7b, c shows both the calculated orientation dependence of the PXR yield and the measurement results. As follows from the figure, there is a satisfactory agreement of experimental data with the results of calculations based on the kinematic model, despite the fact that, generally speaking, the used target thickness exceeded the criterion of applicability of the model.

6.4 The Spectral Characteristics and Yield of PXR Photons

The first experiment, in which the effect of PXR was found, was carried out at the Tomsk synchrotron using a beam of electrons with energy $E = 900$ MeV in 1985 [8]. The experimental arrangement is shown in Fig. 6.8, and the measured radiation spectrum—in Fig. 6.9. A natural diamond with the thickness of 0.35 mm was used as a target, which was oriented at the Bragg angle $\theta_B = 45°$.

To measure spectra of PXR a xenon proportional counter with an aperture $\Delta\theta = 6$ mrad was used. In case of the diffraction of virtual photons on the (110) planes with interplanar distance d = 2.52 Å, from the formula (6.2.6) for $\theta = \theta_B$ the PXR line width is found:

$$\frac{\Delta\omega}{\omega_B} = \frac{\omega - \omega_B}{\omega_B} = \Delta\theta = 0.006. \tag{6.4.1}$$

The line width in this experiment (Fig. 6.9) significantly exceeds the value (6.4.1), since it is determined by the energy resolution of the used detector (~10%). The yield of PXR photons measured for the electron energy 900 MeV for (220) reflexes of diamond with the thickness 0.35 mm (Fig. 6.9), is given in Table 6.1.

The shift of PXR line depending on the change of orientation angle θ_B, as well as in case of changing the observation angle θ_D was investigated in the experiment [11]. The experiment used a silicon crystal, the plane (110) of which was oriented at an angle $\theta_B = 9°15' = 162$ mrad relative to the electron beam with the energy of 900 MeV.

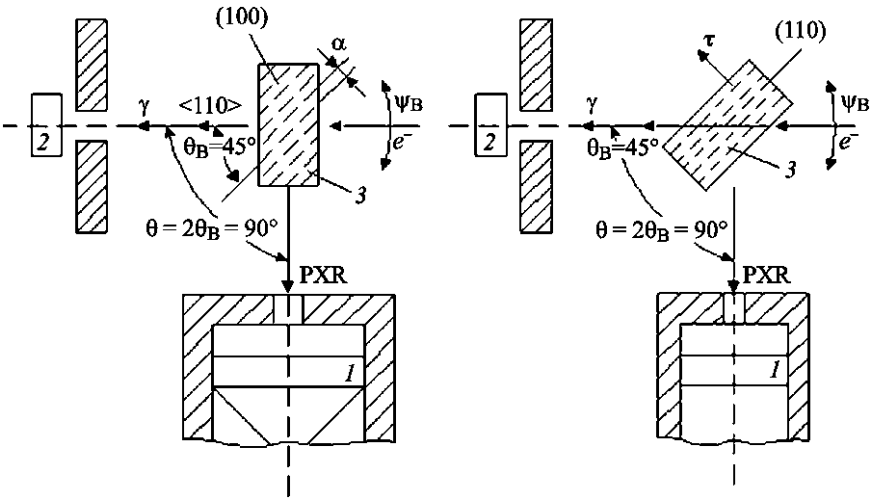

Fig. 6.8 The experimental setup for the PXR registration: 1—detector; 2—orientation system; 3—diamond crystal; orientation for the registration of PXR reflexes: (400), (800)—on the *left*, (220), (440), (660)—on the *right*

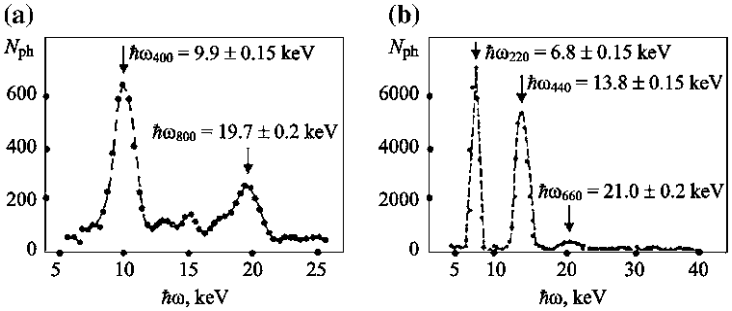

Fig. 6.9 The registered PXR spectra

Table 6.1 The characteristics of PXR for a diamond target and electron energy $E = 900$ MeV

Plane	Energy of photons $\hbar\omega$, keV	Yield of photons ΔN ph. /e$^-$
(220)	6.9	$(1.0 \pm 0.4) \times 10^{-6}$
(440)	13.8	$(5.4 \pm 1.0) \times 10^{-8}$
(660)	20.7	$(8.5 \pm 2.0) \times 10^{-9}$

Figure 6.10 shows the shift of the PXR line, which corresponds to a reflex (220), in case of changing of θ_B for a fixed position of the detector at $\theta_D = 18.5° = 324$ mrad.

The dependence of the line position on the angle θ_B agrees well with the linear dependence (6.2.8). Figure 6.11a shows a similar characteristic measured for different angles of observation θ_D in case of the fixed orientation $\theta_B = 9°15'$. As in the previous case, the line shift in the spectrum is observed, which is in reasonable agreement with the model.

Using the PXR line shift depending on the angle of the crystal rotation (Fig. 6.11b) it is possible to carry out a precision measurement of PXR line width

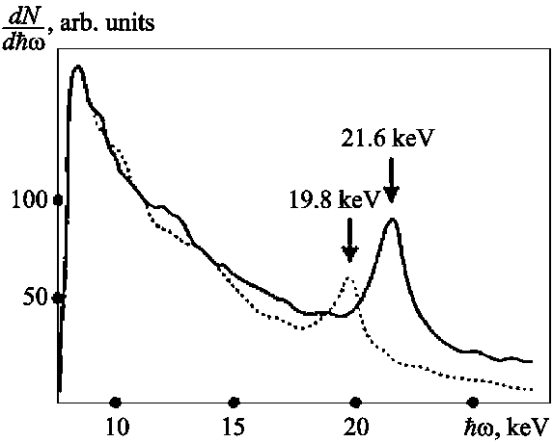

Fig. 6.10 The spectra measured at $2\theta_B = 312$ mrad (the *curve*) and $2\theta_B = 324$ mrad (the *points*)

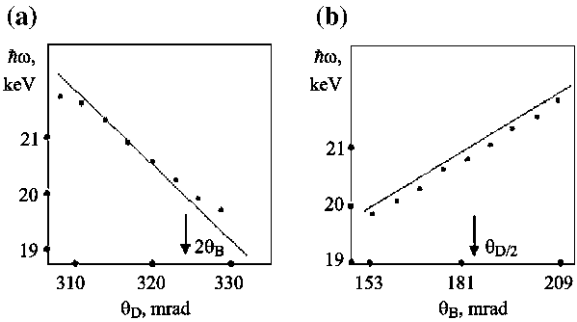

Fig. 6.11 Dependence of the PXR line energy both on the observation angle θ_D in case of $\theta_B = \text{const}$ (**a**) and on the angle of orientation θ_B (**b**). The solid curve is the theoretical model

with accuracy much better than the energy resolution of the spectrometer. The PXR line while changing its position in the spectrum can cross the edge of photoabsorption of the crystalline target material [12]. In this case, the yield of PXR photons is determined by the level of PXR line "cutoff" by the edge of photoabsorption (see Fig. 6.12).

Thus, by measuring experimentally the dependence of the number of PXR photons at a given solid angle N_{PXR} on the angle of the target orientation, it is possible to investigate the shape of line $f(\hbar\omega)$:

$$f(\hbar\omega) = \frac{\partial N_{PXR}}{\partial(\hbar\omega)} = \text{const}\frac{\partial N_{PXR}}{\partial\Delta\theta_B}. \tag{6.4.2}$$

The crystalline (111) germanium target, for which the energy corresponding to the *K*-edge, was equal to 11.16 keV, was used in the experiment [13]. For the plane

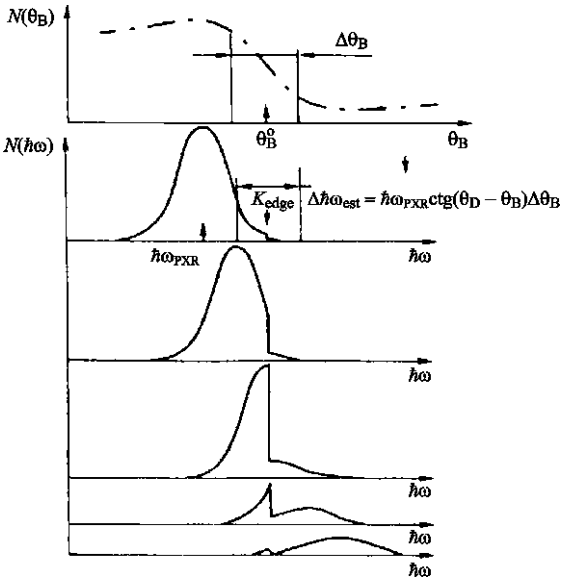

Fig. 6.12 History of a shape of the spectral PXR line in case of changing the orientation angle θ_B

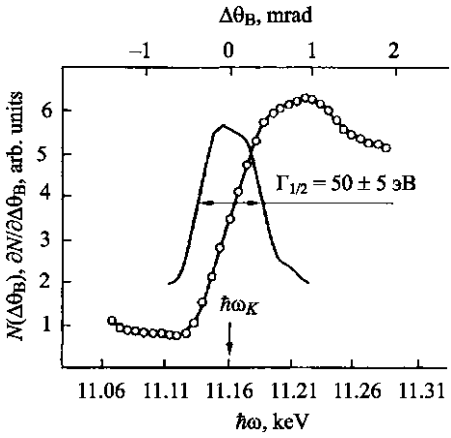

Fig. 6.13 Orientation dependence of the PXR photon yield (*the circles*) and the resulting shape of the spectral line

(111) and $\theta_B = 8°45'$ the PXR line energy coincides with the absorption K-edge. Figure 6.13 shows the orientation dependence of the PXR photon yield on the disorientation angle $\Delta\theta_B$. As can be seen from the figure, the PXR line width at half maximum $\Delta\hbar\omega_{exp} = 50 \pm 5$ eV, which agrees well with the calculated value $\Delta\hbar\omega_{theor} = 65$ eV for the aperture of the forming collimator $\Delta\theta_x \times \Delta\theta_y = 0.9 \times 7.3$ mrad.

6.5 Influence of the Beam Divergence and the Crystal Mosaicity on the PXR Characteristics Features

Let us assume the beam angular distribution is described by the function $F_e(\Delta_x, \Delta_y)$ relative to an average direction of the beam, for which the normalization condition is fulfilled

$$\int d\Delta_x \, d\Delta_y \, F_e(\Delta_x, \Delta_y) = 1. \tag{6.5.1}$$

If the angular distribution of electrons is "narrow" enough in comparison with the angular distribution of PXR,

$$\langle \Delta_{x,y} \rangle \leq \theta_{ph} = \sqrt{\gamma^{-2} + \frac{\omega_p^2}{\omega^2}}, \tag{6.5.2}$$

then a shape of the angular distribution of PXR reflex can be calculated from the convolution:

$$\Lambda_e(\theta_x, \theta_y) = \int d\Delta_x \, d\Delta_y \, F_e(\Delta_x, \Delta_y) \Lambda(\theta_x - \Delta_x, \theta_y + \Delta_y). \tag{6.5.3}$$

The simplest model describing the beam divergence is given by the uniform azimuthally symmetrical distribution

$$F_e(\Delta_x, \Delta_y) = \begin{cases} \frac{1}{\pi\sigma^2}, & 0 \le \sqrt{\Delta_x^2 + \Delta_y^2} \le \sigma \\ 0, & \sqrt{\Delta_x^2 + \Delta_y^2} > \sigma \end{cases} \tag{6.5.4}$$

In this case the convolution (6.5.3) is calculated analytically [14]:

$$\begin{aligned} \Lambda_e(\theta_x, \theta_y) = \frac{1}{4\sigma^2} \Bigg\{ & 2\frac{\theta_x^2 \cos^2 2\theta_B + \theta_y^2}{\theta_x^2 + \theta_y^2} \left[\frac{\theta_x^2 + \theta_y^2 + \theta_{ph}^2 - \sigma^2}{\sqrt{D}} - 1 \right] \\ & - \left(\theta_x^2 - \theta_y^2\right) \sin^2 2\theta_B \frac{\theta_x^2 + \theta_y^2 + \theta_{ph}^2 + \sigma - \sqrt{D}}{\left(\theta_x^2 + \theta_y^2\right)^2} \\ & + 2\left(1 + \cos^2 2\theta_B\right) \ln \frac{\theta_{ph}^2 - \theta_x^2 - \theta_y^2 + \sigma^2 - \sqrt{D}}{2\theta_{ph}^2} \Bigg\}, \\ D = & \left(\theta_x^2 + \theta_y^2\right)^2 + 2\sigma^2 \left(\theta_{ph}^2 - \theta_x^2 - \theta_y^2\right) + \sigma^4. \end{aligned} \tag{6.5.5}$$

For a small beam divergence $\left(\sigma^2 \ll \theta_{ph}^2\right)$ we can obtain the following expansion (keeping the terms not higher than σ^2/θ_{ph}^2) from (6.5.5):

$$\begin{aligned} \Lambda_e\left(\theta_x, \theta_y\right) \approx & \frac{\theta_x^2 \cos^2 2\theta_B + \theta_y^2}{\left(\theta_x^2 + \theta_y^2 + \theta_{ph}^2\right)^2} + \frac{\sigma^2}{\left(\theta_x^2 + \theta_y^2 + \theta_{ph}^2\right)^2} \\ & \times \left[\frac{1 + \cos^2 2\theta_B}{4} - \frac{3\theta_{ph}^2 \left(\theta_x^2 \cos^2 2\theta_B + \theta_y^2\right)}{\left(\theta_x^2 + \theta_y^2 + \theta_{ph}^2\right)^2} \right], \end{aligned} \tag{6.5.6}$$

when $\sigma^2 \to 0$, the last expression coincides with the ideal case (6.3.7).

Figure 6.14a shows the 3D distribution (6.5.5) for $\sigma = 0.5\theta_{ph}$. As expected, the zero maximum for $\theta_x = \theta_y = 0$ becomes smoothed, and moreover with increasing the beam divergence σ this minimum can disappear at all.

The expression (6.5.5) allows us to evaluate "semi-quantitatively" the effect of multiple scattering of the beam in a target and calculate the shape of the PXR angular distribution, if instead of parameter σ we use the root-mean-square angle of multiple scattering (4.1.24), which is calculated for the half-thickness of a crystal.

Similarly, it is possible to take into account the effect of the mosaicity of a crystal. If the normalized distribution of mosaicity $F_m(\alpha_x, \alpha_y)$, which, generally

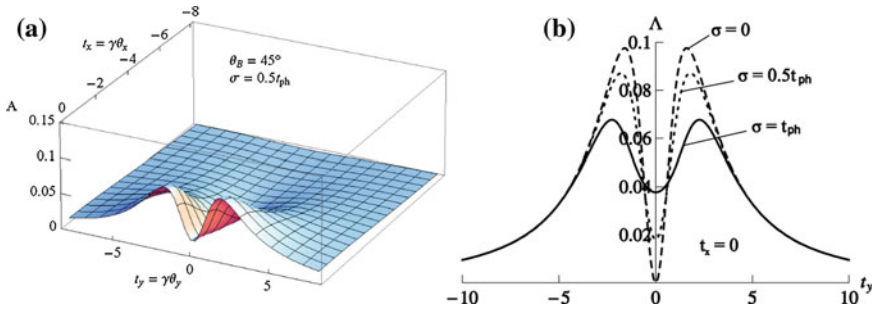

Fig. 6.14 The influence of the electron beam divergence on the angular distribution of PXR: for the same conditions as in Fig. 6.4 (**a**); the angular distribution of PXR for $\sigma = \theta_{\mathrm{ph}}$ (the *solid curve*) and $\sigma = 0.5\theta_{\mathrm{ph}}$ (*dots*) (**b**)

speaking, can be measured by the broadening of the "rocking curve", is determined relative to the maximum of the rocking curve, then for the crystals with a low mosaicity $\langle \alpha_{x,y} \rangle \leq \theta_{\mathrm{ph}}$ the resulting angular distribution of PXR is obtained from the following convolution:

$$\Lambda_{\mathrm{M}}(\theta_x, \theta_y) = \int d\alpha_x \, d\alpha_y \, F_{\mathrm{M}}(\alpha_x, \alpha_y) \Lambda(\theta_x - 2\alpha_x, \theta_y + 2\alpha_y \sin\theta_{\mathrm{B}}). \qquad (6.5.7)$$

Comparing (6.5.3) and (6.5.7), we can conclude that the mosaicity "broadens" the PXR reflex in a diffraction plane twice as much as than the beam divergence.

It is well known that X-ray scattering can occur not only in the perfect crystals possessing a periodicity in all the three axes, but also in one-dimensional crystalline structures, such as pyrolytic graphite with a periodicity $a = 3.4$Å along only one axis. Considering the PXR process as a diffraction of virtual photons on the crystallographic planes, we should expect that for a pyrolytic graphite target the line spectrum of PXR will also be observed. The spectral distribution of PXR from the pyrolytic graphite having thickness 1.5 mm and mosaicity 3.4 mrad was investigated in experiments [15, 16] using 900 MeV electrons. PXR at an angle $\theta_{\mathrm{D}} \approx 18°$ ($\theta_{\mathrm{B}} \approx 9°$) was registered by the semiconductor detector. For the chosen geometry the PXR photon energy, which corresponds to the (200) plane, was equal to $\hbar\omega_{200} = 11.2$ keV.

Figure 6.15 shows the measured PXR spectrum, where the first five diffraction orders are observed clearly.

As is well known, the pyrolytic graphite possesses a high reflectivity for X-rays in the energy range up to ~ 100 keV. With the decreasing of the Bragg angle the PXR lines should be shifted to a harder range. It is interesting to clarify the mechanism of PXR generation in quite a hard range of photon energies. This situation was investigated in experiment [16], where the PXR spectrum was measured at the Bragg angle $\theta_{\mathrm{B}} = 1°58' = 34$ mrad for the same crystal of

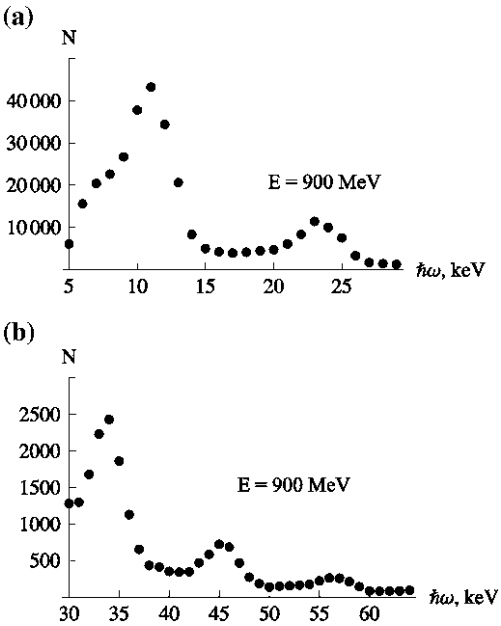

Fig. 6.15 The PXR spectrum generated in the crystal of pyrolytic graphite for orientation $\theta_B \approx 9°$

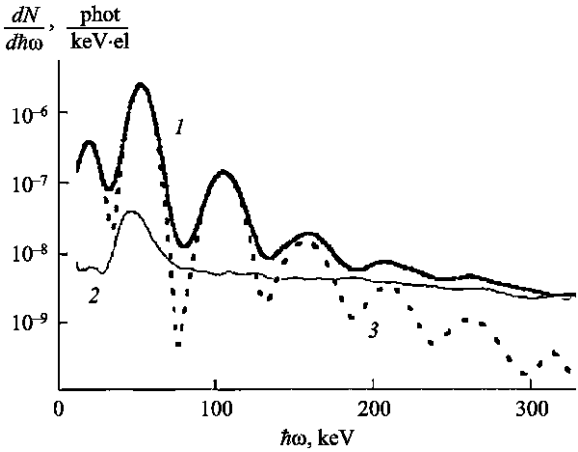

Fig. 6.16 The PXR spectrum for the graphite target orientation $\theta_B = 1°58'$. *Curve* 1 presents the experimental spectrum; *curve* 2—the background; *curve* 3—approximation of the spectrum after the subtraction of the background

pyrolytic graphite. As follows from the measurement results (see Fig. 6.16), the 5 diffraction orders are observed in this case as well, although for the (1000) reflex the energy of PXR photons achieves the value: $\hbar\omega_{(1000)} = 5\hbar\omega_{(200)} \approx 270$ keV.

It is also worth noting a high spectral-angular brightness of PXR, which is generated in the mosaic pyrolytic graphite by electrons with energy 900 MeV, in comparison with PXR in nearly perfect crystals (see Table 6.2).

In conclusion, it should be noted that for small angles of orientation θ_B, where the relation $\gamma\hbar\omega_p \leq \hbar\omega_{PXR}$ is fulfilled, alongside with the PXR generation may occur a diffraction of real photons of bremsstrahlung with an energy

Table 6.2 Yield of PXR photon from pyrolytic graphite

Plane	θ_B	$\hbar\omega_B$, keV	$\Delta N_{PXR}/e^-$, phot/sterad
(200)	$\sim 9°$	11.2	0.45
(200)	$\sim 2°$	55	4.4

$\gamma\omega_{BS} \sim \hbar\omega_{PXR} \geq \gamma\hbar\omega_p$, which are generated in a crystalline target. This leads to the appreciable increasing of the yield of monochromatic photons near the Bragg direction [16].

6.6 The Linear Polarization of Parametric X-ray Radiation

Considering the mechanism of PXR generation as a diffraction of Coulomb field of electrons on the crystallographic planes of a target, we should expect that the PXR photons, corresponding to the Bragg reflex as a whole (i.e. after integration over a cone of angles close to the Bragg direction) will have a linear polarization

$$P \approx \frac{\sin^2 2\theta_B}{2 - \sin^2 2\theta_B}, \tag{6.6.1}$$

in a plane being perpendicular to the diffraction plane.

If we consider PXR photons emitted at a fixed angle close to the Bragg direction, the polarization degree will be close to 100%. For the energy range of PXR photons, which is located outside of the anomalous dispersion region (far from the photoabsorption edges), the components of the PXR field $E_1 = \mathbf{e}_1\mathbf{E}, E_2 = \mathbf{e}_2\mathbf{E}$ will be real (see formulas 6.3.3) and, consequently, the polarization of PXR photons will be linear.

The first experimental investigation of PXR polarization was carried out in work [17], where the (220) reflex on a silicon crystal, which was oriented at an angle $\theta_B = 9°$ concerning to the beam with an energy of 900 MeV, was studied. The analyzed beam of PXR photons is formed by the collimator with aperture $\theta_c = 1$ mrad. The Compton polarimeter was used to measure the degree of linear polarization, in which the photons are scattered at an angle $\sim 90°$, which provides a high analyzing power R in this energy range ($\hbar\omega \sim 20$ keV) $R \approx 0.96$. Scattered photons were detected by two NaI detectors placed at azimuthal angle $\Delta\varphi = 90°$ relative to each other. During the displacement of a collimator (together with the polarimeter) relative to the Bragg direction, in the experiment [17] the Stokes parameter ξ_3 was measured for a given direction of outgoing PXR photons (Fig. 6.17).

The positions of the forming collimator are indicated in Figs. 6.17 and 6.18 by Roman numerals I, II, III. Position I corresponds to the Bragg direction, positions

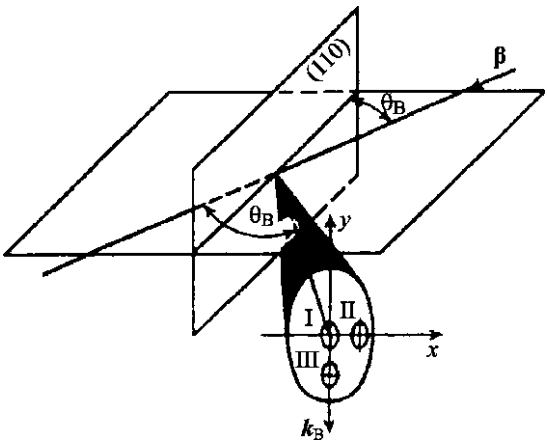

Fig. 6.17 The geometry of an experiment aimed at the investigation of the linear polarization of PXR [17]

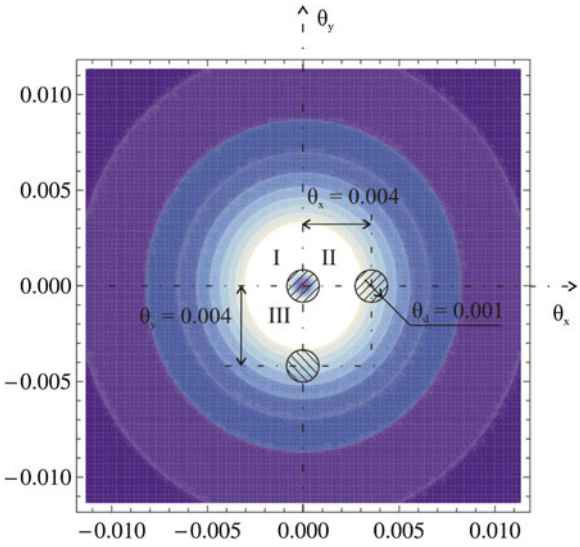

Fig. 6.18 The positions of forming collimators relative to the Bragg direction ($\theta_x = \theta_y = 0$) of the (220) reflex

II, III correspond the polar angle 4 mrad and are shifted at the azimuth angle $\varphi = \pi/2$ (see Fig. 6.18).

The Stokes parameter ξ_3 relative to the plane $(\boldsymbol{\beta}\mathbf{k}_B)$ in the ultrarelativistic approximation is calculated as follows:

$$\langle \xi_3 \rangle = \frac{\Delta N_{\parallel} - \Delta N_{\perp}}{\Delta N_{\parallel} + \Delta N_{\perp}}, \tag{6.6.2}$$

where (see formulas 6.3.3, 6.3.4):

$$\begin{aligned}\Delta N_{\parallel} &= \frac{\alpha\omega_{\mathrm{B}}\left|\chi_g\right|^2}{4\pi c\sin^2\theta_{\mathrm{B}}}\int\limits_{\Delta\Omega} d\Omega\frac{\tilde{E}_2^2}{\left(\theta_x^2+\theta_y^2+\gamma^{-2}+\omega_{\mathrm{p}}^2/\omega^2\right)^2}\\ &\approx \mathrm{const}\int\frac{\theta_x^2\cos^2 2\theta_{\mathrm{B}}}{\left(\theta_x^2+\theta_y^2+\gamma^{-2}+\omega_{\mathrm{p}}^2/\omega^2\right)^2}d\Omega,\\ \Delta N_{\perp} &= \frac{\alpha\omega_{\mathrm{B}}\left|\chi_g\right|^2}{4\pi c\sin^2\theta_{\mathrm{B}}}\int\limits_{\Delta\Omega} d\Omega\frac{\tilde{E}_1^2}{\left(\theta_x^2+\theta_y^2+\gamma^{-2}+\omega_{\mathrm{p}}^2/\omega^2\right)^2}\\ &\approx \mathrm{const}\int\frac{\theta_y^2}{\left(\theta_x^2+\theta_y^2+\gamma^{-2}+\omega_{\mathrm{p}}^2/\omega^2\right)^2}d\Omega.\end{aligned} \tag{6.6.3}$$

The integration in (6.6.3) is carried out over the aperture of the forming collimator.

Table 6.3 shows the results of measurement of parameters ξ_3 in comparison with calculated values.

As follows from the table, there is an agreement observed between the experimental and calculated data in general, since the calculation was performed for the perfect conditions (neglecting the divergence of the electron beam as well as multiple scattering, etc.). The polarization in the center of reflex (along the Bragg direction), as expected, takes rather small values due to averaging over the solid angle.

It should be noted that the tilt angle of the polarization plane is determined from (6.3.3) and (6.3.4):

$$\tan\varphi = \frac{\tilde{E}_1}{\tilde{E}_2} \approx -\frac{\theta_y}{\theta_x\cos 2\theta_{\mathrm{B}}}. \tag{6.6.4}$$

In contrast to the polarization plane slope of X-ray transition radiation, which is described by the expression

$$\tan\varphi_{\mathrm{TR}} \approx \frac{\theta_y}{\theta_x} \tag{6.6.5}$$

the behavior of the slope angle of the linear polarization plane of PXR in the front hemisphere, where $\cos 2\theta_{\mathrm{B}} > 0$ has so-called "hyperbolic" nature. A detailed study of polarization characteristics of PXR was carried out in experiment [18] using the beam of electrons with energy $E = 80.5$ MeV and the silicon crystal (220), which was oriented at an angle $\theta_{\mathrm{B}} \approx 10^\circ$.

Figure 6.19 shows the calculated values of the polarization plane slope angle for the reflex (220) for various orientation angles. As can be seen from the figure for $2\theta_{\mathrm{B}} < 90^\circ$, the behavior of the polarization is hyperbolic. In this case all the PXR photons are polarized in the plane, which is perpendicular to the plane of

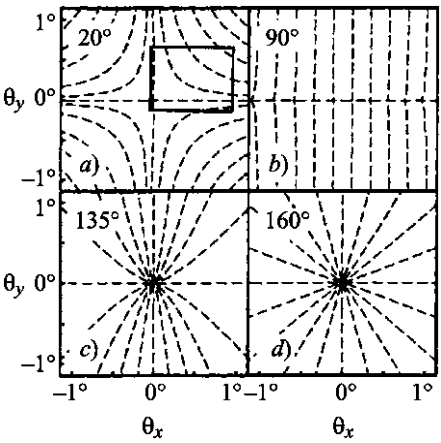

Fig. 6.19 The scheme of the PXR linear polarization plane slope for various angles of observation $2\theta_B$

Table 6.3 Polarization characteristics of PXR

Reflex region	Angular coordinates of the collimator center, mrad		$\xi_{3\ exp}$	$\xi_{3\ theor}$
	θ_x	θ_y		
I	0	0	-0.14 ± 0.06	-0.04
II	4.0	0	0.80 ± 0.08	0.95
III	0	-4.0	$-(0.83 \pm 0.05)$	-0.96

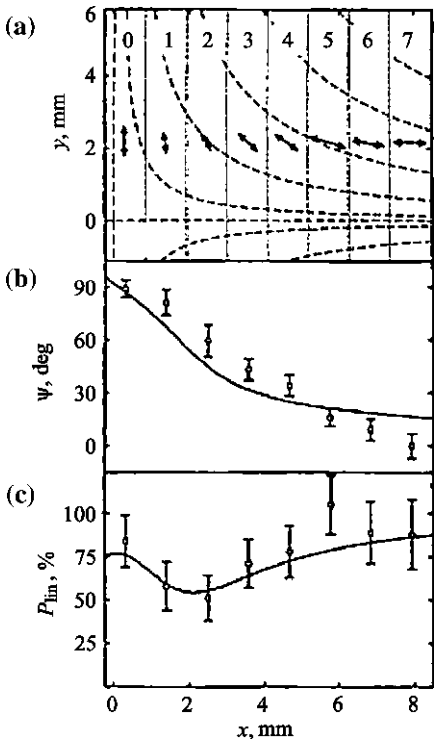

Fig. 6.20 The results of measurements of polarization characteristics of PXR: the layout of the strip polarimeter (**a**); the slope angle of the polarization plane (**b**) and the degree of polarization (**c**)

diffraction ($<\xi_3> \approx -1$), whereas for $2\theta_B > 90°$ the distribution comes nearer to the radial one in the process of increasing angle $2\theta_B$.

In the top left picture the rectangle marks the angular region where the polarization in 8 points on the coordinate θ_x during averaged over the angle θ_y was investigated. The measurement results are shown in Fig. 6.20.

So, using the "off-axis" PXR beam collimation, it is possible to receive a source of monochromatic X-ray radiation with high degree of a linear polarization and with specified slope angle of the polarization plane. In contrast to X-ray diffraction, where the Bragg angle uniquely determines the energy of scattered photons and their polarization, in case of PXR such a strong correlation is absent. Choosing the certain area of the reflex in case of small θ_B, we can obtain the hard X-rays radiation with a high degree of linear polarization, which is impossible for X-ray diffraction (see Eq. (6.6.1)).

6.7 PXR in a Layered Crystalline Target

In the previous chapter it was shown that a choice of parameters of a layered target for a specified Lorentz-factor of a particle allows receiving a peak in the emission spectrum of X-ray transition radiation in the required range of energies. If we consider a layered target, which consists of a set of periodic crystalline targets with parallel orientation of the crystallographic axes but not amorphous foils (see Fig. 6.21), then a transition radiation generated at the exit from the previous layer, will diffract on the subsequent crystalline target. Moreover, the characteristics of real scattered photons (the angle and energy) will be close to the characteristics of PXR photons, which are generated in a crystal target directly (see Sect. 6.2).

In article [19] where both specified processes (as well as the interference between them) were considered in a perfectly oriented target consisting of N crystalline layers with thickness ℓ_1, it was shown that in case of the detection of resulting radiation in the angle cone $\theta_c \leq \gamma^{-1}$ the yield of the diffracted transition radiation is proportional to N^2, whereas the yield of PXR photons is proportional to N.

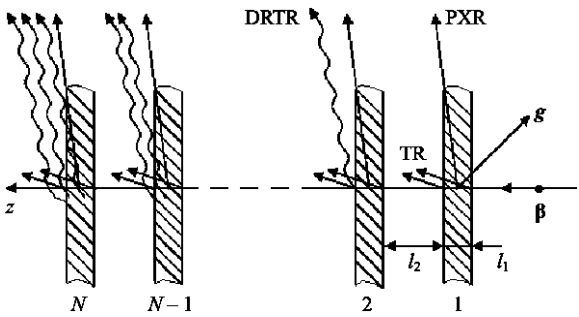

Fig. 6.21 The scheme of generation of PXR and diffraction of resonant transition radiation (DRTR) on the layered crystalline target

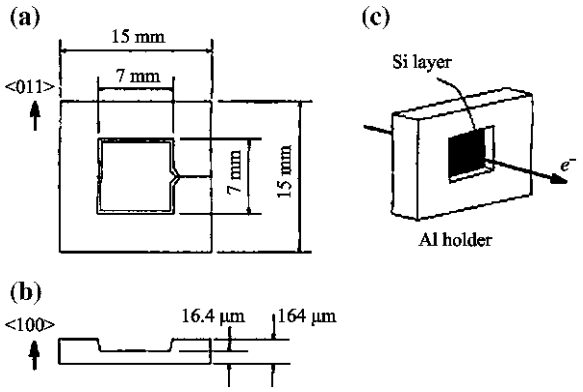

Fig. 6.22 Element of the layered crystalline target

It is clear that for the real layered target due to such causes as the random disorientation of crystalline targets relative to each other, the violation of strict periodicity as well as a spread in values of thickness of the used crystals, destructive interference between the two considered mechanisms, the resulting yield of X-rays close to the Bragg direction is described by dependence $\sim N^{\delta}$, where $1 < \delta < 2$. If the exponent δ is close to one, this means that the quality of a layered crystalline target is low and the target operates as a crystal with thickness $N\ell_1$. In the opposite case, the diffraction of transition radiation will provide a substantial contribution to the total yield of the resulting monochromatic radiation.

For experimental study of the possibility of increasing the radiation generation efficiency in such targets, the silicon micromachining technique was developed by Toshiba Corporation and the layered crystalline targets were made [20] (see Fig. 6.22).

The thickness of an original silicon wafer with axis $\langle 001 \rangle$, which is perpendicular to the target surface, was 164 microns ±5%. In the central part of the wafer with a size 6.8×6.8 mm^2, a workspace having thickness 16.4 mm ±5% was created. The assemblies of 1, 3, 10 and 100 of such elements are used in experiment [20]. The period of 164 μm was chosen due to conditions of generation of monochromatic X-rays with energy $\hbar\omega \approx 14$ keV by the electron beam of the INS synchrotron (Tokyo, Japan) with energy 900 MeV.

Figure 6.23 shows the dependence of a yield of resonant transition radiation photons with energies $\hbar\omega \approx 14.4$ and 35.5 keV from the layered target with the abovementioned parameters on the angle of outgoing photons in the plane of diffraction. Since the first maximum corresponds to the angles $\theta_x \leq \gamma^{-1}$, it is expected that part of the TR photons will diffract on the subsequent crystalline plates.

The emission spectrum at the angles $2\theta_B = 25°8'$ (for $\hbar\omega = 14.4$ keV) and $2\theta_B = 10.4°$ ($\hbar\omega = 35$ keV) was registered in the experiment by a semiconductor Si(Li) detector, in front of which there was a slit collimator with an angular aperture $\theta_x = 1$ mrad in case of $2\theta_B = 25°8'$ ($\Delta\theta_x = 1.16$ mrad in case of $2\theta_B = 10.4°$).

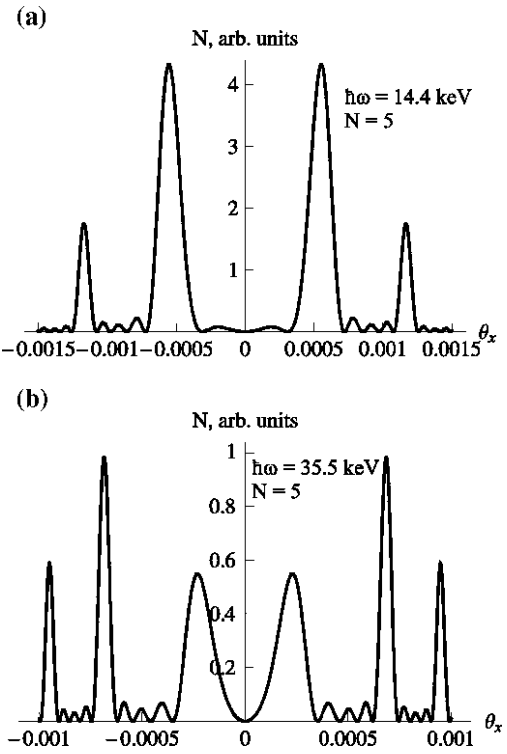

Fig. 6.23 The angular distribution of the resonant transition radiation photons after passing half of the elements of a layered crystalline target

Figure 6.24 shows the emission spectra measured for a layered target consisting of 10 silicon wafers (Fig. 6.24a) as well as 100 wafers (Fig. 6.24b). The full width at half maximum (FWHM) of the peaks was ∼500 eV in the first case and ∼810 eV—in the second one, and was mainly caused by the spectrometer energy resolution.

Figure 6.25 shows the experimental orientation dependences of a photon yield for both orientations. The calculated characteristics for these cases are shown in Fig. 6.26.

It should be noted that despite uncontrolled disorientation of plates relative to each other (which can be called as "macromosaicity"), FWHM of the experimental orientation dependence practically coincides with the calculated value obtained for the perfect crystal. This fact indirectly proves the presence of the appreciable contribution of diffracted transition radiation in the registered spectrum, since the angular distribution of diffracted transition radiation is concentrated in a narrower cone than in case of PXR.

From the data presented in Fig. 6.25 we can estimate the parameter FWHM. In case of $\hbar\omega = 14.4$ keV it is equal to 0.25°, whereas for the energy $\hbar\omega = 35.5$ keV we have 0.13°. The calculated values of these quantities (see Fig. 6.26) are equal to 0.3 and 0.1° respectively (calculations were performed for the pure PXR mechanism in the crystal with thickness $N\ell_1$).

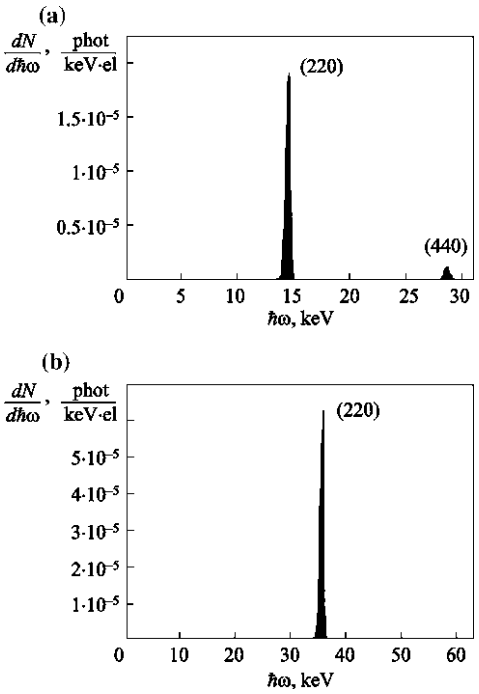

Fig. 6.24 The emission radiation spectrum of a layered crystalline target at the angle $2\theta_B(N = 10)$

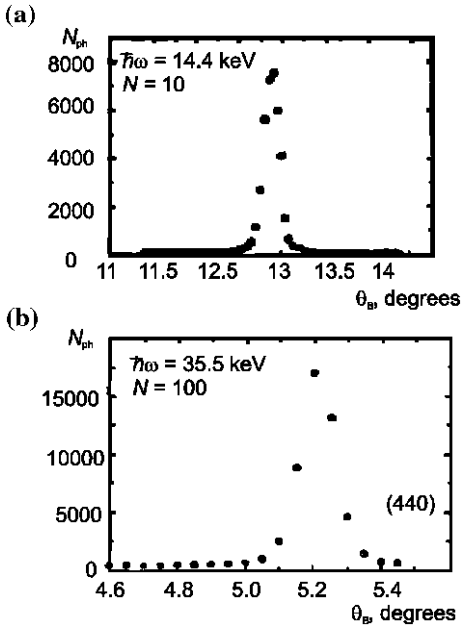

Fig. 6.25 Orientation dependence of the PXR photon yield from the layered crystal target for $\hbar\omega = 14.4$ keV (**a**) and $\hbar\omega = 35.5$ keV (**b**)

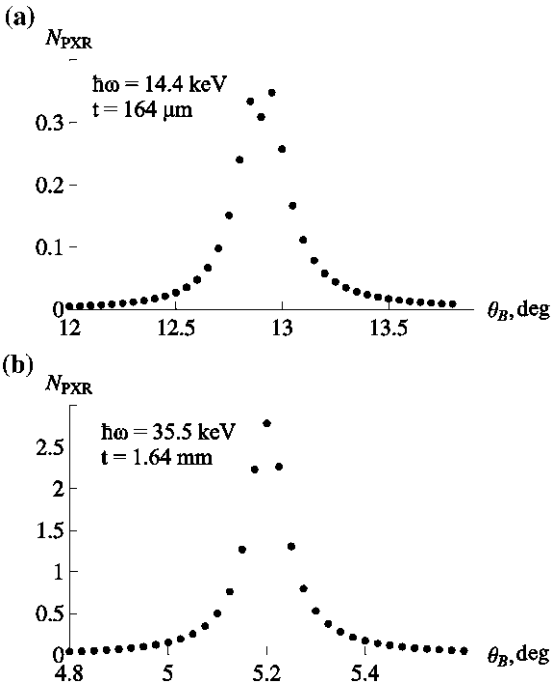

Fig. 6.26 Orientation dependence of the PXR photon yield from a single-crystal with the equivalent thickness

The dependence of the photon yield on the number of crystalline plates is shown in Fig. 6.27.

The yield of photons with energy $\hbar\omega = 14.4$ keV is well approximated by the dependence $\sim N^{1.4}$, which testifies to the generation of radiation via both considered mechanisms. The same figure shows the dependence of the yield of PXR photons with energy $\hbar\omega = 14.4$ keV from a single-crystal with appropriate thicknesses. The comparison shows that the radiation yield from a layered target

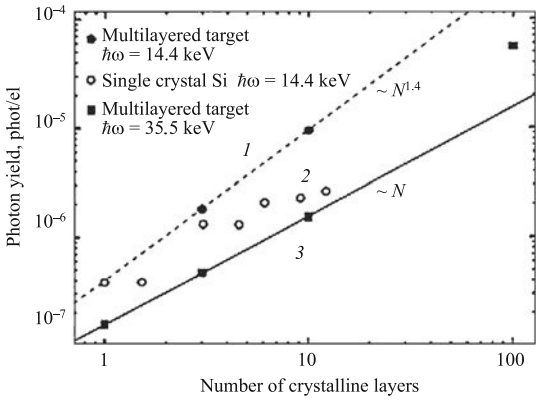

Fig. 6.27 The dependence of the yield of monochromatic radiation from a layered crystalline target (1, 3) and from the crystal with the equivalent thickness (2)

with $N = 10$ approximately 4 times higher than the PXR yield from a single-crystal of the same thickness.

However, *N*-dependence of the photon yield with energy 35.5 keV is linear with a good accuracy. This can probably be explained by the fact that the accuracy of the layered crystalline target manufacturing was insufficient for such energies of scattered photons.

Summarizing, we can say that this kind of layered crystalline targets in case of further improvement of the manufacturing techniques can provide a significant increase in the efficiency of generation of monochromatic X-rays compared to both RTR and PXR.

References

1. Jackson, J.D.: The Classical Electrodynamics. New York, NY (1998)
2. Landau, L.D., Lifshitz, E.M.: Electrodynamics of Continuous Media. Nauka, Moscow (1982). (In Russian)
3. James R.: The Optical Principles of the Diffraction of X-rays. G. Bell, London (1950)
4. Potylitsyn, A.P., Vnukov, I.E.: Parametric X-ray radiation, transition radiation and bremsstrahlung in X-ray region a comparative analysis. In: Wiedelman, H. (ed.) Electron-Photon Interaction in Dense Media, pp. 25–47. Kluwer Academic Publishers, Printed in the Netherlands (2001)
5. Nitta, H.: Kinematic theory of parametric X-ray radiation. Phys. Lett. A **158**, 270 (1991)
6. Baryshevsky, V.G., Feranchuk, I.D., Ulyanenkov, A.P.: Parametric X-ray Radiation: Theory, Experiment and Applications. Springer, Heidelberg (2006)
7. Backe, H., Brenzinger, K.-H., Buskirk, F., et al.: Transition radiation in the X-ray region from a low emittance 855 MeV electron beam. Am. Inst. Phys.: Conf. Proc. **390**, 57–72 (1997)
8. Vorobiev, S.A., Kalinin, B.N., Pak, S., Potylitsyn, A.P.: Detection of monochromatic X-ray emission in the interaction of ultrarelativistic electrons with a diamond single-crystal. JETP Lett. **41**, 1–4 (1985)
9. Didenko, A.N., Adishchev, Yu.N., Kalinin, B.N., et al.: Angular distribution and energy dependence of parametric X-ray radiation. Phys. Lett. A **118**, 87–89 (1986)
10. Shchagin, A., Pristupa, V.I., Khizhnyak, N.A.: A fine structure of parametric X-ray radiation from relativistic electrons in a crystal. Phys. Lett. A **148**, 485–488 (1990)
11. Adishchev, Yu.N., Verzilov, V.A., Potylitsyn, A.P., Uglov, S.R., Vorobyev, S.A.: Measurement of spectral and polarization characteristics of paramentric X-rays in a Si crystal. Nucl. Instrum. Methods B **44**, 130–136 (1989)
12. Adishchev, Yu.N., Kaplin, V.V., Potylitsyn, A.P., Uglov, S.R., Vorobyev, S.A., Babadzhanov, R.D., Verzilov, V.A.: Influence of K_α absorption in (111) Ge crystal on spectral yield of parametric X-rays. Phys. Lett. A **147**, 326–328 (1990)
13. Adishchev, Yu.N., Gogolev, A.S., Kalinin, B.N., et al.: Characteristic and X-ray radiation of relativistic charged particles. Surface X-ray. Synchrotron Neutron Res. **3**, 13–16 (2006). (In Russian)
14. Potylitsyn, A.P.: Influence of beam divergence and crystal mosaic structure upon parametric X-ray radiation characteristics. arXiv: cond-mat/9802279. **1**, 1–18 (1998)
15. Amosov, K.Yu., Andreyashkin, M.Y., Verzilov, V.A., et al.: Parametric X-radiation in a mosaic crystal of pyrolitic. JETP Lett. **60**, 506–510 (1994)
16. Chefonov, O.V., Kalinin, B.N., Naumenko, G.A., et al.: Experimental comparison of parametric X-ray radiation and diffracted bremsstrahlung in a pyrolytic graphite crystal. Nucl. Instrum. Methods B **173**, 18–26 (2001)

17. Adischev, Y.N., Verzilov, V.A., Vorobiev, S.A., et al.: Experimental observation of the linear-polarization of parametric X-ray emission. JETP Lett. **48**, 311–314 (1988)
18. Pugachov, D., They, J., Buschhorn, G.: Polarimetry of coherent polarization radiation. Nucl. Instrum. Methods B **201**, 55–66 (2003)
19. Potylitsin, A.P., Verzilov, V.A.: Parametric X-rays and transition diffracted radiation in crystal stacks. Phys. Lett. A **209**, 380–384 (1995)
20. Takashima, Y., Aramitsu, K., Endo, I.: Observation of monochromatic and tunable hard X radiation from stratified Si single crystals. Nucl. Instrum. Methods B **145**, 25–30 (1998)

Chapter 7
Smith–Purcell Radiation

7.1 The Smith–Purcell Effect

As it was noted before, the transition radiation is a manifestation of so-called "polarization mechanism of radiation", in which the field of a charged particle passing through the medium deforms (polarizes) the electron shells of the medium atoms. It is the dynamic polarization of the medium atoms that becomes a cause for electromagnetic radiation. If a relativistic charged particle flies in a vacuum close to any medium at the distance h, then in this case the particle motion also will be accompanied by a dynamic polarization of the medium atoms and as a consequence by the electromagnetic radiation in the $\lambda \geq 2\pi h/\gamma$ wavelength range, since the effective transverse "size" of the Coulomb field of a moving charge reaches the value $\sim \gamma\lambda$ [1]. Such a type of radiation is called *diffraction radiation*.

By analogy with the resonant transition radiation, it can be expected that the resonant diffraction radiation, appearing at a charge passage near the periodic target, will also be quasimonochromatic.

Such a radiation process is illustrated in Fig. 7.1. The charge, flying at a small distance from the continuously deformed surface target, induces the changing current on the surface, which can be described as a movement of the charge "image" on the periodically deformed surface if the depth of "grooves" is not too large. It is evident that a charge moving by such a periodic trajectory will generate a monochromatic electromagnetic radiation.

In 1953, Smith and Purcell [2] for the first time observed such radiation in the light range by passing an electron beam with energy ~ 300 keV close to a periodic target (standard optical grating) with a period of $d = 1.67$ μm. The diameter of electron beam, which passed practically along the optical grating with length 48 mm, was approximately 150 μm. The radiation was detected at an angle $\theta \approx 20^{o}$ by means of a simple optical scheme (collimators, lens, analyzing grating) via photographic method. The line with wavelength $\lambda \approx 0.56$ μm was observed in a spectrum of radiation for electrons with energy 309 keV.

A. P. Potylitsyn, *Electromagnetic Radiation of Electrons in Periodic Structures*, Springer Tracts in Modern Physics, 243, DOI: 10.1007/978-3-642-19248-7_7,

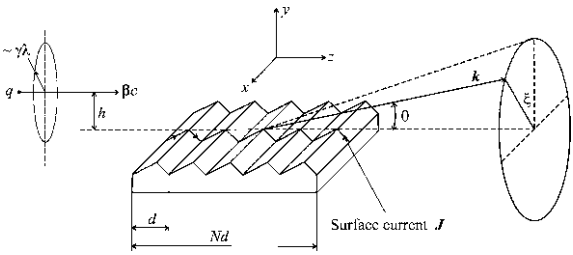

Fig. 7.1 Periodically changing current **J** induced by a flying charge above the deformed conducting surface

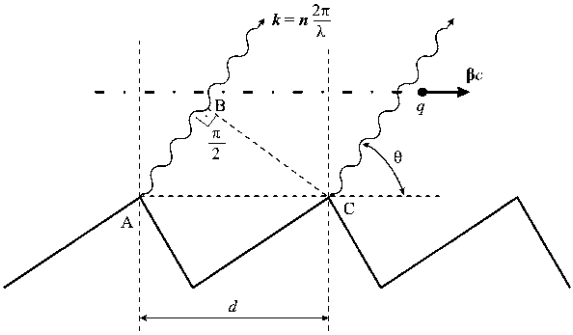

Fig. 7.2 Illustration of derivation of the Smith–Purcell relation

In the cited work Smith and Purcell derived the formula that connected the radiation wavelength with the grating period, the observation angle and velocity of the charge $v = \beta c$:

$$\lambda_n = \frac{d}{n}\left(\frac{1}{\beta} - \cos\theta\right), \tag{7.1.1}$$

based on the Huygens' principle (Fig. 7.2).

Electromagnetic radiation is excited by the field of a flying particle in each cell of the grating. To be easy understood, we consider the plane waves emitted at an angle θ from two successive rulings of the grating initiated by the same charged particle passing along the grating with velocity βc. These waves will have the same phase (i.e. they will interfere constructively), if the time, during which a plane wave emitted from point A (see Fig. 7.2) reaches the point B ($t_1 = d\cos\theta/c$), will be connected with the time needed for a particle to pass a distance d and to excite a plane wave in the point C ($t_2 = d/\beta c$), as follows: $c(t_1 - t_2) = n\lambda,\ n = \pm 1,\ \pm 2,\ \ldots$.

The so-called "dispersion" relation follows from here

$$\lambda_n = \frac{d}{n}\left(\cos\theta - \frac{1}{\beta}\right),$$

where n is the order of diffraction.

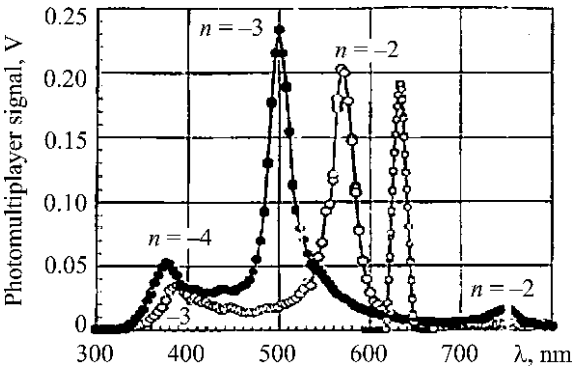

Fig. 7.3 The Smith–Purcell radiation spectra for the electron energy 35 keV (*dark circles*) and 60 keV (*open circles*). The measured emission spectrum of the He–Ne laser (*rectangles*) is shown here as well

The last relation for $n = -1$ ("fundamental" harmonic) Smith and Purcell wrote down as the following formula $\lambda = d\left(\frac{1}{\beta} - \cos\theta\right)$.

In a ultrarelativistic case, the last relationship coincides with the resonant condition (2.4.9), which does not depend on the specific mechanism of generation.

Formula (7.1.1) for the order of diffraction $n = 1$ gives a value of $\lambda = 0.566$ μm for $\beta = 0.782$ ($E = 309$ keV), which is in accordance with the experiment. With an increase of electron energy up to $E = 340$ keV, the shift of the emission line to the region of smaller wavelengths was observed in the experiment. The experimental data [2] confirmed the formula (7.1.1) within the experimental errors accuracy.

After this first observation of the monochromatic radiation appearing during the rectilinear and uniform movement of a charge in a vacuum close to a periodic target (a grating), this effect is called as the *Smith–Purcell effect*.

In the recent experiment [3], the authors studied in details the Smith–Purcell radiation (SPR) in the optical range, generated by an electron beam with energy $E < 60$ keV and current $I < 10$ mA. The beam diameter did not exceed 200 μm, the radiation generated from a grating with period 0.556 μm was detected by a photomultiplier at an angle of $\theta = 80°$. The emission spectrum was investigated by means of a monochromator with resolution of (FWHM, full width at half maximum) $\Delta\lambda = 20$ nm.

Figure 7.3 shows the measured Smith–Purcell radiation spectra for an optical grating with a triangle profile and the period of $d = 0.556$ μm. As follows from the figure, the orders of radiation up to $|n| = 5$ are experimentally observed.

Figure 7.4 shows the dependence of the positions of different order spectral lines upon the electron energy [3]. The solid lines show the results of calculations using Eq. (7.1.1). It is possible to note a good agreement between experimental data and the Smith–Purcell formula. The following paragraphs describe the main models quantitatively explaining the mechanism of the Smith–Purcell radiation (SPR).

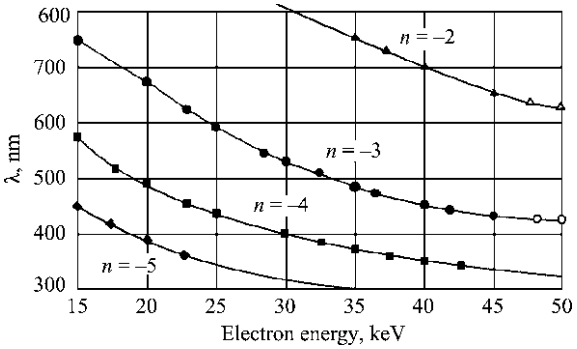

Fig. 7.4 Comparison of the calculated position of the Smith–Purcell radiation lines (*full lines*) with the experiment (*points*)

7.2 The Scalar Theory of the Diffraction of the Electron Coulomb Field from a Flat Semi-Transparent Grating

One of the first models proposed for the calculation of the spectral–angular distribution of the SPR, was developed in the work [4] (see also the review [5]). This model considered the grating with a period d and a number of elements $N \gg 1$, made from perfectly conducting infinitely thin strips having the width a (Fig. 7.5) and located within a plane.

A charge q with velocity $\mathbf{v} = \boldsymbol{\beta} c$ flies above the grating at the distance h (impact parameter). Characteristics of radiation were calculated in half-space under the grating (that is why, the authors called such a grating as flat semi-transparent). The authors assumed that, in accordance with the Huygens–Kirchhoff theorem, a field

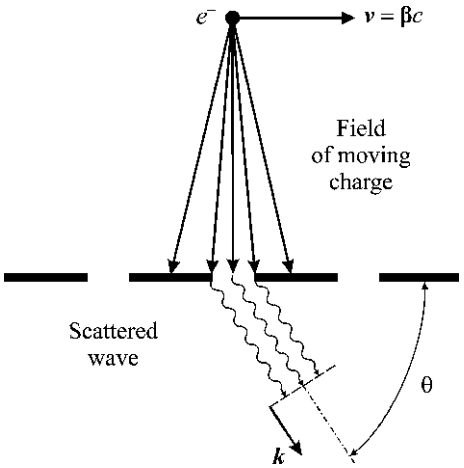

Fig. 7.5 The scheme of generation of the Smith–Purcell radiation from a flat semi-transparent grating

magnitude in a half-space under the grating is determined by its values on the gaps (in the plane of the grating):

$$g(x,y,z) = \int \frac{kg_0(x',0,z')}{2\pi i R} e^{ikR} dS_n, \tag{7.2.1}$$

where $k = 2\pi/\lambda$ is the wave vector modulus, g_0, g are the components of the field describing the radiation with frequency $\omega = 2\pi c/\lambda$, from a flat grating at a distance R; dS_n is the projection of the grating area element on the direction of the wave vector. Except for the Kirchhoff approximation, the authors neglected the influence of grating itself on the field characteristics on the gaps.

Let the charge moves with velocity $\mathbf{v} = \boldsymbol{\beta} c$ along the axis z. Then, according to [5], its field on the grating plane is possible to describe by a scalar function

$$\begin{aligned} g_0(x,0,z) &= \frac{iq}{2\pi c} \int \frac{dk_x}{\sigma(k_x,\omega)} e^{i\left(\sigma h + k_x \kappa + \frac{w}{v} z\right)}, \\ \sigma(k_x,\omega) &= i\sqrt{\left(1-\beta^2\right)\frac{\omega^2}{V^2} + k_x^2}. \end{aligned} \tag{7.2.2}$$

After calculating the integral (7.2.1) with taking into account the grating periodicity, the squared modulus of the function $g(x, y, z)$ gives the spectral–angular distribution of the SPR:

$$\begin{aligned} \frac{d^2W}{d\omega\, d\Omega} = {} & \frac{q^2(d-a)^2}{2\pi c} \frac{VT}{d} \frac{\sin^2\left[\frac{d-a}{2}\frac{\omega}{V}(1-\beta\cos\theta)\right]}{\left[\frac{d-a}{2}\frac{\omega}{V}(1-\beta\cos\theta)\right]^2} \sin^2\theta \\ & \times \exp\left\{-2h\frac{\omega}{V}\sqrt{1-\beta^2\left(1-\sin^2\theta\sin^2\xi\right)}\right\} \\ & \times \sum_n \delta\left[\frac{\omega}{V}(1-\beta\cos\theta)d - 2\pi n\right]. \end{aligned} \tag{7.2.3}$$

Here $T = Nd/\beta c$ is the flight time of a charge above the grating; n is the order of diffraction; θ, ξ are the polar and azimuthal angles of a wave vector. To obtain the angular distribution of radiated energy for the nth order of diffraction, it is necessary to integrate the last expression over the frequency, which is easily carried out using the δ-function:

$$\begin{aligned} \frac{dW_n(\theta,\xi)}{d\Omega} = {} & \frac{2\pi q^2(d-a)^2}{c^3} N\left(\frac{V}{d}\right) \frac{\sin^2\left[n\pi\frac{d-a}{d}\right]}{\left[\pi\frac{d-a}{d}\right]^2} \\ & \times \frac{\sin^2\theta}{\left[1-\beta\cos\theta\right]^3} \exp\left\{-\frac{4\pi n h}{d(1-\beta\cos\theta)}\sqrt{\gamma^{-2}+\beta^2\sin^2\theta\sin^2\xi}\right\}. \end{aligned} \tag{7.2.4}$$

As it follows from the last formula for the first-order diffraction (fundamental harmonic), the maximum radiation yield is achieved for the strip width $a = d/2$.

In this case ($n = 1$), formula (7.2.4) for the radiation of an electron ($q^2 = e^2 = \alpha\hbar c$) is written as

$$\frac{dW_1(\theta,\xi)}{d\Omega} = \frac{2\alpha}{\pi}\beta^3\frac{\hbar c}{d}N\frac{\sin^2\theta}{[1-\beta\cos\theta]^3} \times \exp\left\{-\frac{4\pi h}{\gamma d(1-\beta\cos\theta)}\sqrt{1+\gamma^2\beta^2\sin^2\theta\sin^2\xi}\right\}. \quad (7.2.5)$$

The simple obvious model has allowed receiving an analytical formula, from which important physical consequences follow. The exponent may be written as $\exp\left\{-\frac{4\pi h}{\gamma\beta\lambda}\sqrt{1+\gamma^2\beta^2\sin^2\theta\sin^2\xi}\right\}$, which implies a rigid restriction on the effective impact parameter h:

$$h \le h_{\text{eff}} \approx \gamma\beta\lambda/4\pi. \quad (7.2.6)$$

It is clear that in the nonrelativistic case ($\gamma \sim 1$) condition (7.2.6) is practically impossible to be fulfilled in the optical range ($\lambda \le 1$ μm). As a rule, in experiments the inequality $h \gg h_{\text{eff}}$ is valid, which leads to an exponential suppression of the SPR yield. With the growth of the electron energy (increasing of Lorentz-factor), or with the shift from the optical range to the infrared one (or submillimeter range), the condition (7.2.6) becomes less rigid.

If the impact parameter satisfies the condition $h \le h_{\text{eff}}$, then SPR in the relativistic case is concentrated in the plane, which is perpendicular to the grating, i.e. in the range of azimuthal angles $\xi \le \gamma^{-1}$, since for large azimuthal angles an exponential suppression of the yield occurs (because of the increase of the root in the exponent).

More rigorous models for the description of the Smith–Purcell effect for relativistic particles have been proposed in recent years [6–9], but the received results (including those obtained by numerical methods), qualitatively confirm the given conclusions based on the formula derived by Bolotovskii and Burtsev more than 40 years ago.

7.3 Diffraction of the Coulomb Electron Field at the Optical Grating

This model was established in [10], where authors used the Van den Berg's approach [6], allowing the calculation of the Smith–Purcell radiation characteristics by analogy with the process of electromagnetic wave scattering by a grating with an arbitrary profile. This model for a lamellar grating (see Fig. 7.6) is described below.

The space outside the grating is divided into two areas: the region above the grating ($y \ge 0$, region I) and the area inside the grating grooves ($-b \le y \le 0$,

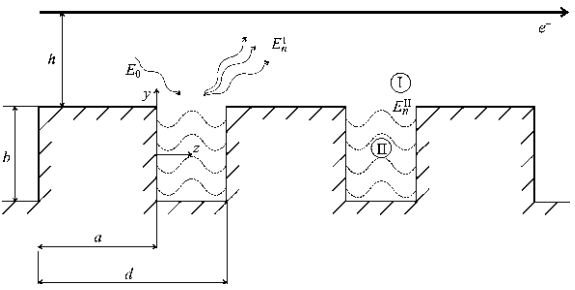

Fig. 7.6 The scheme of the Smith–Purcell radiation generation in the Van den Berg model. The electromagnetic wave propagates in area *I*; in area *II* the radiation is considered as a set of modes

region II). Hereinafter we shall use the following Fourier-components of electric and magnetic fields:

$$\begin{aligned}\mathbf{E}(x,y,z,t) &= \iint \mathbf{E}_\omega(y,z,\eta,\omega)\exp[i(\eta x-\omega t)]d\eta\, d\omega,\\ \mathbf{H}(x,y,z,t) &= \iint \mathbf{H}_\omega(y,z,\eta,\omega)\ \exp[i(\eta x-\omega t)]d\eta\, d\omega.\end{aligned} \tag{7.3.1}$$

The current associated with a passage of the charge e above the grating has the following form:

$$\mathbf{J}_\omega(y,z,\eta,\omega) = \left(\frac{e}{2\pi}\right)^2 \exp(i\alpha_0 z)\delta(y-h)iz.$$

For the y-components of the field in the plane of the grating Maxwell's equations are reduced to the Helmholtz equations:

$$\begin{aligned}&\frac{\partial^2 E_{\omega x}}{\partial^2 y}+\frac{\partial^2 E_{\omega x}}{\partial^2 z}+\left(k^2-\eta^2\right)E_{\omega x} = i\frac{e}{4\pi^2}\sqrt{\frac{\mu_0}{\varepsilon_0}}\,\frac{\eta}{\beta}\times\delta(y-h)\exp(i\alpha_0 z);\\ &\frac{\partial^2 H_{\omega x}}{\partial^2 y}+\frac{\partial^2 H_{\omega x}}{\partial^2 z}+\left(k^2-\eta^2\right)H_{\omega x} = i\frac{e}{4\pi^2}\frac{d}{\partial x}\delta(y-h)\exp(i\alpha_0 z),\end{aligned} \tag{7.3.2}$$

where $\alpha_0 = \omega/v$. The solution of Helmholtz equation in region I is written as:

$$E^I_{\omega x} = E^0_{\omega x} + E^r_{\omega x};\quad H^I_{\omega x} = H^0_{\omega x} + H^r_{\omega x}. \tag{7.3.3}$$

Here $E^r_{\omega x}, H^r_{\omega x}$ are the solutions of homogeneous equations describing the field of a real electromagnetic wave being "reflected" by the grating, whereas $E^0_{\omega x}$, $H^0_{\omega x}$, are the solutions of inhomogeneous equations describing the field of moving charge, which have the form

$$\begin{aligned}E^0_{\omega x} &= \frac{e}{8\pi^2}\sqrt{\frac{\mu_0}{\varepsilon_0}}\,\frac{\eta\alpha_0}{\beta\gamma_0}\exp[i(\alpha_0 z+\gamma_0|y-h|)];\\ H^0_{\omega x} &= \frac{e}{8\pi^2}\mathrm{sgn}(y-h)\exp[i(\alpha_0 z+\gamma_0|y-h|)],\end{aligned} \tag{7.3.4}$$

where $\gamma_0 = i\sqrt{\left(\alpha_0^2+\eta^2+k^2\right)}$.

The value y_0 is pure imaginary and, accordingly, formulae (7.3.4) describe the fields propagating along the z axis with the velocity v and exponentially decreasing with the distance from the trajectory of charge (evanescent waves).

The fields $E^r_{\omega x}$, $H^r_{\omega x}$are represented in the form of infinite series:

$$\begin{aligned} E^r_{\omega x} &= \sum E^r_{x,n} = \sum_{n=-\infty}^{\infty} E_n \exp[i(\alpha_n z + \gamma_n y)], \\ H^r_{\omega x} &= \sum H^r_{x,n} = \sum_{n=-\infty}^{\infty} H_n \exp[i(\alpha_n z + \gamma_n y)], \end{aligned} \tag{7.3.5}$$

where

$$\alpha_n = \alpha_0 + \frac{2\pi n}{d}, \quad \gamma_n = \sqrt{\left(k^2 - \alpha_n^2 - \eta^2\right)}. \tag{7.3.6}$$

For the real values of the parameter γ_n, the fields (7.3.5) correspond to the Smith–Purcell radiation with diffraction order n. In this case, the quantities in the exponent in (7.3.5) are associated with the components of the wave vector (see Fig. 7.1) as follows: $\gamma_n = k \sin\theta \cos\xi$, $\eta = k \sin\theta \sin\xi$, $\alpha_n = k \cos\theta$.

The solutions of the Helmholtz equation in the II region are expressed as a summation with respect to the modes:

$$\begin{aligned} E^{\mathrm{II}}_{\omega x} &= \exp(i\alpha_0 J\, d) \sum_{m=1}^{\infty} G_m \sin\left(\frac{m\,\pi z'}{d-a}\right) [\exp(-ik_m y) - \Gamma_m \exp(ik_m y)], \\ H^{\mathrm{II}}_{\omega x} &= \exp(i\alpha_0 J\, d) \sum_{m=1}^{\infty} F_m \cos\left(\frac{m\,\pi z'}{d-a}\right) [\exp(-ik_m y) + \Gamma_m \exp(ik_m y)]. \end{aligned} \tag{7.3.7}$$

Here the coordinate z' corresponds to the coordinate "inside" the groove

$$\begin{gathered} (0 \le z' \le d-a, \quad z = j\,d + z', \quad j = 0, \pm 1, \pm 2, \ldots), \\ k_m = \sqrt{k^2 - \eta^2 - \left(\frac{m\pi}{d-a}\right)^2}, \quad \Gamma_m = \exp(i\,2k_m d). \end{gathered}$$

From the boundary conditions on the grating surface and fields continuity condition on the boundary between the I and II areas it is possible to get a system of algebraic equations for the unknown coefficients E_n and H_n in expressions (7.3.5).

After finding the fields E_n and H_n, the Smith–Purcell radiation intensity of nth order is calculated in the standard way (per period of an infinitely long grating)

$$\frac{dW_n}{d\Omega} = \frac{\alpha\,\hbar\,c}{d} \frac{\sin^2\theta \cos^2\varphi}{(1/\beta - \cos\theta)^3} |R_n(\theta,\xi)|^2 \exp\left\{-\frac{h\sqrt{1 + (\gamma\beta\sin\xi)}}{h_{\mathrm{int}}}\right\}, \tag{7.3.8}$$

where $h_{\mathrm{int}} = \gamma\,\beta\lambda_n/4\pi$,

$$|R_n(\theta,\xi)|^2 = \frac{4}{e^2}\,\frac{\exp\{2|\gamma_0|h\}}{\left(1-\sin^2\theta\sin^2\xi\right)}\left\{\left|E^2_{x,n}\right|^2+\left|H^2_{x,n}\right|\right\}. \tag{7.3.9}$$

The value of (7.3.9) is called *the radiation factor* and corresponds to the classical coefficient of radiation reflection by a grating [11]. The multiplier $\exp\{2|\gamma_0|h\}$ is introduced to compensate the dependence on impact-parameter h in expressions $E^r_{x,n}$, $H^r_{x,n}$. As it is shown in [10], the radiation factor for the considered grating depends only on the ratios a/d and b/d, as well as on the energy of an initial electron.

So, for the given grating parameters and observation angles, the calculation of angular distributions of the SPR is reduced to finding the radiation factor. Figure 7.7 shows the calculation results of the radiation factor $|R_1(\theta, 0)|$ for electron energies from 1 up to 100 MeV for the grating parameters $a/d = 0.1$ and $b/d = 0.5$ [10]. Using the relation (7.1.1) from (7.3.8) and (7.3.9), we can obtain the angular density of SPR depending on the wavelength.

The model described in the article [9] was used for calculations of SPR characteristics from the grating made of strips with width a and thickness b, separated by vacuum gaps. In this case, apart from the radiation emitted in the half-space through which the electron flies (i.e. in the region with $y \geq 0$, see Fig. 7.6), there can be an emission of the radiation in the half-space with $y \leq -b$. The author [9] has developed an approach which allows calculating not only the radiation factor $|R_n|^2$, but the transmission coefficient $|T_n|^2$ as well, by means of which it is possible to calculate the Smith–Purcell radiation intensity in the half-space $y \leq -b$ after the substitution it into the formula (7.3.8) instead of $|R_n|^2$.

Figure 7.8 shows the results of calculation of both factors for the gratings of different thickness for the electron energy of $E = 855$ MeV.

It should be noted that to find the fields $E^r_{x,n}$, $H^r_{x,n}$ at small polar angles θ it is necessary to solve the system of algebraic equations of high order, which cannot always provide the demanded accuracy.

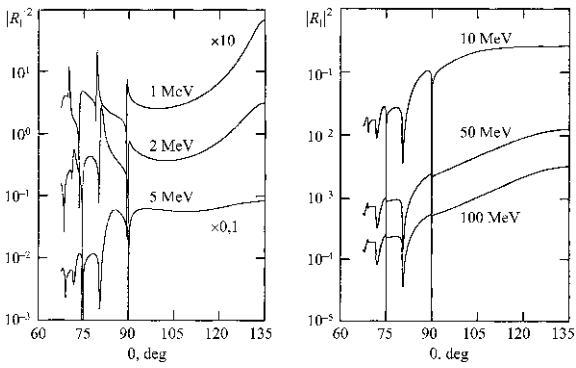

Fig. 7.7 The radiation factor $|R_1|^2$ according to the Van den Berg model for a lamellar grating at different energies of the initial electron ($a/d = 0.5$; $b/d = 0.1$; $\xi = 0$) [10]

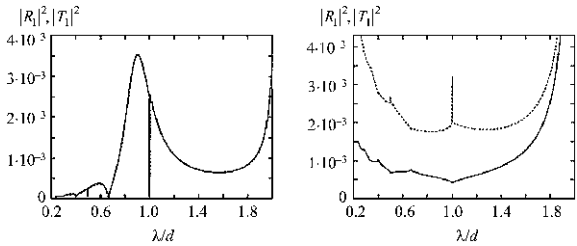

Fig. 7.8 The calculation results of factors $|R_1|^2$ (*solid line*) and $|T_1|^2$ (*dashed line*) for a grating with parameters $a/d = 0.5$; $b/d = 0.01$ (*left*) and $b/d = 0.001$ (*right*)

Besides, the singularities similar to the Rayleigh–Woods anomalies in ordinary optics may appear for the certain wavelengths in a spectrum. Thus, the described method hasn't a wide versatility.

7.4 Radiation of Induced Surface Currents as a Smith–Purcell Effect

One of the simple models describing the Smith–Purcell effect is a model of surface currents [7]. In this model, a charge uniformly moving near periodically deformed surface (grating) induces a current on the surface changing in space and in time, which generates the Smith–Purcell radiation.

According to known rules of electrodynamics [1], the spectral–angular distribution of radiation is determined by the density of induced current **J**(**r**, t) by the following expression:

$$\frac{d^2W}{d\omega\, d\Omega} = \frac{\omega^2}{4\pi^2 c^3}\left|\int dt \int d\,\mathbf{r}\left[\mathbf{n}[\mathbf{n}\mathbf{J}(\mathbf{r},t)]e^{i(\omega t - kr)}\right]\right|^2, \tag{7.4.1}$$

where $\mathbf{k} = \mathbf{n}\cdot\omega/c$ is the photon wave vector, $\mathbf{n} = \{\sin\theta\sin\xi,\ \sin\theta\cos\xi, \cos\theta\}$ is a unit vector along the wave vector. Since the current $\mathbf{J}(\mathbf{r}, t)$ induced on the periodically arranged elements of the grating is a periodic function of variables z and t

$$\mathbf{J}(\mathbf{r},t) = \sum_{m=1}^{N} \mathbf{J}_0\left(x, y, z - md,\ t - \frac{md}{v}\right), \tag{7.4.2}$$

then the integral (7.4.1) is reduced to the following:

$$\frac{d^2W}{d\omega\, d\Omega} = \frac{\omega^2}{4\pi^2 c^3}\left|\sum_{m=1}^{N} e^{imd\omega\left(\frac{1}{v}-\frac{n_z}{c}\right)}\right|^2 \left|\int dt \int dx\, dy\, dz\, \mathbf{J}_0(\mathbf{r},t)e^{i(\omega t - kr)}\right|^2. \tag{7.4.3}$$

In (7.4.2), (7.4.3) the subscript "0" at the vector **J** indicates that the integration is carried out in respect of both the volume occupied by one element and the time interval corresponding to the flight of a particle above one period of the grating.

In (7.4.3) the sum squared reduces to the standard expression [which is similar to the formula (2.4.15)]:

$$F_3 = \left| \sum_{m=1}^{N} e^{imd\omega\left(\frac{1}{v}-\frac{n_z}{c}\right)} \right|^2 = \frac{\sin^2\left[\left(\frac{1}{\beta}-\cos\theta\right)\frac{N\omega d}{2c}\right]}{\sin^2\left[\left(\frac{1}{\beta}-\cos\theta\right)\frac{\omega d}{2c}\right]}$$

$$\approx \sum_{n\neq 0} \frac{N\omega}{|n|}\delta(\omega-\omega_n). \tag{7.4.4}$$

Here, as before, the integer index n defines the so-called "order of diffraction". The argument of δ-function is defined the Smith–Purcell dispersion relationship:

$$\omega_n = \frac{2\pi\,|\,n|\,c}{d(1/\beta-\cos\theta)}. \tag{7.4.5}$$

In such a formulation the problem is most simply solved, when the grating is a set of $N(N \gg 1)$ parallel perfectly conducting strips separated by vacuum gaps, and neglecting the distortion of a moving charge field, which is caused by the presence of a conducting surface near the charge.

Figure 7.9 shows schematically the effective area on the strip surface, where a surface charge is induced (figure corresponds to a fixed time). It is clear that the effective size of this region in the direction of motion becomes much smaller than the impact parameter ($h/\gamma \ll h$, if $\gamma \gg 1$). A field distortion of the initial charge is negligible in this case. As it is known, the surface density of a charge induced on a perfectly conducting plane, is proportional to the perpendicular component of the electric field intensity. In a system of units used in this chapter the coefficient of proportionality is equal to $1/2\pi$:

$$\sigma(x,y,z) = 2\times\frac{E_y(x,y,z)}{4\pi}$$

$$= \frac{q\gamma}{2\pi}\,\frac{y-y_0}{\left[(x-x_0)^2+(y-y_0)^2+\gamma^2(z-z_0-vt)^2\right]^{3/2}}\,\delta(y-y_1)\,. \tag{7.4.6}$$

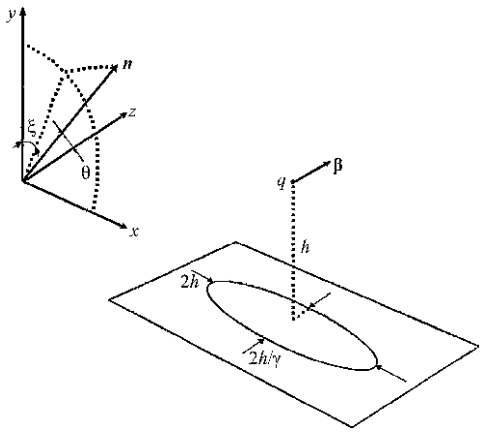

Fig. 7.9 The effective area on a target, where the surface charge is induced by a moving charge q (for the fixed moment of time)

Here $\mathbf{r}_0 = \{x_0, y_0, z_0\}$ designates coordinates of the charge at the time $t = 0$. The delta function describes the fact that the conducting plane is located in parallel to the coordinate plane at a distance y_1 from the origin of coordinates. If a charged particle moves with constant velocity $\boldsymbol{v} = \{0, 0, c\beta\}$ along the axis z (above the conducting strip $z_1 \le z \le z_2$), then the induced current is defined as follows:

$$\mathbf{J}_0(\mathbf{r}, t) = \sigma\, c\boldsymbol{\beta}. \tag{7.4.7}$$

The Fourier's component of the induced current is found by the standard way:

$$\mathbf{J}_0(\omega, \vec{n}) = \int\limits_{-\infty}^{\infty} dt \int\limits_{z_1}^{z_2} dz \int\limits_{-\infty}^{\infty} dy \int\limits_{-\infty}^{\infty} dx \cdot \left(\frac{q\gamma}{2\pi}\right) \times \frac{(y - y_0)\,\delta(y - y_1)}{\left[(x - x_0)^2 + (y - y_0)^2 + \gamma^2 (z - z_0 - vt)^2\right]^{3/2}}\, c\beta\, \mathbf{i}_z\, e^{i(\omega t - kr)}.$$

Here $\mathbf{i}_z$ denotes a unit vector along the axis z. The delta function allows to carry out the integration over y. To calculate the remaining integrals, we will introduce new variables:

$$u = \gamma(vt - z + z_0), \quad \bar{x} = x_0 - x, \quad h = (y_0 - y_1), \quad \kappa = \frac{\omega}{v} - k_z.$$

Thus, it is necessary to calculate the triple integral

$$\mathbf{J}_0(\omega, \mathbf{n}) = \mathbf{i}_z \frac{q}{2\pi} \int\limits_{z_1}^{z_2} dz \int\limits_{-\infty}^{\infty} d\bar{x} \int\limits_{-\infty}^{\infty} du \frac{h}{\left[h^2 + x^2 + u^2\right]^{3/2}} \times \exp\left\{ i \left[\frac{\omega u}{\gamma v} - \frac{\omega z_0}{v} + k_x(\bar{x} - x_0) + \kappa z - k_y y_1 \right] \right\}. \tag{7.4.9}$$

The inner double integral (with respect to $d\bar{x}\, du$) is reduced to the tabulated one, which is written in polar coordinates as follows:

$$I = \int\limits_{-\infty}^{\infty} d\bar{x} \int\limits_{-\infty}^{\infty} du \frac{\exp\left\{ i \left[\frac{\omega u}{\gamma v} + k_x \mathbf{x} \right] \right\}}{\left[h^2 + \bar{x}^2 + u^2\right]^{3/2}} = \int\limits_0^{2\pi} d\xi \int\limits_0^{\infty} \rho\, d\rho \frac{\exp\{i\mu\rho\cos\xi\}}{(h^2 + \rho^2)^{3/2}}, \tag{7.4.10}$$

where $\mu = \sqrt{\left(\frac{\omega}{\gamma v}\right)^2 + k_x^2}$.

The azimuthal integral in (7.4.10) is expressed in terms of Bessel's function of zeroth order, and hence,

$$I = 2\pi \int\limits_0^{\infty} \rho\, d\rho \frac{J_0(\mu\rho)}{\left[h^2 + \rho^2\right]^{3/2}} = 2\pi \frac{\exp\left[-\sqrt{\left(\frac{\omega}{\gamma v}\right)^2 + k_x^2}\, h \right]}{h}.$$

For radiation in a vacuum $k_y = \omega \sin\theta \cos\xi / c$ (see Fig. 7.1). Thus, for the Fourier's component of the induced current we have

$$\mathbf{J}_0(\omega, \mathbf{n}) = \mathbf{i}_z q \exp\left[-\frac{\omega h}{\gamma\beta c}\sqrt{1+\gamma^2\beta^2 \sin\theta \sin^2\xi}\right] \times \exp\left(-ik_y y_1\right)\frac{1}{i\kappa} e^{i\kappa z}\Big|_{z_1}^{z_2}. \tag{7.4.11}$$

After calculating the double vector product we obtain the formula for $n = 1$:

$$\frac{d^2W}{d\omega\, d\Omega} = q^2\frac{\omega^3}{4\pi^2 c^3} N\delta(\omega - \omega_1)\sin^2\theta \times \exp\left(-\frac{2\omega_1 h}{\gamma\beta c}\sqrt{1+\gamma^2\beta^2\sin^2\theta\sin^2\xi}\right)\frac{1}{\kappa^2}\left|e^{i\kappa z_2} - e^{i\kappa z_1}\right|^2. \tag{7.4.12}$$

The last factor in (7.4.12) coincides with the standard multiplier F_2 [see formulas (5.4.12) for $\sigma_1 = \sigma_2 = 0$]. We can obtain from (7.4.12) the angular distribution of the Smith–Purcell radiation of single electron ($q = -e$) for a width strip $a(z_2 - z_1 = a)$ and $n = 1$:

$$\frac{dW_1}{d\Omega} = \frac{\alpha}{2\pi} N\frac{\hbar c}{d}\frac{\sin^2\theta}{\left(\frac{1}{\beta} - \cos\theta\right)^3} \times \exp\left[-\frac{4\pi h}{\gamma\beta d\left(\frac{1}{\beta} - \cos\theta\right)}\sqrt{1+\gamma^2\beta^2\sin^2\theta\sin^2\xi}\right] 4\sin^2\left(\frac{\pi a}{d}\right). \tag{7.4.13}$$

The constant $\alpha = e^2/\hbar c$ is used in the last formula. It should be noted that derivation of the obtained formula (7.4.13) is based on the approach developed in [7], where the concept of induced current on the surface of a flat ideal grating is consistently used. For a grating with $a/d = 1/2$ the formula (7.4.13) completely coincides with formula (7.2.5) found on the basis of the scalar theory of diffraction of relativistic charge field, what indicates the identity of the initial assumptions in both approaches.

The developed model allows to find the characteristics of SPR not only for a flat grating but for one formed by tilted strips (Fig. 7.10).

For strips tilted at an angle θ_0 the model is valid for angles

$$\theta_{\min} \le \theta \le \theta_{\max},$$

$$\theta_{\min} = \arctan\frac{a\sin\theta_0}{d + a\cos\theta_0},$$

$$\theta_{\max} = \frac{\pi}{2} - \arctan\frac{d - a\cos\theta_0}{a\sin\theta_0},$$

where it is possible to neglect the re-scattering of the emitted radiation in subsequent elements of the grating.

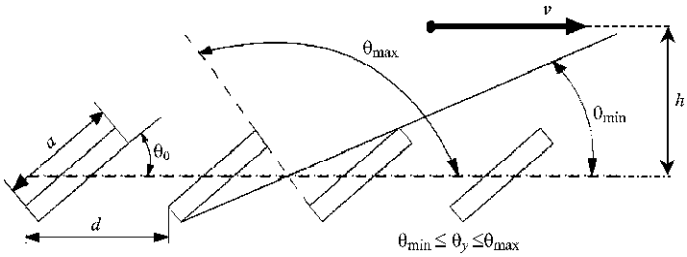

Fig. 7.10 Volume grating made from tilted strips

For such a grating the authors [12] have obtained a formula for the angular distribution of SPR:

$$\frac{dW_n}{d\Omega} = \alpha \frac{2\pi\hbar c}{d} n^2 N \exp\left\{-\frac{4\pi h}{\gamma\beta\lambda_n}\sqrt{1+\gamma^2\beta^2\sin^2\theta\sin^2\xi}\right\} \times \frac{|[\mathbf{n}[\mathbf{n}\mathbf{G}_n]]|^2}{(1/\beta-\cos\theta)^3}. \tag{7.4.14}$$

Here, as before $\mathbf{n} = \mathbf{k}/\omega$ is the unit vector, the vector $\mathbf{G}_n$ is determined by the surface current induced on the surface of a tilted strip:

$$\mathbf{G}_n = \{G_x, G_y, G_z\} = \mathrm{A}\{\tan\theta_0,\ 2ik_y\lambda_e\ \tan\ \theta_0, 1\},$$
$$\mathrm{A} = \frac{2\lambda_e\left(\exp\left[\frac{a\sin\theta_0}{2\lambda_e} + i\chi a\cos\theta_0\right] - 1\right)}{(\tan\theta_0 + 2i\chi\lambda_e)d}. \tag{7.4.15}$$

In formulae (7.4.14) and (7.4.15) the following designations are used:

$$\lambda_e = \frac{\gamma\beta\lambda_n}{4\pi\sqrt{1+\gamma^2\beta^2\sin^2\theta\sin^2\xi}},$$
$$\chi = \frac{2\pi}{\lambda_n}\left(\frac{1}{\beta} - \cos\theta - \sin\theta\sin\xi\tan\theta_0\right). \tag{7.4.16}$$

Introducing, as before, the radiation factor $|R_n|^2$, the formula (7.4.14) can be rewritten in the form similar to (7.3.8) with the following replacement:

$$|R_n|^2 = \frac{2\pi n^2}{\sin^2\theta\cos^2\xi}|[\mathbf{n}[\mathbf{n}\,\mathbf{G}_n]]|^2. \tag{7.4.17}$$

For the case of flat grating, i.e. in case of $\theta_0 = 0$ and $\xi = 0$ instead of (7.4.15) we have

$$\mathbf{G}_n = i\frac{1-\exp\left[i\frac{2\pi na}{d}\right]}{2\pi n}\{0,\ 0,\ 1\}. \tag{7.4.18}$$

Having in mind the relation $|[\mathbf{n}[\mathbf{n}\,\mathbf{G}_n]]|^2 = \mathbf{G}_n^2 - (\mathbf{G}_n\mathbf{n})^2$ for a considered case we obtain

$$|[\mathbf{n}[\mathbf{n}\,\mathbf{G}_n]]|^2 = \frac{1}{\pi^2 n^2}\sin^2\left(\pi n\frac{a}{d}\right)\sin^2\theta. \tag{7.4.19}$$

As it follows from (7.4.19), for the strip width $a = d/2$ in the Smith–Purcell radiation spectrum only the odd orders remain.

It should also be noted that in the case of a flat grating the direct dependence of expression (7.4.14) on the diffraction order n disappears after the substitution (7.4.15) in the initial formula. We shall also note that for a flat grating the radiation factor (7.4.17) in the model of surface currents does not depend on the electron energy as well as on outgoing angle of the SPR photon (at $\xi = 0$) as well:

$$|R_n|^2 = \frac{2}{\pi}\sin^2\left(\pi n\frac{a}{d}\right). \tag{7.4.20}$$

Figure 7.11 shows the SPR angular distribution calculated by the described model. The calculations were carried out for a flat grating ($\theta_0 = 0$) and grating with tilted strips ($\theta_0 = 30^\circ$) for the following parameters: $n = 1, \gamma = 12, d = 8$ mm, $a = d/2$, $\xi = 0^\circ$. As it follows from Fig. 7.11, in the latter case for observation angle $\theta = 30°$, the SPR intensity vanishes (radiation along the surface of a tilted strip is absent). Figure 7.12 shows similar curves for a flat grating with the same parameters for the values $\gamma = 20$ and $\gamma = 50$.

As it follows from the presented results, according to the model of surface currents, with growing of the initial electron energy, the SPR yield is increased in the whole range of polar angles. Finally, Fig. 7.13 shows the azimuthal dependence of the SPR yield for a flat grating (curve 1) and for the grating with tilted strips (curve 2). As it can be seen from the figure, the two-modal distribution is observed in the latter case.

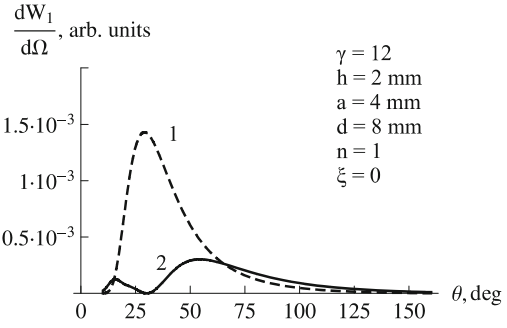

Fig. 7.11 The angular distribution of the Smith–Purcell radiation intensity according to the model of surface currents for a flat grating ($\theta_0 = 0^\circ$, *curve 1*), for the three-dimensional grating ($\theta_0 = 30^\circ$, *curve 2*)

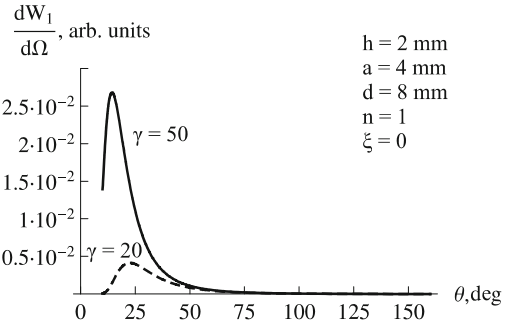

Fig. 7.12 The same as in Fig. 7.11 for a flat grating and various values of Lorentz-factor

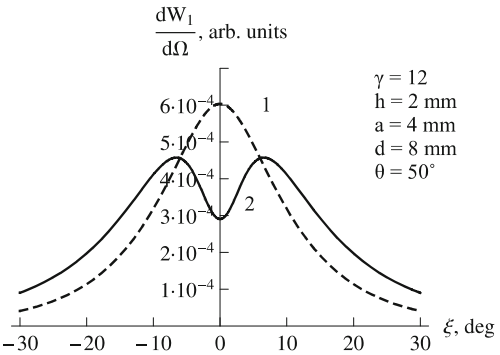

Fig. 7.13 The azimuthal dependence of the SPR yield according to the model of surface currents for a flat grating (*curve 1*) and for the volume grating ($\theta_0 = 30^o$, *curve 2*)

7.5 Smith–Purcell Effect as a Resonant Diffraction Radiation

The relationship between the Smith–Purcell radiation and the resonant diffraction radiation (RDR) is easy to see considering the same grating formed from the perfectly conducting strips, which was studied in the previous paragraph [8]. The diffraction radiation with a wavelength λ occurs during the flight of a charged particle in vacuum near a conducting medium, i.e. if the condition $h \leq \gamma\lambda/2\pi$ is satisfied. In contrast to transition radiation, in case of generation of the diffraction radiation a charged particle does not interact with a material of target directly.

One of the known models of diffraction radiation (DR) is the model of Kazantsev–Surdutovich [13], which describes the DR generation during the flight of a charged particle near a perfectly conducting tilted half-plane. It should be noted that such a description with good accuracy can be used for wavelengths range $\lambda \geq 1$ μm, for targets with polished metallic surface.

In a full analogy with the resonant transition radiation (see Chap. 5) the spectral–angular distribution of the RDR from a flat grating can be written as follows:

$$\frac{d^2W_{\mathrm{RDR}}}{\hbar\, d\omega\, d\Omega} = \frac{d^2W_{\mathrm{DR}}}{\hbar\, d\omega\, d\Omega} F_2 F_3\,, \tag{7.5.1}$$

where the first factor describes the spectral–angular distribution of the elementary processes (diffraction radiation at edge of the half-plane), the second—the interference of radiation on one period (from both edges of the strip), and the third—the interference of N periodically arranged sources. Multipliers F_2, F_3 have the same form as in the X-ray RTR theory:

$$F_2 = 4\sin^2\frac{\varphi_{\mathrm{c}}}{2},$$
$$F_3 = \frac{\sin^2(N\varphi_0/2)}{\sin^2(\varphi_0/2)} \approx 2\pi N\delta(\varphi_0 - 2k\pi).$$

Here, as usually, N is the number of periods of target ($N \gg 1$), the phases φ_{c}, φ_0 are defined as follows:

$$\varphi_{\mathrm{c}} = \frac{2\pi}{\lambda}a\left(\cos\theta - \frac{1}{\beta}\right), \quad \varphi_0 = \frac{2\pi}{\lambda}d\left(\cos\theta - \frac{1}{\beta}\right). \tag{7.5.2}$$

As was to be expected, from the argument of δ-function and the second equation (7.5.2) follows the Smith–Purcell dispersion relation. So, if we have the spectral–angular distribution of diffraction radiation from the edge of the half-plane, it is possible to find all the characteristics of the Smith–Purcell radiation, which is considered as RDR.

The formula for the spectral–angular distribution of diffraction radiation of a charge, moving in parallel to the perfectly conducting half-plane, was found in [13]:

$$\frac{d^2W_{\mathrm{DR}}}{\hbar\, d\omega\, d\Omega} = \frac{\alpha}{2\pi^2}\frac{\exp\left(-\frac{4\pi h}{\gamma\beta\lambda}\sqrt{1+\beta^2\gamma^2\cos^2\psi}\right)}{\beta\sin\psi} \times \frac{\cos^2\psi\cos^2\frac{\varphi}{2}(1-\beta\sin\psi) + \left(\gamma^{-2}+\beta^2\cos^2\psi\right)\sin^2\frac{\varphi}{2}(1+\beta\sin\psi)}{\left(\gamma^{-2}+\beta^2\cos^2\psi\right)\left(\sin\psi\cos\varphi - \frac{1}{\beta}\right)^2}. \tag{7.5.3}$$

Angular variables φ, ψ are shown in Fig. 7.14.

For ultrarelativistic particles DR is concentrated near the plane, which is perpendicular to the plane of the target (it means in the range of azimutal angles $\sim\gamma^{-1}$).

Going to the angular variables θ_x, θ_y, which are connected with a geometry of the problem (Fig. 7.14b)

$$\psi = \frac{\pi}{2} - \theta_x; \quad \varphi = \theta_y, \tag{7.5.4}$$

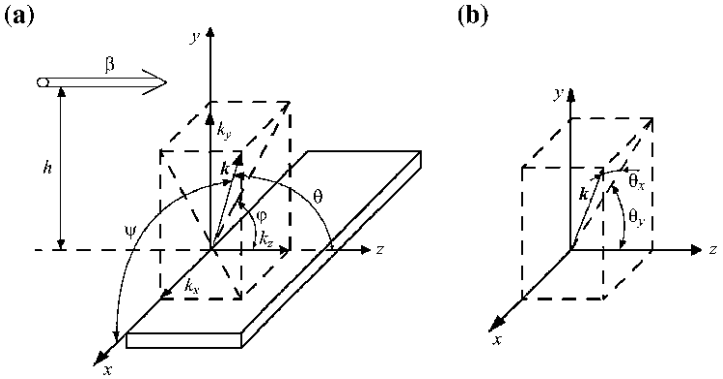

Fig. 7.14 The angular variables for the description of diffraction radiation in case of the parallel passing of a charge above the conducting strip

the expression (7.5.3) is essentially simplified:

$$\frac{d^2W_{\mathrm{DR}}}{\hbar\, d\omega\, d\Omega} = \frac{\alpha}{4\pi^2}\,\frac{\exp\left(-\frac{4\pi h}{\gamma\beta\lambda}\sqrt{1+\gamma^2\beta^2\sin^2\theta_x}\right)}{\beta\cos\theta_x\left(1+\beta^2\gamma^2\sin^2\theta_x\right)\left(\frac{1}{\beta}-\cos\theta_x\cos\theta_y\right)^2}$$
$$\times\left[\gamma^2\sin^2\theta_x\left(1+\cos\theta_y\right)\left(1-\beta\cos\theta_x\right)\right.$$
$$\left.+\left(1+\gamma^2\beta^2\sin^2\theta_x\right)\left(1-\cos\theta_y\right)\left(1+\beta\cos\theta_x\right)\right]. \qquad (7.5.3\,\mathrm{a})$$

Neglecting the terms $\sim\gamma^{-2}$, θ_x^2 instead of expression (7.5.3a) we will have

$$\frac{d^2W_{\mathrm{DR}}}{\hbar\, d\omega\, d\theta_x\, d\theta_y} = \frac{\alpha}{2\pi^2}\,\frac{\exp\left(-\frac{4\pi h}{\gamma\lambda}\sqrt{1+\gamma^2\theta_x^2}\right)}{1-\cos\theta_y}. \qquad (7.5.5)$$

The last expression is valid for outgoing angles $\theta_y \gg \gamma^{-1}$, whereas for angles $\theta_y \sim \gamma^{-1}$ we obtain from (7.5.3)

$$\frac{d^2W_{\mathrm{DR}}}{\hbar\, d\omega\, d\theta_x\, d\theta_y} = \frac{\alpha}{\pi^2}\exp\left(-\frac{4\pi h}{\gamma\lambda}\sqrt{1+\gamma^2\theta_x^2}\right)\frac{\theta_x^2+\theta_y^2}{\left(\gamma^{-2}+\theta_x^2+\theta_y^2\right)^2}. \qquad (7.5.6)$$

It can be noted that the formula (7.5.6) is similar in structure to the formula describing the spectral-angular distribution of transition radiation in case of crossing the boundary "vacuum-perfectly conducting medium", if $h \ll \gamma\lambda/4\pi$.

Let us also write down the relationship between frequently used photon outgoing angles θ, ξ in the coordinate system connected with electron velocity (see Fig. 7.14):

$$\begin{aligned}\cos\psi &= \sin\theta_x = \sin\theta\sin\xi,\\ \tan\varphi &= \tan\theta_y = \tan\theta\cos\xi,\end{aligned} \qquad (7.5.7)$$

as well as the reverse formulae

$$\cos\theta = \cos\theta_x \cos\theta_y = \sin\psi\cos\varphi\,,$$
$$\tan\xi = \frac{\sin\theta_x}{\cos\theta_x \sin\theta_y} = \frac{\cos\psi}{\sin\psi\sin\varphi}. \tag{7.5.8}$$

Integrating (7.5.1) using the δ-function, it is easy to obtain the angular density of energy emitted on a wavelength corresponding to the kth order of diffraction:

$$\frac{dW_k}{d\theta_x d\theta_y} = \frac{4\alpha\hbar c}{\pi} N \frac{1}{\lambda_k\left(1-\cos\theta_y\right)} \exp\left\{-\frac{4\pi h}{\gamma\lambda_k}\sqrt{1+\gamma^2\theta_x^2}\right\}. \tag{7.5.9}$$

The formula (7.5.9) is written for the ratio $a = d/2$, which is maximizing factor F_2.

For $|k| = 1$ from (7.5.9) we can obtain the angular density of energy in the ultrarelativistic case:

$$\frac{dW_1}{d\Omega} = \frac{4\alpha\hbar\, c}{\pi} N \frac{1}{d(1-\cos\theta)^2} \times \exp\left\{-\frac{4\pi h\sqrt{1+\gamma^2\sin^2\theta\sin^2\xi}}{\gamma d(1-\cos\theta)}\right\}. \tag{7.5.10}$$

Comparing the last formula with (7.4.13) at $a = d/2$, we can see that after multiplying the expression (7.5.10) by $(1 + \cos\theta)/2$ the result coincides with formula (7.4.13). Hence, it follows that the different approaches give a close result for the photon outgoing angle $\theta \le \pi/4$, whereas for large values of the angle θ the diffraction scalar theory, as well as a model of induced current, gives a little bit smaller value for the spectral–angular density of RDR.

In the recent work [14] the authors showed that the analytical solution of the diffraction radiation problem in case of flying near the tilted perfectly conducting half-plane [13] (solution of Kazantsev–Surdutovich) has the limited range of applicability. In the cited work the following solution was found, which noticeably differs from the Kazantsev–Surdutovich formula for the parallel flight:

$$\begin{aligned}\frac{dW_k}{d\omega\, d\Omega} &= \frac{e^2}{4\pi^2 c}\frac{\exp\left\{-\frac{4\pi h}{\gamma\beta\lambda}\sqrt{1+(\gamma\beta\sin\theta\sin\xi)^2}\right\}}{\left[1+(\gamma\beta\sin\theta\sin\xi)^2\right](1/\beta-\cos\theta)^2} \\ &\quad\times\left\{\frac{1}{\gamma^2\beta^2}+(\gamma\sin\theta\sin\xi)^2-(\sin\theta\sin\xi)^2\left(\frac{1}{\gamma\beta}-\gamma\cos\theta\right)^2\right\} \\ &= \frac{e^2}{4\pi^2 c}\frac{\exp\left\{-\frac{4\pi h}{\gamma\beta\lambda}\sqrt{1+(\gamma\beta\sin\theta_x)^2}\right\}}{\left[1+(\gamma\beta\sin\theta_x)^2\right]\left[1/\beta-\cos\theta_x\cos\theta_y\right]^2} \\ &\quad\times\left\{\frac{1}{\gamma^2\beta^2}+\gamma^2\sin^2\theta_x-\sin^2\theta_x\left(\frac{1}{\gamma\beta}-\gamma\cos\theta_x\cos\theta_y\right)\right\}.\end{aligned} \tag{7.5.11}$$

After substitution of (7.5.11) in (7.5.1) and subsequent integration over frequencies, it is possible to get a formula describing the angular distribution of the SPR intensity:

$$\frac{dW_1}{d\Omega} = \frac{2\alpha}{\pi} N \frac{\hbar c}{d(1/\beta - \cos\theta)^3} \frac{\exp\left\{-\frac{4\pi h\sqrt{1+(\gamma\beta\sin\theta\sin\xi)^2}}{\gamma\beta d(1/\beta-\cos\theta)}\right\}}{1+(\gamma\beta\sin\theta\sin\xi)^2} \times \left[\frac{1}{\gamma^2\beta^2} + (\gamma\sin\theta\sin\xi)^2 - (\sin\theta\sin\xi)^2\left(\frac{1}{\gamma\beta} - \gamma\cos\theta\right)^2\right]. \quad (7.5.12)$$

Comparing the derived expression with formula (7.3.8), it is possible to obtain an expression for the radiation factor in the model of the resonant diffraction radiation:

$$|R_1|^2 = \frac{2}{\pi} \frac{\left[\gamma^{-2}\beta^{-2} + (\gamma\sin\theta\sin\xi)^2 - (\sin\theta\sin\xi)^2(1/\gamma\beta - \gamma\cos\theta)^2\right]}{\sin^2\theta\cos^2\xi\left[1+(\gamma\beta\sin\theta\sin\xi)^2\right]}. \quad (7.5.13)$$

In contrast to the Smith–Purcell radiation models based on a model of induced currents and the RDR, following from the solution of Kazantsev–Surdutovich [13], the radiation factor (7.5.13) depends on the Lorentz-factor, and as it follows from the obtained formula for radiation in the plane being perpendicular to the grating ($\xi = 0$), with increase of energy of initial particle the value of $|R_1|^2$ decreases as γ^{-2}.

With particle energy increasing, the maximum in the angular distribution of SPR is shifted to the range of small polar angles (Fig. 7.15). As can be seen from the figure, in the range of angles, greatly exceeding the value corresponding to the maximum of the distribution, the SPR yield decreases with increasing of γ. Such a dependence gives the Van den Berg model [10] in contrast to the model of surface currents.

It should be noted that, generally speaking, the dependence of the distribution (7.5.12) on the azimuth angle ξ has a "lobe-shape" character.

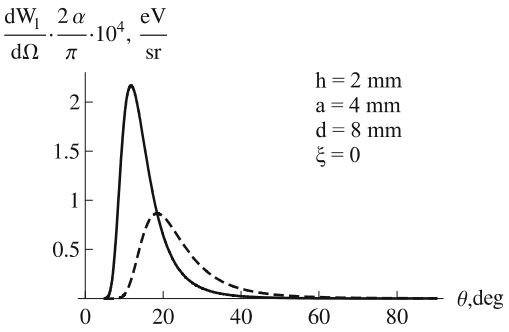

Fig. 7.15 The angular distribution of SPR for a flat grating with the same parameters as in Fig. 7.12 (γ = 20, 50) calculated by the model [14]

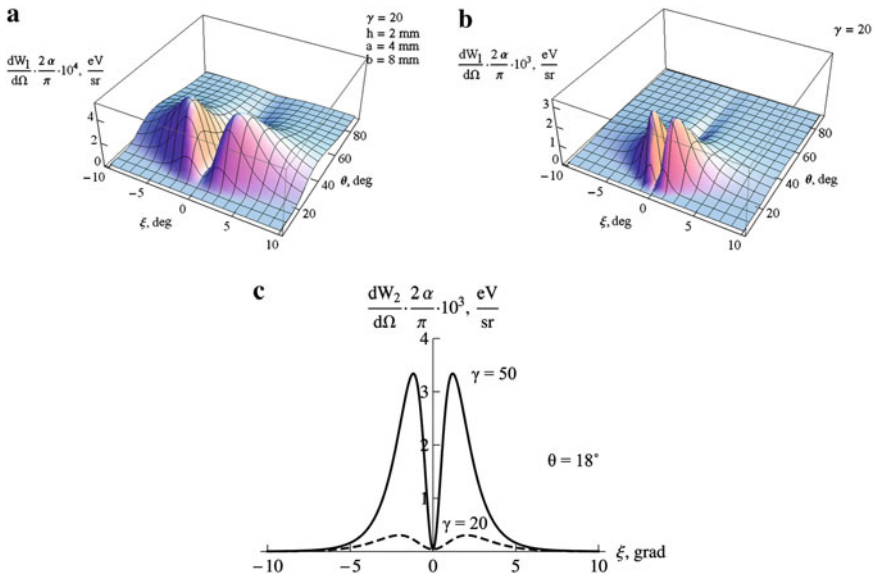

Fig. 7.16 The angular distributions of SPR intensity for various different values of the Lorentz-factor according to the model [14], $\gamma = 20$ (**a**); $\gamma = 50$ (**b**); and azimuthal distribution for both cases (**b**) at $\theta = 18^\circ$

Figure 7.16a, b shows the two-dimensional angular distributions of SPR $dW_1/d\Omega$ for the grating with the same parameters as in Fig. 7.15. As follows from the presented results, the Smith–Purcell radiation intensity for angles $t_x \neq 0$ (azimuthal angles $\xi \neq 0$) can be quite high, see Fig. 7.16c.

Comparing Fig. 7.16a and b, it is possible to note that the radiation intensity in the global maxima grows with the increase of Lorentz-factor, which, as a result, can "overlap" the intensity reduction in the plane being perpendicular to the grating with increasing of γ.

The analytical dependence of the total energy radiated by a particle (radiation losses) cannot be derive even for the simplest flat grating.

The formula for the SPR radiation losses in case of $k = 1$ can be written as

$$W_1 = \int \frac{dW_1}{d\Omega}\, d\Omega = N\frac{\hbar c}{d} Q(h/d, \gamma), \tag{7.5.14}$$

where $Q(h/d, \gamma)$ is a function, which depends only on the ratio h/d and the Lorentz-factor.

Figure 7.17 shows the results of calculations of $W_1(\gamma)$ for two values of $h/d = 1/4, 1/8$. One may see this dependence with accuracy of a few percent may be described by a function

$$W_1(\gamma) \sim \gamma^{1/2}.$$

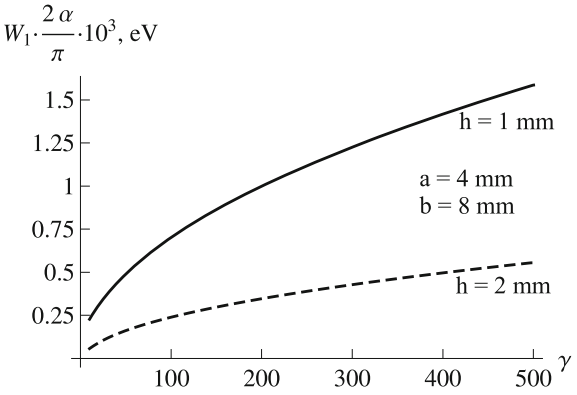

Fig. 7.17 The dependence of the radiation losses through the mechanism of SPR for $k = 1$ depending on the Lorentz-factor for various impact-parameters

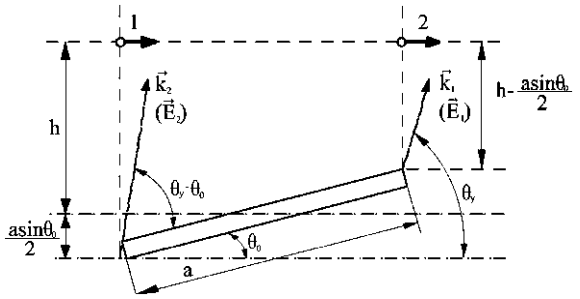

Fig. 7.18 The scheme of diffraction radiation from the inclined strip

It should be noted that the model of surface currents gives a stronger dependence $W_1(\gamma) \sim \gamma^{3/2}$ [12].

7.6 Resonant Diffraction Radiation from Charge Moving Near the Volume Strip Grating

RDR from a charged particle moving near a flat grating consisting of a periodic set of strips, located in a plane was considered in the previous paragraph. A formula for the spectral–angular distribution of diffraction radiation in case of flying near the inclined plane was derived in [14]. In full analogy with the developed approach, so-called volume strip grating, strips of which are inclined relative to the central plane of the grating at an angle θ_0, can be considered. RDR characteristics for such a grating can be calculated by the formula (7.5.1) as well, where the first factor $d^2W_{DR}/\hbar\, d\omega\, d\Omega$ describes the spectral–angular distribution of the DR from the inclined half-plane. The second factor F_2 is determined from the simple scheme (Fig. 7.18).

The electric field of DR from the inclined strip may be found using the principle of superposition of DR fields from the lower and upper edges of the strip with the corresponding phase factor:

$$\begin{aligned}\mathbf{E}_{\text{strip}} &= \mathbf{E}_{\text{low}} + \mathbf{E}_{\text{up}}\, e^{i\Delta\varphi},\\ \mathbf{E}_{\text{low}} &= \mathbf{E}_{\text{DR}}\left(h + \frac{a\sin\theta_0}{2},\ \theta_y\right),\\ \mathbf{E}_{\text{up}} &= -\mathbf{E}_{\text{DR}}\left(h - \frac{a\sin\theta_0}{2},\ \theta_y\right).\end{aligned} \tag{7.6.1}$$

For simplicity, we consider the emission process in the simplest geometry, when the wave vector is placed in a plane which is perpendicular to the strip ($\theta_x = 0$).

The phase $\Delta\varphi$ is determined by the time difference between the fronts of the radiation emitted at an angle θ_y from the edges of the strip, taking into account the time $\Delta t_e = a\cos\theta_0/\beta c$ required for passage of an electron from the point 1 up to the point 2 (Fig. 7.18):

$$\Delta t = \frac{a\cos(\theta_y - \theta_0)}{c} - \frac{a\cos\theta_0}{\beta c}. \tag{7.6.2}$$

A phase shift is found from here [15]:

$$\Delta\varphi = 2\pi\frac{c\,\Delta t}{\lambda} = \frac{2\pi a}{\lambda}\left[\cos(\theta_y - \theta_0) - \frac{\cos\theta_0}{\beta}\right]. \tag{7.6.3}$$

Let us write down the expression for the DR in the form:

$$\mathbf{E}_{\text{DR}}\left(h + \frac{a\sin\theta_0}{2}\right) = \mathbf{E}_{\text{DR}}(h)\exp\left[-\frac{\pi a\sin\theta_0}{\lambda\beta_\perp}\sqrt{1-\beta_\perp^2\sin^2\psi}\right].$$

Using the last formula, the expression (7.6.1) can be written in a more symmetrical form:

$$\begin{aligned}\mathbf{E}_{\text{strip}} = \mathbf{E}_{\text{DR}}(h)\, e^{i\frac{\Delta\phi}{2}}\Bigg\{&\exp\left[-\frac{\pi a\sin\theta_0}{\lambda\beta}\sqrt{1-\beta^2\sin^2\psi}\right]e^{-i\frac{\Delta\phi}{2}}\\ &-\exp\left[\frac{\pi a\sin\theta_0}{\lambda\beta}\sqrt{1-\beta^2\sin^2\psi}\right]e^{i\frac{\Delta\phi}{2}}\Bigg\}.\end{aligned} \tag{7.6.4}$$

The squared modulus expression (7.6.4) can give the spectral–angular distribution of DR from the tilted strip:

$$\frac{d^2W_{\text{strip}}}{d\Omega\, d\omega} = \frac{d^2W_{\text{DR}}}{d\Omega\, d\omega}F_2. \tag{7.6.5}$$

Here $d^2W_{\text{DR}}/d\Omega\, d\omega$ is the spectral–angular distribution of DR from a perfect inclined half-plane, which has the following form [14]:

$$\frac{d^2W}{\hbar\, d\omega\, d\Omega} = \frac{\alpha}{4\pi^2}\ \frac{\left(\cos^2\theta_0 + \gamma^2\sin^2\theta_0\right)\exp\left\{-\frac{4\pi h}{\gamma\beta\lambda}\right\}}{\gamma^2\left[\cos\theta_0 - \beta\cos(\theta-\theta_0)\right]^2 + \sin^2\theta_0}. \tag{7.6.6}$$

The formula (7.6.6) is given for the case $\xi = 0$, i.e. for DR emitted in the plane being perpendicular to the tilted target. The factor F_2 is written as:

$$F_2 = \left|\exp\left(-\chi - i\frac{\Delta\varphi}{2}\right) - \exp\left(\chi + i\frac{\Delta\varphi}{2}\right)\right|^2 = 4\left(\sinh^2\chi + \sin^2\frac{\Delta\varphi}{2}\right). \quad (7.6.7)$$

In the general case, when a DR photon is emitted at angles θ_x, θ_y (or, using standard angular variables θ, ξ) the quantities χ, $\Delta\varphi/2$ in expression (7.6.7) are written as follows:

$$\chi = \frac{\pi a \sin\theta_0}{\lambda\beta}\sqrt{1 - \beta^2\sin^2\psi} = \frac{\pi a \sin\theta_0}{\lambda\beta\gamma}\sqrt{1 + \gamma^2\beta^2\sin^2\theta\sin^2\xi},$$
$$\frac{\Delta\varphi}{2} = \frac{\pi a}{\lambda}\left[\cos\theta\cos\theta_0 + \sin\theta\sin\theta_0\cos\xi - \frac{\cos\theta_0}{\beta}\right]. \quad (7.6.8)$$

For the volume strip grating, an element of which is a tilted strip and a vacuum gap with a period d, the interference factor F_3 is again approximated by a δ-function (if the number of periods $N \gg 1$), the argument of which is determined by a period d, a particle velocity β and polar angle of a photon emission θ. It should be noted that unlike the first two factors ($d^2W/d\omega\, d\Omega$ and F_2) the factor F_3 does not depend on the azimuthal angle ξ. As well as in the previous cases, the δ-function again removes the integration over one variable. For angles of radiation $\theta_{\min} \le \theta \le \theta_{\max}$ (see Fig. 7.10) it is possible to neglect the effects of wave "re-scattering" by subsequent strips.

Figure 7.19 shows the SPR angular distributions, calculated by formula (7.6.6) for a flat grating (the lower curve) and for the grating with tilted strips $\theta_0 = 30^o$ (the upper curve). For convenience of comparison, the lower curve is multiplied by 10. The figure shows that the model [14] does not lead to a SPR yield vanishing along the surface of the strip.

Figure 7.20 shows the results of calculations for $\theta_0 = 0$ (the lower curve) and $\theta_0 = \pi/2$, (the upper one) for $\gamma = 200$. It can be noted, firstly, that the radiation intensity from the "flat" grating is much lower than from the volume strip one,

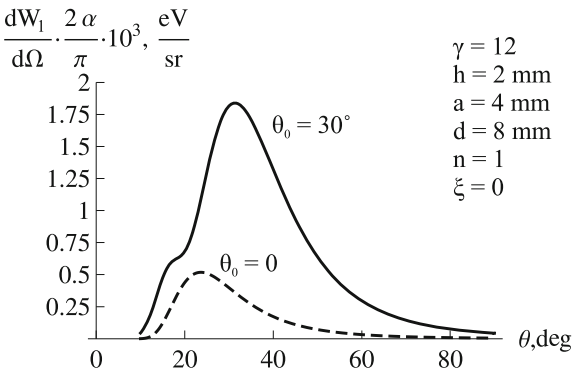

Fig. 7.19 The same, as in Fig. 7.11 according to the model [14]

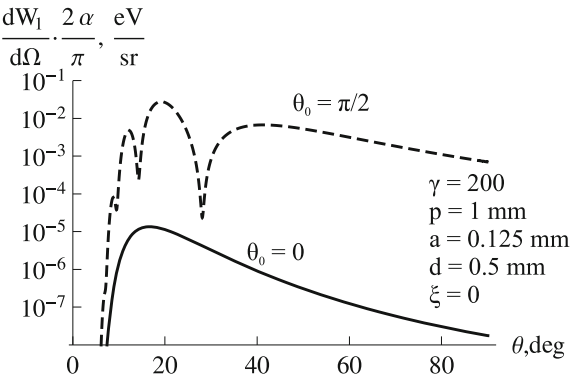

Fig. 7.20 Comparison of angular distributions of SPR for a flat grating ($\theta_0 = 0$) and a volume strip one ($\theta_0 = \pi/2$)

and, secondly, for the latter grating the sharp minima of the radiation intensity for certain values of the polar angle are observed.

For the strip inclination angle $\theta_0 = \pi/2$ the angles corresponding to a SPR yield minima are calculated analytically from the requirement of the zeroth second term in F_2 [see formula (7.6.7)]: $\Delta\varphi/2 = m\pi$, m is integer. Hence we have $a \sin\theta/\lambda = m$.

Substituting the Smith–Purcell ratio $\lambda_n = \frac{d}{n}\left(\frac{1}{\beta} - \cos\theta\right)$ in the last expression, it is possible to find the values of the photon emission angles, for which the radiation intensity is minimal (for the first diffraction order, $k = 1$):

$$\tan\frac{\theta_1^{\min}}{2} \approx \frac{a}{md}, \quad m = 1, 2, 3\ldots \tag{7.6.9}$$

The terms $\sim\gamma^{-2}$ are omitted in the formula (7.6.9).

The dependence of the SPR yield on the ratio a/d is shown in Fig. 7.21 for a flat grating and a perpendicular volume strip one ($\theta_0 = \pi/2$). As was to be expected, in the first case the maximal yield corresponds to the value $a/d = 1/2$, whereas for the second one this dependence has a more complicated form.

For a flat grating the ratio $a/d = 1/2$, providing the maximal SPR yield, is universal, whereas for the volume strip grating this ratio will be determined by the polar angle θ and by the order of diffraction in analogy with the derivation of formula (7.6.9).

For the considered case ($\theta_0 = \pi/2$, $\xi = 0$) it follows from (7.6.8):

$$\frac{a}{d} \approx m\frac{1-\cos\theta}{\sin\theta} = \frac{m}{2}\tan\theta/2, \quad m = 1, 2, 3\ldots \tag{7.6.10}$$

7.7 Experimental Studies of Smith–Purcell Radiation

Many experimental studies of the characteristics of the SPR with electron energies from 20 keV to 28 GeV in the interval of wavelengths from the millimeter range up to optical one have been carried out since the first observation of the

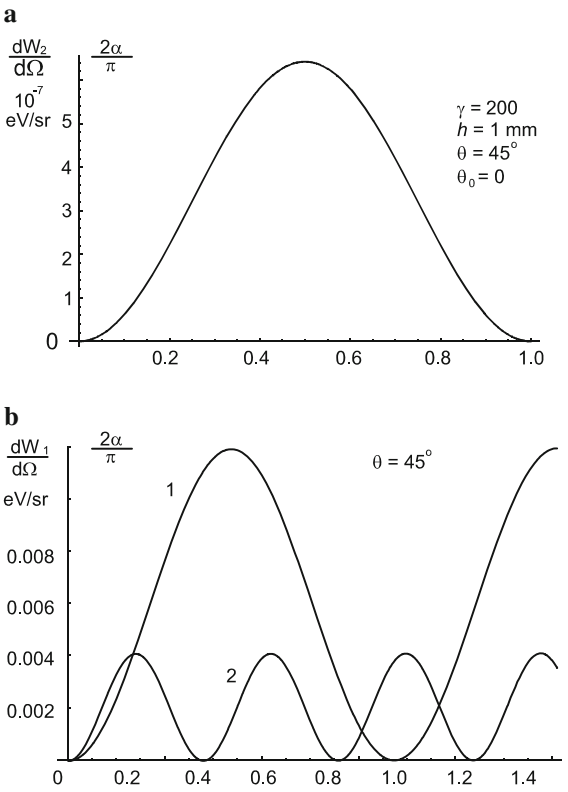

Fig. 7.21 The dependence of the SPR yield on ratio *a/d* for the flat grating **a** and volume strip one **b** for $\theta_0 = \pi/2$ (*curve 1*) and $\theta_0 = \pi/4$ (*curve 2*)

Smith–Purcell effect. This interest is connected, firstly, with the possibility of using of the Smith–Purcell effect for the creation of compact sources of radiation with tunable wavelength, including free-electron lasers, and, secondly, for non-invasive diagnostics of the accelerated beams parameters.

One of the first experiments [16] was carried out with a beam of electrons with energies less than 100 keV and diameter of 200 μm, where the optical grating with a lamellar profile and period of 1.4 μm was used as a target. In this experiment it was shown that the azimuthal distribution of the Smith–Purcell radiation is two-modal with a pronounced minimum in the plane being perpendicular to the grating (at $\xi = 0^{\circ}$). The measurement results are shown in Fig. 7.22.

The results presented in Fig. 7.22 were obtained for a beam with energy 100 keV, with divergence less than 1 mrad and current $I = 0.22$ μA with the aperture of the detector $\Delta\Omega = 0.005$ steradian.

As it can be seen from the figure, in the distribution maximum at $\theta = 106^{\circ}$, $\xi = 55^{\circ}$ the brightness of radiation per 1 μA accelerated current reaches the value

$$\frac{\Delta Y}{\Delta\Omega} = \frac{P}{\Delta\Omega I} = 2.7 \times 10^{-9} \frac{\mathrm{W}}{\mu\mathrm{A} \times \mathrm{sterad}} = 2.7 \times 10^{-3} \frac{\mathrm{eV}}{e^{-} \times \mathrm{sterad}}.$$

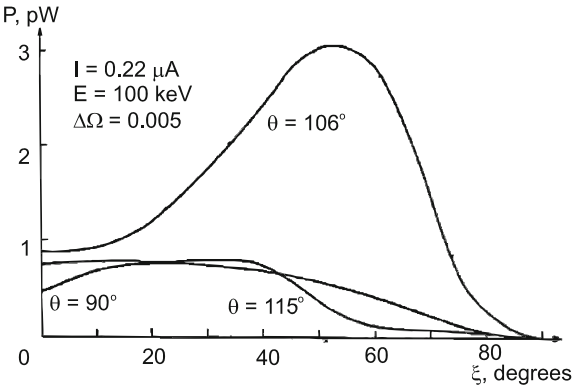

Fig. 7.22 The azimuthal distribution of the Smith–Purcell radiation for various polar angles of observation [16]

As it was noted above, the beam diameter was around 200 μm, i.e. the average distance between an axis of a beam and a grating was about 100 μm. For the radiation wavelength less than 1 μm (the optical range) this distance significantly reduced the transformation efficiency of beam energy into the radiation energy.

As it follows from (7.2.4), the electrons flying above a grating at a distance $h \gg h_{\text{int}}$, where

$$h_{\text{int}} = \frac{\beta\lambda}{4\pi\sqrt{\gamma^{-2} + \beta^2 \sin^2\theta \sin^2\xi}}, \tag{7.7.1}$$

practically "do not see" the grating, i.e. there is no radiation.

In the experiment [17] for the first time there was observed the Smith–Purcell radiation from the relativistic electrons. The beam of electrons with energy 3.6 MeV was generated by the Van de Graaff accelerator with the following parameters:

– beam sizes: 3×6 mm^2 (3 mm in a direction being perpendicular to the grating);
– accelerated current: 50–200 mA.

In the experiment there was used the grating with a triangle profile and a period of 760 μm. The radiation emission spectrum was measured by a monochromator and a helium-cooled InSb-bolometer (see Fig. 7.23).

The measured spectrum for the angle $\theta = 115^{\circ}$ is shown in Fig. 7.24. It follows from the Smith–Purcell formula that an expected value of the wavelength for $|n = 1|$ is $\lambda = 1{,}088$ μm, which is consistent with experiment.

The absolute measurements of the Smith–Purcell radiation power in the far infrared range were carried out in [18] using a beam of electron microscope with energy of 40 keV, current of ~ 100 μA and with various gratings (with the period from 100 up to 250 μm). The maximal brightness of the Smith–Purcell radiation has been obtained for the wavelength $\lambda \sim 500$ μm, where it achieves a value $\Delta Y/\Delta\Omega \sim 10^{-10}$ W/μA × sterad, what is much lower than the Smith–Purcell radiation brightness in the optical range.

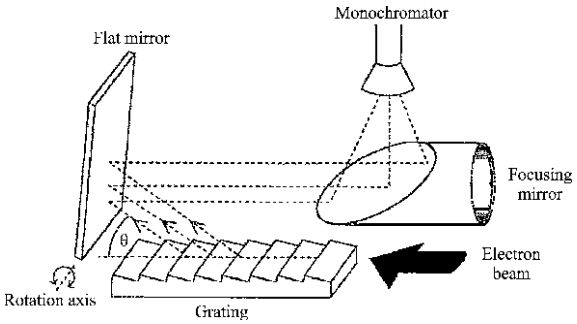

Fig. 7.23 The scheme of the experiment for studying the Smith–Purcell radiation in mm-range

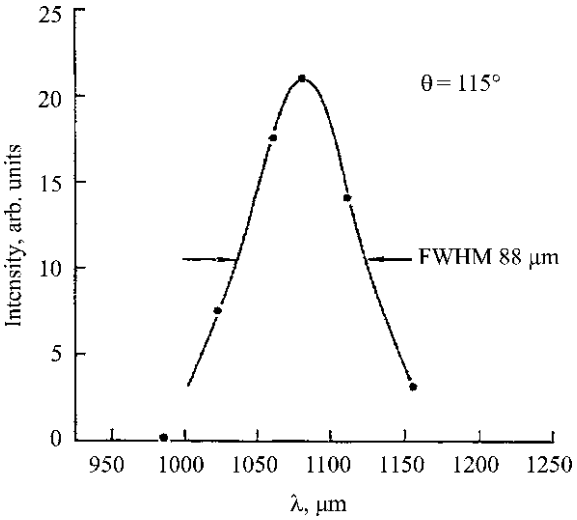

Fig. 7.24 The measured shape of line in the Smith–Purcell radiation spectrum in the experiment [17]

The Smith–Purcell radiation in the optical range generated by a beam of ultrarelativistic electrons with energy of $E = 855$ MeV was studied in the recent experiment [19]. The experimental set-up is shown in Fig. 7.25.

It should be noted that in this experiment the vertical size of a beam (in the direction being perpendicular to the grating) did not exceed 20 μm, which allows to exclude completely the interaction of the peripheral part of the beam (halo) with the material of the grating. Figure 7.26 shows the measurement results of the Smith–Purcell radiation yield for two wavelength ranges 546 ± 15 nm (above) and 360 ± 15 nm (below). The measurements were carried out for the beam passing above the grating with a period of 0.833 μm, at a distance of 127 μm at the angle of observation θ (see Fig. 7.25). The expected positions of the Smith–Purcell radiation peaks are marked by the dashed lines for the different orders of diffraction. The experiment is consistent with the Smith–Purcell formula very well.

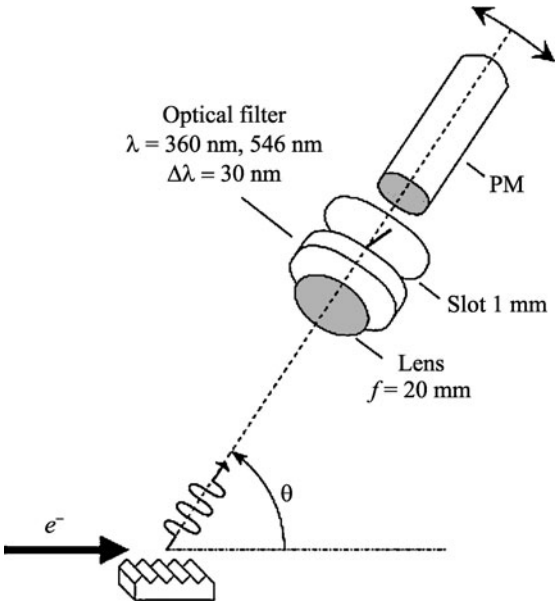

Fig. 7.25 The scheme of the experiment [19] for study of the Smith–Purcell optical radiation from a beam of electrons with energy 855 MeV

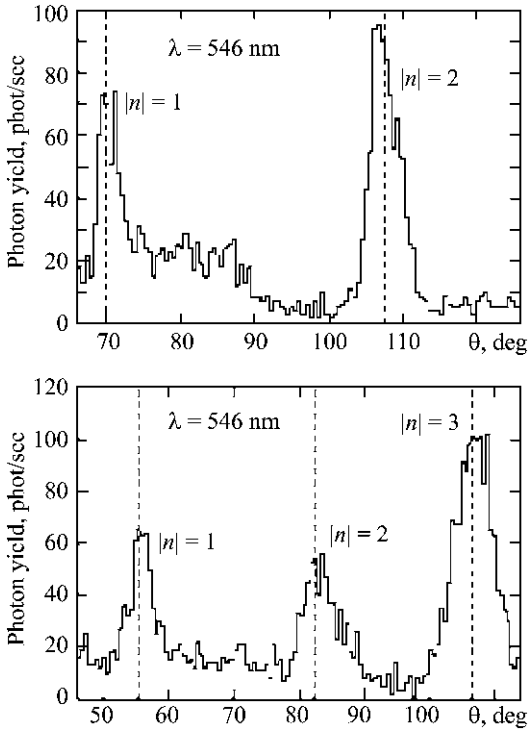

Fig. 7.26 The Smith–Purcell radiation yield for the fixed wavelength of $\lambda = 546 \pm 15$ nm (*above*) and $\lambda = 360 \pm 15$ nm (*below*) depending on an angle of observation θ

The measured photon yield of the Smith–Purcell radiation with wavelength of $\lambda = 0.36$ μm ($\hbar\omega = 3.5$ eV) was $\Delta N/\Delta\Omega \approx 10^{-3}ph/e^-$ × sterad, or going to the radiation brightness,

$$\frac{\Delta Y}{\Delta\Omega} = 3.5 \times 10^{-3} \frac{\text{eV}}{e^- \times \text{sterad}}.$$

As it was noted by the authors of the experiment [19], the measured value is well consistent with the Van den Berg theoretical model [6].

References

1. Jackson, J.D.: The classical electrodynamics. NY (1998)
2. Smith, S.J., Purcell, E.M.: Visible light from localized surface charges moving across a grating. Phys. Rev. **92**, 1069 (1953)
3. Ishizuka, H., Kawamura, Y., Yokoo, K., et al.: Smith–Purcell experiment utilizing a field-emitter array cathode: measurements of radiation. Nucl. Instrum. Methods. A **475**, 593–598 (2001)
4. Bolotovskiy, B.M., Burtsev, A.K.: Emission from charge flying above grating. Opt. Spectrosc. **19**, 470 (1965). (in Russian)
5. Bolotovskiy, B.M., Voskresenskiy, G.V.: Emission from charged particles in periodic structures. Physics-Uspekhi **94**, 377 (1968). (in Russian)
6. Van den Berg, P.M.: Smith–Purcell radiation from a point charge moving parallel to a reflection grating. J. Opt. Soc. Am **63**, 1588–1597 (1973)
7. Brownell, J.H., Walsh, J., Doucas, G.: Spontaneous Smith–Purcell radiation described through induced surface currents. Phys. Rev. E. **57**, 1075–1080 (1998)
8. Potylitsyn, A.P.: Smith–Purcell effect as resonant diffraction radiation. Nucl. Instrum. Methods B **145**, 60–66 (1998)
9. Kube, G.: Calculation of Smith–Purcell radiation from a volume strip grating. Nucl. Instrum. Methods B **227**, 180–190 (2005)
10. Haererle, O., Rullhusen, P., Salone, J.M., et al.: Calculations of Smith–Purcell radiation generated by electrons of 1–100 MeV. Phys. Rev. E **49**, 3340–3352 (1994)
11. Petit, R.: Electromagnetic Theory of Gratings. Springer, Berlin (1980)
12. Brownell, J.H., Doucas, G.: Role of the grating profile in Smith–Purcell radiation at high energies. Phys Rev Special Topics Accelerators and Beams **9**, 092801 (2006)
13. Kazantsev, A.P., Surdutovich, G.I.: Sov. Phys. Dokl. **147**, 74 (1962)
14. Karlovets, D.V., Potylitsyn, A.P.: On the theory of diffraction radiation. JETP **134**, 887–902 (2008)
15. Potylitsyn, A.P., Karataev, P.V., Naumenko, G.A.: Resonant diffraction radiation from an ultrarelativistic particle moving close to a tilted grating. Phys. Rev. E. **61**, 7039 (2000)
16. Gover, A., Dvorkis, P., Elisha, U.: Angular radiation pattern of Smith–Purcell radiation. J. Opt. Soc. Am. B **1**, 723–728 (1984)
17. Doucas, G., Mulvey, J.H., Omori, M., et al.: First observation of Smith–Purcell radiation from relativistic electrons. Phys. Rev. Lett. **69**, 1761–1764 (1992)
18. Goldstein, M., Walsh, J.E., Kimmit, M.F., et al.: Demonstration of a micro far-infrared Smith–Purcell emitter. Appl. Phys. Lett. **71**, 452–454 (1997)
19. Kube, G., Backe, H., Euteneur, H. et al.: Observation of optical Smith–Purcell radiation at an electron beam energy of 855 MeV. Phys. Rev. E. **65**, 056501-1–056515-15 (2002)

Chapter 8
Radiation of Electrons in the Field of Intense Laser Wave

8.1 Scattering of a Weak Electromagnetic Wave on a Rest Electron (Non-Relativistic Approximation)

In the late nineteenth century J. Thomson considered the problem of electromagnetic wave scattering with frequency ω_0 by a free rest particle with mass m and charge e. Thomson solved the task neglecting the influence of the magnetic field of the wave on the movement of particle (in modern terminology—neglecting terms $\sim v/c$, i.e. in the nonrelativistic case). If an initial linearly polarized wave propagates along the axis z and the electric vector oscillation plane coincides with the plane $x0z$, then the free charge e also oscillates in this plane under the influence of an oscillating force $\mathbf{F} = e\mathbf{E}_0 \cos \omega_0 t$ (Fig. 8.1).

If the influence of wave on the electron is weak enough (the amplitude of oscillations is much smaller than the wavelength), then acceleration may be written directly from the Newton's law

$$\dot{\upsilon} = \frac{e}{m}\mathbf{E}_0, \quad \mathbf{E}_0 = \{E_0 \cos \omega_0 t,\ 0,\ 0\}. \tag{8.1.1}$$

In this approximation, the particle oscillates in the plane $z = \text{const}$, i.e. without moving along the wave vector of the incident wave. The oscillation amplitude is easily found from the Eq. (8.1.1):

$$x_m = \frac{eE_0}{m\omega_0^2}. \tag{8.1.2}$$

The intensity of the wave is characterized by the dimensionless parameter of the field strength [see Eq. (2.1.14)]:

$$a_0 = \sqrt{\frac{2e^2\langle \mathbf{A}^2 \rangle}{(mc^2)^2}} = \frac{eE_0}{mc\omega_0} = \sqrt{\frac{2r_0 I \lambda_0^2}{\pi m c^3}}. \tag{8.1.3}$$

A. P. Potylitsyn, *Electromagnetic Radiation of Electrons in Periodic Structures*, Springer Tracts in Modern Physics, 243, DOI: 10.1007/978-3-642-19248-7_8,

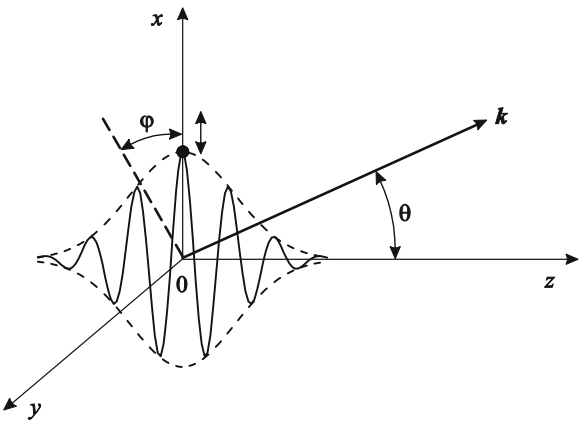

Fig. 8.1 Scattering of a linearly polarized electromagnetic wave on a rest electron. The wave vector of the scattered wave is characterized by the polar angle θ and azimuthal angle φ

In (8.1.3) the symbol $\langle\ \rangle$ denotes the averaging over time, which is significantly greater than the period of wave $T_0 = 2\pi/\omega_0$, r_0 is the classical radius of electron, λ_0 is a wavelength, I is concentration of power of electromagnetic radiation per unit area. If the parameter a_0 satisfies a condition

$$a_0 \geq 1, \tag{8.1.4}$$

it refers to the intense wave.

The amplitude of the oscillations in the field of linearly polarized wave (8.1.2) in the nonrelativistic approximation is expressed through the parameter a_0 and wavelength:

$$x_m = a_0 \frac{\lambda_0}{2\pi}. \tag{8.1.5}$$

It is clear that in a field of the "weak" wave ($a_0 \ll 1$) the amplitude of oscillations is much less than the wavelength, and velocity of a particle $v_x = \dot{x} \sim eE_0/m\omega_0 = a_0 c$ is much smaller than the light speed. For a circularly polarized wave the electric vector of a field can be written as

$$\mathbf{E}(t) = E_0 \cos\omega_0 t \times \left\{ \frac{1}{\sqrt{2}},\ \pm\frac{i}{\sqrt{2}},\ 0 \right\}. \tag{8.1.6}$$

Solving the Eq. (8.1.1) for the field (8.1.6), we can obtain the following equations describing the trajectory of a particle in a parametric form:

$$\begin{aligned} x &= -\frac{eE_0}{\sqrt{2}\, m\omega_0^2} \cos\omega_0 t + x_0, \\ y &= \frac{eE_0}{\sqrt{2}\, m\omega_0^2} \sin\ \omega_0 t + y_0, \\ z &= z_0. \end{aligned} \tag{8.1.7}$$

From (8.1.7) implies that the trajectory is nothing else than a circle of radius R centered at a point $\mathbf{r} = \{x_0, y_0, z_0\}$ and it is located in the plane being perpendicular to the wave vector $\mathbf{k}$:

$$(x - x_0)^2 + (y - y_0)^2 = R^2, \quad R = \frac{a_0\, c}{\sqrt{2}\,\omega_0} = \frac{a_0}{\sqrt{2}\,2\pi}\lambda_0. \tag{8.1.8}$$

The power emitted per unit solid angle in the direction $\mathbf{n} = \{\sin\theta\cos\varphi,\ \sin\theta\sin\varphi\,, \cos\theta\}$ is found according to a known charge acceleration $\dot{\mathbf{v}}$:

$$\frac{dP}{d\Omega} = \frac{e^2}{4\pi\, c^3}\left|[\mathbf{n}[\mathbf{n}\,\dot{\mathbf{v}}]]\right|^2 = \frac{e^2}{4\pi c^3}\left\{|\dot{\mathbf{v}}|^2 - |(\mathbf{n}\,\dot{\mathbf{v}})|^2\right\}. \tag{8.1.9}$$

For a linearly polarized wave from (8.1.9) one may obtain

$$\begin{aligned}\frac{dP}{d\Omega} &= \frac{e^2}{4\pi c^3}\frac{e^2}{m^2}E_0^2\left(1 - \sin^2\theta\cos^2\varphi\right)\cos^2\omega_0 t \\ &= \frac{e^4}{4\pi m^2 c^3}E_0^2\left(\cos^2\theta + \sin^2\theta\sin^2\varphi\right)\cos^2\omega_0 t.\end{aligned} \tag{8.1.10}$$

For the unpolarized initial wave the expression (8.1.10) must be averaged over the two polarization states $\left(E_0^2 = \left(E_{0x}^2 + E_{0y}^2\right)\Big/2\right)$. The same result can be obtained by averaging over the azimuthal angle φ, since there is no a chosen plane of oscillations in the initial state. In addition the expression (8.1.10) must be averaged over time $T \gg T_0$. So, we have

$$\left\langle\frac{dP}{d\Omega}\right\rangle = \frac{e^4}{8\pi\, m^2\, c^3}E_0^2 \times \frac{1}{2}\left(1 + \cos^2\theta\right). \tag{8.1.11}$$

The scattering processes are described by an effective cross-section, which is determined as the ratio of power per unit solid angle (8.1.11) to the density of power flux, i.e. power per unit area in the plane being perpendicular to the wave vector:

$$\left\langle\frac{dP}{dS}\right\rangle = \frac{cE_0^2}{8\pi}.$$

Hence,

$$\frac{d\sigma}{d\Omega} = \left\langle\frac{dP}{d\Omega}\right\rangle\Big/\left\langle\frac{dP}{dS}\right\rangle = \left(\frac{e^2}{mc^2}\right)^2\frac{1}{2}\left(1 + \cos^2\theta\right) = r_0^2\frac{1}{2}\left(1 + \cos^2\theta\right). \tag{8.1.12}$$

Integrating (8.1.12) over the solid angle, it is possible to find the total cross-section of scattering, which is named as the Thomson scattering cross-section:

$$\sigma_{\mathrm{T}} = \frac{8}{3}\pi\, r_0^2.$$

For a circularly polarized wave from (8.1.6) and (8.1.9) it can be obtained

$$\frac{dP}{d\Omega} = \frac{e^2}{8\pi c^3}\left(\frac{eE_0}{m}\right)^2 \left(2 - \sin^2\theta\right)\cos^2\omega_0 t. \tag{8.1.13}$$

After time averaging, we have

$$\left\langle \frac{dP}{d\Omega} \right\rangle = \frac{e^4 E_0^2}{8\pi m^2 c^3}\,\frac{1}{2}\left(1 + \cos^2\theta\right).$$

Thus, for a circularly polarized wave the scattering cross-section is given by the same formula (8.1.12).

8.2 The Motion of Electron in a Field of Intense Electromagnetic Wave

In a field of intense wave the electron velocity can be comparable to the light speed. Therefore the characteristics of particle motion are determined by the relativistic equation:

$$\frac{d\mathbf{P}}{dt} = e\left\{\mathbf{E} + \left[\frac{\mathbf{v}}{c}\mathbf{H}\right]\right\}, \tag{8.2.1}$$

which has an analytical solution for a plane wave (see, for example, [1]). If the wave field is described by the vector potential $\mathbf{A}(\eta)$ ($\eta = \omega_0 t - \mathbf{k}_0\mathbf{r}$ is an invariant phase), then the solution of Eq. (8.2.1) is written as

$$\mathbf{P}(\eta) = \frac{e}{c}\mathbf{A}(\eta) + \mathbf{n}_0 \times mc\frac{1}{2}\left(\frac{e\mathbf{A}(\eta)}{mc^2}\right). \tag{8.2.2}$$

The unit vector $\mathbf{n}_0 = \mathbf{k}_0/|\mathbf{k}_0|$ in (8.2.2) is directed along the wave vector of an initial wave, i.e. along the axis z (see Fig. 8.1). In other words, the second term of (8.2.2) shows that under the influence of intense wave the electron acquires a momentum component along a wave vector. Motion of electron in a field of wave in this direction (being perpendicular to **E** and **H**) is characterized by velocity of drift

$$\mathbf{v}_D = c\boldsymbol{\beta}_D = c^2\frac{\langle \mathbf{P}\rangle}{\langle E\rangle}, \tag{8.2.3}$$

where $\langle E\rangle$ denotes the result of averaging of electron energy moving in a field of "strong" electromagnetic wave. After performing the procedure of averaging for the initial rest electron, it is possible to receive

$$\beta_D = \frac{a_0^2}{4 + a_0^2}. \tag{8.2.4}$$

In a system, which moves along z axis with velocity v_D, the electron, on average, is at rest. Namely in this system (so-called R-system) the equation of the trajectory is written rather simply. Coming back to the laboratory system (L-system) is carried out by a standard Lorentz's transformation.

For a linearly polarized wave in the R-system the trajectory defined by the following equations:

$$\begin{aligned} x_R(\eta) &= x_{0R} - \frac{\lambda_R}{2\pi} 2a \sin\eta, \\ y_R(\eta) &= y_{0R}, \\ z_R(\eta) &= z_{0R} + \frac{1}{2}\frac{\lambda_R}{2\pi} a^2 \sin 2\eta. \end{aligned} \tag{8.2.5}$$

In (8.2.5) λ_R indicates the wavelength in R-system, $a^2 = a_0^2/\left(4 + 2a_0^2\right)$ Without loss of generality, we can put $x_{0R} = y_{0R} = z_{0R} = 0$. Then the equation of a trajectory is expressed by a closed formula: $16(k_R z_R)^2 = (k_R x_R)^2\left\{4a^2 - (k_R x_R)^2\right\}$, where $k_R = 2\pi/\lambda_R$ is the wave vector in R-system.

Figure 8.2 shows the changing of the electron trajectory character in the xz-plane with increasing of parameter a_0 [2]. It should be noted that in case of $a_0 = 0.2$ (see Fig. 8.2) an electron oscillates slightly deviating from the plane $z = \text{const}$, while with growth of this parameter oscillations become larger both along axes x and z. The particle gets the maximal velocity near a point $x_R = y_R = 0$, $(\eta = 0)$:

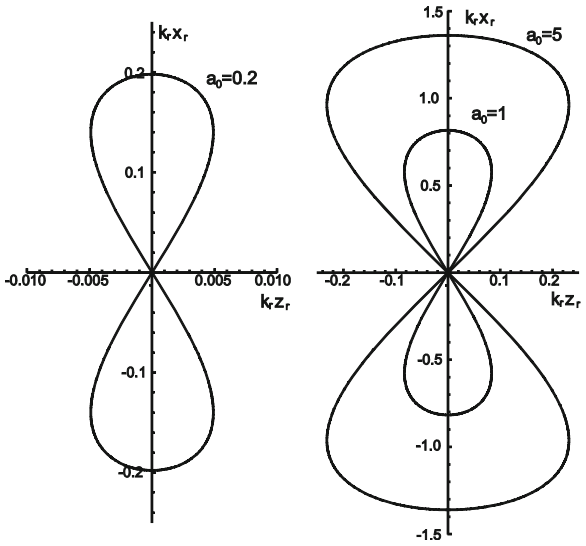

Fig. 8.2 The trajectory of an electron in the R-system under the influence of "strong" linearly polarized wave (the parameter of the field strength $a_0 = 0.2$—on the *left*; $a_0 = 1$ and 5—on the *right*)

$$v_R^{\max} = \frac{2a\sqrt{1+a^2/4}}{1+a^2}c. \tag{8.2.6}$$

For a circularly polarized wave, the trajectory of an electron in R-system represents a circle with a radius

$$R = \frac{a_0}{\sqrt{2}\sqrt{(1+a_0^2/2)}}\frac{\lambda_R}{2\pi}. \tag{8.2.7}$$

For $a_0 \ll 1$ the expression (8.2.7) with accuracy of order a_0^2 coincides with the formula (8.1.8). However, for the intense wave ($a_0^2 \geq 1$) the trajectory radius increases. In case of moving in a circle the linear velocity of a particle remains constant:

$$v_R = \frac{a_0}{\sqrt{2}\sqrt{1+a_0^2/2}}c. \tag{8.2.8}$$

It is clear that in case of $a_0 \geq 1$ the particle motion becomes relativistic.

8.3 Radiation from Electrons in a Field of the Intense Wave (Classical Consideration)

In the R-system an electron performs the periodic motion in the area with the characteristic size $\ell \leq \lambda_0$. The characteristics of electromagnetic radiation in the wave zone (at distances $L \gg \ell \sim \lambda_0$ from the area of movement of charges) can be obtained according to the classical electrodynamics. Since the particle motion is relativistic, even for uniform circular motion with a frequency ω_R (in the case of a circularly polarized wave) a lot of harmonics will be present in the spectrum. In this case, the angular distribution of radiation power on the nth harmonic is calculated in analogy with the synchrotron radiation.

The Schott formula for the angular distribution of the radiation power of a charge moving in a circular orbit with velocity $v = c\beta$, with a frequency ω, can be written as the sum of squares of Bessel's functions and their derivatives (see Eq. (3.6.3)):

$$\frac{dP}{d\Omega} = \frac{e^2\omega^2}{4\pi c}\sum_n n^2\left\{\cot^2\theta J_n^2(n\beta\sin\theta) + \beta^2 J_n'^2(n\beta\sin\theta)\right\}. \tag{8.3.1}$$

In the formula (8.3.1) θ designates an angle between the wave vector and the axis z passing through the center of the orbit perpendicular to its plane. In R-system the frequency ω_R is connected with the frequency ω_0 of the initial wave in L-system by Lorentz's transformation:

$$\omega_R = \omega_0\sqrt{\frac{1-\beta_D}{1+\beta_D}}. \tag{8.3.2}$$

For the drift velocity (8.2.4) from (8.3.2) we have

$$\omega_{\mathrm{R}} = \frac{\omega_0}{\sqrt{1 + a_0^2/2}}. \tag{8.3.3}$$

Since the electron being at the initial moment at rest is carried away by a wave in the direction of its propagation (a drift velocity is directed along the wave vector), the frequency in R-system decreases in comparison with the initial one in case of increasing of a_0. Substituting the dependence of circulation velocity on field strength (8.2.8) into (8.3.1), we obtain the angular distribution of radiation power on the nth harmonic:

$$\frac{dP_{\mathrm{R}}^{(n)}}{d\Omega_{\mathrm{R}}} = \frac{e^2\omega_{\mathrm{R}}^2}{4\pi c}\frac{a_0^2}{1 + a_0^2/2}n^2\left\{2\frac{\cot^2\theta_{\mathrm{R}}}{a_0^2/\left(1 + a_0^2/2\right)}\right.$$
$$\left.\times J_n^2\left(\frac{a_0}{\sqrt{2}\sqrt{1 + a_0^2/2}}n\sin\theta_{\mathrm{R}}\right) + J_n'^2\left(\frac{a_0}{\sqrt{2}\sqrt{1 + a_0^2/2}}n\sin\theta_R\right)\right\}. \tag{8.3.4}$$

Knowing the power of radiation in R-system, we will find the emitted energy for the case, when the wave packet consisting of the N_0 periods (for example, a wave train of laser flash by length $N_0\lambda_R$) falls on the electron:

$$\frac{dW_R^{(n)}}{d\Omega_R} = \frac{dP_R^{(n)}}{d\Omega_R}\Delta t_R, \quad \Delta t_R = \frac{N_0\lambda_R}{c} = \frac{N_0 \times 2\pi}{\omega_R}.$$

Hence, the energy loss on the nth harmonic

$$\frac{dW_R^{(n)}}{d\Omega_R} = \frac{e^2\omega_R N_0}{2c}\frac{a_0^2}{1 + a_0^2/2} \times n^2\left\{2\frac{\cot^2\theta_R}{a_0^2/\left(1 + a_0^2/2\right)}\right.$$
$$\left.\times J_n^2\left(\frac{a_0}{\sqrt{2}\sqrt{1 + a_0^2/2}}n\sin\theta_R\right) + J_n'^2\left(\frac{a_0}{\sqrt{2}\sqrt{1 + a_0^2/2}}n\sin\theta_R\right)\right\}. \tag{8.3.5}$$

To obtain a similar radiation characteristic in the laboratory system it is necessary to apply the Lorentz's transformation separately to the emitted energy and solid angle:

$$\frac{dW_{\mathrm{L}}^n}{d\Omega_{\mathrm{L}}} = \frac{dW_{\mathrm{R}}^n}{d\Omega_{\mathrm{R}}}\gamma_{\mathrm{D}}(1 + \beta_{\mathrm{D}}\cos\theta_{\mathrm{R}})\frac{d\Omega_{\mathrm{R}}}{d\Omega_{\mathrm{L}}}. \tag{8.3.6}$$

Here and hereinafter γ_D denotes the Lorentz-factor, which describes the motion of R-system [see formula (8.2.4)]:

$$\gamma_{\mathrm{D}} = 1/\sqrt{1 - \beta_{\mathrm{D}}^2} = \frac{1 + a_0^2/4}{\sqrt{1 + a_0^2/2}}. \tag{8.3.7}$$

Expressions (8.3.4) and (8.3.5) depend on the angle θ_R in R-system. Let us write the relationship between the polar angles in the R- and L-systems:

$$\cos\theta_R = \frac{\cos\theta_L - \beta_D}{1 - \beta_D \cos\theta_L}, \quad \sin\theta_R = \frac{\sin\theta_L}{\gamma_D(1 - \beta_D \cos\theta_L)}. \tag{8.3.8}$$

Then a multiplier in (8.3.6), received as a result of transformation of energy W_R, reduces to the following:

$$\gamma_D(1 + \beta_D \cos\theta_R) = \frac{1}{\gamma_D(1 - \beta_D \cos\theta_L)}.$$

Bearing in mind that $d\Omega_R/d\Omega_L = d(\cos\theta_R)/d(\cos\theta_L)$, from (8.3.8) it is possible to obtain

$$\frac{d\Omega_R}{d\Omega_L} = \frac{1}{\gamma_D^2(1 - \beta_D \cos\theta_L)^2}. \tag{8.3.9}$$

It should be noted that all the quantities in $dW_R^{(n)}/d\Omega_R$, concern to R-system, so they should be expressed in terms of variables in the L-system:

$$\begin{aligned} \omega_R &= \frac{\omega_0}{\sqrt{1 + a_0^2/2}}, \\ \cot^2\theta_R &= \frac{1}{(1 + a_0^2/2)} \frac{\left[\cos\theta_L - \frac{a_0^2}{2}\sin^2\frac{\theta_L}{2}\right]^2}{\sin^2\theta_L}. \end{aligned} \tag{8.3.10}$$

After all substitutions from (8.3.5) with the account of (8.3.6) we obtain

$$\begin{aligned} \frac{dW_L^{(n)}}{d\Omega_L} = \frac{e^2\omega_0 N_0}{2c} \frac{a_0^2}{\left[1 + \frac{a_0^2}{2}\sin^2\frac{\theta_L}{2}\right]^3} n^2 \\ \times \left\{ \frac{2\left[\cos\theta_L - \frac{a_0^2}{2}\sin^2\frac{\theta_L}{2}\right]^2}{a_0^2\sin^2\theta_L} J_n^2(n\,z) + J_n'^2(n\,z) \right\}, \end{aligned} \tag{8.3.11}$$

where

$$z = \frac{a_0}{\sqrt{2}} \frac{\sin\theta_L}{1 + \frac{a_0^2}{2}\sin^2\frac{\theta_L}{2}}. \tag{8.3.12}$$

As it was noted above, the electron motion in the R-system for the values $a_0 > 1$ becomes relativistic, which leads to the appearance of higher harmonics with $n > 1$ in a spectrum. Due to the fact that in a field of intense wave in case of $n \gg 1$ the dependence of the emitted energy on the initial wave field intensity $a_0 = eE_0/m\,c\,\omega_0$ is more complex than the trivial quadratic dependence (see Eq. (8.3.11)),

the considered process often referred to as nonlinear Thomson scattering. After appropriate Lorentz transformation in the L-system the frequency of harmonic will depend on the angle of observation:

$$\omega_L^{(n)} = n\omega_0 \frac{1-\beta_D}{1-\beta_D \cos\theta_L} = n\omega_0 \frac{1}{1+\frac{a_0^2}{2}\sin^2\frac{\theta_L}{2}}. \tag{8.3.13}$$

Quantum characteristics (for instance, number of photons ΔN) can be obtained using the Planck formula: $\Delta W = \hbar\omega\,\Delta N$.

Thereby, from (8.3.11) the angular distribution of scattered photons is written in the form (index L is omitted):

$$\frac{dN^{(n)}}{d\Omega} = \frac{1}{\hbar\omega^{(n)}}\frac{dW^{(n)}}{d\Omega} = \frac{e^2 a_0^2 N_0}{2\hbar c}\frac{n}{\left[1+\frac{a_0^2}{2}\sin^2\frac{\theta_L}{2}\right]^2} \times \left\{\frac{2\left[\cos\theta_L - \frac{a_0^2}{2}\sin^2\frac{\theta_L}{2}\right]}{a_0^2\sin^2\theta_L} J_n^2(n\,z) + J_n'^2(n\,z)\right\}. \tag{8.3.14}$$

Besides the angular distribution of scattered photons, the process of radiation is often characterized by the scattering cross-section, which is defined from the relationship:

$$\frac{dN}{d\Omega} = \frac{N_{\text{ph}}}{S_{\text{ph}}}\frac{d\sigma}{d\Omega}.$$

Here N_{ph} is the total number of photons in the wave train (which is expressed through energy of flash A and energy of photon $\hbar\omega_0$), S_{ph} is the area of the focal "spot". Their ratio depends on the parameter a_0 and "length" of the train N_0:

$$\frac{N_{\text{ph}}}{S_{\text{ph}}} = \frac{A}{\hbar\omega_0 S_{\text{ph}}} = \frac{1}{\hbar\omega_0}\frac{A}{\tau}\frac{\tau}{S_{\text{ph}}} = \frac{I}{2\pi\hbar c/\lambda_0}\frac{N_0\lambda_0}{c} = I\lambda_0^2\frac{N_0}{2\pi\hbar c^2} = \frac{\alpha\, a_0^2 N_0}{4\, r_0^2}.$$

Then, from the distribution (8.3.14) the cross-section corresponding to radiation on the nth harmonic can be obtained:

$$\frac{d\sigma^{(n)}}{d\Omega} = 2\,r_0^2\frac{n}{\left[1+\frac{a_0^2}{2}\sin^2\frac{\theta}{2}\right]^2} \times \left\{\frac{2\left[\cos\theta - \frac{a_0^2}{2}\sin^2\frac{\theta}{2}\right]^2}{a_0^2\sin^2\theta} J_n^2(n\,z) + J_n'^2(n\,z)\right\}. \tag{8.3.15}$$

Here and hereinafter, the index L is omitted, since the consideration is performed in the laboratory system only. The cross-section summed over all the

harmonics, characterizes the process as a whole, and, generally speaking, differs from the linear Thomson cross-section:

$$\frac{d\sigma}{d\Omega} = \sum_{n=1}^{\infty} \frac{d\sigma^{(n)}}{d\Omega}. \tag{8.3.16}$$

In the "weak" field limit ($a_0^2 \to 0,\ z \to 0$), formula (8.3.16) turns to the Thomson formula:

$$\frac{d\sigma^{(1)}\left(a_0^2 \to 0\right)}{d\Omega} = \frac{r_0^2}{2}\left(1 + \cos^2\theta\right), \qquad \frac{d\sigma^{(n)}\left(a_0^2 \to 0\right)}{d\Omega} = 0, \quad n \geq 2.$$

Figure 8.3 shows the angular distribution for the first harmonic ($n = 1$) for various parameters of the field $a_0 = 0.2; 1; 5$ [see formula (8.3.15)]. As can be seen from the figure, for the weak field the angular distribution practically coincides with the Thomson one, which is given in the same figure, i.e. it is close to isotropic one. One can see, first, the narrowing of the radiation cone, and, secondly, the maximal value of the cross-section $d\sigma^{(1)}/d\Omega_L$ achieves for $\theta_L = 0$ with increase of parameter a_0.

Figure 8.4a shows the similar distributions for harmonics with $n = 2, 3$, in case of $a_0 = 0.2$. It can be noted that in case $a_0^2 \ll 1$ a contribution of higher harmonics is suppressed (i.e. the contribution of harmonics with $n > 1$ can be neglected). With increasing the intensity of wave the relative contribution of higher harmonics increases (see Fig. 8.4b, c). Besides, as for the fundamental harmonic ($n = 1$), there is narrowing of the angular distribution, but the angle corresponding to the maximum of the distribution differs from zero.

Figure 8.5 shows the dependences of "partial" cross-sections

$$\sigma^{(n)}(a_0) = \int \frac{d\sigma^{(n)}(a_0)}{d\Omega} d\Omega$$

on the harmonic number in case of different values of the parameter a_0. The numbers of harmonics n, for which the cross-section decreases by about two orders of magnitude compared with $\sigma^{(1)}$, are marked here as well. So, for $a_0 = 0.3$ (Fig. 8.5a) such suppression is achieved already on the third harmonic, whereas for $a_0 = 1$ (Fig. 8.5b)—only on the seventh one. It is clear that with increasing of the

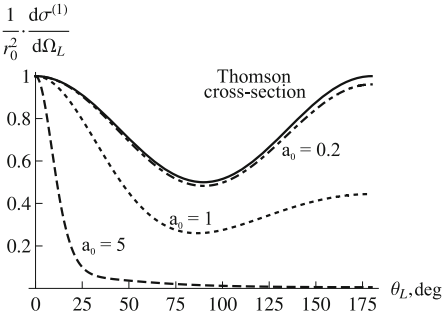

Fig. 8.3 The angular distribution of a scattered radiation on the first harmonic for different values of parameter a_0

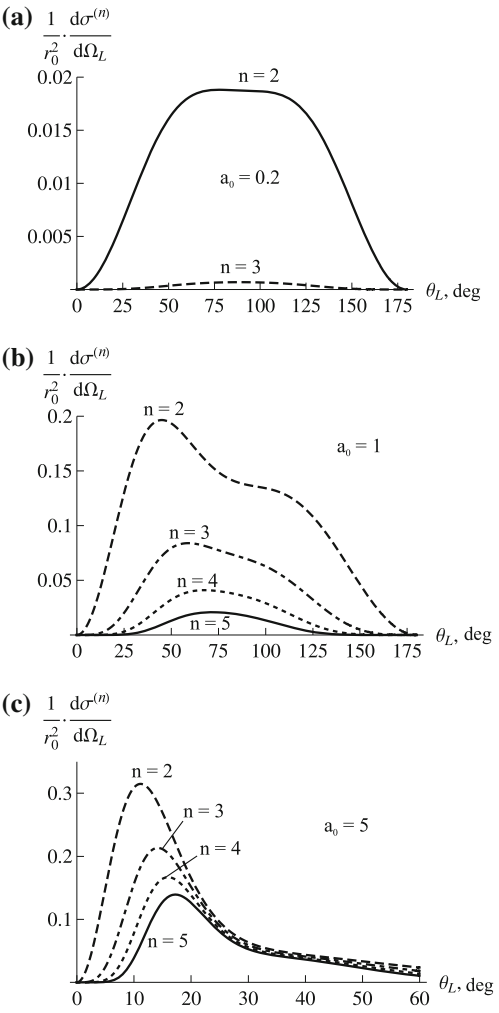

Fig. 8.4 The angular distribution of a scattered radiation on the higher harmonics for various values of parameter a_0

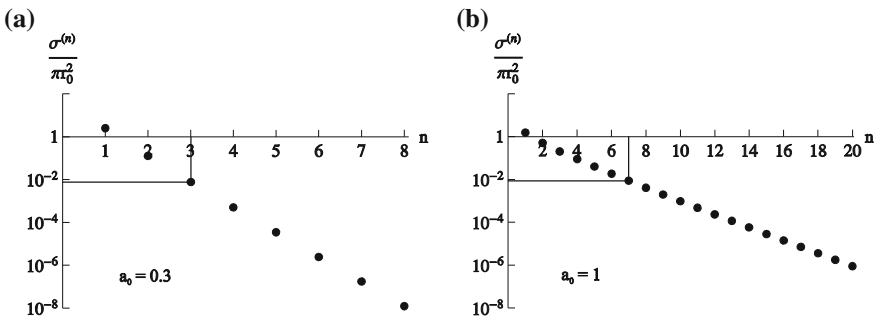

Fig. 8.5 Dependence of the "partial" cross-sections of intense wave scattering by a rest electron for the parameter $a_0 = 0.3$ (**a**) and $a_0 = 1$ (**b**)

initial wave field strength it is necessary to take into account the contribution of a large number of harmonics for the correct calculation of the scattered radiation characteristics.

Dependence of the total cross-section

$$\sigma(a_0) = \sum_{n=1}^{\infty} \sigma^{(n)}(a_0) \approx \sum_{n=1}^{n_{\max}} \sigma^{(n)}(a_0)$$

on the parameter a_0 is shown in Fig. 8.6. For values $a_0 \to 0$ the cross-section coincides with the Thomson one, as it should be. It is necessary to specify that the cross-section σ (for $a_0 = 5$) was calculated taking into account of the harmonics contributions up to $n_{\max} = 120$. As can be seen from the figure, the total cross-section decreases with an increase of a_0.

For further estimations we will use the angular distributions of energy losses and the number of emitted photons on each harmonic (8.3.11) and (8.3.14). In the analyzed case (radiation of an electron in a field of a circularly polarized wave), the summation over all the harmonics in Eq. (8.3.11) can be carried out analytically using the known relationships [3]:

$$\begin{aligned} \sum_{n=1}^{\infty} n^2 J_n^2(nz) &= \frac{z^2(4+z^2)}{16(1-z^2)^{7/2}}, \\ \sum_{n=1}^{\infty} n^2 J_n'^2(nz) &= \frac{4+3z^2}{16(1-z^2)^{5/2}}. \end{aligned} \tag{8.3.17}$$

Then, the angular distribution of total energy losses can be written as

$$\begin{aligned} \frac{dW}{d\Omega} = \sum_{n=1}^{\infty} \frac{dW^{(n)}}{d\Omega} = \frac{1}{2}\alpha N_0 \times \hbar\omega_0 \frac{a_0^2}{\left[1+\frac{a_0^2}{2}\sin^2\frac{\theta_L}{2}\right]^3} \frac{1}{16(1-z^2)^{7/2}} \\ \times \left\{ \frac{\left[\cos\theta_L - \frac{a_0^2}{2}\sin^2\frac{\theta_L}{2}\right]^2}{\left[1+\frac{a_0^2}{2}\sin^2\frac{\theta_L}{2}\right]^2} (4+z^2) + (1-z^2)(4+3z^2) \right\}, \end{aligned} \tag{8.3.18}$$

where z is given by formula (8.3.12).

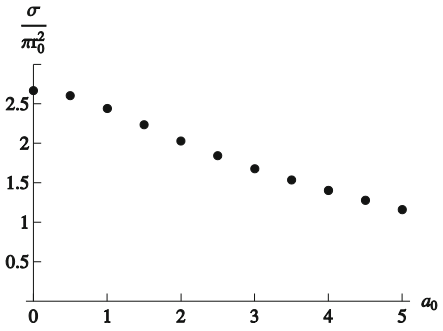

Fig. 8.6 Dependence of the total scattering cross-section, being summed over 120 harmonics, on the parameter a_0

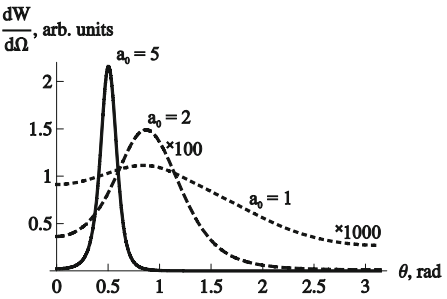

Fig. 8.7 The angular distributions of energy losses for various values of the parameter a_0 (the curve corresponding to $a_0 = 1$ is multiplied by 1,000, the curve for $a_0 = 2$ is multiplied by 100)

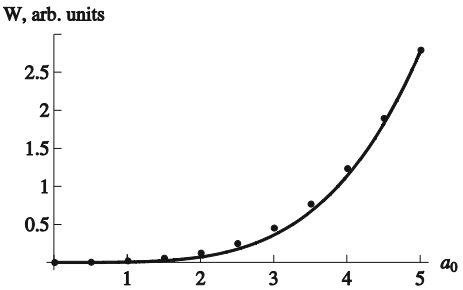

Fig. 8.8 Dependence of the total energy losses on the parameter a_0

The distribution (8.3.18) is shown in Fig. 8.7 for different values of a_0. It can be noted that the distribution becomes narrower with growth of a_0 and, for example, in case of $a_0 = 5$ it is concentrated along the conical surface with an apex angle $\theta_m \approx 0.5$ rad $\approx \gamma_D^{-1}$.

Integrating the expression (8.3.18) over the solid angle, we can obtain the dependence of the total energy losses on the field strength a_0, which is shown in Fig. 8.8

As it follows from the figure, the dependence of the energy losses on the strength parameter a_0 may be approximated by the polynom

$$W = 0.193\pi\alpha N_0 \hbar\ \omega_0 a_0^4 = 0.00443\ N_0 \hbar\ \omega_0 a_0^4$$

(see the solid curve in the Fig. 8.8).

Figure 8.9 shows the distributions $dW^{(n)}/d\Omega$ for the fixed observation angles (in vicinity of $\theta_L \approx \gamma_D^{-1}$) for $a_0 = 5$. The angular distributions have maxima for $n_m \sim 30$–80 (depending on the observation angle), and the harmonics with $n \gg n_m$ are observed in the spectrum also. An estimation of the harmonic number n_m, which corresponds to the maximum of $dW^{(n)}/d\Omega$, can be obtained from the analogy between the nonlinear Thomson scattering and synchrotron radiation of electron moving in the R-system in a circular orbit with radius $R = a_0\, c/\omega_0 \left(2 + a_0^2\right)^{1/2}$ [see equation (8.2.7)]. For $a_0 \gg 1$ the orbital motion becomes relativistic one, and the characteristic frequency of radiation is given by the formula:

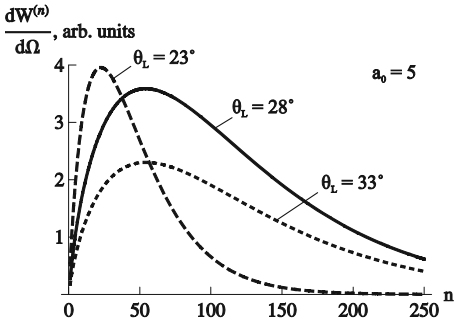

Fig. 8.9 Dependence of energy losses $dW^{(n)}/d\Omega$ in case of $a_0 = 5$ for the fixed polar angles θ_L on the harmonic number n

$$\omega_{\mathrm{c}}^{R} = \frac{3}{2}\,\frac{1}{\left(1-\beta_R^2\right)^{3/2}}\,\frac{c}{R} = \frac{3\sqrt{2}}{2a_0}\left(1+\frac{a_0^2}{2}\right)^{3/2} \times \omega_0.$$

[see expression (8.2.7) for the relative velocity of the electron $\beta_{\mathrm{R}} = v_{\mathrm{R}}/c$ in orbit]. In case of going from R- to the L-system, the typical frequency is calculated taking into account the transformation of angles:

$$\omega_{\mathrm{c}}^{L} = \omega_{\mathrm{c}}^{R}\gamma_{\mathrm{D}}(1+\beta_{\mathrm{D}}\,\cos\theta_{\mathrm{L}}), \quad \cos\theta_{\mathrm{L}} = \frac{\cos\theta_R + \beta_{\mathrm{D}}}{1+\beta_{\mathrm{D}}\cos\theta_R}.$$

In the R-system, the maximum of synchrotron radiation intensity is directed along the tangent to the orbit, i.e. for $\theta_{\mathrm{R}} = \pi/2$. Thus, from the previous formulae, we obtain

$$\omega_{\mathrm{c}}^{L} = \omega_{\mathrm{c}}^{\mathrm{R}}\gamma_{\mathrm{D}}(1+\beta_{\mathrm{D}}\,\cos\theta_L),$$

$$\cos\theta_L = \frac{\cos\theta_R + \beta_{\mathrm{D}}}{1+\beta_{\mathrm{D}}\cos\theta_R}.$$

For the considered case ($a_0 \gg 1$)

$$\omega_{\mathrm{c}}^{R} \approx \frac{3}{4}a_0^2\,\omega_0,$$

therefore, in L-system

$$\omega_{\mathrm{c}}^{L} \approx \frac{3}{4\sqrt{2}}a_0^3\,\omega_0.$$

In other words, the characteristic frequency in the radiation spectrum corresponds to the harmonic number n_m:

$$\omega_{\mathrm{c}}^{L} = n_m\,\omega_0, \quad n_m = \frac{3}{4\sqrt{2}}a_0^3 \gg 1,$$

whereas the emission spectrum becomes practically continuous. For the case $a_0 = 5$ the obtained approximate formula gives a value of $n_m \approx 66$.

The same value can be evaluated in another way. Let's calculate the number of photons N_{ph} emitted by an electron in case of interaction of electron with the wave train by $N_0\lambda_R$ length [see expression (8.3.14)]:

$$N_{\text{ph}} = \sum_{n=1}^{n_{\max}} N^{(n)} = \sum_{n=1}^{n_{\max}} \int d\Omega \frac{dN^{(n)}}{d\Omega}. \tag{8.3.19}$$

Knowing the total energy losses, it is possible to find the average energy of the emitted photons:

$$\langle \hbar\omega \rangle = \frac{W}{N_{\text{ph}}}.$$

This value is associated with the characteristic energy of photons, which corresponds to the maximum of SR spectrum using the well known relation

$$\langle \hbar\omega \rangle = 0.308 \langle \hbar\omega_{\text{c}} \rangle.$$

From here it is possible to find the appropriate harmonic number:

$$n_c = \frac{\langle \hbar\omega_{\text{c}} \rangle}{\hbar\omega_0} = \frac{W}{0.308 N_{\text{ph}} \hbar\omega_0}.$$

Figure 8.10 shows the distribution of the emitted number of photons on each harmonic $N^{(n)}$ (i.e. the result of integration of expression (8.3.14) over the solid angle) for the parameter $a_0 = 5$. As it can be seen from the figure, the photon yield decreases monotonically, but rather slowly, with the increase of the harmonic number. Choosing the harmonic maximal number $n_{\max} = 150$, it is possible to calculate by the formula (8.3.19) the number of photons N_{ph}, which will differ slightly from the "true" total number of photons (i.e. from the result of summing of the series (8.3.19) up to $n_{\max} = \infty$):

$$N_{\text{ph}} \approx 0.17. \tag{8.3.20}$$

Knowing the value of the total energy $W(a_0 = 5) = 2.79\,\hbar\,\omega_0$ (see Fig. 8.8), we find the required harmonic number:

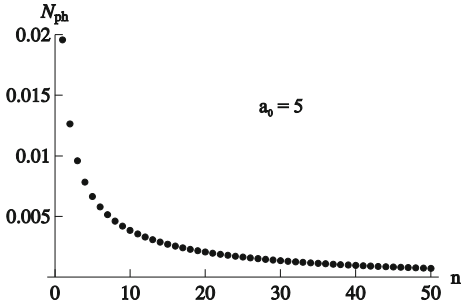

Fig. 8.10 The dependence of the number of scattered photons N_{ph} on the harmonic number per one period of the incident wave for $a_0 = 5$

$$n_m = \frac{2.79}{0.308 \times 0.17} = 53,$$

which agrees with the previously obtained estimation satisfactorily.

In other words, if the frequency of an initial wave corresponds to the energy of photons $\hbar\omega_0 \approx 2$ eV, the peak in the spectrum will correspond to the energy $\hbar\omega_c \approx n_m \hbar\omega_0 \approx 130$ eV, whereas the maximal energy of the emitted photons can reach values $\hbar\omega_{\max} \sim 0.5$ keV.

The spectral–angular distribution of the radiation of the helium atom electrons in the field of Ti:Sa-laser with power $P = 50 \times 10^{12}$ W and the duration of the flash $\tau = 30 \times 10^{-15}$ s was investigated in the experiment [4]. The achieved intensity of the laser flash was 7×10^{19} W/cm^2, which corresponds to the parameter of strength $a_0 = 5.6$. They observed photons with the energy of maximum $\hbar\omega = 150$ eV in the measured spectrum of scattered radiation for the observation angle $\theta = 0°$, but the boundary energy in the spectrum exceeded $\sim$1,000 eV. The authors of this experiment have estimated the yield $N_{\text{ph}} = 5 \times 10^{10}$ photons per flash (after integrating over the angular distribution and over the radiation spectrum). The estimation of the photon number emitted by one electron under the influence of electromagnetic field with $a_0 = 5$ per period of the primary wave was derived in the previous section: $N_{\text{ph}} \approx 0.17$. For the Ti:Sa laser wavelength $\lambda \sim 1$ μm and the flash duration $\tau \sim 3 \times 10^{-14}$ s the number of periods is $N_{\text{ph}} \sim c\tau/\lambda \sim 10$. The number of electrons N_e in the area of interaction of laser flash with a gas jet may be estimated as

$$N_e \approx n_e V = n_e \frac{\pi d_{\text{ph}}^2}{4} D \approx 10^{11}, \quad \text{for } n_e = 10^{18}\,\text{cm}^{-3}.$$

Thereby the estimation of a photon yield per shot may be obtained using the quantity (8.3.20):

$$N_{\text{tot}} \simeq N_{\text{ph}} \times N_e \times N_0 \simeq 1.7 \times 10^{11} \sim 10^{11}\,\text{phot/flash},$$

which agrees with experiment good.

The obtained experimental results demonstrate the possibility of creating a new type of X-ray source based on the process of nonlinear Thomson scattering.

8.4 Scattering of a Weak Electromagnetic Wave on a Moving Electron (the Linear Compton Effect)

In the previous paragraph we considered the scattering of electromagnetic wave by the rest electron. In case of the wave scattering by a relativistic electron, the scattered photon frequency shifts to a hard part of spectrum due to the Doppler effect, i.e. the frequency of visible laser photons can be transformed into radiation of the X-ray or γ-range. This effect can be used for creation of sources of a hard radiation.

For certainty, we shall consider the laser photon scattering ($\hbar\omega_0 \leq 3$ eV) by a relativistic electron. In the most interesting case, when the electron momentum and the wave vector are antiparallel (the backward Compton scattering, BCS), in the R-system, where an initial electron is at rest, the photon energy is about γ times higher than in the laboratory system.

Indeed, from (8.3.2) it follows $\omega_R = \omega_0\sqrt{\frac{1-\beta_D}{1+\beta_D}}$.

In the considered case (head-on-collision) there should be substituted the negative value—β_0 instead of the velocity β_D, because the electron momentum and its velocity are directed along a negative direction of z-axis (Fig. 8.11).

Thus, we have the formula for the photon energy:

$$\hbar\omega_{0R} = \hbar\omega_0\sqrt{\frac{1+\beta_0}{1-\beta_0}} = \hbar\gamma_0\omega_0(1+\beta_0),$$

where γ_0 denotes the Lorentz-factor of the initial electron

$$\gamma_0 = \frac{1}{\sqrt{1-\beta_0^2}}.$$

For the electron energy $E \leq 5$ GeV ($\gamma \leq 10^4$), the photon energy in R-system will satisfy the condition $\hbar\omega_{0R} \ll mc^2$, which, in case of a weak field, allows to consider this process as the Thomson scattering (neglecting the energy transfer to electron and the frequency changing of the scattered photon). In this approximation, turning again in the L-system result is:

$$\omega_L = \gamma_0\omega_R(1-\beta_0\cos\theta_R) = \gamma_0^2\omega_0(1+\beta_0) \times \left(1-\beta_0\frac{\cos\theta_L+\beta_0}{1+\beta_0\cos\theta_L}\right) = \omega_0\frac{1+\beta_0}{1+\beta_0\cos\theta_L}. \tag{8.4.1}$$

In ultrarelativistic case ($\beta_0 \to 1$, $\gamma_0 \gg 1$), instead of the angle θ_L it is more convenient to use the angle θ, which is measured in L-system from the direction of the electron momentum (see Fig. 8.11):

$$\theta = \pi - \theta_L.$$

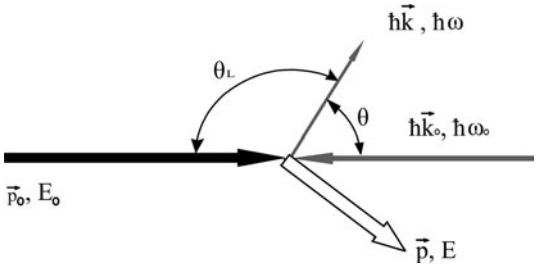

Fig. 8.11 Kinematics of the backward Compton scattering

Then, the frequency of the scattered photon in L-system is given by the relation:

$$\omega_L = \omega_0 \frac{1+\beta_0}{1-\beta_0\cos\theta} \approx 4\gamma_0^2\omega_0 \frac{1}{1+\gamma_0^2\theta^2}. \tag{8.4.2}$$

In (8.4.2) the terms proportional to γ^{-3}, θ^3 and higher are omitted.

The maximal energy of the scattered photon [at an angle $\theta = 0$ ($\theta_L = \pi$), i.e. in the direction of the electron momentum] is $4\gamma^2$ times as higher than the energy of the initial photon:

$$\hbar\omega_{L\,\max} = \hbar\omega_0 \frac{1+\beta_0}{1-\beta_0} \approx 4\gamma_0^2\hbar\omega_0, \quad \gamma_0 \gg 1 \tag{8.4.3}$$

The angular distribution of scattered photons is obtained by transformation of cross-section (8.1.12) in L-system (the indices L are omitted here again):

$$\frac{d\sigma}{d\Omega} = \frac{r_0^2}{2} \frac{\left(1-\beta_0^2\right)}{\left(1-\beta_0\cos\theta\right)^2} \left[1 + \frac{\left(\cos\theta-\beta_0\right)^2}{\left(1-\beta_0\cos\theta\right)^2}\right]. \tag{8.4.4}$$

Since the expression (8.4.2) gives the relationship connected the scattered photon energy and the scattering angle, the cross-section (8.4.4) can be rewritten as

$$\frac{d\sigma}{d\Omega} = \frac{r_0^2}{2}\left(\frac{\omega}{\omega_0}\right)^2 \frac{\left(1-\beta_0\right)}{\left(1+\beta_0\right)} \left\{1 + \frac{1}{\beta_0^2}\left[\frac{\omega}{\omega_0}\left(1-\beta_0\right) - 1\right]^2\right\}. \tag{8.4.5}$$

Let us introduce a new dimensionless variable

$$S = \frac{\omega}{\omega_{\max}} = \frac{1-\beta_0}{1-\beta_0\cos\theta} \approx \frac{1}{1+\gamma_0^2\theta^2}, \tag{8.4.6}$$

through which the cross-sections (8.4.5) can be expressed in a simpler way. After a trivial integration of this cross-section over the azimuthal angle, and bearing in mind the relation

$$d(\cos\theta) = \frac{1-\beta_0}{\beta_0 S^2} dS,$$

we obtain the spectrum of scattered photons (because the variable S is nothing else than the energy of the scattered photon in units $\hbar\omega_{\max}$):

$$\frac{d\sigma}{dS} = \pi r_0^2 \frac{1+\beta_0}{\beta_0^3} \left\{1 + \beta_0^2 - 2S\left(1+\beta_0\right) + S^2\left(1+\beta_0\right)^2\right\}. \tag{8.4.7}$$

In the ultrarelativistic limit ($\beta_0 \to 1$), it follows from (8.4.7) that the radiation spectrum is described by the universal function, which describes the spectrum of radiation in a helical undulator also [5]:

$$d\sigma/dS = 4\pi r_0^2\left[1 - 2S + 2S^2\right], \quad 0 < S \leq 1. \tag{8.4.8}$$

In this approximation, neglecting the terms $\sim \gamma_0^{-2}$ we have

$$\omega/\omega_0 = 4\gamma_0^2/\left(1 + \gamma^2\theta^2\right),$$

and the cross-section (8.4.5) can be written in the form

$$d\sigma/d\Omega = 4r_0^2\,\gamma_0^2\left(1 + \gamma_0^4\theta^4\right)\Big/\left[1 + \gamma_0^2\theta^2\right]^4. \tag{8.4.9}$$

The cross-section (8.4.9) is a rapidly decreasing function of the variable $\gamma_0\theta$. Writing an element of solid angle as

$$d\Omega = d\left(\gamma_0^2\theta^2\right)d\varphi/2\gamma_0^2,$$

the cross-section (8.4.9) can be integrated over the variable $\gamma_0\theta$ between the limits from zero to infinity: $\sigma = 8\pi r_0^2/3$. Because of the used approximations the calculated result coincides with the classical Thomson cross-section as expected.

A more correct description of the considered process (the linear Compton effect on a free electron) is carried out in the framework of quantum electrodynamics. This approach takes into account the quantum recoil effect, i.e. a transfer of the momentum to the scattered electron, what leads to the modification of the formula (8.4.2):

$$\hbar\omega = \hbar\omega_0 \frac{1 + \beta_0}{1 - \beta_0\cos\theta + \frac{\hbar\omega}{\gamma_0 mc^2}(1 + \cos\theta)}. \tag{8.4.10}$$

The differential cross-section of the Compton scattering on a moving electron for any energy of particle and any geometry may be written through so-called invariant variables [6]. The following set of invariant variables, which are determined by the kinematics of the scattering process is used often:

$$x = \frac{2pk_0}{(mc^2)^2}, \quad y = \frac{pk_0 - pk}{pk_0}. \tag{8.4.11}$$

Here p, k_0, k denote four-momentum of the initial electron and photon as well as scattered photon, respectively ($p = \{\gamma_0 mc^2,\ \mathbf{p}\},\ k_0 = \{\hbar\omega_0, \hbar\mathbf{k}_0\},\ k = \{\hbar\omega,\ \hbar\mathbf{k}\}$). For the head-on collision of laser photon with ultrarelativistic electron we have

$$\begin{aligned} x &= \frac{2\gamma_0\hbar\omega_0(1 + \beta_0)}{mc^2} \approx \frac{4\gamma_0\hbar\omega_0}{mc^2}, \\ y &\approx \frac{\hbar\omega}{\gamma_0\beta_0 mc^2}. \end{aligned} \tag{8.4.12}$$

In a system, where the initial electron is at rest, the frequency of the initial photon is

$$\omega_{0R}^* = \gamma_0\omega_0(1 + \beta_0). \tag{8.4.13}$$

In other words, the parameter x characterizes the initial photon energy (in units mc^2) in the considered system. If $x \ll 1$, then the process of Compton scattering in a good approximation can be regarded as Thomson scattering.

The variable y coincides with the ratio of the scattered photon energy to the energy of the initial electron with high accuracy. It is easy to obtain the interval of variation of this parameter from the kinematics of the process:

$$0 \le y \le y_{\max} = \frac{x}{1+x}. \tag{8.4.14}$$

The spectrum of scattered photons in the invariant variables can be written as follows:

$$\frac{d\sigma}{dy} = \frac{2\pi r_0^2}{x}\left\{\frac{1}{1-y} + 1 - y - 4\frac{y(x-xy-y)}{x^2(1-y)^2}\right\}. \tag{8.4.15}$$

After integrating the cross-section (8.4.15) over the variable y in the limits (8.4.14), which is easily carried out analytically, we can obtain the dependence of the BCS total cross-section on the parameter x:

$$\sigma(x) = \frac{2\pi r_0^2}{x}\left\{\left(1 - \frac{4}{x} - \frac{8}{x^2}\right)\ln(1+x) + \frac{8}{x} + \frac{1}{2} - \frac{1}{2(1+x)^2}\right\}. \tag{8.4.16}$$

The expansion follows from the obtained cross-sections for values $x \ll 1$

$$\sigma \approx \frac{8}{3}\pi r_0^2\left(1 - x + \frac{13}{10}x^2\right).$$

It is clear that for Compton scattering on a rest electron ($\gamma_0 = 1,\ \beta_0 = 0$) $x = 2\frac{\hbar\omega_0}{mc^2}$, the cross-section (8.4.16) describes the standard behavior of the scattering cross-section, which decreases with the growth of the initial photon energy. The exact cross-section in the discussed case of a head-on collision with ultra-relativistic electron can be written through the traditional variables as

$$\frac{d\sigma}{d\Omega} = \frac{r_0^2}{2}\frac{(1-\beta_0)}{(1+\beta_0)}\left(\frac{\omega}{\omega_0}\right)^2 \times \left[\frac{1-\beta_0\cos\theta}{1+\beta_0}\frac{\omega}{\omega_0} + \frac{1+\beta_0}{1-\beta_0\cos\theta}\frac{\omega_0}{\omega} - \frac{(1-\beta_0^2)(1-\cos^2\theta)}{(1-\beta_0\cos\theta)^2}\right]. \tag{8.4.17}$$

If the initial beam of photons is polarized, the scattered photons will be also polarized. Let us consider the polarization characteristics of a scattered γ-radiation in detail. The cross-section of polarized photons scattered by an unpolarized electrons was obtained in the invariant variables in [6], from which the needed expressions can be easily derived. Since the process involves two photons, then, generally speaking, the polarization characteristics of the initial and final photons have to be described in two different coordinate systems. However, since we are

interested in the scattering of photons into the small range of angles $\theta \sim \gamma^{-1} \ll 1$ (i.e. momenta of the initial and final photons are practically antiparallel to each other), it is possible to use one system of coordinates for polarization of both photons. Further, since the averaging of a yield of scattered photons over the azimuthal angles takes place during experiment, for obtaining of useful expressions it is necessary to choose a fixed frame of reference. The most important frame is defined by the experimental setup, but not by the scattering plane. If through $\xi_i^{(1)}$ and $\xi_i^{(2)}$ we define the Stokes parameters of the initial and scattered photons, respectively, then for the cross-section it is possible to obtain the following expression:

$$d\sigma = 2r_0^2 \frac{dyd\varphi}{x}\{F_0 + \left(\xi_3^{(1)} + \xi_3^{(2)}\right)F_{03} + \xi_1^{(1)}\xi_1^{(2)}F_{11} + \xi_2^{(1)}\xi_2^{(2)}F_{22} + \xi_3^{(1)}\xi_3^{(2)}F_{33}\Big\}, \tag{8.4.18}$$

where

$$F_0 = \left(\frac{1}{x} - \frac{1}{x(1-y)}\right)^2 + \frac{1}{x} - \frac{1}{x(1-y)} + \frac{1}{4}\left(1 - y + \frac{1}{1-y}\right),$$
$$F_{03} = -\left(\frac{1}{x} - \frac{1}{x(1-y)}\right)^2 - \frac{1}{x} + \frac{1}{x(1-y)},$$
$$F_{11} = \frac{1}{x} - \frac{1}{x(1-y)} - \frac{1}{2},$$
$$F_{22} = \frac{1}{4}\left(1 - y + \frac{1}{1-y}\right)\left(1 + \frac{2}{x} - \frac{2}{x(1-y)}\right),$$
$$F_{33} = \left(\frac{1}{x} - \frac{1}{x(1-y)}\right)^2 + \frac{1}{x} - \frac{1}{x(1-y)} + \frac{1}{2}.$$

For a correct averaging of the obtained expression over the azimuthal angle, let us introduce an explicit dependence on the azimuthal angle φ (the angle between the scattering plane and the plane of reference).

The Stokes parameters $\xi_i^{(1,2)}$ introduced in (8.4.18) are defined in the system related to the scattering plane, so instead of them we substitute the expressions

$$\begin{aligned} &\xi_1^{(1)} - \xi_1^{(1)}\cos(2\varphi) - \xi_3^{(1)}\sin(2\varphi); \\ &\xi_2^{(1)} \to \exp(i\varphi)\xi_2^{(1)}; \\ &\xi_3^1 \to \xi_1^{(1)}\sin(2\varphi) + \xi_3^{(1)}\cos(2\varphi), \end{aligned} \tag{8.4.19}$$

which connect the Stokes parameters of the initial photon in the system, rotated at an angle φ with the initial values.

The Stokes parameters of scattered photons ξ_i^2 are transformed by the formulae similar to (8.4.19) by replacing $\varphi \to -\varphi$ (which corresponds to a return to

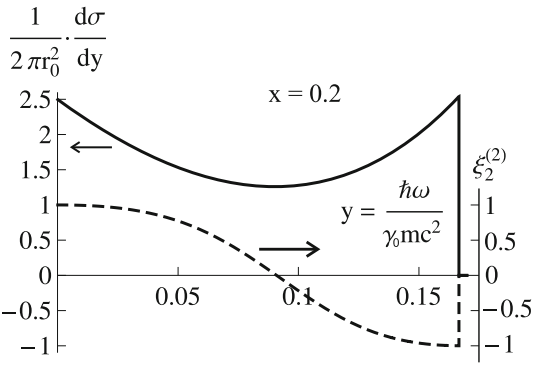

Fig. 8.12 The BCS spectrum for $x = 0.2$ (*left scale*) and circular polarization of scattered photons for $\xi_2^{(1)} = 1$ (*right scale*) for the total cone of radiation

the initial reference plane). After substitution of obtained expressions and integrating over the azimuthal angle we obtain

$$
\begin{aligned}
d\sigma &= 4\pi r_0^2 \frac{dy}{x}\left\{F_0 + \xi_1^{(1)}\xi_1^{(2)}F_1 + \xi_2^{(1)}\xi_2^{(2)}F_2 + \xi_3^{(1)}\xi_3^{(2)}F_3\right\},\\
F_1 &= -\frac{1}{2}\left(\frac{1}{x} - \frac{1}{x(1-y)}\right)^2,\\
F_2 &= \frac{1}{4}\left(1 - y + \frac{1}{1-y}\right)\left(1 + \frac{2}{x} - \frac{2}{x(1-y)}\right),\\
F_3 &= \frac{1}{2}\left(\frac{1}{x} - \frac{1}{x(1-y)}\right).
\end{aligned}
\tag{8.4.20}
$$

As in the case of undulator radiation, the spectral and polarization characteristics of the beam of scattered photons are determined by an aperture of the beam collimation.

For the collimation angle $\theta_c \gg \gamma^{-1}$ the minimal value of the variable y (see Eq. (8.4.12)) is $y_{\min} \approx 0$, whereas $y_{\max}(\theta = 0) = x/(1+x)$. Figure 8.12 shows the spectrum of scattered photons and the dependence of circular polarization on the photon energy for this case, which was calculated from the expression

$$
\xi_2^{(2)}(x,y) = \frac{F_2(x,y)}{F_0(x,y)}\xi_2^{(1)}. \tag{8.4.21}
$$

The results shown in Fig. 8.12 are obtained for $\xi_2^{(1)} = +1$. As it follows from the figure, for photons scattered strictly backwards and having the maximal energy, a circular polarization will be 100%, but opposite in sign (for example, the right-circular polarization of the laser photon is transformed into the left-circular one).

Figure 8.13 illustrates the possibility of monochromatization of photon beam in case of choosing of the collimation angle $\theta_c < \gamma^{-1}$. The emission spectrum and the degree of circular polarization are calculated for the collimation angle $\theta_c = 0.7\gamma^{-1}$. As it can be seen from the figure, a "hard" collimation allows to produce a scattered photon beam with a high circular polarization.

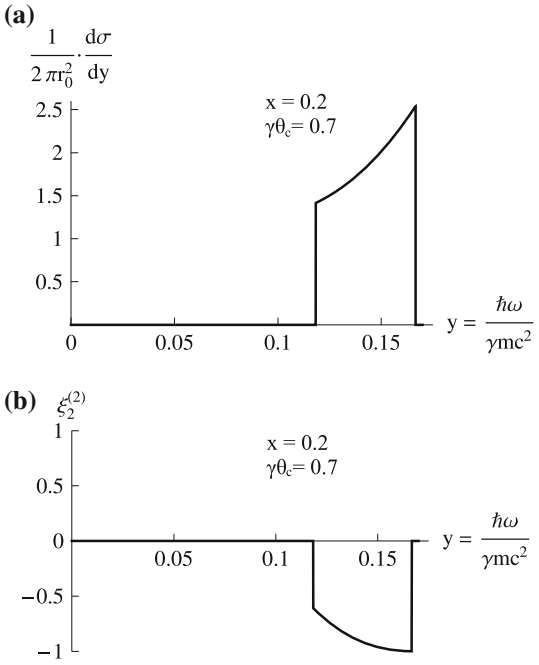

Fig. 8.13 The same for the collimator aperture $\gamma\theta_c = 0.7$

For such a beam it is possible to determine the average value of circular polarization:

$$\langle \xi_2^{(2)}(t_c)\rangle = \int_{y_{min}}^{y_{max}} \frac{dy}{x} F_2(x,y) \Big/ \int_{y_{min}}^{y_{max}} \frac{dy}{x} F_0(x,y), \tag{8.4.22}$$

where $y_{min} = \frac{x}{1+x+t_c^2}$, $y_{max} = \frac{x}{1+x}$. For values $x \ll 1$ the expression (8.4.22) can be written as

$$\langle \xi_2^{(2)}(t_c)\rangle \approx -\frac{1+t_c^2}{1+t_c^2+\frac{2}{3}t_c^4}, \tag{8.4.23}$$

The average circular polarization is noticeably reduced with increasing of the collimator aperture.

Figure 8.14 shows the dependence of average polarization on the collimation angle, where the solid curve corresponds to the exact calculation by the formula (8.4.22) for $x = 0.5$, while the dashed line refers to calculation by formula (8.4.23).

The technique described was used to produce monochromatic gamma beams for investigation of photonuclear processes [7–9]. For some purposes parameters of available lasers (or accelerators) do not allow to achieve needful gamma beam

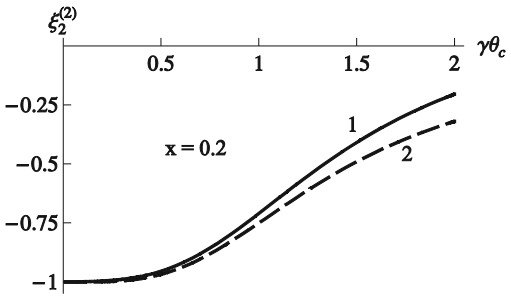

Fig. 8.14 Dependence of the averaged degree of the circular polarization on the collimator aperture [*curve 1* the exact calculation; *curve 2* the approximation of (8.4.23)]

characteristics (photon energy, tunability, intensity and so on). Authors of the work [9] have carried out the BCS experiment at the electron–positron collider VEPP-2M with energy of electrons (positrons) 650 MeV. The initial photon beam with energy of photons ~ 100 eV was generated by positrons passing through a helical undulator and then scattered by a counter propagating electrons. As a result they have obtained circularly-polarized γ-quanta with energy $\sim$300 MeV which were used to measure a polarization of the stored electron beam.

Other scheme has been realized in the experiment [10] where authors used infrared photons generated by a free-electron laser (FEL) instead photons from an ordinary laser. In the such FEL an undulator was placed into an optical resonator (cavity) to provide a feedback. FEL photons circulated in this cavity and scattered by the same electron beam which was produced the FEL radiation. During head-on-collisions the intense X-ray beam there was obtained.

Photons are emitted in a FEL with wavelength (see Eq. (3.3.5)):

$$\lambda_{\mathrm{FEL}} = \frac{\lambda_{\mathrm{u}}}{2\gamma^2}\left(1 + \frac{K^2}{2}\right), \tag{8.4.24}$$

and, consequently, as a result of intracavity BCS process a photon wavelength becomes shorter:

$$\lambda_{\mathrm{BCS}} = \frac{\lambda_{\mathrm{FEL}}}{4\gamma^2}\left(1 + \gamma^2\theta^2\right) = \frac{\lambda_{\mathrm{u}}}{8\gamma^4}\left(1 + \frac{K^2}{2}\right)\left(1 + \gamma^2\theta^2\right). \tag{8.4.25}$$

In the cited work electrons with Lorentz-factor $\gamma \approx 100$ were used to produce FEL radiation in the wavelength range $\lambda_{\mathrm{FEL}} = 3.5$–$7\,\mu$m. The FEL spectral line shift in this range was performed by changing an undulator gap. Consequently, energy of X-ray photons can be changed in the interval $\hbar\omega_{\mathrm{BCS}} = 7$–$14$ keV with small step (see Eq. (8.4.25)).

Formulas (8.4.18) and (8.4.20) are valid for any values of ω_0 and β_0. However, with growing of intensity of the laser field (in other words, with increasing of concentration of photons in the interaction region) the probability of interaction of one electron with a few photons increases, i.e. process becomes nonlinear:

$$e^- + n\gamma \to e^{-\prime} + \gamma', \quad n = 2, 3, 4, \ldots$$

In the next paragraphs the peculiarities of the nonlinear Thomson and Compton scattering processes on the ultra-relativistic electrons are considered.

8.5 Radiation of a Relativistic Electron in a Field of Strong Electromagnetic Wave

Let us consider, as in the previous paragraph, the head-on collision of laser photons and the ultrarelativistic electron with the energy, at which the change in frequency of the photon scattering in the R-system can be neglected [11]. If the laser "flash" contains a train of N_0 periods, the periodic trajectory of electron passing through this wave train contains $2N_0$ oscillations. In this case, as usual, the interference factor F_N can be approximated by a δ-function, whose argument determines the dispersion relation connecting the frequency of the emitted photon and the photon outgoing angle. In the L-system this relation is given as follows:

$$\omega_n = \frac{n\omega_0(1+\beta_0)}{1-\beta_0\cos\theta+\frac{a_0^2}{4}(1-\beta_0)(1+\cos\theta)} \approx n\frac{4\gamma_0^2\omega_0}{1+\frac{a_0^2}{2}+\gamma_0^2\theta^2}. \tag{8.5.1}$$

The angular distribution of energy losses in the L-system of relativistic electrons on the nth harmonic can again be obtained from the expression (8.3.5) with the account of (8.3.6) and (8.3.9):

$$\frac{dW_L^{(n)}}{d\Omega_L} = \frac{e^2\omega_0 N_0}{4c}\frac{a_0^2}{\left(1+a_0^2\right)}\frac{(1-\beta_{\mathrm{D}})}{\gamma_{\mathrm{D}}^2(1-\beta_{\mathrm{D}}\cos\theta_L)^3} \times n^2\left\{\frac{(\cos\theta_L-\beta_{\mathrm{D}})^2\gamma_{\mathrm{D}}^2}{\sin^2\theta_L}J_n^2(nz)+J_n'^2(nz)\right\}, \tag{8.5.2}$$

where $z = \frac{a_0}{\sqrt{2}\sqrt{1+a_0^2/2}}\frac{\sin\theta_{\mathrm{L}}}{\gamma_{\mathrm{D}}(1-\beta_{\mathrm{D}}\cos\theta_{\mathrm{L}})}$.

Here, as before, β_{D} indicates the drift velocity, i.e. the velocity of a system, where the electron, on average, is at rest. It is clear that the drift velocity will depend not only on the initial electron velocity β_0, but also on the field strength parameter a_0. In a system, which moves parallel to the trajectory of an electron with velocity β_0, the electron at the initial moment is at rest, and under the influence of intense wave it acquires the velocity of drift [see formula (8.2.4): $\beta'_{\mathrm{D}} = a_0^2/\left(4+a_0^2\right)$].

Then, using the relativistic law of addition of velocities when returning to the initial L-system, we get

$$\beta_{\mathrm{D}} = \frac{-\beta_0+\beta'_{\mathrm{D}}}{1-\beta_0\beta'_{\mathrm{D}}} = \frac{-4\beta_0+a_0^2(1-\beta_0)}{4+a_0^2(1-\beta_0)}. \tag{8.5.3}$$

For the most interesting relativistic case it follows from (8.5.3) that $\beta_{\mathrm{D}} < 0$, since the axis z of L-system is directed along the wave vector. The polar angle θ_L in (8.5.2) is measured namely from this direction.

In the ultrarelativistic limit $\left(\gamma_0^2 \gg a_0^2\right)$ from (8.5.3) we obtain

$$\beta_{\mathrm{D}} \approx -\beta_0 + \frac{a_0^2}{4\gamma_0^2},$$

$$\gamma_D^2 \approx \frac{\gamma_0^2}{1 + a_0^2/2}. \tag{8.5.4}$$

The relativistic particle emits photons in a narrow cone along the particle velocity, and therefore, by analogy with the case considered in paragraph 8.4, instead of the angle θ_L we will use the angle θ in respect to the vector $\boldsymbol{\beta}_0$:

$$\theta = \pi - \theta_L, \quad \theta \leq \gamma^{-1},$$

and accordingly

$$1 - \beta_D \cos\theta_L = \frac{1}{2\gamma_0^2}\left(1 + \frac{a_0^2}{2} + \gamma_0^2\theta^2\right),$$

$$z = \frac{\sqrt{2}a_0\gamma_0\theta}{1 + \gamma_0^2\theta^2 + a_0^2/2}.$$

For calculations it is convenient to use a variable $t = \gamma_0^2\theta^2$, through which the element of the solid angle $d\Omega = dt\, d\varphi/2\gamma_0^2$ is expressed.

The angular distribution of energy losses on the nth harmonic is written as follows:

$$\frac{dW^{(n)}}{dt\, d\varphi} = \frac{e^2\omega_0 N_0}{c} \frac{4a_0^2\gamma_0^2}{\left(1 + a_0^2/2 + t\right)^3} n^2 \left\{ \frac{\left(1 + a_0^2/2 - t\right)^2}{2a_0^2 t} J_n^2(nz) + J_n'^2(nz) \right\}. \tag{8.5.5}$$

As before, the angular distribution of the total energy losses can be obtained carrying out the summation over all the harmonics [see (8.3.17)]:

$$\frac{dW}{dt\, d\varphi} = \sum_{n=1}^{\infty} \frac{dW^{(n)}}{dt\, d\varphi} = \alpha\hbar\,\omega_{\max} N_0 \frac{a_0^2}{\left(1 + a_0^2/2 + t\right)} \times \frac{1}{16(1 - z^2)^{7/2}}$$
$$\times \left\{ \left(\frac{1 + a_0^2/2 - t}{1 + a_0^2/2 + t}\right)^2 \left(4 + z^2\right) + \left(1 - z^2\right)\left(4 + 3z^2\right) \right\}. \tag{8.5.6}$$

Here $\hbar\omega_{\max} = 4\gamma_0^2\hbar\omega_0$ is the maximal energy of the scattered photon [see expression (8.4.2)]. As it will be shown below, in case of interaction of intense wave with ultrarelativistic electron ($a_0 \geq 1$), the maximal energy of the scattered photon will decrease.

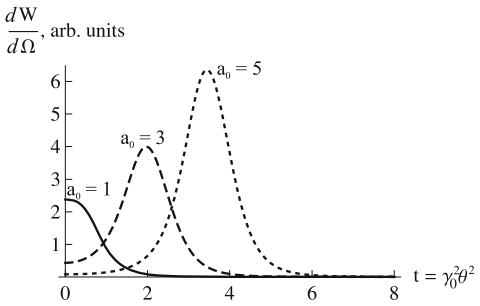

Fig. 8.15 The angular distribution of energy losses for the nonlinear Thomson scattering on a moving electron, depending on the variable $t = \gamma_0^2\theta^2$ for $a_0 = 1, 3, 5$

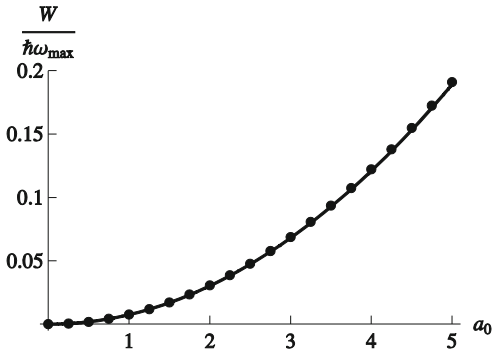

Fig. 8.16 Dependence of the total energy losses of the nonlinear Thomson scattering as a function of the parameter a_0 (per one period of the incident wave)

Figure 8.15 shows the angular distributions of energy losses for several values of the parameter $a_0 = 1, 3, 5$. As it can be seen from the figure, with increasing of the wave intensity, the cone of radiation angles grows. The maximum in the distribution corresponds to the angle $t_m = \gamma\,\theta_m \approx a_0^2/2$.

Figure 8.16 shows the dependence of total energy on the parameter a_0:

$$W(a_0) = \int_0^{\infty} dt \int_0^{2\pi} \frac{dW(a_0)}{dt\,d\varphi} d\varphi.$$

As it follows from the figure, the calculated curve is well approximated by a quadratic dependence $W = 0.33\ \pi\alpha\hbar\omega_{\max} N_0 a_0^2$. It should be noted that a similar dependence for a rest electron ($W \sim a_0^4$, see Fig. 8.8) differs from the quadratic one due to the fact that the Lorentz-factor of a rest electron, which is drifting under the action of a strong wave, is proportional to a_0^2. It means the dependence shown in Fig. 8.8, can be written as $W = \text{const} \times a_0^4 \approx \text{const} \times \gamma_D^2\, a_0^2$. This dependence is consistent with the result for the scattering on the relativistic electron (see Fig. 8.16), where the dependence on γ_0^2 is included into the expression for $\hbar\omega_{\max}$. In order to calculate the number of emitted photons and the cross-section, we use the relationship between the scattering angle and the frequency of nth harmonic in the L-system (8.4.1):

$$\omega_L = n\omega_0 \frac{1-\beta_D}{1-\beta_D \cos\theta_L} \approx n\omega_0 \frac{1+\beta_0}{\frac{\gamma_0^2}{2}+\frac{a_0^2}{4\gamma_0^2}+\frac{\theta^2}{2}} = \frac{4\gamma_0^2 n\omega_0}{1+\frac{a_0^2}{2}+t}. \tag{8.5.7}$$

The last formula is obtained using the approximate expressions (8.3.13). Then from (8.3.14) we obtain

$$\frac{dN^{(n)}}{dt\,d\varphi} = \frac{1}{\hbar\omega_L}\frac{dW^{(n)}}{dt\,d\varphi} = \frac{\alpha N_0 a_0^2}{\left(1+\frac{a_0^2}{2}+t\right)^2} \times n\left\{\frac{\left(1+a_0^2/2-t\right)^3}{2a_0^2 t}J_n^2(nz) + J_n'^2(nz)\right\}. \tag{8.5.8}$$

Note that formula (8.5.8) completely coincides with the expression for the spectral photon density of the nth harmonic, which is radiated by an electron in a helical undulator with a period $\lambda_0/2$, the number of periods N_0 and undulator parameter $K = a_0/\sqrt{2}$.

In order to obtain the spectral distribution of photons from the angular one, we use the relationship (8.5.7) again, and for the energy of the emitted photon we will use, as before, the dimensionless variable $\left(\hbar\omega_{\max}^{\text{lin}} \approx 4\gamma_0^2\hbar\omega_0\right)$:

$$S = \frac{\hbar\omega}{\hbar\omega_{\max}^{\text{lin}}} = \frac{n}{1+a_0^2/2+t}.$$

Then, after integrating over the azimuth, from (8.5.8) we obtain the spectral distribution of the emitted photons on each harmonic:

$$\frac{dN^{(n)}}{dS} = 2\pi\alpha N_0 a_0^2 \left\{\frac{\left[n-S\left(2+a_0^2\right)\right]^2}{2Sa_0^2\left[n-S\left(1+\frac{a_0^2}{2}\right)\right]}J_n^2(nz) + J_n'^2(nz)\right\}, \tag{8.5.9}$$

where

$$z = \frac{\sqrt{2}\,a_0}{n}\sqrt{Sn - S^2\left(1+a_0^2/2\right)}, \quad 0 \le S \le \frac{n}{1+a_0^2/2}. \tag{8.5.10}$$

The total photon spectrum is determined by the sum of "partial" spectra:

$$\frac{dN}{dS} = \sum_{n=1}\frac{dN^{(n)}}{dS}.$$

Having integrated the expression (8.5.9), we can get the "partial" photon yield on the nth harmonic, which is proportional to the length of the train N_0 and has a complicated dependence on the harmonic number and the field intensity and, generally speaking, depends on the Lorentz-factor of the initial electron indirectly.

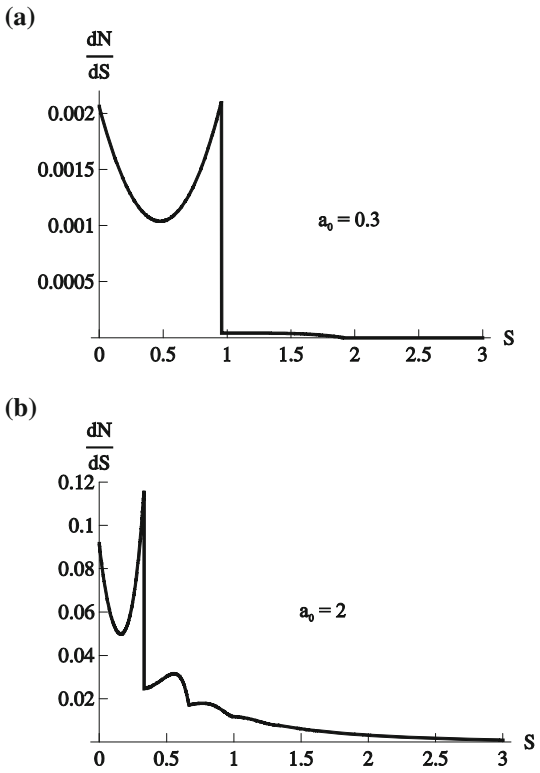

Fig. 8.17 The photon spectrum of the nonlinear Thomson scattering: for the weak field ($a_0 = 0.3$) (**a**), for the strong one ($a_0 = 2$) (**b**) per one period of the incident wave

For a weak field ($a_0^2 \ll 1$) the expression in braces will be proportional to $(a_0^2)^{n-1}$, which, obviously, leads to a strong suppression of radiation on the higher harmonics. Figure 8.17a, b shows the photon spectra for $a_0 = 0.3$ and $a_0 = 2$. In the first case, the main part of radiation is concentrated on the first harmonic, whereas in the second case a significant contribution is observed in the spectrum, at least from 7 harmonics [$S_{\max} \approx 2.4$, which corresponds to $n_{\max} \approx 7$, see expression (8.5.9)]. Expanding the expression placed in braces in (8.5.5), for small values of the parameter $a_0^2 \ll 1$ we obtain:

$$\begin{aligned} &\frac{dN^{(1)}}{dS} \approx \pi \alpha N_0 a_0^2 \left(1 - 2S + 2S^2\right), \\ &0 \le S \le S_{\max} = \frac{1}{1 + a_0^2/2}. \end{aligned} \tag{8.5.11}$$

After elementary integration we get an estimation of the number of emitted photons: $N \approx N^{(1)} = \frac{2}{3}\pi \alpha N_0 a_0^2$.

The average energy of the emitted photons is found from the spectrum (8.5.11):

$$\langle S\rangle \approx S\int\limits_0^{S_{\max}} S\frac{dN^{(1)}}{dS}d \Bigg/ \int\limits_0^{S_{\max}} \frac{dN^{(1)}}{ds}ds \approx \frac{1}{2},$$

$$\langle \hbar\omega\rangle = \langle S\rangle\, \hbar\omega_{\max} = \frac{1}{2}\hbar\,\omega_{\max}.$$

The same value can be calculated, knowing the total radiation losses. In approximation of $a_0^2 \ll 1$ from (8.5.6) it follows the expansion:

$$\frac{dW}{dt} \approx \pi\,\alpha\,\hbar\omega_{\max} N_0 a_0^2 \frac{1+t^2}{(1+t)^5},$$

and, consequently,

$$W = \int\limits_0^{\infty} dt\frac{dW}{dt} = \frac{\pi}{3}\alpha\hbar\omega_{\max} N_0 a_0^2.$$

Hence it follows that the average energy of the photon is determined as

$$\langle \hbar\omega\rangle = \frac{W}{N} = \frac{1}{2}\hbar\omega_{\max}, \tag{8.5.12}$$

in complete analogy with the characteristics of the undulator radiation in case of $K^2 \ll 1$.

For the radiation in the intense wave field the number of emitted photons can be estimated in R-system (because the number of emitted photons is the invariant, only their average energy is changing). In R-system the electron emits per one turn the number of photons, which is proportional to the Lorentz-factor of the orbital motion:

$$n_{\text{ph}} \approx \frac{5}{\sqrt{3}}\pi\,\alpha\,\gamma = \frac{5}{\sqrt{3}}\frac{\pi\,\alpha}{\sqrt{1-\beta_R^2}} = \frac{5}{\sqrt{3}}\pi\,\alpha\sqrt{1+\frac{a_0^2}{2}} \approx \frac{5}{\sqrt{6}}\pi\,\alpha\,a_0.$$

Then, the estimation of the photon average energy is calculated similarly to (8.5.12):

$$\langle \hbar\omega\rangle = \frac{W}{N_0 n_{\text{ph}}} = \frac{0.31\,\pi\,\alpha\,\hbar\omega_{\max} N_0 a_0^2}{\frac{5}{\sqrt{6}}\pi\,\alpha\,a_0 N_0} \approx 0.15\,\hbar\,\omega_{\max} a_0.$$

Unlike the linear regime ($a_0 \to 0$), the average energy of photons in the considered case depends linearly on the field parameter a_0, and for $a_0 > 7$ exceeds the value $\hbar\,\omega_{\max} = 4\gamma_0^2\omega_0$, which is typical for the linear case (see Fig. 8.17a). From the distribution of photons (8.5.9) it is easy to go over to the cross-section of the process, using the relationship (8.3.15) again:

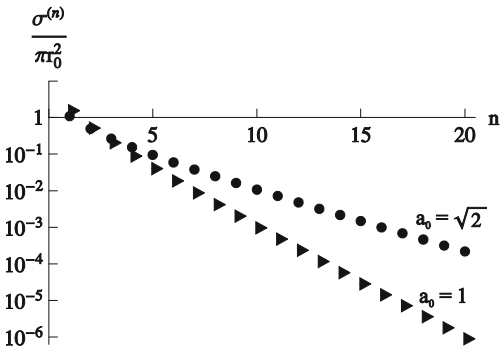

Fig. 8.18 Dependence of the "partial" cross-sections of the nonlinear Thomson scattering on the harmonic number for $a_0 = \sqrt{2}$; $a_0 = 1$

$$\frac{d\sigma^{(n)}}{dS} = \frac{4r_0^2}{\alpha a_0^2 N_0}\frac{dN^{(n)}}{dS} = 8\pi r_0^2\left\{\frac{\left[n - S\left(2 + a_0^2\right)\right]^2}{2S a_0^2\left[n - S\left(1 + a_0^2/2\right)\right]}J_n^2(nz) + J_n'^2(nz)\right\},$$

where z and S are defined by (8.5.10).

Figure 8.18 shows the dependence of "partial" cross-sections on the harmonic number

$$\sigma^{(n)} = \int_0^{n/\left(1+a_0^2/2\right)} dS\frac{d\sigma^{(n)}}{dS}, \tag{8.5.13}$$

which are calculated for parameters of the wave strength $a_0 = 1$ and $a_0 = \sqrt{2}$. As it follows from a comparison of the obtained dependence for $a_0 = 1$ with the similar one calculated for a rest electron (see Fig. 8.5b), the cross-section (8.5.13) does not depend on the Lorentz-factor, as was to be expected, since both for moving and for a rest electron the approximation $2\gamma_D \hbar\omega_0 \ll mc^2$ is used which allows to neglect the recoil effects.

8.6 Nonlinear Compton Scattering

The correct account of recoil effects in a field of strong electromagnetic wave is carried out within framework of quantum electrodynamics. One of the important consequences of the strict theory of effects being nonlinear in respect of the field

strength (including the nonlinear Compton scattering) is the increase of "effective" mass of electron (positron) [12]:

$$m_{\text{eff}}^2 = m^2\left(1+\frac{a_0^2}{2}\right).$$

Another important consequence is a "broadening" of the BCS-spectra due to nonlinear effects. Following [13], the cross-section of the BCS nonlinear process with the absorption of n photons using the invariant variables (8.4.11) can be written as:

$$\frac{d\sigma^{(n)}}{dy} = \frac{4\pi r_0^2}{xa_0^2}\left\{-4J_n^2 + \frac{a_0^2}{2}\left(1-y+\frac{1}{1-y}\right)\left(J_{n-1}^2 + J_{n+1}^2 - 2J_n^2\right)\right\}. \tag{8.6.1}$$

It should worth noting that the non-linearity parameter ξ^2 introduced in work [14] [see Eq. (3) there] is connected with the laser strength parameter a_0^2 which is used in this book (see Eq. (2.1.14)) as following $\xi^2 = a_0^2/2$.

In (8.6.1) J_m^2 are the Bessel's functions of the order $m = n-1,\ n,\ n+1$ in respect to the same argument

$$z_n = \sqrt{2}na_0\sqrt{\frac{y}{(1-y)nx}\left[1-\frac{y}{1-y}\frac{\left(1+a_0^2/2\right)}{nx}\right]}. \tag{8.6.2}$$

The spectral variable y varies within the limits

$$0 \le y \le y_{\max}^{(n)} = \frac{nx}{1+nx+a_0^2/2}. \tag{8.6.3}$$

The number of "absorbed" photons n in quantum electrodynamics can be compared with the number of harmonics of the scattered radiation in the classical electrodynamics.

Apparently, the maximum possible photon energy for the first harmonic ($n = 1$) will be less than for a linear BCS process because of the effective increasing of the electron mass in a wave field:

$$y_{\max}^{(1)} = \frac{x}{1+x+a_0^2/2} < y_{\max} = \frac{x}{1+x}$$

(see Eq. (8.4.14)).

For a weak field $a_0 \ll 1$ and, hence $z_n \ll 1$. Having written instead the Bessel's functions their expansions for $z_n \ll 1$ and keeping the first-order terms, we obtain

$$\begin{aligned} J_n^2(z_n) &\approx \frac{1}{(n!)^2}\left(\frac{z_n}{2}\right)^{2n}, \\ J_{n-1}^2(z_n) &\approx n^2\left(\frac{z_n}{2}\right)^{-2}\frac{1}{(n!)^2}\left(\frac{z_n}{2}\right)^{2n}, \\ J_{n+1}^2(z_n) &\approx \frac{1}{(n+1)^2}\left(\frac{z_n}{2}\right)^{2}\frac{1}{(n!)^2}\left(\frac{z_n}{2}\right)^{2n}. \end{aligned} \tag{8.6.4}$$

Then, it is possible to write down the cross-section of nonlinear BCS for $n = 1, 2$ in case of $a_0 \ll 1$ in explicit form:

$$\begin{aligned}\frac{d\sigma^{(1)}}{dy} &= \frac{2\pi r_0^2}{x}\left\{-4f_1 + \left(1 - y + \frac{1}{1-y}\right)\left(1 - a_0^2 f_1 + \frac{a_0^4 f_1^2}{4}\right)\right\},\\ \frac{d\sigma^{(2)}}{dy} &= \frac{2\pi r_0^2}{x} a_0^2 \frac{y}{(1-y)^2 x^2}\\ &\quad \times \left\{-4f_2 + \left(1 - y + \frac{1}{1-y}\right)\left(1 - a_0^2 f_2 + \frac{1}{9} a_0^4 f_2^2\right)\right\}.\end{aligned} \tag{8.6.5}$$

In formulae (8.6.5) the following designations are used

$$f_1 = \frac{y\left(x - xy - y - \frac{1}{2} y\, a_0^2\right)}{x^2(1-y)^2}, \qquad f_2 = \frac{y\left(2x - 2xy - y - \frac{1}{2} y\, a_0^2\right)}{4x^2(1-y)^2}.$$

We can show that $d\sigma^{(n)}/dy \sim \left(a_0^2\right)^{n-1}$, from which it follows that in case of $a_0 \to 0$ the cross-section $d\sigma^{(1)}/dy$ coincides with the linear BCS one, whereas $d\sigma^{(n)}/dy \to 0$ for all $n \geq 2$.

Generally, the cross-section of nonlinear BCS process is calculated by means of summation of expressions (8.6.1) over all possible numbers of the absorbed photons:

$$\frac{d\sigma}{dy} = \sum_{n=1}^{\infty} \frac{d\sigma^{(n)}}{dy} \approx \sum_{n=1}^{n_{\max}} \frac{d\sigma^{(n)}}{dy}. \tag{8.6.6}$$

Figure 8.19 shows the dependence of cross-section of linear BCS process on the variable y (the spectral distribution of scattered photons) for $x = 0.2;\ 0.4$.

The similar distributions for the nonlinear BCS process ($a_0^2/2 = 1$) are shown in Fig. 8.20 for $x = 0.2$ (solid curve) and $x = 0.4$ (dashed line), where the summation in formula (8.6.6) was carried out up to $n_{\max} = 20$.

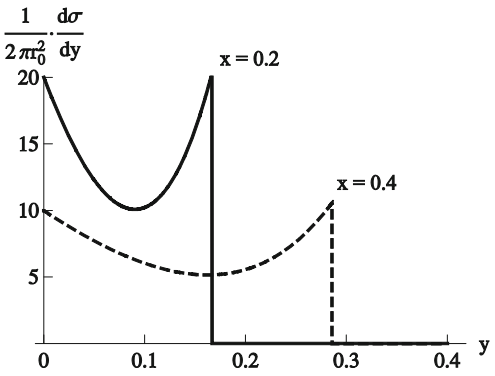

Fig. 8.19 Dependence of the cross-section of the linear BCS process on the relative energy of the scattered photon y for various values of parameter x

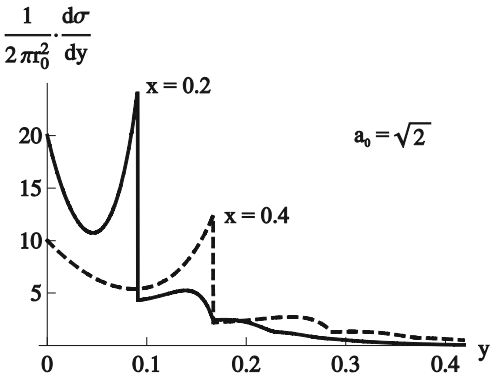

Fig. 8.20 Dependence of the cross-section of the nonlinear BCS process on the relative energy of the scattered photon y for various values of parameter x

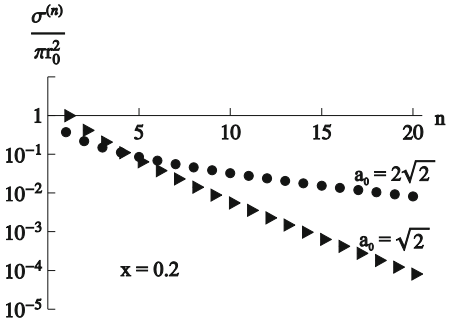

Fig. 8.21 Dependence of the "partial" cross-sections of the nonlinear BCS process on the harmonic number in case of $x = 0.2$ for various values of parameter a_0

Figure 8.21 shows the behavior of the "partial" cross-sections $\sigma^{(n)} = \int \frac{d\sigma^{(n)}}{dy} dy$ for $x = 0.2$ in case of increasing n (number of absorbed photons). The lower curve was obtained for $a_0^2/2 = 1$, from which it follows that for $n = 8$ the cross-section drops by two orders of magnitude, whereas the upper curve is calculated for $a_0^2/2 = 2$, which decreases more smoothly.

Comparing the spectra of linear and nonlinear BCS processes (see Figs. 8.19, 8.20), it is possible to note that the total cross-section of the nonlinear process

$$\sigma = \sum_{n=1}^{\infty} \sigma^{(n)} = \sum_{n=1}^{n_{\max}} \sigma^{(n)}$$

(in other words, the number of scattered photons) decreases as compared with the linear case (about 24% for $x = 0.2$ and 16% for $x = 0.4$ in case of $a_0^2/2 = 1$). However the average energy in the spectrum

$$\langle y \rangle = \int y \frac{d\sigma}{dy} \Big/ \int \frac{d\sigma}{dy} dy$$

does not vary practically.

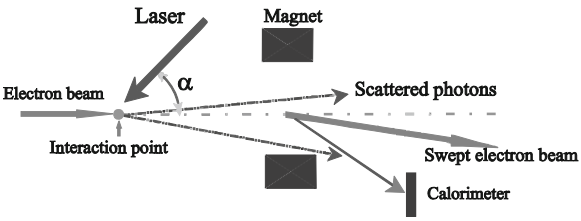

Fig. 8.22 The experimental setup for the nonlinear Compton scattering detection

The experiment devoted to observation the nonlinear Compton scattering process was carried out in 1996, at the Stanford linear accelerator (SLAC) using electrons with energy $E_0 = 46.6$ GeV [14]. The experimental setup is shown in Fig. 8.22. A laser beam with a wavelength $\lambda_0 = 1.054$ μm overlaps with the electron beam at the interaction point at the angle $\alpha = 17^\circ$. The energy of laser flash was equal to 0.8 J, that for the focal spot with area $S = 60\,\mu m^2$ and duration of flash $t = 1.5 \times 10^{-12}$ s provided the field intensity up to $I_{\max} \approx 10^{18}\,\mathrm{W/cm^2}$ (i.e. $a_0/\sqrt{2} = 0.6$).

The scattered electrons are detected in this experiment and their energy is measured as well. For the chosen geometry

$$x = 2\gamma_0 \frac{\hbar\omega_0}{mc^2}(1 + \cos\alpha) = 0.83.$$

Thus, the maximal energy of photons in the linear BCS process

$$\hbar\omega_{\max} = E_0 y_{\max}^{\mathrm{lin}} = E_0 \frac{x}{1+x}.$$

Otherwise, the minimal energy of the scattered electrons in this case was $E_{\min} = E_0 - \hbar\omega_{\max} = E_0/(1+x) = 25.5$ GeV.

The presence of scattered electrons with energy lower than $E_{\min}$ indicates the appearing of the significant nonlinearity of the BCS process, since

$$y_{\max}^{(n)} = \frac{nx}{1 + nx + a_0^2/2} < y_{\max}^{\mathrm{lin}}.$$

Figure 8.23 shows the spectra of scattered electrons for the considered parameters, calculated in accordance with formulae (8.6.1), i.e. for the ideal case. The experimental spectra should differ slightly.

The scattered electrons with energies from 12.5 up to 20.5 GeV, i.e. in the forbidden energy range for the kinematics of a linear BCS process, were registered in the experiment. Figure 8.24 shows the experimental yield of scattered electrons with energy corresponding to the left part ("tail") of distribution dN/dE (Fig. 8.23) for $n = 2, 3, 4$; in case of changes in field intensity of laser flash in comparison with results of numerical simulation.

As it follows from the figure, the experiment agrees with theory well.

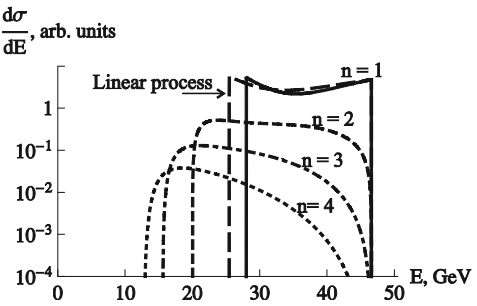

Fig. 8.23 Dependence of the "partial" cross-sections ($n = 1, 2, 3, 4$) of the nonlinear BCS-process on the energy of the scattered electron for conditions of experiment [14]. Here is also shown the cross-section of a linear BCS process (*dashed line*)

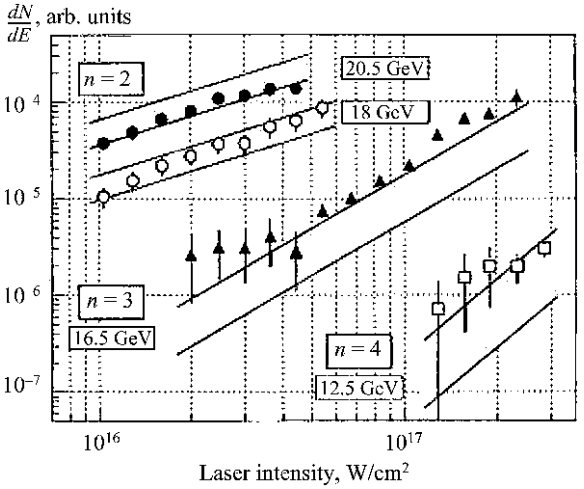

Fig. 8.24 Comparison of dependence of the experimentally measured yields of scattered electrons on the intensity of laser flash with theoretical estimations

8.7 The Laser-Synchrotron X-ray Source

The authors of works [15, 16] have proposed the concept of a tunable monochromatic X-ray source, based on the process of scattering of intense laser radiation by the electron beam from a compact storage ring with energy about 100 MeV. The term "laser-synchrotron source" is suggested in these studies, since in this case the resulting radiation is considered from the point of view of emission in the "light undulator".

Figure 8.25 shows the proposed scheme. The electron bunches are circulating in a storage ring with a diameter of $\sim$2 m (i.e. the orbit circumference is $\sim$6 m, that corresponds to the passage frequency of bunches $\sim 5 \times 10^7$ Hz). The laser radiation is "injected" into the optical resonator, being reflected from the mirrors of which the laser photons can repeatedly collide with the electron bunches. The duration of laser flashes and their frequency, as well as the parameters of the optical resonator should be matched with the characteristics of the storage ring. So, for example, for the Fabry–Perot's resonator with reflection coefficient of mirrors

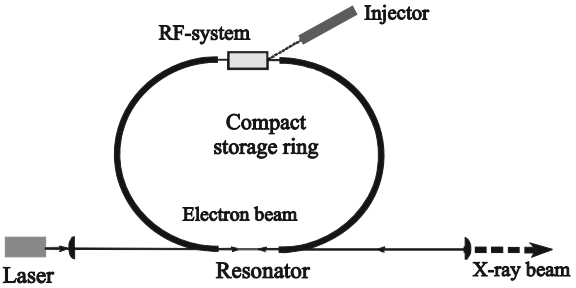

Fig. 8.25 The scheme of laser-synchrotron X-ray source

$R = 0.999$ the optical laser with average power of ~ 400 W, can provide a yield of the scattered photons up to $\sim 10^{14}$ phot./s for the current circulating in an orbit ~ 0.1 A [17]. For electron energy $E_0 = 100$ MeV and laser photons with a wavelength $\lambda_0 \sim 1$ μ the maximal energy of scattered photons is $\hbar\omega_{\max} \approx 160$ keV.

However, the calculations of the spectral–angular characteristics of radiation, which is generated by the collision of electron and photon beams with the specified distributions in space and time, is more convenient to carry out considering this process as the backward Compton scattering.

As it was already noted, the spectral distribution of scattered photons is described by cross-section (8.4.15), which completely coincides with the spectrum of undulator radiation in case of $x \to 0$. In the considered case $x \approx 1.6 \times 10^{-3} \ll 1$. Consequently, in a good approximation we may use the variable:

$$y = \frac{\hbar\omega}{\gamma_0 mc^2} \approx \frac{x}{1 + \gamma^2\theta^2} \times \frac{1}{2}.$$

It should be noted that the "soft" part of the spectrum ($y < x/2$) is formed due to photons scattered at the angles $\theta > \gamma^{-1}$. It is clear, if we introduce a hard collimation of the radiation beam, it is possible to achieve significant monochromatization of X-ray beam radiation (at the cost of some loss of intensity).

Figure 8.26b shows the BCS spectrum obtained for collimation angle $\theta_c = \gamma^{-1}/2\,(y_{\min} = 0.8)$. As can be seen from the figure, in the last case the monochromaticity $\Delta\omega/\omega_{\max}$ achieves $\sim 20\%$.

The electron–photon interaction, which leads to generation of a beam of hard scattered photons, occurs in case of collision of accelerated electron bunches, with the focused laser radiation, which also represents a sequence of photon bunches.

As a result, the intensity of the scattered photons is determined not only by the number of electrons and photons in the colliding bunches, but also by their "overlap" in the space and time. A special characteristic, which takes into account all these factors, is introduced for the colliding bunches—the so-called luminosity L [18]. By definition for head-on-collisions,

$$L = 2cN_{\text{ph}}N_e \int dV \int dt f_{\text{ph}}(x, y, z + ct) f_e(x, y, z - \beta ct), \tag{8.7.1}$$

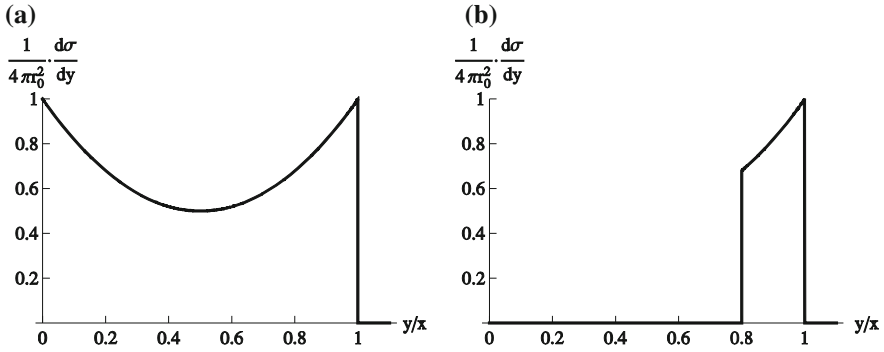

Fig. 8.26 The spectrum of scattered photons: in the total cone under the condition $2\gamma\hbar\omega_0/mc^2 \ll 1$ (**a**); in case of collimation $\theta_c = 0.5\gamma$ (**b**)

where N_{ph}, N_e are the number of particles in the photon and electron bunches; f_{ph}, f_e are the normalized distributions of photons and electrons in the bunches.

To perform the analytical evaluation we shall consider the monodirected electron and photon bunches with a Gaussian distribution in the transverse and longitudinal directions (along the axis z):

$$\begin{aligned} f_e &= \frac{2}{(2\pi)^{3/2}\sigma_e^2\ell_e}\exp\left\{-\frac{r^2}{\sigma_e^2}-\frac{(z-\beta ct)^2}{2\ell_e^2}\right\}, \\ f_{ph} &= \frac{2}{(2\pi)^{3/2}\sigma_{ph}^2\ell_{ph}}\exp\left\{-\frac{r^2}{\sigma_{ph}^2}-\frac{(z+ct)^2}{2\ell_{ph}}\right\}, \\ r^2 &= x^2+y^2. \end{aligned} \tag{8.7.2}$$

In (8.7.2) the transverse sizes of the bunches are characterized by the variances σ_{ph}, σ_e, whereas the length of the bunches—by the values ℓ_{ph}, ℓ_e. The luminosity for the distributions (8.7.2) is calculated analytically

$$L = 2N_eN_{ph}\frac{1}{\pi\left(\sigma_e^2+\sigma_{ph}^2\right)} \tag{8.7.3}$$

As one can see from here the luminosity does not depend on the bunch lengths ℓ_{ph}, ℓ_e for a head-on collision (in other words, on the interaction time). The number of scattered photons is determined by the luminosity and the cross-section σ:

$$N_2 = L\sigma = 2N_eN_{ph}\frac{\sigma}{\pi\left(\sigma_e^2+\sigma_{ph}^2\right)}. \tag{8.7.4}$$

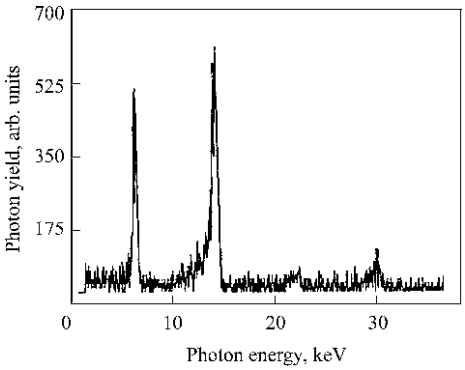

Fig. 8.27 The spectrum of scattered photons by the electrons with energy E = 20 MeV [19]. Peak at 7.35 keV corresponds to the scattering of the first harmonic of a laser with $\lambda_1 = 1.064\,\mu m$, peak at 14.8 keV—the second harmonic ($\lambda_2 = 0.53\,\mu m$)

Let us express the number of photons in the laser flash N_{ph} through the power density of the focused laser radiation I:

$$I = P/S_{\text{ph}}\left[\text{W/cm}^2\right],$$

where P is the power of laser flash, S_{ph} is an area of the laser flash focus. If A is the total energy of the flash, then

$$P_{\text{ph}} = \frac{A}{\ell_{\text{ph}}/c} = \frac{A}{\omega_0}\frac{c\omega_0}{\ell_{\text{ph}}} = N_{\text{ph}}\frac{\hbar\, c\, \omega_0}{\ell_{\text{ph}}}. \tag{8.7.5}$$

As a rule, the radius of the accelerated electron beam σ_e in the modern electron accelerators considerably exceeds the minimal attainable radius of laser focus σ_{ph}, therefore from (8.7.4) we obtain:

$$N_2 = 2N_e\frac{P}{\pi\sigma_e^2}\frac{\ell_{\text{ph}}\sigma}{c\omega_0} = 2N_e I\frac{\ell_{\text{ph}}\sigma}{c\omega_0} \tag{8.7.6}$$

The one of the first experiments concerning the generation of monochromatic X-ray in case of scattering of laser radiation on the accelerated electron bunches was carried out at the linear accelerator at the Accelerator Center in Idaho (USA) with electron energy of 20 MeV [19]. There was used the solid-state laser Nd:YAG with a peak power of 100 MW. The wavelength of the first harmonic was equal to 1.064 μm, and of the second one—0.532 μm. During the head-on collision with 20 MeV electrons in a spectrum of the scattered radiation the lines with energy $\hbar\omega_2^{(1)} \approx 7.5$ keV, $\hbar\omega_2^{(2)} \approx 15$ keV should be observed. The spectrum of photons emitted within the collimation angle $\theta_c \ll \gamma^{-1}$ was measured in the experiment.

The experimental results are shown in Fig. 8.27, demonstrating two narrow lines which energy corresponds to the calculation. The small peaks in the range of photon energies $\hbar\omega > 20$ keV are caused by overlapping of signals in the detector (pile-up effect).

In order to estimate the yield of photons, formula (8.7.4) can be used. The charge of each bunch in the accelerator was equal to 8 nC (i.e. $N_e = 5 \times 10^{10}$). The transverse dimensions of the electron bunch at the interaction point were equal to $\Delta x = 4.8$ mm and $\Delta y = 2.8$ mm, what corresponds to the electron beam area $S = \pi \Delta x \Delta y/4 = 10.5$ mm^2. The number of photons can be estimated from the energy of the laser flash (0.75 J for the first harmonic and $N_{ph}^{(1)} = 4 \times 10^{18}$ photons). The laser radiation was focused with a spot with diameter of 0.24 mm for the first harmonic and 0.12 mm for the second one.

For the cross-section calculation we shall integrate the expression (8.4.9) over the polar angle in the range $0 \le \theta_c \le 0.3\gamma^{-1}$:

$$\sigma_c = 8\,\pi\, r_0^2 \gamma^2 \int_0^{0.3/\gamma} \frac{1 + (\gamma\theta)^4}{\left[1 + (\gamma\theta)^2\right]^4} \theta d\,\theta = 0.28\,\pi\, r_0^2 = 0.07 \times 10^{-24}\,\mathrm{cm}^2.$$

Substituting the obtained value in the numerator of the formula (8.7.4) and replacing the transverse area of a cylindrical electron bunch $\pi\sigma_e^2$ with the area of elliptic one $\pi \Delta x \Delta y/4$, we have $N_2^{(1)} \approx 0.3 \times 10^6$ photon/bunch. The experimental value of the yield for both lines $N_2^{(1)} + N_2^{(2)}$ is equal to 3×10^5 photons/bunch.

The usage of a storage ring together with an optical resonator instead of a linear accelerator to provide the multiple interaction between the electron and photon bunches, as proposed in [16], will allow to increase the efficiency of X-rays generation by several orders of magnitude. So, for example, the estimations [17] show that it is possible to obtain the operational beam of monochromatic X-rays with energy $\hbar\omega \approx 33$ keV using the storage ring with an electron energy $E \sim 100$ MeV and current 100 mA and a commercial solid-state laser. Such a system can provide the yield of X-ray photons in the form of a train of subpicosecond duration with the number of photons up to 10^{11}/s.

It should be expected that advancements in the accelerator and laser technology in the near future allow to develop and create a qualitatively new sources of monochromatic X-rays with tunable energy.

References

1. Nikishov, A.I., Ritus, V.I.: Sov. Phys. JETP. **46**, 776 (1964)
2. Sarachik, E.S., Schaffert, G.T.: Classical theory of the scattering of intense laser radiation by free electrons. Phys. Rev. D. **1**, 2738–2753 (1970)
3. Alan, J., Daniel, Z. (eds.) Gradshteyn and Ryzhik's Table of Integrals, Series, and Products. AP (1996)
4. Phuoc, K.Ta., Rousse, A., Pittman, M., et al.: X-ray radiation from nonlinear Thomson scattering of an intense femtosecond laser on relativistic electrons in a helium plasma. Phys. Rev. Lett. **91**, 195001-1–195001-4 (2003)
5. Rullhusen, P., Artru, X., Dhez, P.: Novel Radiation Sources Using Relativistic Electrons. World Scientific, Singapore (1998)

6. Akhiezer, A.I., Berestetzkiy, V.B.: Quantum Electrodynamics. Moskow, Nauka (in Russian) **71** (1989)
7. Federici, L., Giordano, G., Matone, G., et al.: Backward Compton scattering of laser light against high-energy electrons: Ladon photon beam at Frascati. Nuovo Cimento B **59**, 247 (1980)
8. D Angelo, A., Bartalini, O., Bellini, V., et al.: Generation of Compton backscattering X-ray beams. Nucl. Instrum. Methods A **455**, 1–6 (2000)
9. Kezerashvili, G.Ya., Lysenko, A.P., Shatunov, Y.M., Vorobiev, V.P.: Colliding beam polarization measurement using superconducting helical undulator at VEPP-2M storage ring. Nucl. Instrum. Methods A **314**, 15–20 (1992)
10. Glotin, F., Ortega, J.-M., Prazeres, R., et al.: Tunable X-ray generation in a free-electron laser by intracavity compton backscattering. Phys. Rev. Lett. **77**, 3130 (1996)
11. Esarey, E., Ride, S.K., Sprangle, P.: Nonlinear Thomson scattering of intense laser pulses from beams and plasmas. Phys. Rev. E. **48**, 3003–3021 (1993)
12. Nikishov, A.I., Ritus, V.I.: Trudy FIAN **111**, (1979). (In Russian)
13. Ivanov, Yu.S., Kotkin, G.L., Serbo, V.G.: Complete description of polarization effects in emission of a photon by an electron in the field of a strong laser wave. Eur. Phys. J. C. **36**, 127–1945 (2004)
14. Bula, C., McDonald, K.T., Prebys, J., et al.: Observation of nonlinear effects in Compton scattering. Phys. Rev. Lett. **76**, 3116–3119 (1996)
15. Sprangle, P., Ting, A., Esarey, E., Fisher, A.: Tunable, short pulse hard X-rays from a compact laser synchrotron source. J. Appl. Phys. **72**, 5032 (1992)
16. Huang, Z., Ruth, R.D.: Laser-electron storage ring. Phys. Rev. Lett. **80**, 976 (1998)
17. Bessonov, E.G., Vinogradov, A.V., Gorbunkov, M.V., et al.: Laser electron-beam X-ray source for medical applications. Phys. Usp. **46**, 872–876 (2003)
18. Wiedeman, H.: Particle Accelerator Physics, 2nd edn. Springer, New York (1999)
19. Chouffani, Kh., Wells, D., Harmon, F., et al.: Laser-Compton scattering from a 20 MeV electron beam. Nucl. Instrum. Methods A. **495**, 95–106 (2002)

Chapter 9
Conclusion

As it was shown above, the radiation in periodic structures posesses a quasi-monochromatic spectrum, and a monochromaticity degree (spectral line width at half maximum) depends on the number of periods N_0, an angle θ_c of radiation collimation and a degree of nonlinearity of the process. Position of a line in a spectrum is determined by the period of structure, the photon emission angle and energy of the initial electron.

During the interaction of modulated electron beam (the distance between bunches is about 1 cm) with a 1 cm period grating, the Smith–Purcell monochromatic radiation is generated in the terahertz range [1], which can be used in biology, medicine, etc. In the process of backward Compton scattering of laser photons by ultrarelativistic electrons with an energy 2 GeV, the energy of scattered photons achieves hundreds of MeV [2]. The characteristics of photon beams from such different sources can be calculated using rather simple approaches described in the book presented.

Alongside with the creation of such beams aimed at various purposes, the monochromatic radiation generated by electrons in periodic structures, "carries" the information about the parameters of the initial electron beam. Electrons moving in a vacuum close to an optical grating or trough the laser flash, have lost an energy only through the radiative mechanisms (in this case through the Smith–Purcell radiation or BCS process), whereas other dissipative mechanisms, which occur during the passage of electrons through the solid-state targets, do not exist. Since the radiation losses via considered mechanisms are insignificant, then, as a rule, the parameters of the initial electron beam do not be practically distorted. By measuring the radiation characteristics such as monochromaticity, angular distribution, polarization, parameters of an initial electron beam can be determined. This approach is called non-perturbative diagnostics and it acquires the particular importance in designing X-ray free electron lasers or electron–positron colliders, where the low-emittance beams are used and methods of traditional diagnostics are practically inapplicable.

In the experiment [3] in order to measure the transverse sizes of electron beam there was used the BCS process, where the laser beam with a diameter smaller than

A. P. Potylitsyn, *Electromagnetic Radiation of Electrons in Periodic Structures*, Springer Tracts in Modern Physics, 243, DOI: 10.1007/978-3-642-19248-7_9,

the electron beam was directed perpendicularly to the electron momentum. By analogy with the diagnostics, where a thin wire is used, which is intersected by the electron beam, the described method was named "laser wire technique". Recently, there have been appeared proposals on usage the Smith–Purcell radiation for measuring of longitudinal sizes of the electron bunches of accelerators and such experiments have already begun [4].

Beams of circularly-polarized γ-rays will be used to generate the longitudinally polarized positrons for their acceleration in the designed electron–positron collider. As a source of circularly-polarized γ-quanta there is suggested to use either the backward Compton scattering of circularly-polarized laser photons by the beam of ultrarelativistic electrons or beam of undulator radiation from a helical undulator.

The beam of circularly-polarized laser radiation with a wavelength of $\lambda = 532$ nm scattered by the 1.28 GeV electrons in experiment [5], allowed to produce the circularly-polarized photon beam with maximal energy $\hbar\omega = 56$ MeV, which was used then to produce e^+e^- pairs in an amorphous target. Measurements of longitudinal polarization of positrons with energy in the range 28–44 MeV have shown that the average longitudinal polarization of positrons P_ℓ was 73%.

The first experiment [6] concerning a generation of polarized positrons using undulator radiation was performed in 2006 on the 46.6 GeV electron beam, which passed through the helical undulator with a period of 2.54 mm, length 1 m and a parameter $K = 0.17$. The circularly-polarized undulator radiation with energy of the first harmonic $\hbar\omega = 7.9$ MeV was generated. Positrons were generated by such a beam in the amorphous tungsten target with thickness of 0.2 rad. lengths. Authors of the experiment [6] have measured the longitudinal polarization of positrons with energy 4.6–7.4 MeV and obtained the value $P_\ell = 66-76\,\%$.

Recently the Lyncean Technologies, Inc (USA) has established the new facility—Compact Light Source, based on BCS process using a commercial laser and miniature storage ring (room size scale), see [7]. They have obtained a hard X-ray beam which allow to use one for applications to new methods of imaging in biology and medicine [8].

Undoubted progress of the accelerator and laser technology allowing to receive the operational beams (including the polarized ones) with unattainable earlier parameters has led to the fact that an up-to-date scientist in the field of accelerator physics should know much wider range of the questions from the classical and quantum electrodynamics, laser physics, solid state physics, etc. This book may be considered as the attempt to give the such basis.

References

1. Korbly, S.E., Kesar, A.S., Sirigiri, J.R. Temkin, R.J.: Observation of frequency-locked coherent terahertz Smith–Purcell radiation. Phys. Rev. Lett. **94**, 054803-1–054803-4 (2005)

2. Kezerashvili, G.Ya., Milov, A.M., Wojtsekhowskii, B.B.: The gamma ray energy tagging spectrometer of ROKK-2 facility at VEPP-3 storage ring. Nucl. Instrum. Methods A **328**, 506–511 (1993)
3. Sakai, H., Honda, Y., Sasao, N., et al.: Measurement of an electron beam size with a laser wire beam profile monitor. Phys. Rev. Special Topics **4**, 0228011–0228016 (2001)
4. Blackmore, V., Doucas, G., Perry, C., et al.: First measurements of the longitudinal bunch profile of a 28.5 GeV beam using coherent Smith–Purcell radiation. Phys. Rev. ST-AB **12**, 032803 (2009)
5. Omori, T., Fukuda, M., Hirose, T., et al.: Efficient propagation of polarization from laser photons to positrons through Compton scattering and electron–positron pair creation. Phys. Rev. Lett. **96**, 114801 (2006)
6. Alexander, G., Barley, J., Batygin, Y., et al.: Observation of polarized positron from an undulator-based source. Phys. Rev. Lett. **100**, 210801 (2008)
7. http://www.technologyreview.com/biomedicine/20149/
8. Bech, M., Bunk, O., David, C., et al.: Hard X-ray phase-contrast imaging with the compact light source basen on inverse Compton X-rays. J Synchrotron. Radiat. **16**, 43–47 (2009)

Index